Towards an Ytterbium based optical waveform synthesizer

Dissertation
zur Erlangung des Doktorgrades Dr. Rer. Nat.

eingereicht an der Fakultät für Mathematik, Informatik und Naturwissenschaften
Fachbereich Physik
Universität Hamburg

vorgelegt von
Ing. IOGS, M.Sc. Anne-Laure Calendron

Hamburg, Dezember 2014

Erstgutachter: Prof. Franz X. Kärtner
Zweitgutachter: Prof. R. J. Dwayne Miller

Selbstständigkeitserklärung

Hiermit bestätige ich, die vorliegende Dissertation selbst verfasst und keine weitere als die angegebenen Quellen und Hilfsmittel verwendet zu haben.

Acknowledgements

I would like to acknowledge first Prof. Franz X. Kärtner for the great opportunity he gave me to work on this exciting and challenging project during my PhD thesis.

Inside the group, I would like to greatly thank Huseyin Cankaya for his contribution to this project and the intensive lab work. I thank the whole group and in particular Giovanni Cirmi, Damian Schimpf, Oliver Mücke and Michael Hemmer in Hamburg and Jeff Moses at MIT for the helpful discussions. With regards to the cryogenic amplifier, I would like to acknowledge Luis E. Zapata and the 1J team (Hua Lin, Wenqian Ronny Huang, Fabian Reichert, and Kelly Zapata).

Furthermore, I would like to thank Max Lederer from the European-XFEL GmbH for fruitful discussions.

I am extremely grateful to the CFEL engineering team: the mechanical engineering team with Lars Gumprecht, Thomas Tilp, Andrej Berg, Tjark Delmas, Julia Maracke and Matthias Schust and the electronic technicians Johann Derksen and André Hömke. The mechanical and electrical engineers made possible the realization of several modules of the laser system, among others the regenerative amplifier, the cryogenic amplifier and the compressors of the pump line.

I also would like to thank the secretary Christine Berber for her dedicated work and all her support in the administrative jungle.

At last, I thank my family, my boyfriend and my friends for their support and encouragements during this time, especially Joachim Meier and Cyril Brûlebois for their proof-reading of the manuscript.

Abstract

Molecular and atomic structures and dynamics have been unraveled with the development of ultrafast, high-energy optical lasers, delivering pulses from the infra-red to the X-rays. Soft X-Rays attosecond pulses can be generated via high-harmonic generation from an optical high-energy, single-cycle laser. Coherent pulse synthesis of few-cycle, high-energy pulses is a promising technique to generate isolated attosecond pulses for its scalability in spectral bandwidth and energy. Here we consider pulse synthesizer based on OPCPAs. Four major parts compose a waveform synthesizer: first a pump line scalable to high energies, second a broadband carrier-envelope phase (CEP) stable front-end, third a sequence of parametric amplification stages to amplify the front-end pulses to high energies, and fourth synchronization and stabilization of the pulses. The state of the art waveform synthesizers rely on Ti:sapphire pump lasers, which are advantageous for the mature technology and the ultrashort pulses, but are intrinsically limited in achievable average power. This limitation in the waveform synthesizer pump line can be overcome by using alternative laser materials, like ytterbium doped hosts. In this thesis, the developments toward an ytterbium based waveform synthesizer are presented.

The pump line of the synthesizer realized in this work consists of a seed oscillator with chirped fiber Bragg grating pulse stretcher and two main amplifiers. The pulse energy of the regenerative amplifier reaches 6.5 mJ at 1 kHz repetition rate. Its output is split in two: one part is compressed to 615 fs transform-limited pulses to drive the front-end. The second part seeds a multi-pass amplifier based on composite thin-disk technology, which boosts the energy up to 72 mJ. With the compressed pulses of the regenerative amplifier, the front-end based on white-light generation is demonstrated with a passive CEP stability of 90 mrad over 11 h. The best adapted parameters for white-light supercontinuum generation with sub-picosecond long pulses were found after an experimental study. A narrow-band fraction of the super-continuum is parametrically amplified. The complete electric field of the amplified signal was retrieved from a FROG measurement. The smooth and well-behaved phase is a proof that the broadband pulse generated by white-light continuum remains a single, compressible pulse. The corresponding CEP stable idler generates a CEP stable supercontinuum, which is split in the channels of the waveform synthesizer. These broadband pulses are then amplified to the µJ level with parametric amplifiers. The pulse synthesis and the dispersion management is discussed.

Kurzfassung

Die Struktur der Materie auf der molekularen und atomaren Skala und ihre Dynamik wurde durch die Entwicklung von ultrakurzen, hoch-energetischen Lasern, die vom infrarotem bis im EUV-Bereich Spektren aufweisen, aufgelöst. Die Erzeugung von weichen Röntgen, attosekunden-Pulsen werden durch die Konversion von hoch-energetischen, Einzel-Zyklus optischen Impulsen durch die Erzeugung von hohen Harmonischen ermöglicht. Die kohärente Pulssynthese von hochenergetischen Pulsen mit wenigen Zyklen ist aufgrund der Skalierbarkeit der spektralen Bandbreite und der Energie eine vielversprechende Technologie, um isolierte attosekunden-Pulse zu erzeugen. Ein Frequenzsynthesizer besteht aus vier Hauptbestandteilen: erstens aus zu hohen Energien skalierbaren Pumplasern, zweitens einem breitbandigen Front-end mit stabiler Träger-Einhüllenden Phase, drittens einer Folge von hochenergetischen Verstärkungsstufen, und viertens einem Pulssynchronisations- und Stabilisierungssystem. Die Ti:Sapphir Laser, worauf die gegenwärtigen Frequenzsynthesizer typischerweise basieren, sind in der erreichbaren Durchschnittsleistung begrenzt. Diese Begrenzung kann mit alternativen Lasermaterialien, wie Ytterbium dotierten Grundmaterialien, überwunden werden. Diese Dissertation stellt die Architektur sowie die Implementierung eines skalierbaren Ytterbium-basierten Frequenzsynthesizers und den "Synthesizer Front-ends" dar.

Der in dieser Arbeit vorgestellte Pumplaser des Synthesizers besteht aus einem Seedoszillator mit frequenzverschobenen Faser Bragg Gitter Strecker und zwei Hauptverstärkern, einen regenerativen Verstärker sowie einen mutipass Verstärker. Die aus dem regenerativen Verstärker extrahierte Pulsenergie erreicht 6.5 mJ bei 1 kHz Pulswiederholungsrate. Der Ausgang ist in zwei Pfade aufgeteilt: ein Teil wurde auf 615 fs transformationslimitierte Pulslänge komprimiert, um das "Front-End" anzutreiben. Der zweite Teil wird in einem Multi-pass-Verbundscheibenverstärker auf 72 mJ erhöht. Das auf Weißlichtsuperkontinuum basierende und mit dem Ausgang des regenerativen Verstärkers angetriebene Front-end demonstriert eine passive CEP Stabilität von 90 mrad über 11 Stunden Dauer. Eine experimentelle Studie hat die für die Weißlichterzeugung mit sub-pikosekunden langen Pulsen am besten angepassten Laser-Parameter bestimmt. Ein schmallbandiger spektraler Anteil des Superkontinuums wird parametrisch verstärkt. Das komplette elektrische Feld des verstärkten Signals wird aus einer FROG-Messung erfasst. Die gleichmäßige Phase beweist, dass sich der breitbandige, durch Weißlichtkontinuum erzeugte Puls wie ein einzelner und komprimierbarer Puls verhält. Der entsprechende CEP stabile Idler erzeugte ein weiteres CEP stabiles Superkontinuum, das zwischen den Armen des Synthesizers aufgeteilt wird. Diese breitbandigen Pulse werden anschließend durch parametrische Verstärkung auf das µJ Niveau gebracht. Die Pulssynthese und das Dispersionsmanagement wird diskutiert.

Résumé

Le développement de lasers ultra-rapides à haute énergie, livrant des impulsions dont le spectre s'étend de l'infra-rouge aux rayons X, a permis l'exploration de la matière et de sa dynamique à l'échelle moléculaire et atomique. Les impulsions attosecondes avec un spectre dans le domaine des rayons X sont produites par multiplication de fréquence d'un laser optique produisant des impulsions ayant une durée de quelques cycles optiques à haute énergie. La synthèse cohérente d'impulsions à haute énergie et longues de quelques cycles optiques est une technique prometteuse pour produire des impulsions attosecondes, car elle est extensible en largeur de bande spectrale et vers les hautes énergies. Un synthétiseur de fréquences est composé de quatre parties principales: en premier lieu, une ligne de pompe extensible à de hautes énergies, en second lieu une partie frontale à basse énergie avec une large bande spectrale stable en phase, en troisième lieu une succession d'amplificateurs amenant la partie frontale à de hautes énergies, et enfin une synchronisation et une stabilisation des impulsions. Les synthétiseurs de fréquence à la pointe de la technologies reposent sur des lasers Ti:saphir qui sont intrinsèquement limités en puissance moyenne. Cette limitation peut être surmontée en utilisant d'autres matériaux lasers dopés par exemple à l'Ytterbium. Cette thèse présente les développements vers un générateur de fonctions optiques, aussi nommé synthésiseur de fréquences, reposant sur un laser de pompe dopé à l'Ytterbium.

La ligne de pompe du synthétiseur de fréquences réalisé dans ce travail consiste en un oscillateur suivi d'un étireur à réseau de Bragg fibré avec dérive de fréquence et de deux amplificateurs principaux. L'énergie des impulsions en sortie de l'amplificateur régénératif atteint 6.5 mJ à 1 kHz de fréquence de répétition. De cette sortie divisée en deux parts, l'une est amplifiée à 72 mJ par un amplificateur multi-passes dont le module de gain est un disque composite. La seconde partie est comprimée pour donner des impulsions longues de 615 fs proche de la limite de Fourier et qui fournit les impulsions d'entrée de la partie frontale à basse énergie. Cet avant est composé d´un étage de génération de lumière blanche et fournit des impulsions avec une relation de phase fixe entre la porteuse et l´enveloppe; la stabilité de la phase est de 90 mrad sur 11 h. Les paramètres les plus adaptés à la génération de lumière blanche avec des impulsions proche de la picoseconde sont déterminés à partir d'une étude expérimentale. Une partie limitée en spectre du super-continuum est amplifée paramétriquement. Le champ électrique complet de ce signal amplifié est recouvré à partir d'une mesure de FROG. La monotonie de la phase spectrale du super-continuum prouve que des impulsions individuelles et compressibles sont générées à cet étage. L'idler correspondant est stable en phase et génère un supercontinuum avec une relation de phase fixe entre la porteuse et l´enveloppe, qui est divisé entre les branches du synthétiseur. Les impulsions à large spectre sont ensuite am-

plifiées jusqu´au µJ avec des amplificateurs paramétriques et la gestion de la dispersion est discutée.

Contents

1 Introduction

Einstein explained the principle of light amplification by stimulated emission (LASER) in 1916 [1]. Then Schawlow and Townes, in 1954, implemented the first Maser in the microwave domain [2]. In 1960, Maiman demonstrated the first optical laser [3]. From that time onwards, lasers have never stopped changing our lives. They form the fundamental technology behind modern telecommunications, are ubiquitous in industrial manufacturing and enable numerous medical applications, just to name a few of the many applications. They are universally used in research areas such as biology and physics.

Since the invention of the Ti:Sapphire laser in the 80's [4], ultrashort, solid-state lasers offer high energy, femtosecond pulses for studying fast transitions between molecular states. At the beginning of the 2000's, the development of attosecond sources opened the door to real time observation of electron dynamics in atoms [5]. Combining ultrashort pulses with high energies and high repetition rates permits the realization of real-time movies of atomic and molecular dynamics [6, 7]. Another interesting science case is the study of ultrafast charge transport from atoms on surfaces, which was shown to occur on an attosecond time scale [8, 9].

With ultra-broadband, high energy pulses sub-cycle by nature, it should be possible to obtain single attosecond pulses at multiple spectral ranges, from the ultra-violet (UV) to the extreme ultra-violet (EUV). The corresponding photon energies range then from $\sim$20 eV up to keV, beyond the water-window. High pulse energies are required to generate EUV pulses and to perform novel EUV pump-probe experiments. To eliminate the effects due to pulse trains on a target, research groups strike at developing isolated attosecond pulse sources.

EUV and X-ray pulses have been generated via two different mechanisms: EUV, attosecond pulses are generated by high harmonic generation (HHG) from an optical laser [5, 10], whereas X-Ray pulses are produced by free-electron lasers or inverse Compton scattering based sources [11, 12, 13, 14, 15].

HHG for producing attosecond pulses can be described within certain limitations by the three-step model [16], illustrated in figure 1.1: A high-energy laser is focused into a gas target and the very intense laser field leads to tunnel ionization of the weakest bound electron. The first half cycle of the driving laser pulse bends the electric field of the atom, so that an electron tunnels out of the potential well, as shown in figure 1.1a. The freed electron is accelerated by the laser field during the next half cycle (figure 1.1b) before it returns to the parent ion (figure 1.1c) and eventually recombines (figure 1.1d). Depending on the ionization time, the trajectories of the freed electrons may return or not. During recombination an X-ray pulse is emitted. The tunneling of the electron takes place only above a certain threshold field strength, making this process strongly dependent on the electric field of the incoming laser beam. If several electric field cycles in the pulse

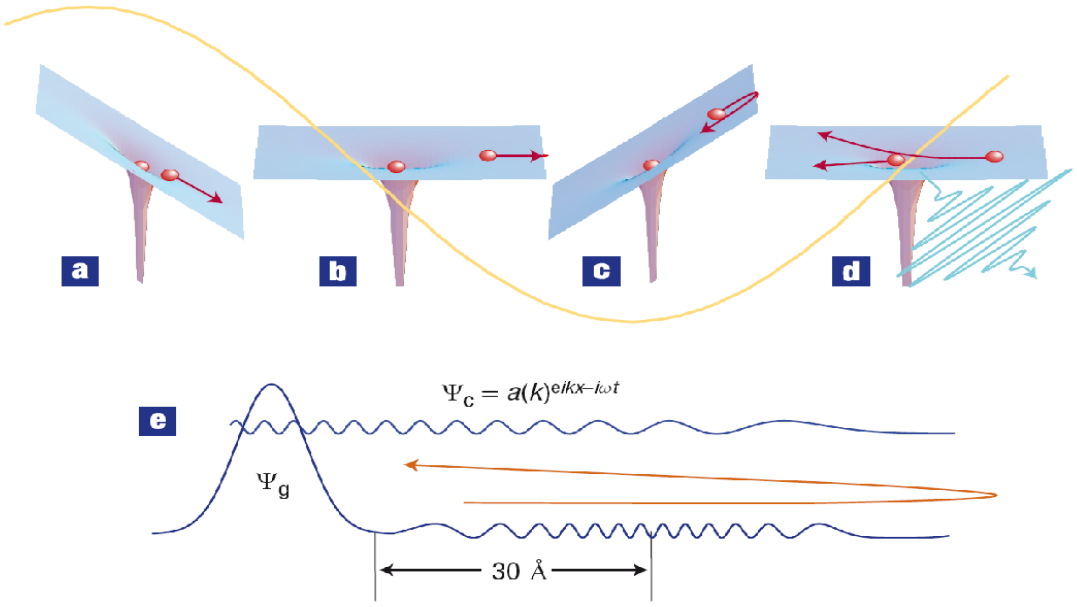

Figure 1.1: Representation of the 3-step model; figure from [10]

reach this threshold, electrons are released and accelerated in each cycle, leading to an attosecond pulse train. The photon energy of the emitted X-ray pulses increases with the central wavelength of the driving field, whereas the efficiency decreases rapidly with the driving wavelength [17, 18]. There is then a trade-off between the cut-off energy of the emitted field and the efficiency; thus a high energy broadband source will be the optimum solution to achieve different cut-off energies with an efficiency and wavelength adapted to the desired experiment, by tuning and selecting the corresponding spectral domains.

In a pump-probe experiment, a pulse excites the object to study, and another one probes the new state reached by the system; by delaying the probe from the pump, the deexcitation of the system is sucessfully monitored. In case of a pulse train for the pump or the probe, the excitation results from the accumulation of pump pulses, and the temporal resolution decreases. For pump-probe experiments studying the atomic and molecular dynamics, single isolated attosecond pulses are therefore preferred. An efficient way to generate isolated attosecond pulses is to develop high-energy single or even sub-cycle laser sources. The stability of the carrier envelope phase of these sources is necessary, because HHG is driven by the electric field of the pulses: a change in the carrier envelope phase (CEP) induces a change in the strength of the electric field, hence in the electron tunneling and recombination.

For this application, high energy lasers and sub- to few cycle pulses are necessary. Curently, an extensive development program towards such sources is undertaken at the Center for Free-Electron Laser Science (CFEL) in Hamburg. A first frequency syntheziser for generating sub-cycle pulses is being developed [19, 20] based on a commercial, high energy Ti:sapphire pump laser. The scalability of this system in average power is limited

by the available Ti:sapphire pump, and the scalability in spectral width is given by the broadband supercontinuum based front-end. A second system aims at overcoming the limitations in average power scaling of the first one, scaling even further the spectral width and the energy. In this work the early developments toward completion of this system are being addressed.

In its final state, this ultrasfast source is envisioned to deliver mJ level sub- to few cycles pulses covering 4 octaves of spectral bandwidth, from 400 nm to 5 µm. In the CEP stable front-end, broadband pulses will be generated, and will be amplified with parametric amplifiers pumped with a high energy laser. This pump laser for amplification is composed of a Joule class, sub-picosecond laser. The amplified pulses will then be synthesized to single-cycle pulses; the output pulses, covering the visible to the mid-infrared (MIR), might be used in pump probe experiments, or for EUV to soft-X-ray generation via HHG.

In this dissertation, the initial developments towards this laser source delivering high energy, ultrashort pulses at 1 kHz repetition rate will be presented: this is realized with a frequency syntheziser constituted of four main parts, which are the pump line, the front-end, the amplification of the signal coming from the front-end, and the synchronisation, recombination and dispersion management of the pulses. The high energy pump line has been developed up to the first stage of cryogenically cooled multi-pass amplifiers, the front-end for generation of extremely wide pulses has been demonstrated, and the concepts of the amplification of the pulses from the front-end with the high energy pulses from the pump line have been worked out.

In the pump line, based on ytterbium doped laser materials, an Yb:KYW dual-crystal regenerative amplifier with high beam quality delivers pulses with several mJ energy at 1 kHz repetition rate compressible to sub-picosecond duration. This is the highest energy demonstrated from an Yb:KYW regenerative amplifier reported to date. With the Yb:YAG cryogenically cooled composite thin-disk multi-pass amplifier, the stretched pulses from the regenerative amplifier have been further amplified by one order of magnitude. The stretcher and compressor of the pump line have been implemented with chirped fiber Bragg gratings and a grating compressor, respectively. The front-end, composed of a first white-light stage followed by two parametric amplifiers driving a second white-light stage, has demonstrated passive CEP stability over 11 h. This shows the conservation of the phase over both white-light stages and is the first report of white-light generation with sub-picosecond long pulses.

The structure of this thesis is the following.

Chapter 2 explains and justifies the general concept of the laser source: first the state of the art for generating single to sub-cycle pulses is presented. Among the different possibilities, this frequency syntheziser uses the parallel amplification for generating high energy, sub-5 fs pulses. Second, the options for the front-end are presented, and the choice of a passively CEP stable one justified. Third, the different modules constituting the pump line are presented.

Chapter 3 presents the first amplifier of the pump line, a regenerative amplifier with 7 decades of amplification, delivering >5 mJ pulses at 1 kHz. The results with

two different crystals, Yb:CALGO and Yb:KYW, are presented and compared to simulations of the laser dynamics.

Chapter 4 concerns the power amplifier. This multipass, cryogenically cooled Yb:YAG booster amplifies the pulses from the regenerative amplifier up to 72 mJ thanks to its shaped end-cap bonded to the thin-disk gain module and the cryogenic temperature.

Chapter 5 summarizes first the different concepts for a stretcher and compressor adapted to the complete pump line. The implemented chirped fiber Bragg grating stretcher stretches the pulses up to 0.65 $^{\mathrm{ns}}/_{\mathrm{nm}}$, while a Treacy compressor recompresses the pulses from the regenerative amplifier to 615 fs.

Chapter 6 demonstrates a CEP stable front-end with two stages of white-light generation in bulk. The first white-light stage is driven with the compressed pulses from the regenerative amplifier, then the spectral region around 2 µm is amplified with parametric amplification, from which the resulting idler is passively CEP-stable. This idler is used to generate the second supercontinuum.

Chapter 7 presents calculations of frequency conversion of the spectral regions created with the second white-light generation and mostly of the pump line. This requires the generation of second and third harmonic of the pump line, which is presented theoretically and experimentally for the second harmonic. The first experimental implementations of the parametric amplifiers are shown.

Chapter 8 describes first the future implementation of the compensation of the slow drifts leading to timing jitter and CEP noise and second the principle of the recombination of the different spectral bands into sub-cycle laser pulses. Some calculations of the dispersion management are shown, the experimental realization being kept for the future.

2 Design strategies for high-energy, few-cycle laser systems

The study of dynamics of molecules, atoms and electrons, with the ultimate goal of making time resolved studies, necessitates high energy, attosecond to few-femtosecond pulses. A sub-cycle pulse is a pulse with a duration shorter than one electric field cycle of the central frequency. Because of Fourier transform relationships, this corresponds to a spectrum extending over several octaves.

This chapter details first the methods to generate sub- to few cycle pulses and explains the choice of a parallel frequency synthesizer, then presents its constitutive parts: the front-end, the pump line and the parametric amplifiers. The second section details different concepts for the implementation of the front-end, before discussing the different solutions and justifying the chosen one. Section 2.3 presents the chirped pulse amplification method to amplify ultrashort pulses to high energies. The last section presents the pump line concepts.

2.1 Pulse synthesis using frequency synthesizers

In different laboratories, several concepts have been investigated to reach sub-cycle pulses. Most successful were hollow-core fiber compressors [21, 22] and frequency synthezisers [23, 24, 25].

In the first approach, ultrashort, few-cycle pulses from a Ti:sapphire oscillator are amplified to the mJ level and then spectrally broadened via self-phase modulation (SPM) in a hollow-core fiber compressor [26, 27]; the pulse duration after amplification is typically around 35 fs and reaches the single-cycle regime after the hollow-core fiber compressor. The shortest pulse duration was achieved at MPQ, Munich [22, 28]: the broadened spectrum was divided into three parts for fine tuning of the dispersion compensation, then recombined to reach sub-fs with a final energy amounting to 330 µJ. The shortest pulse duration at mJ energy was demonstrated by Böhle *et al.* in 2014, with 3 mJ pulses compressed to 4 fs [21]. Further energy scaling was implemented to reach terawatt pulses [29, 30]. This approach, limited to the spectral broadening achievable in the hollow core fiber compressor, was extended via cross-phase modulation to the range 300 nm to 930 nm with 380 µJ, however at the time of writing the pulses were not yet recompressed over the full bandwidth [31]. Hollow-core fiber compressors are the current state of technology, but limited in energy, and the spectral broadening is difficult to scale up further; moreover this method needs very long setups of several meters. Up to now, the maximal energy after compression amounted to 3.4 mJ for ∼3 m long fibers [21].

Generation of broad spectral ranges via nonlinear effects, such as white-light generation in bulk-materials or nonlinear frequency conversion, overcomes the bandwidth limitation and reaches longer wavelengths, suitable for higher cut-off energies in HHG. Both generation schemes are limited to relatively low output energies. In the case of white-light generation, the output energy of the broadened spectrum reaches only the nJ level due to the nature of the filamentation process. In the case of nonlinear frequency conversion, such as difference and sum frequency conversion, the currently available aperture of the crystals in combination with the conversion efficiency is the limiting factor. The generated spectral bandwidths must then be further amplified to the mJ level with amplifiers. Two different kinds of amplifiers exist: traditional laser amplifiers, based on a gain medium storing the energy from a pump laser, and parametric amplifiers, in which a strong pump laser exchanges instantaneously its energy to a weak signal. The first ones are limited in the choice of the gain material, which do not cover the spectral range from the visible to MIR, and have a limited amplification bandwidth; the broadest one, Ti:sapphire, amplifies only from 750 nm to 900 nm (FWHM). High gain amplification leads to strong narrowing of the spectrum. With energy storage and its transfer to the amplified pump, the energy difference between pump and laser photon energy is transferred as heat into the material. On the contrary, in an optical parametric amplifier (OPA), described in section 7, a high energy, sub- to few picosecond long, narrow-band pump pulse transfers its energy nonlinearly to the broadband signal. Parametric amplifiers do not store energy in the crystals, avoiding the subsequent heat transfer; the broadband gain, obtained by adjusting the phase-matching between the pump and the signal, minimizes spectral gain narrowing.

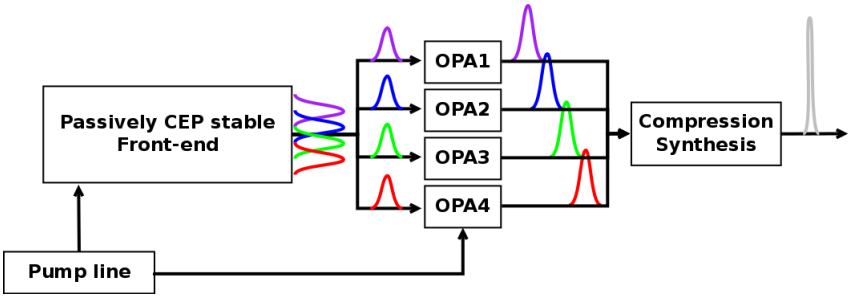

(a) Parallel synthesis scheme

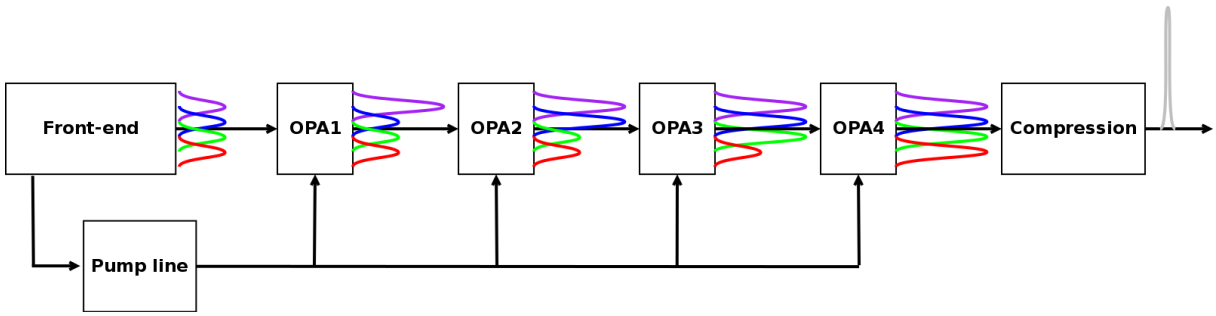

(b) Serial synthesis scheme

Figure 2.1: Schemes for frequency synthesis: (a) parallel and (b) serial.

In OPAs, the phase-matched bandwidth is limited to less than one octave: a spectral bandwidth covering several octaves has hence to be amplified progressively. Two methods emerged during the last decade: the parallel and the serial approaches, as displayed in figure 2.1. In the serial one, the spectral parts of the wide spectrum are amplified one after the other in series, and was demonstrated in [25]. This is advantageous to avoid splitting and recombining the pulses, but has the drawback on the uncertainty of the phase at the interface and overlap spectral regions. The dispersion compensation for compressing in time the pulses after amplification has to include the full bandwidth. The phase in the overlap region of the partial spectra has not yet been characterized and the recompression of the pulses was not yet demonstrated; the quality of the recompression is thus, at the time of writing, still an open question.

The parallel approach circumvents this problem by splitting before and recombining after amplification of the spectra. By limiting each channel to sub-octave bandwidth, the complexity of the dispersion compensation is relaxed inside each channel, but the recombination adds timing problems, jitter and stability issues. This has already been demonstrated for 2 channels in [32], and a synthesizer with 3 channels is being built in our CFEL labs [20].

Since the parallel approach is the most scalable method in bandwidth and energy, the generation of sub-cycle pulses for attosecond experiments will be based on a parallel frequency synthesizer. This work concerns the realization of this system described in the next paragraphs.

The whole system is consequently mainly divided into these four parts: the front-end, the pump-line, the parametric amplification and last but not least the synthesis. The front-end or seed source incorporates the generation of the broadband seed, either through nonlinear conversion of the spectrum of an ultrashort Ti:sapphire oscillator, or through white-light generation. The so-called pump line consists of high-energy amplifiers around 1 µm delivering high energy pulses in the range of a picosecond duration to pump the powerful OPAs and chirped pulse OPAs (OPCPA) at various wavelengths. The third part encompasses the amplification of the frond-end by the pump line. The last part concerns the synthesis of the separately amplified spectral regions to one single cycle pulse; moreover this part encompasses the stabilization of the whole system, as well in space as in time for compensating jitter problems, the stabilization of the CEP of the pulses, and the dispersion compensation.

To start with, an oscillator delivers a high repetition rate pulse train of several tens of MHz. Its spectrum has to match the wavelength of the pump line: a 10 nm wide spectral component at 1030 nm will serve as seed for the pump amplifier chain. Either the spectrum of the pulses out of the oscillator itself covers nearly one octave, or it is limited to a few nanometers and has to be broadened to be the starting point of the seed line.

The general concepts of the pump and seed lines are schematically shown with block diagrams in figure 2.2 (a) and (b): the exact implementation of both lines is detailed in the next sections. In the pump line, the pulses out of the oscillator are stretched (*Stretcher*), amplified with several stages of power amplifiers (PA_1) to (PA_n), and finally recompressed (*Compressor*). The seed line includes oscillator (*Oscillator*), nonlinear broadening (*NL Broad.*) to reach the desired spectral width and pre-compensation of the dispersion (*Disp.*

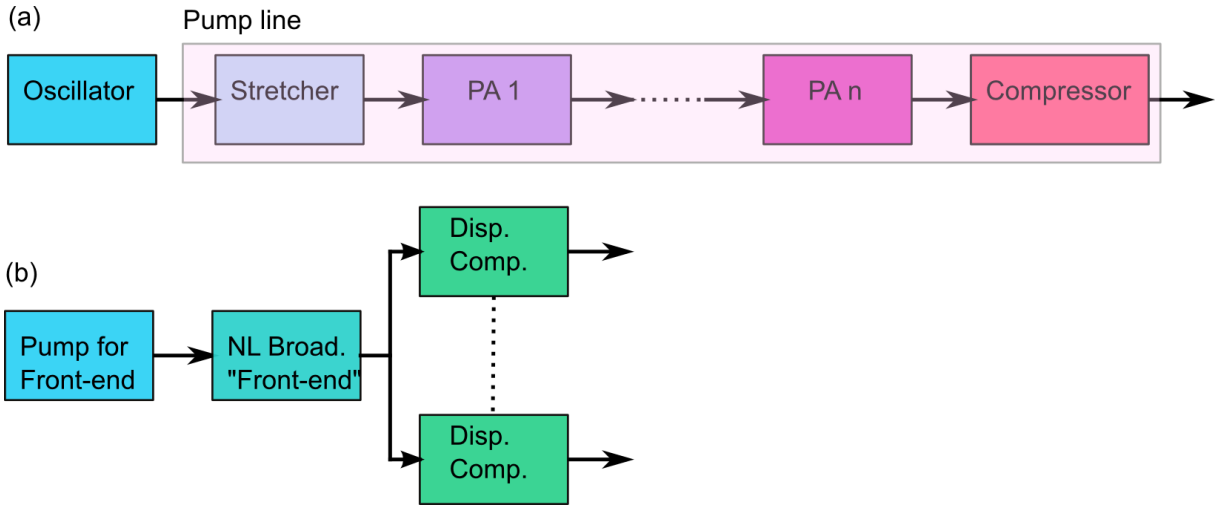

Figure 2.2: General scheme of (a) the pump and (b) the seed lines. The abbreviations stand for: *PA1* to *PAn* power amplifier 1 to n, *NL Broad.* nonlinear broadening, *Disp. Comp.* dispersion precompensation.

Comp.) before parametric amplification and recombination. The oscillators in the pump and seed lines of figure 2.2 might be one single oscillator or two synchronized with each other. The scheme with a single oscillator avoids jitter issues due to the imperfect synchronization of two separate oscillators. The module for nonlinear broadening (*Front-end*) includes the CEP stabilization of the spectrally widened pulses.

After the module for nonlinear broadening, the wide spectral range is split into the parallel channels for separate dispersion management and further amplification. A possible scheme for the optical parametric chirped pulse amplification (OPCPA) stages is shown in figure 2.3. The different spectral regions of the pulses broadened in the CEP stable front-end are amplified in this example in several channels parallel to each other. Each amplification line encompasses a first parametric amplification stage (*OPCPA1*), a dispersion management module (*Disp. Man.*), several further amplification stages (*OPCPA2* to *OPCPAn*) and a pre-compression module (*Pre-Comp.*). The final compression of the pulses is realized after the synthesis in the module *Combination - compression*. The dispersion management and compression of the pulses will be detailed in section 8.3.

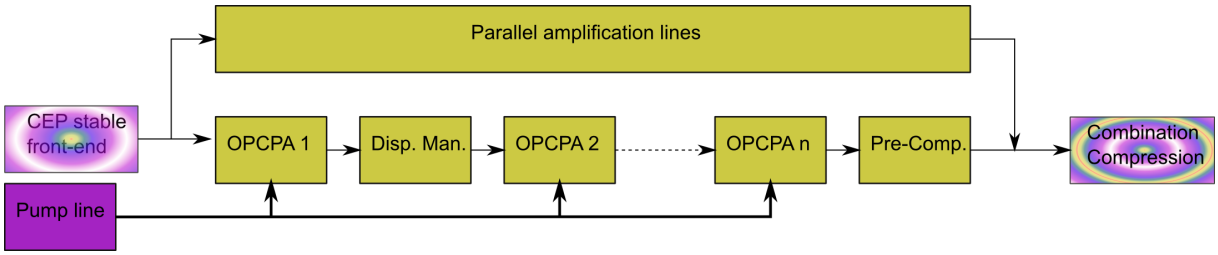

Figure 2.3: Scheme of the OPCPA stages: n OPCPA stages amplify the CEP stable pulses from the front-end. *Disp. Man.* is the dispersion management for an efficient amplification in the OPCPAs and *Pre-Comp.* a pre-compression of the pulses before the final compression after the synthesis.

Specifications of the laser system

The pump line has to be scalable to very high energies at a kHz repetition rate with picosecond to sub-picosecond pulses, which is possible with ytterbium based lasers.

For the intended attosecond pulse generation, the desired spectrum ranges from 400 nm to 5 µm. The amplified spectral ranges in the parallel frequency synthesizer are limited by the achievable bandwidth in the OPCPAs, meaning by the phase-matching bandwidth. The amplification will take place by dividing the spectral bandwidth as represented in figure 2.4. The spectral gap between 1200 nm and 1800 nm is due to the phase-matching limitation of β-baryium borate (BBO)-based OPAs pumped at 1 µm. The advantage of using the well-known crystal BBO is its high reliability and manufacturing reproducibility, as explained in detail in section 7, as well as the scalability to mJ-level energies due to a high damage threshold and a high effective nonlinear coefficient. As the absorption edge of BBO is located at 2.2 µm, other crystals have to be used to amplify longer wavelengths.

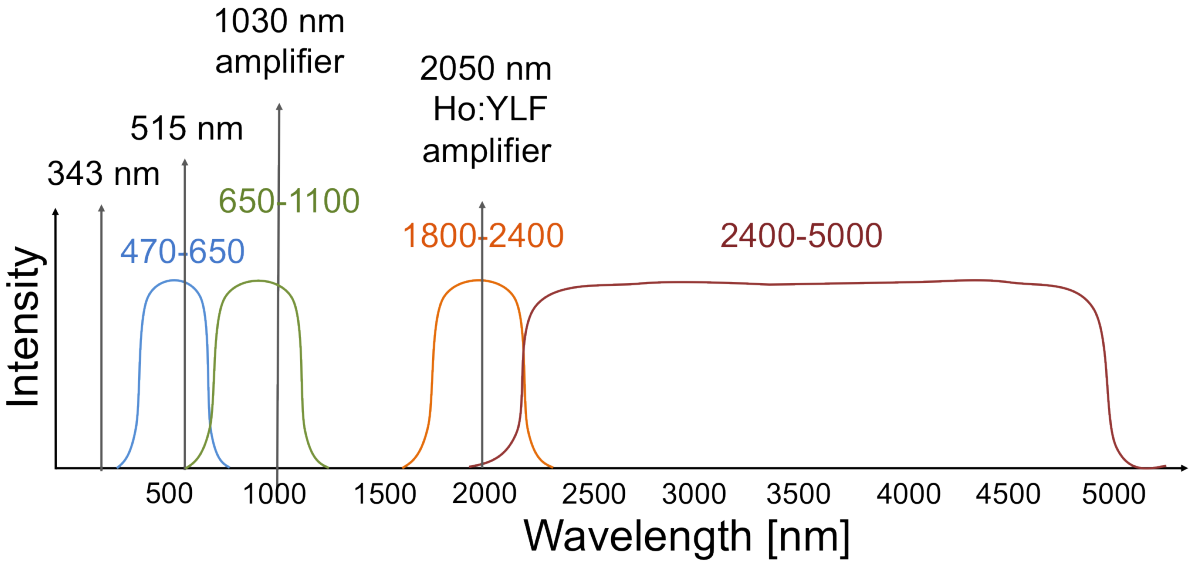

Figure 2.4: Spectral regions of the Yb-based frequency synthesizer

The pump for the parametric amplification of the domains extending up to 2.5 µm is either the direct output of a 1 µm pump line or its second or third harmonics. The amplification of the mid-infrared (MIR) spectral range covering 2.4 µm to 5 µm would not be very efficient with an OPA pumped with 1 µm radiation, though it can be done. For this reason, a secondary pump line working with Ho:YLF laser amplifiers at 2 µm is being developed in parallel [33].

The next sections describe the different existing elements or modules constituting the whole system, followed by a discussion of the front-end and pump line concepts.

2.2 Front-end

The front-end concepts can be divided into two categories: the first ones are based on a broadband Ti:sapphire oscillator whose spectrum is extended towards longer wavelengths

through nonlinear mechanisms like pulse broadening in a fiber or difference frequency generation (DFG) and toward shorter ones with sum frequency generation (SFG). The second ones are based on white-light generation. The different potential seed sources are also categorized according to the CEP stabilization mechanisms, either passive or active.

2.2.1 Constitutive elements of the front-end

The Ti:sapphire seed oscillator

The Titanium:Sapphire oscillator available for this experiment delivers sub-5 fs pulses, whose spectrum covers more than one octave. This kind of oscillator operates at a working point which is usually sensitive to environmental fluctuations or other disturbances, *e.g.* air humidity susceptible to modify the dispersion management inside the cavity. This is limiting a reliable operation of the complete laser system. An enhanced Kerr-effect is required to reach the octave-spanning spectrum and leads to intensities on the crystal close to the damage threshold of the material.

Nonlinear conversion by SFG and DFG

The spectrum of the Ti:sapphire laser would be divided into several parts to "seed" the nonlinear conversion stages that extend the spectrum into the visible and the MIR. As the energy in each pulse reaches ∼5 nJ, only 1 nJ to 2 nJ can be used for each nonlinear process. The resulting spectra would be used to seed the OPA or OPCPAs, which are extremely sensitive to superfluorescence, occurring with too low seed energy. Consequently, it is necessary to optimize the photon conversion efficiency. As demonstrated in [34] and used in [35], adiabatic conversion is the ideal solution: by slowly adjusting the phase-mismatch parameter over the propagation, the seed pulse adapts to the frequency converted pulse, and 100% photon conversion efficiency can be theoretically achieved between signal and idler.

The process and some experimental results are presented in detail in appendix 10A. From a spectrum covering 550 nm to 950 nm, adiabatic sum frequency generation (SFG) generated an idler between 410 nm and 505 nm with 92% average photon conversion and adiabatic difference frequency conversion (DFG) covering 1.8 µm–5 µm has also been demonstrated [36].

White-light generation

Spectral broadening can be accomplished with supercontinuum generation, either in bulk or in fiber. The generation in bulk crystals relies on filament broadening [37]: the plasma created by high intensity in the medium leads to beam defocusing, while self-focusing refocuses it; at the equilibrium, a filament is formed. With the plasma formation, new spectral components are created. In a fiber, self-phase modulation is the main mechanism underlying the broadening, allowing to keep a smooth spectral phase for compressing the pulses. Experimental results have demonstrated fiber broadening over more than one octave, however with 20 dB amplitude variations over the whole spectrum [38]. The results published about white-light generation in bulk [39] show on the contrary less

spectral density dynamic, which is of advantage for further amplification stages, and spectral coverage from the visible to the mid-infrared.

The detailed results of the white-light generation (WLG) are shown in chapter 6.1.

The CEP stabilization

The CEP can be passively or actively stabilized [23, 40]. In the passive stabilization, the random component of the CEP is cancelled out during the parametric process. The phase relationship between pump, signal and idler follows this conservation law similar to the energy conservation law:

$$\phi_3 - \phi_1 - \phi_2 = \text{const} \tag{2.1}$$

In the case of SFG, where two pulses at frequencies ω_P and ω_S are mixed nonlinearly to produce the sum frequency ω_I, equation (2.1) can be rewritten as: $\phi_I = \phi_P + \phi_S - \pi/2$. The phase of the generated pulse contains both the random phase of the pump and of the signal pulses. In the case of DFG, where the difference between the frequencies ω_P and ω_S is generated, the phase of the resulting pulse is given by: $\phi_I = \phi_P - \phi_S - \pi/2$. If the pump and signal waves have the same phase, the phase of the resulting idler is a constant. This means that DFG may be used with a passive stabilization scheme, but not SFG. In the front-end version with SFG, the oscillator pulses have to be actively CEP stabilized.

Passive CEP stabilization can be implemented with white-light continuum seeding an OPA [39]. The pump pulses are split, once for generating white-light, second for pumping the parametric amplification of the signal coming from the white-light. Following the same phase relationship 2.1 as for DFG, the random part of the CEP cancels out in the generated idler. The latter is further used as a CEP stable pulse.

The active stabilization consists in actively controlling the oscillator with the help of a feedback loop. This requires a frequency ω and its doubled frequency 2ω. After doubling the fundamental frequency, the two beams at 2ω interfere and the beat note is detected. The generated signal is fed back to the oscillator's pump, the intra-cavity dispersion or the intra-cavity mirror on a piezo controlled holder.

The stabilization of the CEP might be improved by adding a feed-forward loop with high bandwidth as demonstrated in [41]. This technique corrects for foreseeable CEP drifts and for the noise coming from the f-2f interferometer itself. The resulting noise with the feed-forward loop only was decreased by a factor of three when the feed-back loop was also on.

2.2.2 Possible front-end schemes

Different concepts for the front-end have been envisaged under the following aspects: their scalability for increasing the spectral width and the complexity of the system. The spectral width towards MIR is requested for applications such as scaling HHG towards the water-window. A system with a high complexity in terms of stages presents more risks for failures: if one of the stages composing the front-end fails, the whole amplification chain is disturbed, in the best case only partially operating on a spectral sub-domain. The

targeted applications necessitate long operation time of the full laser driver, for example for acquiring experimental data.

The possible front-ends can be categorized into two main groups: actively CEP stabilized or passively CEP stable ones. In the following, the discussion will be limited to the two concepts shown in figure 2.5 (active version) and 2.6 (passive version).

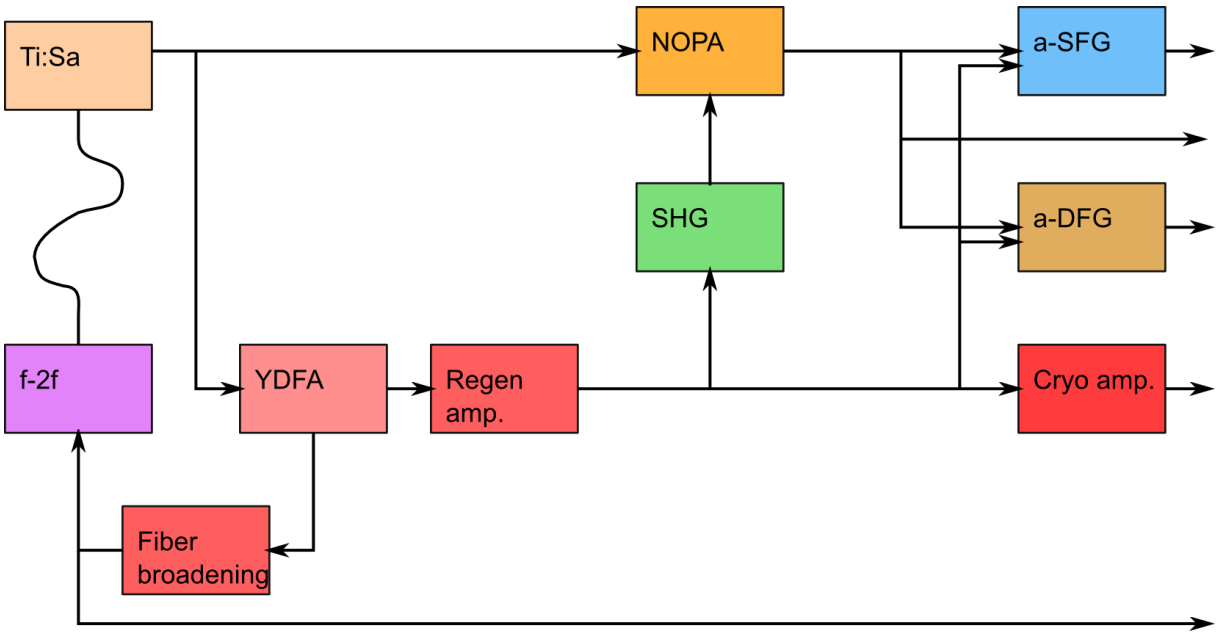

Figure 2.5: Front-end of the Yb based frequency synthesizer — version based on Ti:sapphire oscillator and adiabatic frequency conversion. The curved line represents the electronic feed-back to the oscillator for CEP stabilization.

The active stabilized front-end, which was the first version of the front-end, shown in figure 2.5, begins with a Ti:sapphire oscillator delivering 500 mW, 20 fs long pulses centered around 800 nm, at 85 MHz repetition rate. Its spectrum extends from 570 nm to 1100 nm (*cf.* figure **??**). The amplification of the region close to 1030 nm from the Ti:sapphire to high energy and power will create the pump for amplifying the rest of the spectrum.

In the seed line, the Ti:sapphire spectrum is divided and additional spectral components are created by several mechanisms, like wave-mixing and self-phase modulation. To amplify the spectral bandwidth without superfluorescence, the signal energy has to be at the nJ level after frequency conversion. Contrarily to traditional frequency conversion, adiabatic frequency conversion ensures close to 100% photon conversion. The low energy of the Ti:sapphire oscillator has to be first amplified with a non-collinear OPA (NOPA) pumped with the second harmonic of the 1 µm, so that the energy contained in each spectral domain reaches the nJ level. With sum frequency generation (SFG), the spectrum is extended in the visible from 410 nm to 520 nm. With difference frequency generation (DFG), the mid-infrared part from 1.3 µm to 5 µm is obtained. Through spectral broadening in a photonic crystal fiber (PCF), the range between 900 nm and 1300 nm is covered. The hole between 520 nm and 570 nm is covered either by second-harmonic generation (SHG) of the 900-1300 nm, or by SFG between the Ti:sapphire spectrum and the 1.8 µm

amplified with a Thulium doped fiber amplifier. The range 900 nm to 1300 nm, spectrally broadened in a fiber, has hence to be divided into 3 parts, one for further amplification, one for SHG and one for CEP stabilization of the Ti:sapphire oscillator.

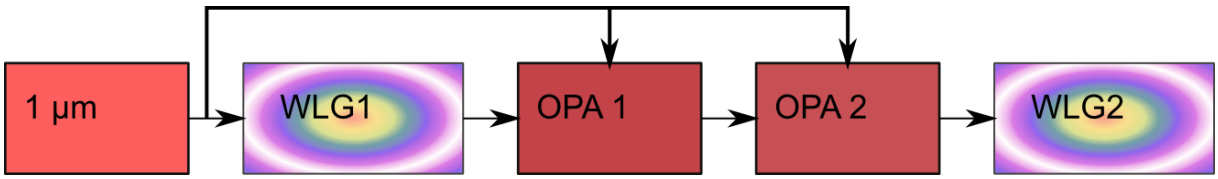

Figure 2.6: Front-end of the Yb based frequency synthesizer — version with passively CEP stable front-end based on white-light generation. The idler on the OPA stages is passively CEP stable, because of the substraction of the phases between pump and signal.

On figure 2.6, a passively CEP stable version is shown, similar to the one demonstrated in [20]. After the first white-light generation stage, 200 nm spectral width centered around 2 µm are amplified with two OPA stages. The idler of the second one, centered around 1.97 µm, is passively CEP stable, because pump and signal come from the same fundamental pump pulse and the phases cancel out. The second WLG stage broadens the spectrum from 470 nm to more than 2.5 µm. OPA3 is the first amplification stage of the near-infrared (NIR) channel before pre-compensation of the dispersion with, *e.g.*, a spatial light modulator (SLM). The spectral extent depends on the material used for white-light generation and is limited in the visible by the material bandgap. For example, WLG in YAG extends down to 500 nm. For the first experiments intended with the synthesizer, this spectral coverage is sufficient; if needed later, the region 420-510 nm can be implemented with SFG or WLG in CaF_2 or BaF_2 driven at 1 µm or 515 nm.

Another passively CEP stable version is based on a similar scheme than demonstrated by Okumura *et al.* in [42]. A non-collinear optical parametric amplifier was pumped and seeded by a common 400 nm second-harmonic pulse from a Ti:sapphire regenerative amplifier. The idler and its second-harmonic were consequently passively CEP stable; their angular dispersion was compensated by adaptive dispersion control with a deformable mirror. This method is really appealing for its use of the idler and its SHG, usually considered as parasitic, in the NOPA crystal; the compensation of the angular dispersion is however not trivial. A remaining angular dispersion may be kept over the amplification stages and prevent sub-cycle pulse synthesis.

The first version has the strong advantage of full scalability in the spectral domain. Experimentally however, the synchronization of the Ti:sapphire with the output pulses from the regenerative amplifier was proven to be difficult due to the fast jitter coming from the regenerative amplifier and its compressor (*cf.* chapter 8.1). In this experiment, the Ti:sapphire has been synchronized with a 1 µm oscillator seeding the regenerative amplifier; the resulting jitter was more than a few picoseconds. However, the white-light measurements performed in the Ti:sapphire frequency synthesizer [20] and on the XFEL pump-probe laser [43] showed the potential for long-term stable and passively CEP stable white-light based front-end. It was therefore decided to implement the latter version. One must however note that non-ideal environmental conditions in a typical laboratory force

the need for additional further stabilization schemes, even with a passively CEP stable setup. Due to the need for aligning and combining different broadband laser beams with interferometric accuracy, the whole passively CEP stable system behaves similarly to an interferometer. For example, thermal changes and air flow influence the pointing stability of the setup, as well as the timing jitter and CEP stability of the pulses. This must either be addressed by extreme control of the environmental conditions — quite unrealistic — or by implementing feedback loops. These feedback loops may however be significantly slower than for active CEP stabilization.

Compared with the scheme of Okamura *et al.*, even if the WL-based passively CEP stable version uses the passively CEP stable idler of an OPA, the angular dispersion is not problematic, because it is much less than the natural beam divergence: the spectral bandwidth of the idler is narrowed to keep the pulse duration above 50 fs for the WLG. The chosen, implemented version is the WL based passively CEP stable one, described in chapter 6.

2.3 High energy pump laser

Optical parametric amplifiers, with 10 to 20% conversion efficiency in the high energy, low gain stages, require consequently high energy pump pulses. Besides, for the intended applications, the whole system is intended to work at 1 kHz repetition rate, as a compromise between technical difficulties the laser development would encounter at higher repetition rates and acquisition time for the experiment. These technological issues concern mainly the thermal management and the optical damage arising with the combination of high energies and increasing repetition rate; on the other side, a high repetition rate allows a reduced acquisition time during experiments. Some experiments like coherent electron diffraction imaging necessitate the superposition of a high number of shots: a higher repetition rate minimizes the acquisition time and therefore, among others, the risk of failure of the experimental setup. The combination of high energy and relatively high repetition rate leads to high powers, meaning thermal loading in the amplifying media. The developed laser media for high energy are either Ti:sapphire or ytterbium doped materials. Ti:sapphire based laser systems may reach very high energies [44], but are limited by the thermal load and are not suitable for high average powers [45]. Yb based materials have demonstrated both high energies and high average powers [45]. Whereas the frequency synthesizer demonstrated in [20] relies on a commercial kHz Ti:sapphire driving laser and is limited by the latter, the frequency synthesizer developed in this thesis aims at higher energies in the pump line to amplify an even broader bandwidth to several mJ's: the pump line will hence be ytterbium based.

The amplification line first consists of an oscillator followed by a fiber amplifier with $\sim$10 nJ output energy, second of a regenerative amplifier and third of a high power amplifier that may ultimately reach up to 1 J energy at 100 Hz repetition rate. For high energy amplifiers, cryogenically cooled Yb:YAG is a very promising material for its excellent thermo-optical properties and low saturation fluence [46]. As already demonstrated by Hong *et al.* at MIT [46], energies as high as 40 mJ can be achieved with only a few passes though the gain crystal. The laser emission of Yb:YAG is centered around 1029 nm within the tuning bandwidth of the seed oscillator.

The pump line began to be assembled during the experiments with the first front-end version, meaning with the Ti:sapphire oscillator. The Ti:sapphire laser delivers only a few pJ at this wavelength, even with intra-cavity gain enhancement, and the power amplifier needs several mJ to be able to efficiently amplify the pulses up to the 100 mJ or 1 J level. Therefore, as shown in figure 2.7, the oscillator and the following fiber amplifier (*YDFA*) are followed by a regenerative amplifier (*Regen*) to bridge the gap with amplification of 6 to 7 orders of magnitude. Its output is then split into two lines, one compressed (*Compressor*) to drive the CEP-stable front-end (*FE*), and one further amplified with a cryogenically cooled power amplifier (*Yb-Cryo Amp*) before compression with another compressor (*Compressor*).

The power amplifier (*Yb-Cryo Amp*) is divided into 2 stages: the first one is operating at 150 K, reaching 100 mJ, and the second one at 77 K to reach the Joule level. The cryogenic cooling narrows the gain bandwidth of the Yb:YAG crystal to ∼0.8 nm, leading to picosecond pulses after compression. The amplifying stage working at 150 K preserves a bandwidth of ∼1.5 nm, limiting the gain narrowing over the total amplification chain. The actual concept of the cryogenic amplifier is different from the one presented in [46]: a better scalability is offered with a highly doped composite thin disk (1 mm thickness) bonded to a 4 mm undoped end-cap.

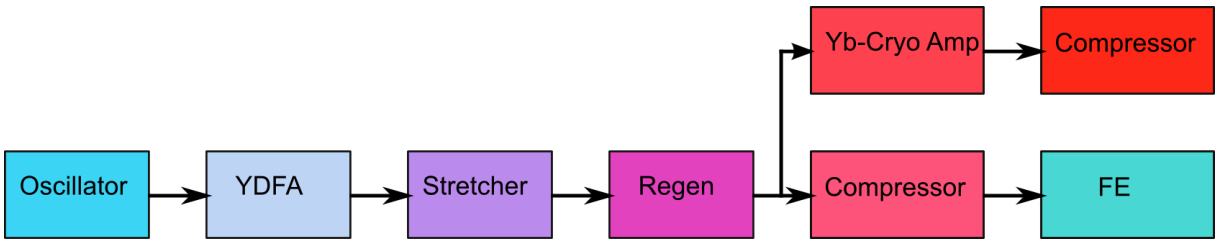

Figure 2.7: Scheme of the pump line. The abbreviations stand respectively for: *YDFA* ytterbium doped fiber amplifier, *Regen* regenerative amplifier, *Yb Cryo Amp* cryogenically cooled ytterbium YAG multipass amplifier, *FE* front end.

Due to gain narrowing in each amplifier stage, the pump pulse duration increases significantly after the regenerative amplifier to 700 fs and after the cryogenic amplifier to several picoseconds. The first OPA stage, with low energy, high gain, is better pumped with the shorter output pulses of the regenerative amplifier to reduce the superfluorescence (*cf.* chapter 7). The total energy neeeded after the regenerative amplifier for this pumping and, in parallel, seeding the power amplifiers, amounts to >5 mJ.

Chirped Pulse Amplification

Amplification of ultrashort pulses to high energies is constrained by the nonlinearities accumulated by the traveling pulse and ultimately by the damage threshold of the material, both limitations scaling with the intensity of the laser pulses. In order to remain below the threshold for nonlinearities and damage, the pulse peak intensity I, expressed as $I = \frac{fE}{\pi w_0^2 \tau}$ where f is a factor depending on the temporal pulse shape and equals 1 for flat-top beam and 2 for a gaussian beam, can be decreased either by increasing the spot size w_0, radius at $1/e^2$ or the FWHM pulse duration τ, while increasing the pulse energy

E. Material constraints, such as the maximal reliably manufacturable aperture, homogeneity or surface quality over a large aperture, as well as the resulting cost, limit the scaling through spot size increase. In the case of a laser system, the laser dynamic limits the maximal spot sizes: transparent pumping and gain storage require power proportional to area. Ultrashort pulses have a significant spectral width allowing stretching the pulses in time by adding chirp. After amplification, this added chirp needs to be removed for recompressing the pulses to the minimum pulse duration. Figure 2.8 illustrates the stretching and compression of ultrafast pulses before and after amplification; this process is called chirped pulse amplification (CPA).

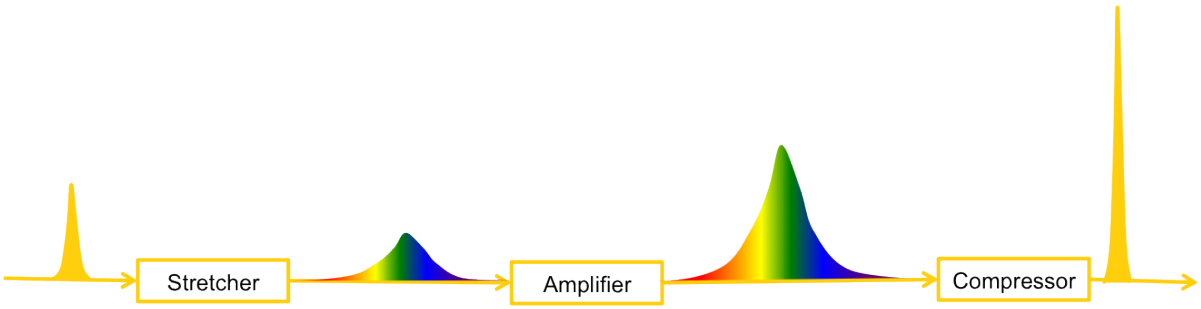

Figure 2.8: Scheme of the chirped pulse amplification: by stretching the pulses in time, the peak power and consequently the intensity of the pulses are decreased to avoid nonlinearities and damage of the material. They are recompressed after amplification.

CPA has been first introduced by Maine *et al.* in 1988 [47] and widely developed to reach TW then PW peak powers. This scheme, traditionally used for amplification with regenerative amplifiers and/or power amplifiers, has been extended in [48] to the optical parametric amplification, in the optical parametric chirped pulse amplification scheme: the same argumentation of decreasing the peak intensity for avoiding damages and nonlinearities holds for the parametric amplification.

In the frequency syntheziser, the CPA scheme will be implemented in the high energy pump line for amplifying the picosecond pulses to the mJ or J level, as well as for the broadband parametric amplification for amplifying the pulses out of the front-end from the nJ level to the mJ level.

2.4 Summary

This chapter first described the state-of-the-art concepts for generating single- to sub-cycle pulses at high energies, such as hollow-core fiber compressor, serial and parallel frequency synthesizers, and presented their limitations. The laser system needed for the intended future experiments is based on parallel frequency synthesis. Second, its constituting modules have been presented: the 4 constitutive elements are the pump line, with a regenerative amplifier and two stages of a cryogenically cooled Yb:YAG thin-disk multipass amplifier, the CEP-stable front-end, based on white-light generatiuon in bulk and parametric amplification, the parametric amplification of the generated spectrum, and the recombination and compression of the amplified spectral domain.

A passive CEP stable system minimizes the need for synchronization, control and feedback loops; environmental conditions and issues in a non-ideal laboratory setup, like thermal drifts, have been addressed. For this reason, after experimental trials of an active stabilized front-end, the final front-end has been built on passively CEP stable WLG, similarly as in [20]. The details about the experiments concerning the previous, active CEP stabilized version (adiabatic frequency conversion, fiber amplifier details and simulations of broadening in fiber) may be found in the appendices 10a and **??**b.

The next chapters will describe first the pump line, then the front-end and its amplification.

3 Regenerative amplifier

In the pump line leading to a J-level system to pump the parametric amplifiers of the frequency synthesizer as shown in figures 2.2 and 2.7, the last power amplifiers need sufficient input energy to reach saturation, which is in the mJ level. The gap between low-energy, high repetition rate oscillator and the power amplifiers can be bridged efficiently with a regenerative amplifier (*Regen* on the figure 2.7) bearing 6 to 7 decades of gain. A part of its output is split off for the CEP stable front-end. To seed the high power amplifier, 1 mJ in the 2 nm spectral range around 1029 nm, stretched to 0.8 $^{\mathrm{ns}}/_{\mathrm{nm}}$ is necessary. For the first white-light generation stage of the front-end, sub-picosecond pulses are the key to ensure spectral broadening with high pulse-to-pulse stability.

This chapter will describe the regenerative amplifier for the amplification of the nJ level, stretched oscillator to the mJ level. After a first section explaining the general concept of a regenerative amplifier, the state of the art is presented; the choice for a non-commercial regenerative amplifier in the pump line is then justified. The properties of suitable gain materials are reviewed. The following sections detail simulations of the laser dynamic and cavity design. The last section presents the experimental results obtained with two gain materials: Yb:CALGO (ytterbium doped $CaGdAlO_4$) and Yb:KYW (ytterbium doped potassium yttrium tungstate).

3.1 General concept of a regenerative amplifier

In a regenerative amplifier, a seed pulse is stored in a laser cavity, depleting the stored energy during each pass through the gain medium. After amplification, a switching mechanism releases the pulse, as described in [49]. Between two consecutive pulses, the stored energy is regenerated during the pumping phase. In order to avoid damaging the components at the high energies reached after several decades of amplification, the chirped pulse amplification technique, demonstrated by Maine *et al.* [47] and described in section 2.3, decreases the peak power by temporally stretching the pulses before the amplifier and recompressing the output pulse afterwards.

The switching unit works, *e.g.*, with polarization, as represented in figure 3.1 for a linear cavity. In (a), the seed pulse with vertical polarization is reflected on the TFP, goes through the Pockels cell without polarization change before its polarization is rotated by 90° by passing twice through the $\lambda/4$ waveplate. Horizontally polarized, it traverses the TFP and passes twice through the crystal. If the Pockels cell is switched off as in (b), the pulse sees only for the second time the waveplate changing its polarization back to vertical polarization, which is reflected by the TFP. If the Pockels cell has been changed to operate as a quarter-waveplate as in (c), then the pulse goes through 2 quarter-waveplates, and its

polarization remains horizontal: the pulse is thus imprisoned in the cavity. After passing through the gain medium, the pulse sees twice a $\lambda/2$ waveplate as long as the Pockels cell is switched on. The seeder pulses arriving during this period, as in (d) also see twice $\lambda/2$ and cannot enter the cavity. In the case of a ring cavity, the Pockels cell is set to $\lambda/2$ and the seed pulse travels only once through the amplifying medium.

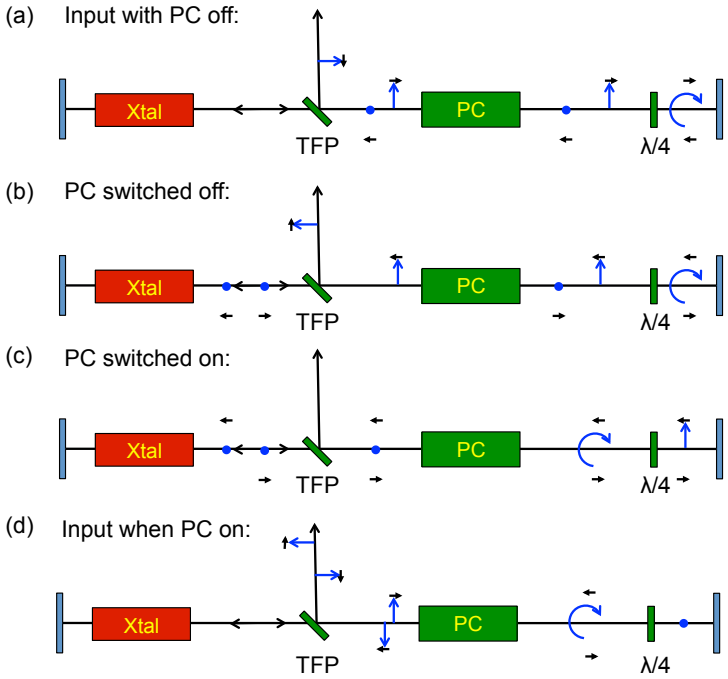

Figure 3.1: Switching diagram of a regenerative amplifier: (a) Introduction of a seed pulse in the laser cavity. (b) With Pockels cell and waveplate set in open position, the seed pulse leaves the cavity after one round-trip. (c) With Pockels switched, the pulse is imprisoned in the cavity and amplified. (d) During amplification, further incoming seed pulses are rejected without passing through the gain medium. The elements are abbreviated with Xtal for crystal, TFP for thin-film polarizer, PC for Pockels cell and $\lambda/4$ for quarter-waveplate.

A drawback with this method of implementing the switch is that the seed pulse passes through the amplifying medium twice when the switch is off, leading to twice the amplification by the small signal gain. This is typically not a problem if the amplification of the desired pulse is large enough: the contrast is then high enough (typically >500) for the intermediate, non-amplified pulses to represent only a small leakage. It may however become a problem if high contrast output is required, *e.g.* when successive amplifying stages may further amplify the leaked signal by themselves. In such situations, a different switching scheme or contrast enhancement by a secondary switch must be used.

Notations are defined in the timing diagram in figure 3.2: $T_k = 1/f_{rep}$ is the period of the amplifier, T_g the amplification time when the cavity is closed, T_P the pumping time and T_R and $T_{R,s}$ the round-trip times of the amplifier and of the seed. The first graph, figure 3.2(a) represents the switching on and off times: *Gate* refers to the gating of the switching mechanism; the cavity is closed, *i.e.* the losses are minimized when $Gate = 1$. In figure 3.2(b), the evolution of the pump fluence Φ_P during pumping time and amplification

cycle is represented. Figure 3.2(c) shows schematically the evolution of the population inversion n_2 with the pumping cycles, while figure 3.2(d) illustrates the amplification of a seed pulse during the build-up time; its fluence is denoted Φ_L.

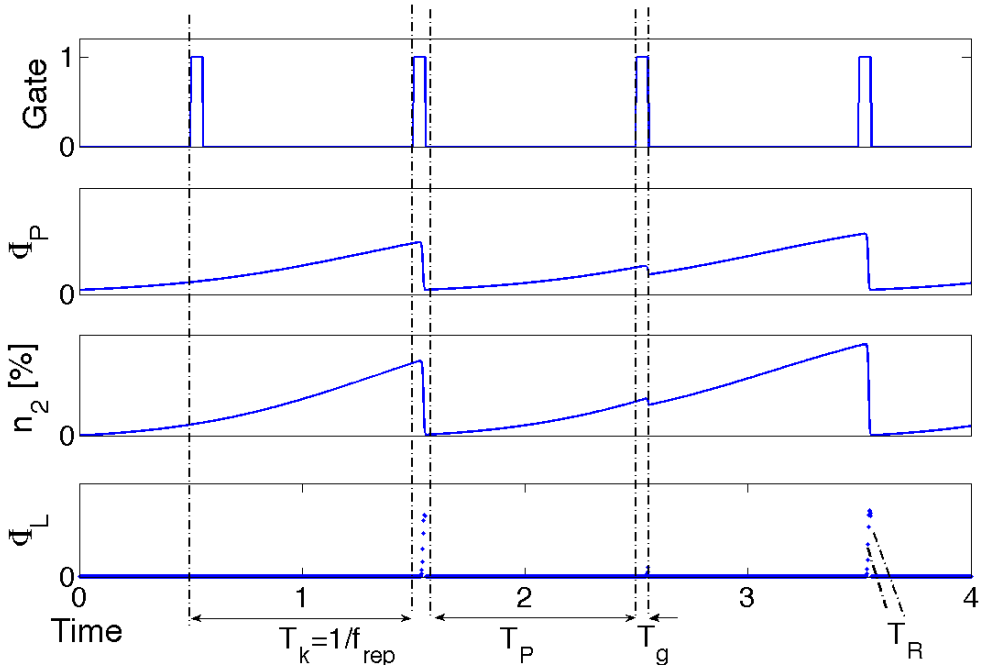

Figure 3.2: Timing diagram of a regenerative amplifier

There are two possibilities for pumping in time: continuous-wave (CW), where the pump is continuously switched on, and periodic, where the pump is periodically switched on and off. The quasi-CW (QCW) is a particular case, with a pumping time suitable for materials with long lifetimes (>100 µs). The time between two cycles is called pumping dead time. QCW pumping effectively reduces the thermal load in the gain medium, and thereby also reducing the thermal aberrations. A factor of 1.5 to 2 times the gain medium lifetime is usually sufficient to saturate the inversion; a longer pumping time increases the thermal load inside the crystals without resulting in higher output power.

The design objective for the regenerative amplifier is to amplify the 1 nJ pulses >5 mJ in Yb:CALGO or Yb:KYW. The spectrum of the seed pulses should cover 4.5 nm full-width half-maximum (FWHM) centered at 1029.5 nm and stretched to 2.35 ns in time. The beam quality parameter M^2 has to be better than 1.3. The details of the stretcher are presented in chapter 5. The next section will present the state of the art for regenerative amplifiers working at the mJ level, and is followed by a section detailing the laser and thermo-mechanical characteristics of different crystals.

3.2 State of the art

Several laser geometries have been developed over the last decades: slab, thin-disk and fiber are among the most popular ones and will be briefly discuss in the following section.

Fiber lasers [45, 50] scale with the length of the laser medium. Though this geometry is highly efficient for high power lasers, the dimension of the fiber core limits the maximal achievable energy, even with high stretching ratios. This is hence not a suitable laser architecture for this laser system, aiming at several mJ at kHz repetition rate.

Typically, the slab or bulk lasers [45] have a gain medium much longer in the direction which is longitudinal to the laser mode and they are pumped either longitudinally or from the side. The cooling is transversal to the laser propagation. In the case of long slabs, fluorescence stays mainly inside the slab and adds heat to the crystal and its holder. At high average powers, thermal effects limit this geometry. Thin-disk lasers [45] consist of a thin-disk contacted to a heat sink: the cooling through a large surface, longitudinally with the pump and laser beams, allows to remove a higher heat load than in the case of the slab laser. Thermal bulging (*cf.* chapter 4) decreases with the thinness of the disk, acting as a 1D geometry, however preventing a high gain even though the crystals are typically highly doped: several passes are required for the pump to store energy and for the laser to extract it efficiently. The multiplication of passes to absorb the pump as well as to extract the energy, similarly to [51, 52] with 20 pump passes and 13 passes for extraction, induces a complex mechanics to have a stable laser cavity and leads to very long beam paths. The thin-disk geometry will be discussed in detail in the chapter 4 dealing with the high energy stage of the pump line.

Thin-disk lasers were first developed by A. Giesen in 1994 [53]. Yb:YAG regenerative amplifiers based on this technology demonstrated energies as high as 25 mJ at 3 kHz repetition rate with 1.6 ps pulse duration after compression, based on Yb:YAG [54]. Tuemmler *et al.* at the Max Born Institute demonstrated a regenerative amplifier with 165 mJ at 100 Hz, followed by a multipass amplifier to achieve 300 mJ, with nearly transform limited recompressed pulses to <2 ps; the regenerative amplifier is pumped by 1 J in 1 ms pulse duration using 1 kW pump diodes. [55].

Because of its high gain, Yb:YAG is well suited to achieve high energies [56, 57, 58], but the gain narrowing reduces the bandwidth of the output pulse to ∼1 nm, corresponding to 1.1 ps transform limited pulses. For white-light continuum generation, as in the CEP-stable front-end, this is not short enough. Other media, like Yb:KYW or Yb:CaF_2, have a higher gain bandwidth and can be used to achieve shorter output pulses, as in [59, 60]. Nickel *et al.* demonstrated 9 µJ at 200 kHz and with 280 fs short pulses, however the average power of 1.8 W is still quite low [59]. The average power was increased to 4 W in 2008 by Rivier *et al.* [61] and 9 W with significantly degraded beam quality of M^2=5.4. In [62], a double-thin disk Yb:KYW multipass amplifier has been demonstrated, delivering promising results: 17 mJ at 100 Hz and 5.5 nm spectral bandwidth, or 27 mJ with 3 mJ input energy saturating the gain. In 2014, Kessler *et al.* have demonstrated 16.6 J, 150 fs long pulses from CaF_2, showing that this material is well adapted to amplify up to TW peak power, but at ten Hz [60].

Other materials are also promising candidates for regenerative amplifiers. For example, in 2007, a Yb:Lu_2O_3 in an oscillator with 32.6 W average power was demonstrated by Peters *et al.* [63]. Based on the achieved output power of the oscillator, the possibility to build a high power regenerative amplifier is expected. Another example would be Yb:$CaGdAlO_4$. The group of F.Druon demonstrated in 2011 [64] an Yb:$CaGdAlO_4$ based q-switched thin-disk oscillator with 1 mJ at 1 kHz.

In the bulk approach, the power scaling is based on a compromise between the crystal length and the pump and laser mode sizes. With the improvement of the Yb:KYW crystal quality, more than 20 W were extracted from a dual-crystal cavity in continuous-wave operation, or 14 W as a regenerative amplifier with repetition rates varying between 350 and 1000 kHz [65]. Non-published experiments have also shown 20 W out of one single crystal with good beam quality, limited by the thermal lensing and bulging of the crystal.

In general, another way to scale the power and energy out of a resonator or a regenerative amplifier is to increase the number of gain modules, as in [66, 67] and [65]. The work from [67] is the base for a commercialized regenerative amplifier from Amplitude Systèmes (France), able to deliver 1.8 mJ at 1 kHz repetition rate. Another commercially available system, the Pharos from Light Conversion, delivers up to 2 mJ at the same repetition rate and central wavelength. Because of the lack of a commercially available system reaching the energy needed for the frequency synthesizer, a new regenerative amplifier has been designed and developed.

Considering the advantages of the different approaches, a design based on a bulk crystal laser-head has been chosen, whereas the booster amplifier relies on a composite thin-disk design. In the regenerative amplifier, the determining criteria are the possibility to keep the cavity length relatively short (<5 m) and the high gain per pass in the crystal. Because of its thermal conductivity, enhanced by the cryogenic cooling, and of its high gain, Yb:YAG is chosen for the first version of the 100 mJ amplifier; this sets the wavelength of the whole pump line of the few-cycle laser to 1029.5 nm. Details about the booster amplifier are given in chapter 4.

Several crystals were tested: Yb-doped CALGO for its spectrally wide emission cross-section and good thermal properties, and Yb-doped KYW for its emission spectrum closely matching the wavelength of the booster amplifier.

The regenerative amplifier has to deliver 5 to 10 mJ at its output, at a center wavelength of 1029.5 nm ± 0.5 nm. The beam quality parameter M^2, has to be better than 1.3 to ensure a good spatial beam profile for the next amplifier stages. In the further amplification stages, either the cryogenic amplifier or the OP(CP)As, the presence of inhomogeneities in the beam profile would either lead to hot-spots or be transferred to the amplified signal. In spots with high intensities, the pulse accumulates higher nonlinearities during propagation, leading to a less compressible beam.

The pulse duration of the regenerative amplifier is constrained by two factors: the shortest possible pulse duration is needed for the first parametric amplification stages, and the spectral bandwidth has to be limited to efficiently seed the cryogenically cooled Yb:YAG amplifier. A spectral width of 3 to 5 nm seems to be a good compromise, with a theoretical Fourier-transform limited pulse of less than 400 fs, assuming hyperbolic secant square ($sech^2$) pulses. In light of the gain-narrowing in the subsequent cryogenically cooled Yb:YAG booster amplifier, the necessary stretching ratio is estimated to be 0.8 $^{ns}/_{nm}$ (*cf.* section 4). The repetition rate of the whole system is 1 kHz.

To design the regenerative amplifier, the laser characteristics such as pump absorption, stored energy, and extraction need to be taken into account. These depend on material parameters such as emission and absorption cross-sections. During this design step, the beam sizes will be fixed and set as input parameter for the cavity design. To respect this

logical development of the design, the next section will discuss the different crystals, in order to restrict the choice of crystal hosts for the effective simulations and design. After this design step, further optics inside the cavity will be discussed.

3.3 Crystals

Fulfilling the above mentioned specifications requires a careful choice of the laser medium. To match the emission wavelength of Yb:YAG, ytterbium doped hosts are well-suited. The properties of several hosts for Yb doping are compared in table 3.1 and table 3.3. Both tables summarize the known values for the thermo-mechanical and optical properties of the doped host, indicating doping concentration and temperature.

The listed parameters are abbreviated with their symbol: Poisson ratio ν, thermal expansion coefficient α_T, volumic thermal expansion coefficient α_{vol}, nonlinear refraction index coefficient n_2, thermal conductivity κ, change in refractive index with temperature. dn/dT. The laser parameters are the number of active ions inside the gain medium N_T, the emission and absorption cross-sections at pump and laser wavelengths $\sigma_{a,P}$ and $\sigma_{e,L}$, the absorption and emission wavelengths λ_P and λ_L, the emission bandwidth $\Delta\lambda$ and the fluorescence wavelength λ_F. For the comparison of the different media, the saturation intensity $I_{sat,P}$ is given.

The hosts Lu_2O_3, Sc_2O_3 and $LuScO_3$ belong to the family of the sesquioxydes, very promising for high power laser applications due to its high thermal conductivity. In the family of the tungstate hosts, KYW and KGW are biaxial materials with emission and absorption cross-sections higher than in YAG for ytterbium doping.

Host	T	Doping	n_0	α_T	α_{vol}	κ	dn/dT
	K	%	[]	$10^{-6}K^{-1}$	$10^{-6}K^{-1}$	$W.K^{-1}.m^{-1}$	$10^{-6}K^{-1}$
CALGO [68, 69, 70, 71]	300	2	1.85	–	36.4	a=6.9, c=6.3	(5%) a=-7.6, c=-8.6
KYW [72, 73]	300	2	(undoped) p=1.9979, m=2.0396, g=2.0869	p=2.9, m=10.7, g=15.2	30-35	–	p=-14.6, m=-8.9, g=-12.4
KGW [68, 73]	300	2	(undoped) p=2.0135, m=2.0458, g=2.0860	–	16	3.8	p=-10.6, m=-8.4, g=-15.2
Lu_2O_3 [63, 74, 75]	300	2.8	1.91	8.6	25.8	10.8 - 12	9.1
Sc_2O_3 [63, 74, 75]	300	2.38	1.97	9.6	28.8	6.4	7 - 8.9
$LuScO_3$ [74, 75]	300	2.58	1.939	9.1	27.3	3.5	9
YAG [68]	300	5	1.82	6.7	20.1	5.7	–
CaF_2 [68, 76]	300	5	1.4287	19	56	5.2	-11.3

Table 3.1: Thermo-optical and mechanical parameters of the different crystal hosts. The doping level is indicated.

From the comparison of the thermo-mechanical crystal properties given in table 3.1 for doped hosts, table 3.2 for undoped hosts and of the laser properties given in table 3.3, some hosts are suitable for this laser system. YAG is well-known and its manufacturing

Host	T	α_T	α_{vol}	κ	dn/dT
	K	$10^{-6}K^{-1}$	$10^{-6}K^{-1}$	$W.K^{-1}.m^{-1}$	$10^{-6}K^{-1}$
CALGO [68, 69]	300	–	36.4	11.4 [68] / 9.3 [77]	–
KYW [72, 78]	300	$\alpha_p = 2.0$, $\alpha_m = 10.3$, $\alpha_g = 15.9$	30-35	3.3	p=-14.6, m=-8.9, g=-12.4
KGW [68, 73, 78]	300	–	16	3.3	p=-10.6, m=-8.4, g=-15.2
Lu_2O_3 [63, 74]	300	–	–	12.2 - 12.6	–
Sc_2O_3 [63, 74]	300	–	–	15.5 - 17.3	–
$LuScO_3$ [74]	300	–	–	3.6	–
YAG [68, 79, 76, 80]	300	6.1-7	18.3-21	11.2 - 10.7	7.8 - 8.9 - 9
YAG [79, 80]	100	2.0	6.0	46.1	1
CaF_2 [68, 76, 78, 81]	300	18.99	56	9.7	-17.9

Table 3.2: Thermo-optical and mechanical parameters of the different undoped crystal hosts

very reproducible; this is a convenient crystal due to its thermo-mechanical coefficients. But its emission bandwidth, given in table 3.3, is not broad enough to sustain sub-picosecond pulses after 6 decades of amplification. Sesquioxydes are highly interesting for their thermo-mechanical properties, but their emission cross-section is too narrow for sub-picosecond pulses after this amplification factor. CALGO, KYW, and CaF_2 are interesting for their compromise between thermal and optical properties.

Some parameters, like the lifetime, the thermal expansion coefficient and the thermal conductivity, vary with the doping concentration. In [77], measurements of the thermal conductivity show a strong decrease of the thermal conductivity of Yb:CALGO with increasing ytterbium doping. The exact ratio of gadolinium and calcium atoms influences the decrease of the thermal conductivity. The value of 9.3 $^{W}/_{\mathrm{m\,K}}$ for the undoped material is close to the one measured previously by Petit *et al.* [68] (11.4 $^{W}/_{\mathrm{m\,K}}$). It decreases rapidly with increased doping level to reach a limit value depending of the exact composition of the material: this limit is 4.5 $^{W}/_{\mathrm{m\,K}}$ for 80%Gd 20%Ca material, *ca.* 4.3 $^{W}/_{\mathrm{m\,K}}$ for 75%Gd 25%Ca material and only 3.5 $^{W}/_{\mathrm{m\,K}}$ for 60%Gd 40%Ca material. For 2% doped crystals, the value of 6.3 $^{W}/_{\mathrm{m\,K}}$ on the c-axis, lies well in the measurement uncertainty range [77] and is half the value of YAG. The thermal conductivity is also higher for undoped Sc_2O_3 (15.5 $^{W}/_{\mathrm{m\,K}}$) and Lu_2O_3 (12.2 $^{W}/_{\mathrm{m\,K}}$) as for the doped material, according to [63]. This decrease of the thermal conductivity leads to the observation that highly doped materials are limited by thermal effects under high pump conditions.

Because the wavelength of this specific setup should be centered at 1029.5 nm, and as pulses compressible to less than 1 ps are needed, the laser medium has to have a sufficient amplification bandwidth around 1030 nm. Two cases are considered: Yb:KYW (ytterbium doped tungstate) and Yb:CALGO. Yb:CALGO has a lower emission cross-section than Yb:KYW, but a much better thermal conductivity [83, 84]. It is thus possible to increase the pump beam size in the crystal to reduce the accumulation of nonlinear effects, and to pump strongly to achieve a high gain. Their nonlinear coefficients are

Host	T	Dop.	N_T	τ_L	$\sigma_{a,P}$	$\sigma_{e,L}$	λ_P	λ_L	$\Delta\lambda$	λ_F	$I_{sat,P}$	$I_{sat,L}$
	K	%	$10^{20}cm^{-3}$	µs	$10^{-20}cm^2$	$10^{-20}cm^2$	nm	nm	nm	nm	kW/cm^2	kW/cm^2
CALGO [68, 69, 64]	300	2	2.5	420	1	0.8	979	1045	50	1011	48.3	56.6
KYW [72, 78]	300	2	1.2	320	13.4	3	981	1023	24	—	4.7	20.2
KGW [78]	300	2	1.2	320	1.33	2.8	981	1025	20	993	47.6	21.6
Lu_2O_3 [82, 63, 74]	300	3	8.55	820	3.0	1.3	976.0	1030	13	—	8.3	18.1
Sc_2O_3 [82, 63, 74]	300	3	10.1	800	4.5	1.5	975.1	1040	12	—	5.7	15.9
$LuScO_3$ [82, 74, 75]	300	3	9.3	800	3.1	1.7	975.7	1040	22	—	8.2	14.1
YAG [78, 76]	300	5	6.9	951	0.75	2.1	940	1031	9	1007	29.6	9.7
CaF_2 [78, 76, 81]	300	2.59	6.35	2400	0.54	0.25	979	1045	70	1005	15.7	3.2

Table 3.3: Laser parameters of the different Yb doped crystals

similar (9×10^{-16}cm^2/w). Simulations and calculations of regenerative amplifiers based on these materials are shown below.

3.4 Design of the regenerative amplifier

3.4.1 Laser dynamics

Simulating the dynamic processes in a regenerative amplifier has to be realized on two different time scales: the coarse one deals with one round-trip, and the fine one divides one round-trip into smaller time-steps. Looking at the round-trip time scale lets us notice the evolution of the pulse from one round-trip to another. This way, bistability can be simulated among other dynamical behaviours: the residual gain after one amplification cycle is used as input for the regenerative phase of the next period.

The fine time-scale needed to pass the medium can be ignored provided the medium is thin and has a homogenous gain over its length. This is true for thin-disks or for thin slabs. It is completely insufficient for fibers or rods, where the absorption of the pump leads to different gain values along the amplifying material.

In principle, simulation methods like the one described above are able to accurately predict the principal behaviour of the dynamical processes in a regenerative amplifier and have the extra advantage of short computational efforts. The simplification for short crystals may result in inaccurate results when longer crystals are used. In the case of long crystals, a more complex numerical method should be used to attain accurate numerical values for the output energy. To simulate this experiment, two situations were detailed. The first one assumed that the crystals are thin enough to calculate only the total gain dynamically, similarly to the one described in [85], whereas the second one solved the laser differential equations in time and space.

In order to estimate the reliability of the numerical values of calculated energies, one must consider possible sources of errors. A corresponding, accurate model of the resonator and pump system must be available to provide correct spot sizes of pump and laser. Losses may be estimated from the properties of the individual intra-cavity elements. The gain can be estimated from the absorption and emission cross-sections. In part the literature values for the spectroscopic properties vary significantly, probably as a result of different crystal qualities and of calculating the absolute values of emission cross-sections with the Füchtbauer-Ladenburg equation, called the reciprocity method [86, 87]. Also, there is typically a mismatch between the linewidth of a laser-diode and the spectral width of an absorption line. An effective absorption coefficient must be estimated in this case. In the Yb:KYW case, the values taken for emission and absorption cross-sections at pump and laser wavelengths were 16×10^{-20} cm^2, 13×10^{-20} cm^2, 2.2×10^{-20} cm^2, and 0.52×10^{-20} cm^2, respectively [88].

The equations solved in the first simulation are the following [85]:

$$\frac{dg}{dt} = \frac{g_0 - g}{\tau_L} - \frac{gE}{E_{sat}T_R} \tag{3.1a}$$

$$\frac{dE}{dt} = \frac{E}{T_R}(g - l) \tag{3.1b}$$

with E the energy of the laser pulse to amplify, E_{sat} the saturation energy defined as $E_{sat} = \frac{hc}{\lambda_L \sigma_{e,L}}$ with $\sigma_{e,L}$ the emission cross-section at laser wavelength, g the gain and l the intra-cavity losses.

The initial conditions of the amplification phase were set to $E(0) = E_{seed}$ and $g(0) = g_2$, where the gain at the end of the pumping phase g_2 is defined by:

$$g_2 = g_0 + (g_1 - g_0)e^{\left(-\frac{T_K - T_G}{\tau_L}\right)} \tag{3.2}$$

g_1 is the gain at the beginning of the pumping phase and g_0 the small signal gain for CW-pumping.

Equations 3.1 were solved in Mathcad with a Runge-Kutta solver 4^{th} order.

The energy of 100 consecutive output pulses were calculated for a gate length varied between 1 and n round-trips, n being a natural integer. The simulation was verified with a laser built previously on a 2-crystal cavity and delivering 8 W at 500 kHz repetition rate [65]: this model gives an approximate result of the energy after amplification, but displays well the bistability of the system and reproduces the experimental observations of the influence of all parameters.

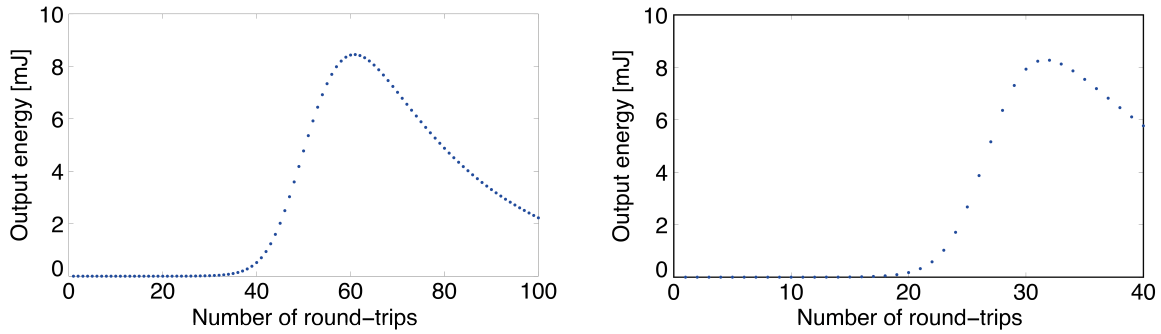

(a) Calgo **(b)** KYW

Figure 3.3: Dynamic of the regenerative amplifier: the output energy was calculated for Yb:CALGO and Yb:KYW crystals.

In the case of a low repetition rate regenerative amplifier, *e.g.* a repetition rate of 1 kHz, it is possible to pump it in the quasi-continuous wave regime if the lifetime is shorter than the period of the amplified pulse train. As the life-time of Yb:KYW and Yb:CALGO are about 300 µs and 420 µs respectively, this is possible with both materials. As shown in figure 3.3, there is no bistability under such conditions. Thanks to the strong pumping it is possible to achieve a high gain in the crystal; the desired, maximum output energy can be extracted in only 30 to 60 round trips. The effects of saturation in the crystal and intra-cavity losses can be observed: after reaching a maximum the energy decreases again.

More detailed simulations were performed by solving the differential equations governing the dynamics of the pump and seeder fluences. To scale up the power a design with two crystals was simulated. The rate equations 3.4 have been derived for a quasi-three level system, similarly as in [89], for the pump and amplified laser fluences $\Phi_{P,i}$ and Φ_L, with i

integer referring to the pump of the i^{th} crystal, and for the population inversion n_i of the i^{th} crystal defined as:

$$n_i = n_{1,i} - f_L n_{2,i} \tag{3.3}$$

f_L is the ratio of the absorption and emission cross-sections at laser wavelengths, and $n_{1,i}$, $n_{2,i}$ the populations of the energy levels 1 and 2. The fluences $\Phi_{P,i}$ and Φ_L are related respectively to the pump and laser energies $E_{P,i}$, E_L and waists w_P, w_0 with the relationships: $\Phi_{P,i} = {}^{E_P}/_{\pi w_P^2}$ and $\Phi_L = {}^{E_L}/_{\pi w_0^2}$.

$$\begin{aligned}\frac{\mathrm{d}n_i}{\mathrm{d}t} = &\left(\left(\sigma_{a,P} + \sigma_{e,P}\right) n_i + \left(f_L \sigma_{e,P} - \sigma_{a,P}\right) n_T\right) \frac{\Phi_{P,i}}{h\nu_P \mathrm{d}t} \\ &- \left(\sigma_{a,L} + \sigma_{e,L}\right) \frac{\Phi_L}{h\nu_L \mathrm{d}t} n_i - \frac{n_i + f_L n_T}{\tau_f}\end{aligned} \tag{3.4a}$$

$$\frac{1}{\Phi_{P,i}} \frac{\mathrm{d}\Phi_{P,i}}{\mathrm{d}z} = \frac{\left(f_L \sigma_{e,P} - \sigma_{a,P}\right) n_T + \left(\sigma_{a,P} + \sigma_{e,P}\right) n_i}{1 + f_L} \tag{3.4b}$$

$$\frac{1}{\Phi_L} \frac{\mathrm{d}\Phi_L}{\mathrm{d}z} = \sigma_{e,L} n_i \tag{3.4c}$$

$$\frac{1}{\Phi_L} \frac{\mathrm{d}\Phi_L}{\mathrm{d}t} = -\frac{1}{T_R} \tag{3.4d}$$

The indices L, P, a, and e respectively indicate laser, pump, absorption, and emission. σ symbolizes the cross sections and τ_f the upper-state lifetime. The cavity photon lifetime T_R is defined as: $T_R = (2d/c\alpha)$, with d optical cavity length, α total cavity losses, and c speed of light in vacuum. The frequencies ν_L and ν_P, related to the wavelengths λ_L and λ_P with $\nu_L = {}^{c}/_{\lambda_L}$ and $\nu_P = {}^{c}/_{\lambda_P}$, correspond to the laser and central pump frequency respectively. The first equation describes the evolution of the population inversion in each crystal depending on the pump and laser fluences. The pump is described in each crystal with equation 3.4b; the pump fluence was assumed as flat-top in time and space. The growth of the laser fluence over the crystal length, given in equation 3.4c, depends on the population inversion; the intra-cavity losses are solved over time in equation 3.4d.

These differential equations were solved via Matlab routines and a self-written ODE (Ordinary Differential Equation) solver using Euler and Runge-Kutta algorithms. The choice between both algorithms is a trade off between computing time and precision, using the Euler solver for equations 3.4b to 3.4d and the Runge-Kutta 4^{th} order solver for equation 3.4a. In the simulation, the propagation of pump and laser beam through the crystal is computed in one step, according to the assumption of crystals short compared to the time resolution. The pump and laser fluences are initialized at $t = 0$ over the first crystal in the propagation direction z, whereas the population inversion is set to 0. The pump is initialized for all t at the entrance of the crystal with a pulse flat-top in time, according to the QCW pumping. The actual algorithm solved first equation 3.4a for both crystals at time t, using $\Phi_{P,i}$ and Φ_L calculated at $t-1$, then the pump and laser fluences are propagated at time t over the crystal length. During the propagation over z, ODE 3.4c and equation 3.4d were solved for each slice, the fluences at the end of one slice being the initial condition of the next one.

The parameters used in the simulation are summarized in table 3.4. The pump duration of 550 µs corresponds to ∼1.5× lifetime of the crystal.

Parameter	Unit	Target value KYW	Experimental value KYW	Target value CALGO
Repetition rate, f_{rep}	kHz	1	1	1
Pumping time, T_P	μs	550	550	1000
Pumping pause	μs	450	450	0
Round trips, RT	–	32	32	55
Pump power, P_P	W	60	60	60
Pump spot sizes, w_P	μm	320	340	300
Mode spot sizes, w_0	μm	300	375	300
Losses, α	%	5	6	5

Table 3.4: Parameters used for solving the rate equations in the case of 2% doped-Yb:KYW and 2.5% doped Yb:CALGO. For KYW, both parameter sets correspond to the targeted parameters during the design phase and to the actual experimental parameters.

The pump and laser beam parameters are chosen according to the experimental setup for the plain and dashed curves in figure 3.4, whereas the dash-dotted curve shows the original targeted values. The losses are estimated from the intra-cavity elements, and fine-tuned to match the experimental results. Three cases are simulated: first for the targeted parameters, second with the actual experimental parameters, assuming an absorption coefficient $\alpha = \sigma_{a,P} n_T$ of 17.2 cm^{-1}, with numbers given in table 3.3, and last an effective absorption coefficient of 12.0 cm^{-1}, to account for the spectral mismatch between pump diode and absorption line of Yb:KYW. The pump light is not fully absorbed due to its FWHM bandwidth of 4.2 nm, compared to the 3.6 nm absorption bandwidth (FWHM) of Yb:KYW.

Figure 3.4a shows the evolution of the inversion and amplification over 10 cycles, and figure 3.4b zooms into one amplification cycle. The energy obtained in each cycle is constant and no sign of bistable behaviour is observed. In the simulation, 32 cavity round trips are used for one regenerative amplifier cycle to show saturation and losses. Taking the two different assumed pump absorption coefficients into account, respectively 8 mJ and 6.5 mJ output energy are expected for a repetition rate of 1 kHz.

With the targeted value of 320 µm radius for the spot sizes inside the crystals, which is 15% smaller than the experimental one, more than 10 mJ output energy at 1 kHz is expected. The other parameters remained the same as given in table 3.4.

Similarly, figure 3.5 illustrates the expected values for the Yb:CALGO based regenerative amplifier. The simulation has been realized with the parameters given in table 3.4.

The time resolution is equal to the one of the Yb:KYW simulation and equals one round-trip. This simulation assumes 5% intra-cavity losses and 300 µm pump and laser spot sizes. The expected output energy reaches 8 mJ, before decreasing due to losses. The net inversion of ∼ 20% is higher than in the case of Yb:KYW in light of the higher doping concentration. The maximum output energy is reached after 53 round trips.

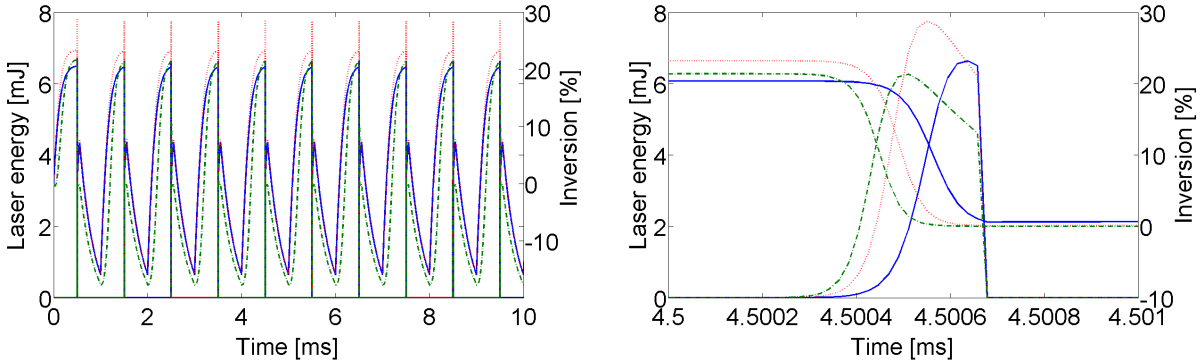

(a) 10 periods **(b)** One amplification cycle

Figure 3.4: Solution of the differential rate equations in the case of Yb:KYW regenerative amplifier: the plain, blue curves are the simulations with 17.2 cm^{-1} absorption coefficient, the dashed, red ones with 12.0 cm^{-1} absorption coefficient and the dash-dotted, both with the experimental spot sizes, and the green ones with the targeted spot size and full absorption coefficient.

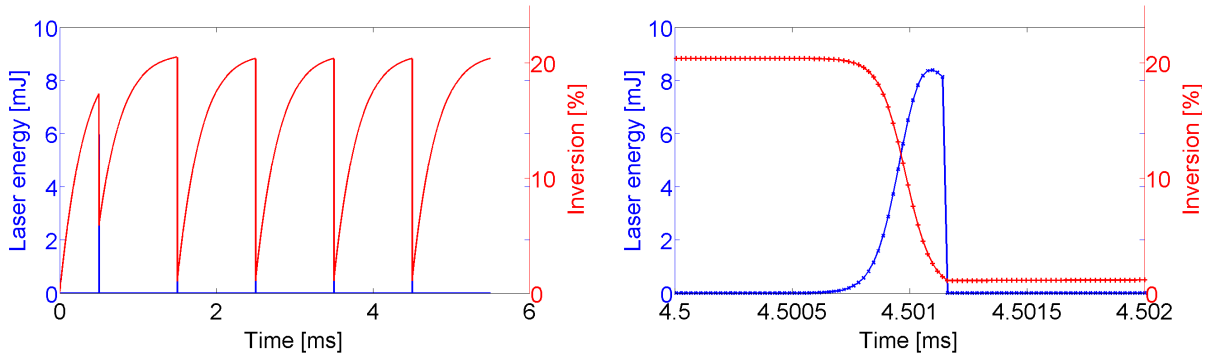

(a) 10 periods **(b)** One amplification cycle

Figure 3.5: Solution of the differential rate equations in the case of Yb:CALGO regenerative amplifier.

3.4.2 Avoiding bistability

Bistability or chaotic behaviour originate when the inversion in the gain medium is not constant from the end of one period to the end of the next one. If, for example, the gain is not completely depleted when the pump is switched on for the next period P_n, then the gain at the beginning of the amplification phase of the next period P_n could differ from the one of the preceeding period P_{n-1}. The second seed pulse is then amplified to a different level and can reach another energy than the previous pulse. If the system does not reach stability with all amplified pulses at the same energy, it can still stabilize with two or more distinct output energies, *i.e.* it undergoes a bifurcation, with a new stable periodic energy fluctuation emerging. Since the system is sensitive to small changes and fluctuations it can become chaotic. Figure 3.6 shows an example of this chaos: the energy of the output pulses is displayed versus the number of cavity round-trips.

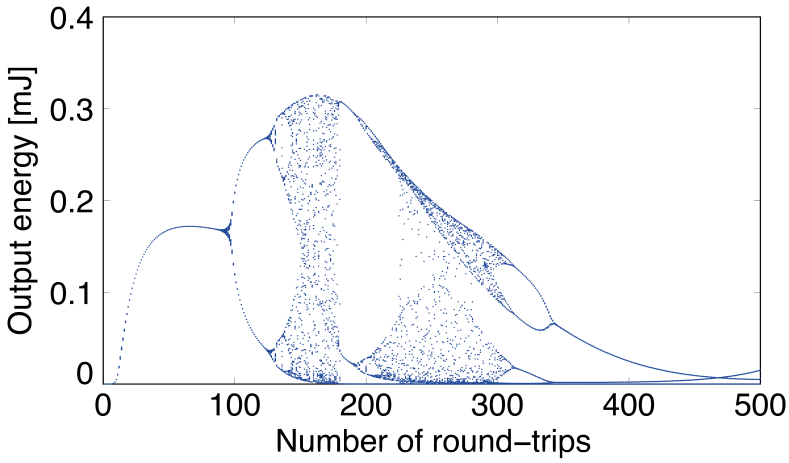

Figure 3.6: Example of a regenerative amplifier showing regions of multi-pulse stability: for each amplification time, given here in round-trips, 50 consecutive amplification cycles were calculated. The inversion at the end of one period is fed as input parameter to the next one.

Bistability and chaotic behaviours, studied in [85, 90, 91], are influenced by the repetition rate and the lifetime of the active ions in the gain material: if the time between one amplification cycle and the next pumping cycle is 2-3 times longer than the decaying time of the active ions, then the inversion decays systematically to 0 during this pause. The start inversion for the next pumping cycle is therefore constant. In the cases where the pumping deadtime is equal to or shorter than the life-time, bistability may occur, depending on the seed energy and the cavity losses. A strong seed pulse depletes indeed the gain in a few round trips.

The fine time-scale simulation explains the evolution of the pulse during the round-trip: the gain in the crystal is modeled more precisely over small steps in the crystals and not at once. It is then possible to integrate the chirp and the different gain seen for the leading and the trailing edge of the pulse into the model.

Both simulation approaches may be used in different cases: one can neglect the simulation over several round-trips *e.g.* if the laser is pumped in quasi-continuous wave regime and the lifetime of the crystal is shorter than the "dead-time": during the pumping pause, the inversion in the crystal decreases completely due to relaxation. During the next pumping time, the inversion builds up from 0 to the same value as during the previous pumping periods. This is explained above in figure 3.2.

3.4.3 B-Integral calculations

During propagation through a medium, a pulse accumulates nonlinear phase shift due to the intensity dependence of the refractive index, called Kerr-effect. It induces self-focusing in the spatial domain and self-phase modulation in the temporal domain. The refractive index is defined by: $n = n_0 + n_2 I$, where I represents the intensity, n_0 the linear refractive

index and n_2 the nonlinear refractive index coefficient. The phase shift, or B-integral, accumulated during propagation in a material with length l_{mat} follows equation 3.5.

$$B = \frac{2\pi}{\lambda_L} \int_0^{l_{mat}} n_2 \cdot I(z)\, dz \tag{3.5}$$

The peak intensity is calculated as: $I = \frac{fE}{\tau \pi w_0^2}$, where the factor f depends on the beam profile and equals 1 for flat-top or 2 for Gaussian beams in space.

During amplification to high energies, the nonlinear phase shift has to be minimized to avoid phase front and beam profile distorsions which are detrimental to the applications of this laser system: OPCPA pumping, WLG and THz generation. This is realized by reducing the intensity, which can be achieved first by stretching the pulses in order to implement the chirped pulse amplification scheme (CPA) and second by increasing the spot sizes.

Accumulation of nonlinear phase concerns mainly the crystal and the Pockels cell, as these components are the longest in the cavity, and secondarily the waveplate and the thin-film polarizer. The nonlinearities of air are negligible in this experiment due to the low nonlinear refractive index and the highly stretched pulses. The cavity design aims to find the optimum between the material length, fixed in the case of the Pockels cell, but adaptable for the crystal, and the spot sizes, in order to decrease the nonlinearities whilst keeping the gain high as needed according to the simulations of the amplification dynamics.

The B-integral values were calculated with the n_2 values of the materials found in the literature. These can however vary by nearly a factor of 2, as in the case of Yb:KYW [92, 93]. The summary of the material parameters is shown in table 3.5, while table 3.6 describes the cavity parameters taken for the calculation.

Material	n_2 $[10^{-16} cm^2/W]$	Ref.
KYW	9-15	[93, 92]
CALGO	9	
BBO	3.1-5	[94, 95]
BK7	3.7	[96]
Quartz	3.2-2.7	[96, 97]
FS	3.2-2.7	[96, 97]
Air	1.9×10^{-4}	[98]
TGG	17	[99]

Table 3.5: Material parameters for calculation of the nonlinear phase shift in the regenerative amplifier

The length of the Pockels cell, waveplate and TFP are respectively 40 mm, 1.4 mm and 2 mm, the angle of incidence on the TFP being 56°. For the calculations, 1 mm beam radius in the switching elements and 320 µm in the crystals are assumed. The number of relevant round trips in the cavity is taken to be 10 and the output pulse has 10 mJ energy: the nonlinear phase accumulated during the round-trips with low energy can be neglected due to the low number of total round-trips needed. The spot sizes in the Pockels cell and crystals are taken as constant, because of the collimation of the beam in the switching elements and the very short length of the gain media. Assuming a Gaussian

Component	Pockels cell	Crystal	Crystal	Waveplate	TFP
Material	BBO	CALGO	KYW	FS	Quartz
Effective length [mm]	40	2.5	3	2	1.4
Spot size [μm]	1000	320	320	1000	1000
Number	1	2	2	1	1
Total	0.22-0.34	0.74	0.98-1.48	0.006-0.008	0.016-0.02

Table 3.6: Cavity parameters for B-integral calculations in the regenerative amplifier and the nonlinearity accumulated through a full amplification cycle in the cavity. 10 relevant round-trips and Gaussian pulses stretched to 2.3 ns with a maximum energy of 10 mJ have been considered.

spatial shape and a Gaussian temporal profile of 2.3 ns, the total nonlinear phase lies between 1.2 and 1.8, depending on the nonlinear refractive index taken into account for 3-mm long Yb:KYW, FS and BBO. The temporal profile of the pulse is however not Gaussian because of the sharp spectral filtering in the stretcher based on chirped fiber Bragg gratings (*cf.* chapter 5); as a comparison, the intensity is reduced by a factor of 0.88 for $sech^2$ pulses, leading to a B-integral value in the range 1.1 - 1.6.

In the case of the 2.5 mm long Yb doped CALGO crystals, with a $5{\cdot}10^{-16} cm^2/W$ value for the nonlinear refractive index coefficient of BBO [95], the nonlinear phase cumulates to 0.85 for a pulse Gaussian in space and time, or 0.75 for a $sech^2$ pulse.

An increase of the spot sizes to 350 µm relaxes the nonlinear cumulated phase in the crystals to 0.6 for Yb:CALGO and 0.74-1.2 for Yb:KYW.

These values are high for a bulk laser, but no beam distorsion nor spectral broadening are to be seen experimentally. All these values have also to be mitigated with some considerations on the pulse duration: in this estimation, the shortest experimental output pulse duration has been considered throughout the amplification, whereas the incoming pulse in the regenerative amplifier is 3.6 ns long in reality and shortens due to gain narrowing. This means that this calculation overestimates the nonlinear phase-shift.

3.4.4 Thermal lensing

The spot sizes of the laser and pump modes in the crystals determined with the simulations are used for the cavity design. The resonator is based on a dual-crystal resonator similar to the one shown in [65]. This approach distributes the thermal load and lowers the thermal effects when compared with a single-crystal cavity. The second condition set on the cavity design is the insensitivity of the spot sizes with respect to thermal changes in the crystals.

Thermal lensing is due to the change of the refractive index and the mechanical deformations of the crystal, both caused by non-uniform temperature distribution, caused by the finite, and typically non-uniform, pump beam profile. The higher the pump intensity, the stronger the thermal effects. The temperature profile follows the propagation and the beam profile of the pump beam whilst the cavity is non-lasing. The absorbed energy is partly emitted as fluorescence and partly converted into heat. Under lasing conditions

the absorption of the pump increases and energy is extracted, thus reducing the thermal load.

The mechanical deformations, caused by strain and shear stress, lead to surface bulging. They depend on the thermal expansion coefficient and thermal conductivity of the material [100].

In the case of ytterbium doping, the quantum defect is low compared with the one of other ions such as for example neodymium, which is advantageous to reduce the thermal effects: comparing both ions in the YAG host the quantum defect for ytterbium ions pumped at 942 nm is 9% and 24% for neodymium ions pumped at 808 nm. ytterbium ions have a two-level manifold reducing parasitic effects like excited state absorption, upconversion or cross-relaxation.

Thermal lensing effects in ytterbium doped materials have been extensively investigated in [56, 101, 102]. Estimation of the thermal lens under lasing and non-lasing conditions can be performed using the formulas 3.6 given in [102].

$$D_{th,b} = AP_{abs}(1 - \eta_P \eta_r \frac{\lambda_P}{\lambda_F}) \text{ before threshold} \tag{3.6a}$$

$$D_{th,a} = AP_{abs}(1 - \eta_P((1-\eta_l)\eta_r \frac{\lambda_P}{\lambda_F} + \eta_l \frac{\lambda_P}{\lambda_L})) \text{ after threshold, lasing} \tag{3.6b}$$

$$= AP_{abs}(1 - \frac{\eta_P \eta_r}{\sigma_{e,L} \frac{I\lambda_L}{hc} \eta_r \tau_{rad} + 1}(\frac{\lambda_P}{\lambda_F} + \sigma_{e,L} \frac{I\lambda_L}{hc} \tau_{rad} \frac{\lambda_P}{\lambda_L})) \tag{3.6c}$$

The already defined laser and pump wavelengths λ_L and λ_P and the fluorescence wavelength λ_F are parameters of these equations. The strength of the thermal lens $f_{th} = {}^1/_{D_{th}}$ depends on the quantum defect $\eta_p = \lambda_P/\lambda_L$, the radiative quantum efficiency of the upper manifold $\eta_r = \tau_{nr}/(\tau_{nr} + \tau_{rad})$, the laser extraction efficiency η_l and on the fractional thermal load η_h given by:

$$\eta_h = 1 - \eta_p \left((1-\eta_l)\eta_r \frac{\lambda_P}{\lambda_F} + \eta_l \frac{\lambda_P}{\lambda_L} \right) \tag{3.7}$$

The radiative and non-radiative lifetime τ_{rad} and τ_{nr} are used to define the lifetime $\tau_f = \left(\tau_{rad}^{-1} + \tau_{nr}^{-1}\right)^{-1}$. The coefficient A is a constant of the material, depending on the thermo-optic coefficient and pump diameter, defined as :

$$A = \frac{\chi}{2 * \pi c \kappa w_p^2} \tag{3.8}$$

where c is the speed of light and the thermo-optic coefficient χ in K^{-1} is given by:

$$\chi = dn/dT + (n_0 - 1) * (1 + \nu) * \alpha_T + 2 * n_0^3 * \alpha_T * C_{r,\theta} \tag{3.9}$$

Most material parameters have been defined in table 3.1, and $C_{r,\theta}$ is the photoelastic coefficient.

Equations 3.6 were used for calculating the thermal lens for Yb:KYW, with the material parameters given above in section 3.3; the missing photoelastic coefficient $C_{r,\theta}$ of KYW

has been approximated with the one of KGW of $6.1\times10^{-15}s^3/kg$ as given in [102]. The value for χ was $2.12\times10^{-15}K^{-1}$ and consequently A was 7.65 $m^{-1}W^{-1}$. The thermal lens was calculated to be ∼240 mm under lasing conditions, assuming a 350 µm pump spot size, 60 W pump power and 10 W output power. As the cavity had been designed for 300 mm to 350 mm thermal focal length, this thermal lens value leads the cavity close to the stability limit, below the region insensitive against thermal lensing. This induced a dramatic increase of the spot sizes from 320 µm to ∼400 µm in both crystals, decreasing the gain.

Lowering the pump absorption by decreasing the doping concentration reduces the thermal lensing. The consequent drop in the gain can be compensated by increasing the crystal length, however at the expense of more nonlinear phase shift accumulation. The pump wavelength determines the quantum efficiency, meaning the heat load dissipated in the crystal. ytterbium ions doped media present several absorption peaks: the one with highest absorption and broadest line is located at 933 nm for Yb:KYW or 938 nm for Yb:YAG, corresponding to 10% quantum defect. A second absorption line, narrower and weaker, is located at 974 nm to 982 nm depending on the host, and is called zero-phonon line. The quantum defect at the zero-phonon line amounts to less than ∼ 5%. Even though pumping in this line is of great advantage to minimize the thermal load, its narrow width has to be matched by the spectral width of the pumping laser diode as closely as possible; this is a limitation for zero-phonon line pumping, *e.g.*, in cryogenically cooled YAG. The values determined with this calculation are giving a starting point for the cavity design.

3.4.5 Cavity design and experimental setup

The cavity has to fulfill several conditions, besides the necessary spot sizes in the crystals for the gain and in the transmissive elements to minimize the nonlinear phase shift. The laserhead will be pumped over a large range of pump powers, either continuously or quasi-CW, thus the thermal lens will change dramatically. Consequently, a first condition on the cavity design is the accomodation of a wide thermal lensing range by a stable cavity. Secondly, the beam parameters have to be insensitive with respect to the thermal lens over a similar range, thus allowing the output beam parameters to remain stable.

As demonstrated in [103], both conditions are fulfilled when the crystal is inserted at a distance equal to one Rayleigh length of the laser mode from its waist, as shown in figure 3.7. The crystal is thus located close to the waist of the pump beam, but not in a waist of the resonator mode, the divergence of the latter being negligible over a short crystal length. To implement a dual-crystal cavity, corresponding to the simulated design, this module with one crystal is symmetrized around the waist of the laser mode. The waist is allowed to vary freely with the variations of the thermal lens.

The chosen resonator, as schematically represented in figure 3.8, is based on a segmented design, separating the easy to align short resonator containing the gain modules from the extended resonator including the Pockels cell and other switching elements. The short resonator comprises mirrors M1, M2, M3, both dichroic mirrors (DC) and the output coupler OC1. The high reflector M1 could also be replaced with an output coupler. This cavity is extended with the mirrors M4 to M7 to include the Pockels cell (PC), the

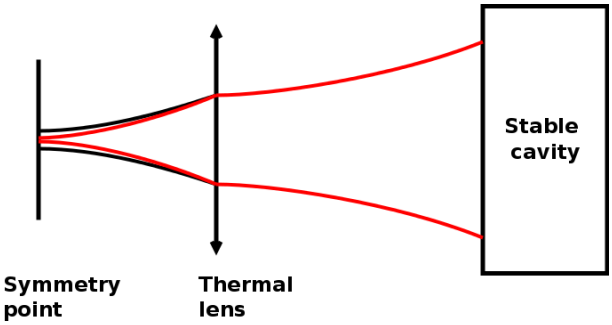

Figure 3.7: Scheme of the position of the crystal with respect to the waist of the resonator mode to minimize the influence of the thermal lens on the resonator mode. The black line represents the resonator mode for the estimated thermal lens, and the red one its change in case of a stronger one. Similarly, the waist would increase for a lowered one.

quarter-waveplate ($\lambda/4$) and the thin-film polarizer (TFP). The short cavity is divided into two halves around the symmetry point S between the crystals. Each half forms a stable resonator in itself with identical beam parameters and is used to characterize the crystals independently.

At least an 0.8 mm radius was required in the Pockels cell to minimize nonlinearities, setting a constraint on the cavity design. As the alignment sensitivity of the end mirror depends on the spot size, the switching elements are inserted in the middle of a 4-f telescope. This 4-f telescope is described by the identity ABCD matrix and acts as a zero-q transformation. It images the beam parameters from the position of the output coupler OC2 onto the end mirror of the long cavity M7. This ensures that the beam parameters in the short cavity are not modified by the extension to the long one.

This dual-crystal cavity was designed to be insensitive to variations of the thermal lenses in the crystals from 280 mm to more than 800 mm focal length. As mentioned ealier, the thermal lens in the case of Yb:KYW for CW pumping was expected to have a focal length between 300 mm and 350 mm. In QCW pumping, the average thermal load is decreased and the resulting thermal lens weaker. The strength of the thermal lens can be estimated by measuring the waist at the symmetry point.

In the case of Yb:KYW, the 3 mm long 2%-doped Yb:KYW crystals, cut along the n_g-axis, were pumped and emitted polarized along the n_m-axis. The water cooling of the slab was performed along the n_p-axis. These cut and cooling directions have been choosen to optimize the cooling: from the values given in table 3.1, the thermal conductivity is the highest and the linear thermal expansion coefficients the lowest along n_p.

The Yb:CALGO crystals were pumped polarized along the a-axis because of the higher absorption cross-section of $2.7 \times 10^{-20} cm^2$ in comparison with a polarization along the c-axis with absorption cross-section of $1.1 \times 10^{-20} cm^2$. Two ytterbium doping concentrations for the CALGO hosts were tested: 2% and 5% in the crucible. Considering the segregation coefficient of 0.49% of ytterbium in the CALGO host, the effective concentrations were around 1% and 2.5%; the latter nomenclature will be used in the following. The advantage of low-doped crystals lies in the lower absorption at the entrance surface, thus reducing thermal bulging and the total thermal lensing. In light of the high absorption of the 2.5%-

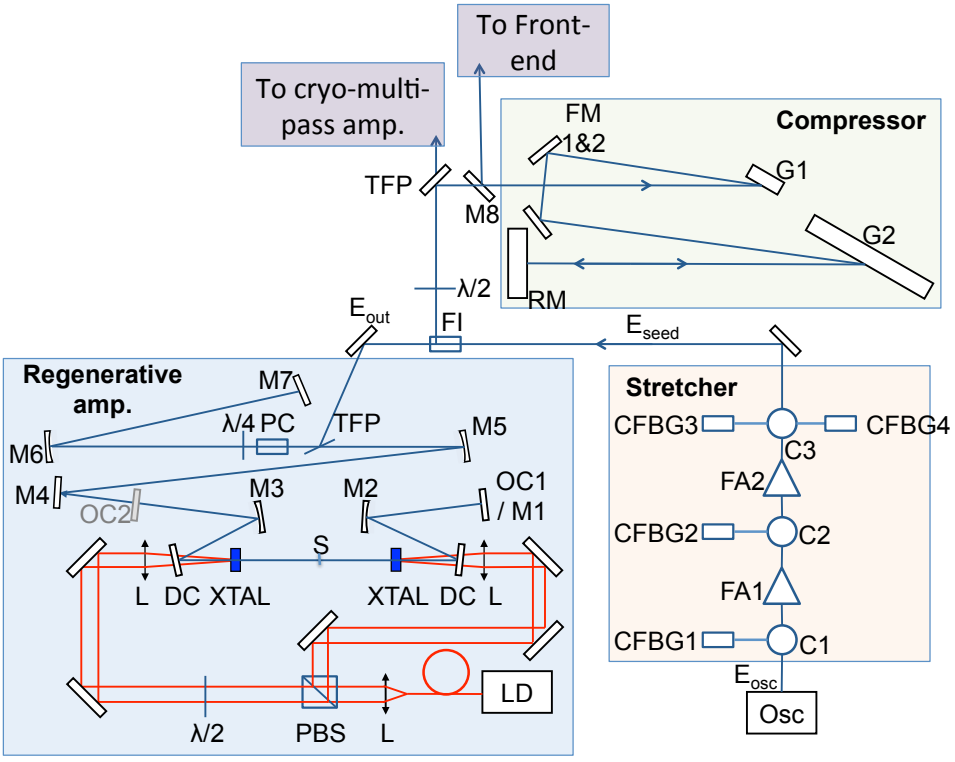

Figure 3.8: Layout of the dual-crystal cavity of the regenerative amplifier. The abbreviations of the components are L for lenses, DC dichroic mirror, PBS polarization beam splitter, LD laser diode, $\lambda/2$ and $\lambda/4$ half- and quarter-waveplate, XTAL1 and XTAL2 both Yb:CALGO or Yb:KYW crystals, PC Pockels cell, TFP thin film polarizer. M1 to M6 are high reflectors, M1 and M2 curved mirrors with 500 mm radius of curvature, while M4 and M5 have 1000 mm radius of curvature, and OC1-2 are output couplers. S denotes the symmetry point of the short cavity, located between OC1 and OC2. OC2 is removed to operate the long cavity, from OC1 to M6. For cavity-dumped operation, OC1 is replaced by a high reflector and the switching elements are inserted.

doped crystal, shorter crystals could be used, decreasing the nonlinearities when operating as a regenerative amplifier. The crystal lengths were 1.5 mm for the 2.5% doped crystal and 2 mm for the 1%-doped one.

The laser diode, model P2-120-0982-2-TKS-C from nLight, delivered a maximum power of 120 W through a multi-mode fiber with NA 0.22 and 200 µm mode-field diameter. Its wavelength was tuned to the peak absorption of Yb:KYW at 981 nm or of Yb:CALGO at 979 nm by temperature control. In the case of Yb:CALGO, the 4 nm spectral bandwidth of the diode was well matched to the 8 nm absorption bandwidth of the laser medium. The laser diode could be operated either in continuous-wave or quasi-continuous-wave modes. The 3 m long delivery fiber ensured nearly complete depolarization and homogenization of the pump. The pump beam was collimated before being split into two beams by a polarizing beam splitter working as a polarization analyzer, to pump both crystals equally. To match the crystals a-axis, the polarization was rotated in one arm with a half-waveplate. An additional pair of lenses focused the beams into the crystals. A magnification of 1:3 ensured mode-matching between pump and laser modes.

The cavity has been designed to minimize nonlinearities during amplification: the laser mode radius was 350 µm at $1/e^2$ in the crystals. To achieve these beam radii, the mirrors M2 and M3 had a radius of curvature of 500 mm and M5 and M6 of 1000 mm. The relatively large spot size in the crystals limited the available gain.

The regenerative amplifier is a part of the amplification chain to high energy of the frequency synthesizer (*cf.* section 2.3). In the version shown in figure 2.5, the broadband pulses out of the oscillator and the pulse from the pump chain have to be synchronized for both frequency conversion and parametric amplification. The synchronous arrival time of both pulses inside the nonlinear crystals is required, with a precision within a tenth of the pump pulse duration. In the version shown in figure 2.6, this problem is circumvented by splitting the output of the regenerative amplifier for front-end and pump line. For further experiments however, the whole laser system might have to be synchronized very precisely with an external laser source or other instruments. The timing of the amplified pulses should hence be controlled. External factors such as environmental temperature and humidity changes might influence the optical path length, meaning the exact arrival time of the pulses. Thermal drift occurs time scales between several seconds to hours, and can be compensated with feedback loops: the timing drift is measured, and a signal is sent to a delay line on piezo or motor stage to adjust the optical length. The limitation of the compensation comes from the range of the piezo or of the motorized translation stage. During the long amplification path in the regenerative amplifier, a slight change in the cavity length is multiplied by the number of round trips and has a high influence on the timing. For this reason, a cavity with the shortest possible length is chosen. The details of the calculations of thermal drifts are given in chapter 8.1.

Two cavities with different lengths are shown in appendix 10B, with the variations of the spot size on the end mirror and of the waist in the crystal versus the focal length of the thermal lens. The cavity with a total length of 5 m offers the advantage of a large insensitivity to the changes of the thermal lens, but the long amplification beam path would lead to a possible thermal drift of ±800 µm for ±1 K environmental temperature change. The second cavity shown, with 3.8 m length, is shorter, but the stability domain

against variations of the thermal lens is reduced. Experimentally, the first cavity has been chosen and the breadboard stabilized in temperature to ±0.1 K.

In case of a too strong thermal lens, which might be due to the lack of measurements of dn/dT for CALGO, an elliptic pump scheme has been thought of: the area would be kept equal to the one for cylindrical pumping geometry, but the beam waist decreased in the cooling direction.

Experimentally the designed cavity was fully operational at both full CW pump power and at reduced duty-cycle quasi-CW pump power in the cavity-dumped and regenerative amplifier regimes.

3.4.6 Component specifications

In this section, some key components as well as some design specificities are discussed: the Pockels cell for the switching and the isolator for separating the input from the output of the linear cavity.

Pockels cell

The Pockels cell is part of the switching mechanism for opening and closing the cavity, together with the quarter waveplate (WPZ $\lambda/4$) and the thin film polarizer (TFP). The Pockels cell operates when switched as a quarter waveplate; the combination with the WPZ $\lambda/4$ corresponds to a half waveplate ($\lambda/2$) (*cf.* section 3.1).

The Pockels cell is based on the Pockels effect, *i.e.* the induction of birefringence in a medium by the application of an electric field. The refractive index of the material changes linearly with the applied electric field. This effect exists in crystals without inversion symmetry, like BBO (β-Barium borate, $\beta - BaB_2O_4$), RTP (Rubidium Titanyl Phosphate, $RbTiOPO_4$) or KD*P (Potassium Dideuterium Phosphate). The voltage leading to a $\pi/2$ phase shift, $V_{\pi/2}$, is given by the formula:

$$V_{\pi/2} = \frac{d}{L_{PC}} \frac{\lambda}{4 n_o^2 r_{eo}} \tag{3.10}$$

where λ is the wavelength, n_o the refractive index and r_{eo} the electro-optic coefficient, depending on the material, the crystal cut, the position of the electrodes and the geometry of the crystallographic cell. The Pockels cell has a length L_{PC} and the distance between the electrodes is d. To decrease the required voltage, two cells are combined, each switching half and driven with the same high-voltage source; such a Pockels cell is called "double-cell".

The electro-optic coefficients, or Pockels coefficients, are specific to the crystal and the matrix of all electro-optic coefficients can be reduced to a few elements, considering the Kleinmann symmetry. [104, 105] The modelling of the Pockels effect is detailed in [104].

Let us consider two particular cases: BBO and KD*P cells, both easily commercially available. BBO belongs to the 3m point symmetry group and KD*P to the 4_2m, so the relevant coefficients are $r_{22} = 1.7 \times 10^{-12}$ and $r_{63} = 10.6 \times 10^{-12}$, respectively. This leads to a quarter-wave voltage $V_{\pi/2} = 21\ kV$ (5.4 kV for a double cell, 40 mm long, about 10 mm between the electrodes) in case of BBO and $V_{\pi/2} = 6.9\ kV$ (3.4 kV for a 40 mm

long single cell, with about 10mm between the electrodes) in case of KD*P. The KD*P one has an advantage concerning the lower high voltage required, but 5.4 kV at 1 kHz delivered from a high voltage driver is now state of the art.

The main inconvenience in using KD*P Pockels cells is the hygroscopy of the crystal, which reduces the lifetime of the cell. A package with sealed windows on both sides limits this issue. The pulses propagate however through a longer material. KD*P additionally suffers from gray-tracking. Other materials such as KDP might be used for the Pockels cell, however KDP is also highly sensitive to gray-tracking. Considering the available voltage of a high voltage driver and the significantly higher life-time of a BBO-based PC, BBO was chosen as material in this setup.

Minimizing the accumulation of nonlinearities, as explained in the previous section, requires a large beam diameter in the Pockels cell, thus a large aperture of the device. After comparison of the existing Pockels cells on the market, a BBO double cell with 7 mm aperture was chosen: the Lightgate 7 from Gooch&Housego.

At high average powers, depolarization might occur in the Pockels cell. With the absorption of the crystal, some heat is transferred into the lattice and induces strain in the crystal. This induced deformation of the crystal lattice changes the refractive index and induces a depolarization of the beam passing through.

The temperature of the crystal on the beam path is given for a Gaussian spatial distribution by:

$$T(r) = T_0 + \frac{P_{abs}}{2\pi\kappa C L}(1 - \frac{r^2}{w_0^2}) \tag{3.11}$$

with $P_{abs} = \alpha L P$ the absorbed power into the crystal, T_0 the temperature at the crystal boundary ($r = w_0$), r the cylindrical coordinates, C a constant depending on the geometry of the beam (1 for Gaussian, 2 for flat-top), κ the thermal conductivity, L the length of the cell, T the temperature, α the absorption coefficient in the crystal and w_0 the beam waist at $1/e^2$.

The depolarization results from the combination of 2 effects [106, 107]: the temperature increase leads to a change of the refractive index, according to the formula given for cylindrical symmetry in the cylindrical coordinates (r, θ):

$$P_{out}/P_{in} = \frac{\int_0^{2\pi}\int_0^w I_{out}\, r dr d\theta}{\int_0^{2\pi}\int_0^w I_{in}\, r dr d\theta} \tag{3.12}$$

where $I_{in} = |A_0 \exp(-\frac{r^2}{w^2})|^2$ and $I_{out} = I_{in}\exp(-\alpha L)\sin(\frac{\Gamma_1}{2})^2$.
Γ_1 is defined as: $\Gamma_1 = \frac{2\pi n_o^3 r_{eo} V}{\lambda}\left(1 + \frac{3\Delta T(r)}{n_o}\frac{\partial n_o}{\partial T} + \frac{\Delta T(r)}{r_{eo}}\frac{\partial r_{eo}}{\partial T}\right)$ with n_o the ordinary index of the material and r_{eo} the electro-optic coefficient of the Pockels cell.

The integration of P_{out}/P_{in} for a spatially flat-top beam results in:

$$P_{out}/P_{in} = e^{-\alpha L}\left(\frac{1}{2} + \frac{\sin q}{2q}\right) \tag{3.13}$$

and for a Gaussian beam in:

$$P_{out}/P_{in} = \frac{e^{-\alpha L}}{4 + q^2}\left(4\cos^2\frac{q}{2} + q\sin q + \frac{q^2}{2}\right) \tag{3.14}$$

with:

$$q = \frac{P_{abs}}{2C\kappa L}\left(\frac{3}{n_0}\frac{\partial n_0}{\partial T} + \frac{1}{r_{eo}}\frac{\partial r_{eo}}{\partial T}\right) \tag{3.15}$$

The ratio $^{P_{out}}/_{P_{in}}$ is defined as the power going through crossed polarizer and analyzer. When no voltage is applied, the transmitted power is equal to 0, and for a half-wave voltage V_π, without depolarization and absorption, the ratio between output power and input power would be equal to 1.

In the literature, the absorption measurements of BBO vary between 0.001 cm^{-1} (UltiCrystal website) and 0.0001 cm^{-1} (Cleveland website), leading to absorption losses between ∼1.1% and 0.01% respectively, considering the worst case of 20 mJ pulse energy at 1 kHz and 20 round-trips with a non-negligible energy. No depolarization problem has been observed experimentally.

Isolator

The isolator is used to separate the input from the output of the regenerative amplifier and prevents feedback into the oscillator. Feedback could lead to damage of the oscillator. The optical isolator consists of a Faraday rotator located between an input polarizer and an output analyzer.

The Faraday rotator uses the Faraday effect, which is a magneto-optic effect: in the presence of a strong magnetic field in a medium, the polarization of the light is rotated proportionally to the component of the magnetic field in the propagation direction. This effect has been discovered by Faraday in 1845 and described by Rayleigh in 1901 [108]. The typically used photo-magnetic material for Faraday rotators is Terbium Gallium Garnet (TGG).

The polarization of the light is turned non-reciprocally in forward and backward directions by respectively 45° and -45°. The axes of the polarizer and analyzer are rotated by 45°. In the forward direction, the laser light is polarized by the input polarizer. In the case of a linear polarized input beam, the polarizer is aligned to turn the linear polarization onto the wanted direction – horizontally in the designed system. The polarization is then rotated by the Faraday rotator by 45°, and transmitted by the analyzer. The polarization of the output beam is then rotated by 45° from the input beam; the polarization is further rotated with a half-waveplate to vertical. In the backward direction, the laser light is rotated first by 45° by the half-waveleplate, and further turned by −45° by the Faraday rotator. This means than the polarizer reflects the laser light and does not transmit it.

The isolator is a critical element to protect the modules before the regenerative amplifier — oscillator and stretcher — from the regenerative amplifier output: as the beam output from the linear-cavity regenerative amplifier has to be perfectly aligned with the seed beam, the leakage through the isolator would come back into the previous modules, which would cause some perturbations and could even lead to damage.

In the design of this experiment, the bulk Yb:KYW solid-state oscillator is followed by a fiber based stretcher. In view of the losses in the stretcher, two fiber amplifiers reamplify the pulses before the regenerative amplifier (*cf.* section 5).

The isolation given by one commercial isolator is generally between 30 and 44 dB respectively, which means that from 10 mJ at 1 kHz, still 10 µJ or 0.4 µJ, corresponding

to 10 mW and 0.4 mW, could go back into the fiber amplifier, which would certainly lead to damage. Two isolators in series reduce the leakage to ∼10 pW, considering the minimum 30 dB attenuation, which is enough to prevent damage.

The maximal transmission of 90 to 92% of the seed beam through one isolator needs to be taken into account in the required energy after the stretcher.

Furthermore, the isolator has to withstand the high energy out of the regenerative amplifer. The maximum parameters with a pulse energy of 20 mJ, 1 mm beam radius corresponding to the maximum aperture of a commercially available isolator (7 mm) and 1.2 ns pulse duration, lead to an intensity of 0.53 $^{GW}/_{cm^2}$ and to a fluence of 640 $^{mJ}/_{cm^2}$. With the nonlinear refractive index given in table 3.5 of 17 $\times 10^{-16} cm^2/w$ for TGG, a nonlinear phase shift of 40 µrad is accumulated by the pulse in the Faraday isolator.

Considering all parameters, the isolator from EOTech has been chosen in light of its high damage threshold and high isolation. Experimentally two bulk isolators have been used. It would have been possible to replace the first isolator after the stretcher by one fiber coupled isolator to increase the mechanical stability of the system, but the available fiber isolator exhibited too high losses.

3.5 Experimental results of the regenerative amplifier for different laser crystals

The results are presented chronogically first for the Yb:CALGO crystals, published in [109], then for the Yb:KYW ones, published in [110].

3.5.1 Yb:CALGO

Continuous-wave operation

The crystals are first tested in the short, single-crystal cavity. The distance between the crystal and the symmetry point S, as defined on figure 3.8, was set to 157 mm for the 1%-doped crystal. With 2.5% output coupling and 52 W incident pump power (40% absorbed), 11.9 W are extracted at a wavelength of 1045 nm with a beam quality parameter M^2 better than 1.2.

To compensate for the stronger thermal lens then expected of the 2.5%-doped crystal the distance between the crystal and point S is adjusted to 107 mm. This also decreases the spot-size inside the crystals and results in a higher available gain. 11 W are extracted from the 2.5%-doped crystals with 60 W incident pump power, thereof 80% absorbed, and with 5% output coupling. The slope efficiency, measured with respect to the incident and absorbed pump power, is 23% and 32% respectively. The free-running wavelength decreases from 1056.7 nm to 1047.8 nm whilst the output coupling is increased from 2.5% to 7.5% to maximize the output power.

The free-running wavelength of the laserhead with the 1%-doped crystal is closer to the one of the seeder than the one with the 2.5%-doped crystal, indicating a higher achievable gain. Also the larger spot sizes in the 1%-doped crystals than in the 2.5%-doped ones, in light of the change of the distance of the crystal to the symmetry point, allow a reduction

of the nonlinear phase shift in the regenerative amplifier operation. For those two reasons the experiment is continued exclusively with the 1%-doped crystal cavity.

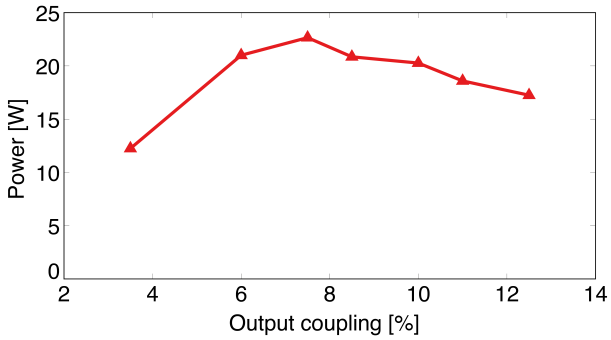

Figure 3.9: Variation of the power versus output coupling for a beam quality parameter $M^2 < 1.2$ for the two crystal cavity.

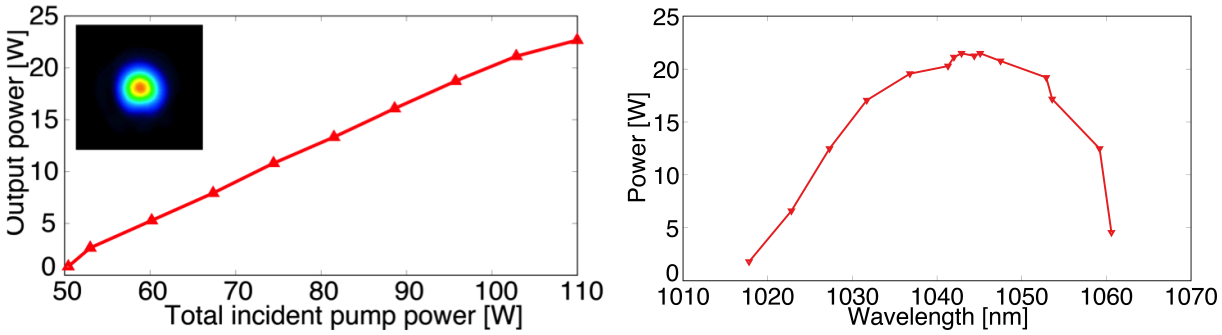

(a) Slope **(b)** Tuning curve

Figure 3.10: Characterization of CW laser head with two 2% crystals. (a) Power characterization of the laser head with the beam profile in the focus as inset. (b) Measured tuning curve. The measurements were taken with a 7.5% output coupler and with the cavity aligned for a beam quality parameter better than 1.2 at maximum output power of 23 W.

An experimental determination of the strength of the thermal lens is obtained by measuring the beam parameter of the one crystal cavity in the symmetry point: the beam size varies at this point with the thermal lens. The result gives a focal length of the thermal lens of 320 mm at nearly full pump power, which lies well in the estimated range for the cavity design.

In the short two crystal cavity, the optimum output coupling to achieve maximum output power was first determined. For this purpose the output coupler was varied while adjusting the pump power to keep the beam quality parameter M^2 between 1.1 and 1.2. The spatial properties of the beam were measured with a commercial device (Metrolux M2 Monitor ISO) according to the 4-sigma algorithm [111]. For high output couplers, the limitation was due to the available pump power. The optimum output coupling was

determined to be 7.5% as shown in figure 3.9, which corresponds to 305 W intra-cavity power. For output couplers below 6%, the intra-cavity power is nearly constant, reaching 350 W. It decreased to 138 W for a 12.5% output coupler.

The cavity has been further characterized with the 7.5% output coupler. Figure 3.10a shows the output power versus incident pump power of the short, two-crystal cavity, with the beam profile in the focus of a lens as inset. The beam quality parameter M^2 is better than 1.2 on both axes. During these measurements, the free-running wavelength of the laser is around 1042 nm. Changing from the short to the long cavity without the switching elements no noticeable change of power is observed and the free-running wavelength is still around 1042 nm. The maximum output power obtained is as high as 23 W for an input pump power of 112 W. The slope efficiency is measured to be 37% and the threshold is at 54 W pump power.

The wavelength was tuned by inserting a birefringent filter in the cavity [112]; the result is shown in figure 3.10b for the 7.5% output coupler and at 112 W pump power. The cavity was easily tunable over a bandwidth as wide as 42 nm, beginning at 1017.8 nm with 1.8 W and ending at 1060.6 nm with 4.5 W output power. More than 20 W are extracted between 1040 nm and 1047 nm. The output power dropped off at long wavelengths because of the reduced emission cross-section of CALGO, and for short wavelength due to the reabsorption losses in the ytterbium ions, from the emission and absorption cross-section curves of the material.

Cavity-dumping and regenerative amplifier operation

In order to demonstrate cavity dumped and regenerative amplifier operation, the electro-optic switch presented in [49] and explained above is inserted in the cavity.

The repetition rate aimed at is 1 kHz, corresponding to a 1 ms period, which is long compared to the upper state lifetime of the gain material of 420 µs. To store the maximum possible energy, a pump duration corresponding to one to two upper state lifetimes is necessary. Increased pump duration leads to higher heat dissipation in the crystal, thus raises thermal effects. To avoid this a well-known solution lies in quasi-CW operation of the pump diode. As the cavity is designed to be insensitive to the thermal lens and as the product of lifetime and repetition rate is close to 1/2, both CW and QCW pumping schemes are demonstrated.

A Stanford Research pulse-delay generator DG645 is used to synchronize the Pockels-cell, the pulsed power supply of the laser diode and the seed laser.

During alignment one of the crystals was damaged and had to be replaced; however, the new crystal limited the output power to 16.5 W for 105 W of input power. This loss of power was attributed to either a higher concentration of color centers or to impurities in the new crystal, as at the time of the experiments the crystal growth was still not fully reproducible. These additional losses could not be compensated. The additional intra-cavity loss of 2 % due to the switching elements further reduces the maximum output power at the free-running wavelength of 1045 nm to 10.9 W in CW-operation.

In cavity-dumped operation, under both CW and QCW pumping conditions 4 mJ-pulses at a repetition rate of 1 kHz were extracted. The similarity of the output-power suggests that the CALGO crystals were not limited by thermal gain quenching. Due to the insensitivity of this cavity, the beam quality is similar for both pumping schemes, even

though the thermal load was reduced during the non-lasing time. The extraction time was 3.72 µs long for CW-pumping and 3.79 µs in QCW pumping with a pump duration of 650 µs. The amplification durations corresponded to 186 and 187 round trips, respectively.

For seeded operation, a commercial Yb:KYW bulk oscillator running at a central wavelength of 1030 nm and delivering 16-nJ, 210-fs pulses at 42.5 MHz repetition rate was used. The 6.5 nm spectral bandwidth of the seeder could sustain 170 fs long pulses. To reduce nonlinear effects the seed pulses are chirped [49], before injection into the regenerative amplifier. They are stretched to the stretching ratio necessary for the amplification stages located after the regenerative amplifier. The stretcher consists of four chirped fiber Bragg gratings and fiber circulators. The 210 fs compressed oscillator pulse had to be attenuated before coupling in the fiber, to avoid nonlinearities. Two ytterbium-doped fiber amplifiers were inserted in the stretcher to compensate for the low input energy and for the losses of the stretcher, such that the pulse energy was 1 nJ at the stretcher output. The output pulses were 3 ns long and their bandwidth was limited to 4.5 nm by the combination of the bandwidth of the CFBGs and the fiber amplifiers. The CFBGs were designed to compensate for the higher-order dispersion of a grating compressor, thus enabling a theoretical recompression to Fourier-limited pulse duration.

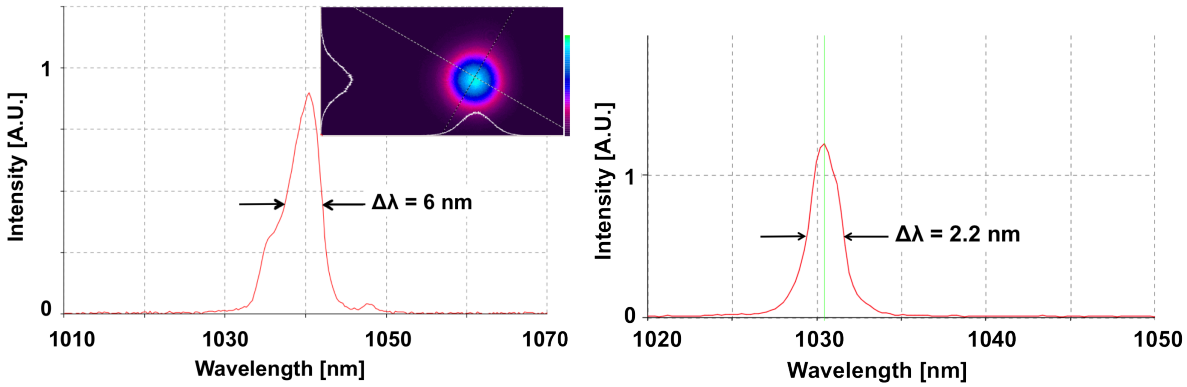

(a) Spectrum CD **(b)** Spectrum seeded

Figure 3.11: Output spectra for both cavity-dumped (a) and regenerative amplifier (b) operations of the Yb:CALGO laser. Both spectra were measured at a repetition rate of 1 kHz and with 118 W of pump power.

Figure 3.11 shows the spectra in both cavity-dumped (CD) and seeded operation for CW pumping. In the cavity-dumped case, the beam profile is shown in the inset of figure 3.11a. The M^2-parameter is in both cases 1.2. In the first case, the spectrum is centered at 1040 nm with a bandwidth of 6 nm (FWHM). This spectrum corresponds to the maximum gain of the laser, but it does not overlap well with the seeding spectrum centered at 1029.5 nm. Seeded, as much as 3 mJ are extracted with a 2.2 nm wide spectrum, while the central wavelength shifts to 1031 nm. Both behaviours, gain narrowing and spectral shift, are consistent with the observed tuning curve, which reflects the available gain at each wavelength. As shown in figure 3.10b, the gain reaches a maximum for wavelengths between 1040 nm and 1047 nm, whereas it reaches only two-thirds of its value at 1030 nm, with a decreasing slope towards shorter wavelengths, thus shifting the pulse to longer wavelength during regenerative amplification.

The optimal amplification occurs for 2.53 µs extraction time, corresponding to 125 round trips and a single-pass gain G_0 per crystal of 1.03. The high number of round-trips, due to the low single-pass gain, compensated for the intra-cavity losses, among others the ones of the Pockels cell, and the reduced amplification of the gain peak of the material. The transform-limited pulse duration is 500 fs. In light of the strong wavelength shift, the energy comprised in 1 nm around 1029.5 nm represents only a small fraction (20%) of the total pulse energy. This would prevent efficient seeding of the following amplifiers.

The energy in cavity-dumped operation at 1 kHz is consistent with the lifetime of the material (420 µs) and the CW power. The energy extracted by the seed pulse is also consistent with the gain available around 1030 nm.

Even though Yb:CALGO has a broad emission bandwidth, the spectral shape of the gain is responsible for gain-narrowing, especially for seed spectra not centered on the maximum gain of the material. A short seed-pulse would have to be centered at this wavelength range to be amplified while minimizing gain-narrowing and taking advantage of the broad emission of the material.

Due to the crystal damages and lower gain at 1030 nm than at 1042 nm, a Yb:KYW crystal has also been tested, whose results are presented below.

3.5.2 Yb:KYW

In a similar way to the Yb:CALGO case, the system has been first characterized in CW, then in CD operation, and finally as a regenerative amplifier.

Continuous-wave results

The cavity was optimized in the CW regime to extract maximum power with a diffraction limited beam, while keeping the spot-sizes in the crystals larger than 300-µm spot-size radius. In both crystals the smallest signal absorption is 65%. Figure 3.12a shows the slope efficiency obtained with different output couplers. For this measurement, an attenuator composed of a half-waveplate and a polarization beam splitter has been inserted in the pump path to vary the pump power while keeping the pump wavelength constant. The maximum output power is obtained with 15% output coupling and with a slope efficiency of 40.3%. The free-running wavelength is 1031 nm. The high threshold at 55 W incident pump power is due to the increased spot size inside the crystals. The tuning curve measured for 112 W pump power and 15% output coupling is displayed in figure 3.12b. The laser head is tunable between 1021 nm and 1033 nm with a maximum output power of 19.4 W at 1031 nm. Then the center wavelength of the stretched seed pulses is matched with the wavelength for maximum gain.

After insertion of the switching elements, which introduced some additional losses, the maximum output power dropped to 19 W for optimum output coupling obtained by adjusting the quarter-waveplate and the Pockels cell. Figure 3.13 shows the beam profile measurement with the beam analyzer M2-200s from Spiricon, at the output located at the TFP. The beam parameter M^2 is better than 1.1, but the beam size was slightly larger than expected. By measuring the beam waists for different pump power, *i.e.* various thermal lenses, the strength of the thermal lens was estimated to be stronger than expected.

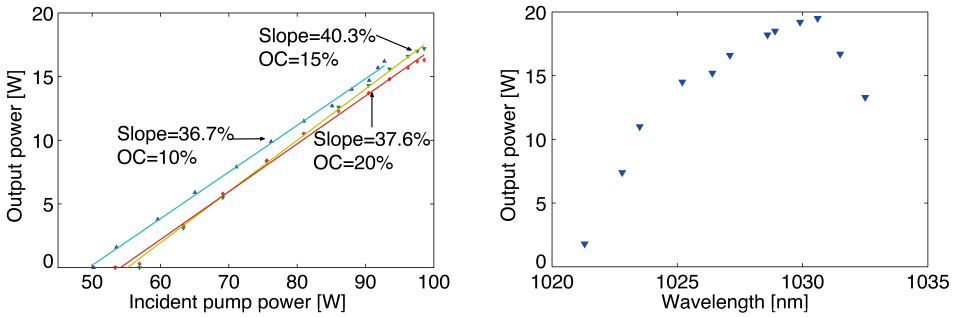

(a) (b)

Figure 3.12: Characterization of the dual-crystal laser head in continuous-wave operation. (a) slope efficiency for different output couplers. (b) tuning curve obtained for 112 W pump power and 15% output coupling.

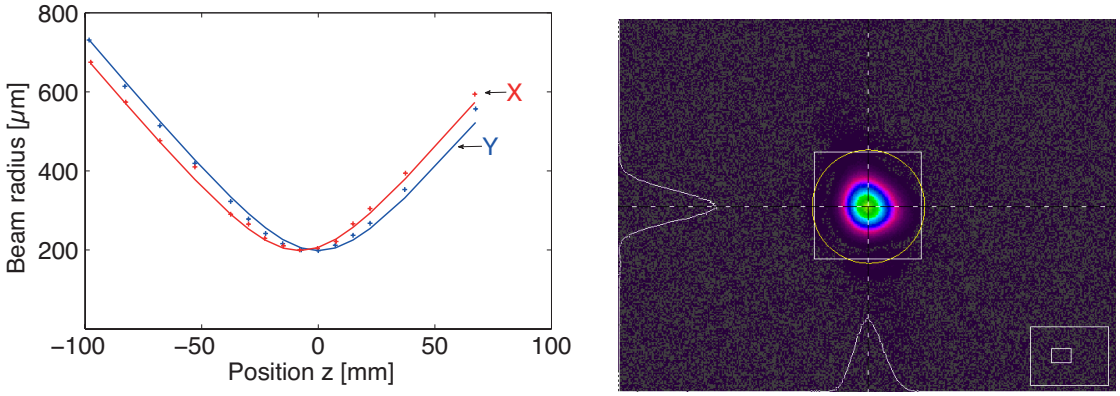

(a) (b)

Figure 3.13: Measurement of beam profile: the caustic corresponded to a nearly diffraction-limited beam with $M^2 < 1.1$.

Using equations 3.6, the thermal lens was calculated to be 250 mm under the pumping conditions of this laser head. The cavity was designed so that the spot size in the crystal is insensitive to focal lengths of the thermal lens longer than 280 mm. Below this value the spot size increases exponentially with a decrease in focal length; for a value below 210 mm, the cavity becomes unstable. Re-calculating the spot sizes in the cavity taking the 250 mm thermal focal strength in both crystals into account results in an output beam diameter of 1.7 mm in agreement with the measurements. In this configuration, the spot sizes in the crystals are 350 to 400 µm wide, minimizing drastically nonlinearities at the expense of gain.

This has been confirmed by estimating the dimensions of the pump spots in the crystals, knowing that the pump spots have been adapted: they match the laser mode and the gain is maximized. In this estimation, the crystal have been imaged on a CCD, as shown in figure 3.14. Left and right crystals refer experimentally to the crystals 1 and 2. Comparing the lightened diameter of the spot size in the crystal to the crystal edge, the beam diameter of the flat-top pump was estimated.

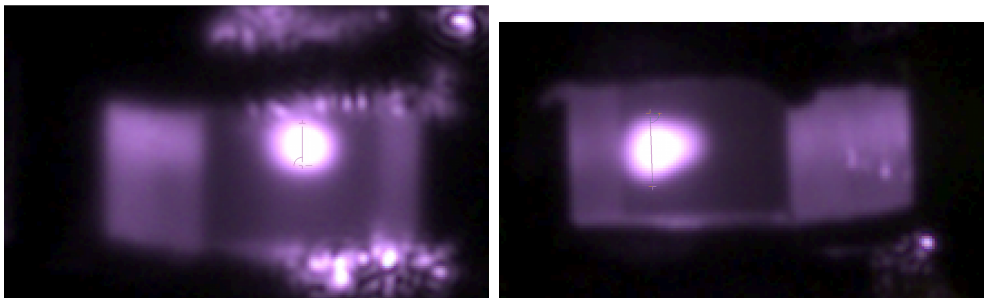

(a) **(b)**

Figure 3.14: Pump spots in both crystals: (a) crystal 1, left in the experiment, and (b) crystal 2, right in the experiment.

Cavity dumping and regenerative amplifier

After continuous-wave characterization, the cavity was operated first in cavity-dumped (CD) regime and then as a regenerative amplifier. The Pockels-cell driver is triggered with the pulse delay generator from SRS model DG645. The laser diode was operated in QCW and CW regimes. In QCW operation, the pump duration is set to 500 µs, corresponding to 1.5 times the lifetime of Yb:KYW, which reduces the thermal load in the crystals. The maximum energy extracted from the cavity-dumped laser head is 5.5 mJ at 1 kHz repetition rate at full pump power (120 W). As shown in figure 3.16a, the output energy measured by varying the pump power is limited only by the available pump power. The extraction time was set for 125 W pump power to 804 ns, corresponding to 38 round trips.

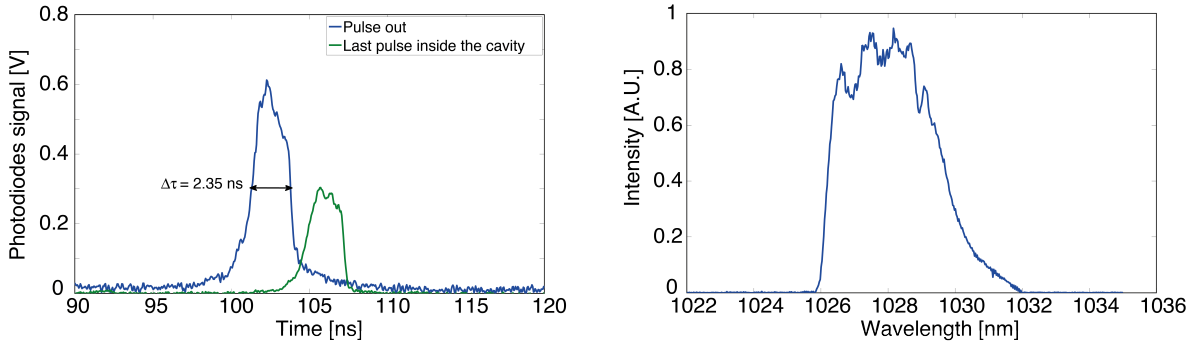

(a) Stretched pulse **(b)** Spectrum

Figure 3.15: Stretched pulse measured in time and spectrum at the output of the KYW regenerative amplifier. The pulse was measured in time with the EOT 3500 detector and in spectrum with the spectrometer ANDO AQ6315 with <0.1 nm resolution. The operating conditions were a repetition rate of 1 kHz with 120 W pump power at 50% duty-cycle, a build-up time of 804 ns for CD operation and 640 ns for regenerative amplifier operation, seeded with 0.6 nJ energy.

In seeded operation the repetition rate was varied between 100 Hz and 1750 Hz, the highest repetition rate achievable with the high voltage driver. The maximum energy of

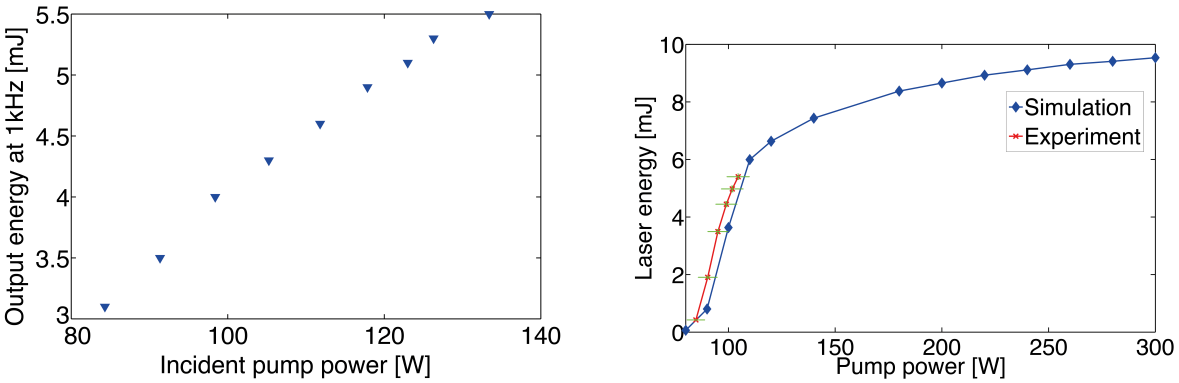

(a) Cavity dumped **(b)** Regenerative amplifier

Figure 3.16: (a) Energy extracted in cavity-dumped operation and as regenerative amplifier versus incident pump power. The extraction time is set to 804 ns and 640 ns, respectively. The graph (b) shows both simulation and experimental results.

6.5 mJ is extracted at a repetition rate of 1 kHz using 0.6 nJ seed pulses. At this seed energy the extractable energy is nearly constant for repetition rates below 1400 Hz; above this value the extractable energy begins to decrease, as expected considering the lifetime of Yb:KYW. To achieve a gain of 60 dB, 31 round trips, corresponding to 640 ns, are required. Most of the discrepancies between simulations with the absorption coefficient of 17.2 cm^{-1} and experimental results originate from the difficulty in modeling the absorption of pump light in the experiment due to the uncertainty in the exact effective pump absorption coefficient. The simulation with the lower effective absorption coefficient of 12.0 cm^{-1} predicts 6.5 mJ output energy which is consistent with the experimental results.

Figure 3.16b shows the variation of the output energy with the incident pump power, experimental and simulated, for a fixed amplification time. The error bars in the experimental values are related to the in-situ pump power measurement. By increasing the pump power in the simulations, without considering the limitations due to thermal effects, the output energy would roll-over for high pump powers to reach nearly 10 mJ.

The narrowing of the amplified output spectrum is illustrated in figure 3.17. The 4.9 nm wide seed spectrum is centered at 1030 nm. Filtering by the CFBGs and the spectral reshaping in the fiber amplifiers significantly narrows the output spectrum compared to the oscillator spectrum. Some self-phase modulation at the entrance of the fibers is believed to cause the shoulders in the seed spectrum. The spectral centering has been optimized for overall match to the cryogenic amplifier at 1029 nm after the regenerative amplifier. The output spectrum of the cavity-dumped laser was 5.7 nm wide centered at 1028 nm wavelength. The output spectrum of the seeded regenerative amplifier was the overlap of both seed and cavity dumped spectra.

In figure 3.18, the oscilloscope signals corresponding to the pulse build-up in both CD and regenerative amplifier regimes are displayed with the output pulse and the end of the gating signal. The delay on the oscilloscope between the end of the gate and the pulses was due to the delay between the trigger signal and the signal delivered by the pulse delay generator. The duration of the cavity round-trip amounted to 21 ns, corresponding to

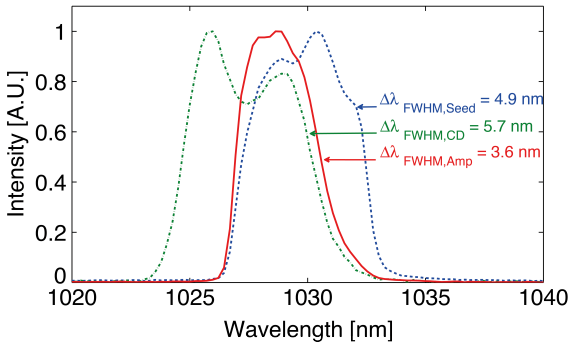

Figure 3.17: Measured spectra of the seed, the cavity-dumped laserhead and the regenerative amplifier. The measurement was taken with OceanOptics spectrometer HR4000, with 120 W pump power at 50% duty-cycle and for a build-up time of 804 µs for CD operation and 640 µs for regenerative amplifier operation seeded with 0.6 nJ energy

3.15 m cavity length. The pulse was switched out of the cavity after the pulse build-up saturated.

3.6 Summary

This chapter reported on the regenerative amplifier which is a key-element of the pump-line for the Yb based waveform synthesizer. Simulations have been carried out to find optimum conditions for parameters such as crystal length, concentration and spot sizes in order to reach several mJ output energy. Two crystals have been tested experimentally: Yb:CALGO and Yb:KYW.

The simulation of the regenerative amplifier dynamics implemented first a simple model solving the Franz-Nodvik equations for gain and extracted energy and second the numerical integration of the coupled equations describing the laser dynamics. The evaluation of the thermal lens inside the crystal was done with the formulas estimating the strength of the thermal lens under lasing and non-lasing conditions given in [56]. Both dynamic analysis and thermal lens estimation as well as calculations of the nonlinearities accumulated during propagation have been considered in the cavity design and were used as a starting point for the experimental realization.

In the first implementation, 1% and 2.5% doped Yb:CALGO bulk crystals were used in a high power CW laser and in cavity dumped and seeded operation. In the single crystal cavity 11.1 W at a free-running wavelength of 1051 nm was extracted from the 2.5% doped crystal as well as above 10 W for a wavelength tuned between 1048 nm and 1057 nm. The CW output power from the 2% doped dual-crystal cavity was as high as 23 W at 1042 nm wavelength; the laser showed a smooth tuning behaviour between 1017.8 nm and 1060.6 nm. In cavity dumped operation, pulses with an energy of 4 mJ and a spectrum centered at 1040 nm were extracted at a repetition rate of 1 kHz, in good agreement with the wavelength of the highest gain of the material. When the laser head was used as a regenerative amplifier at the same repetition rate, the 1 nJ seed pulses

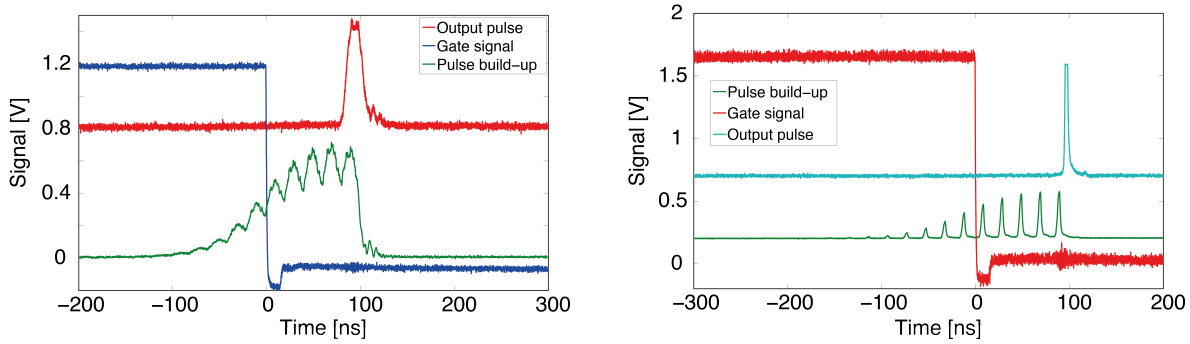

(a) Cavity dumped operation

(b) Seeded operation

Figure 3.18: Signals on the oscilloscope of the gate, the pulse building up and the pulse switched out of the cavity in cavity-dumped operation and in regenerative amplifier regime. The signals were measured with the Thorlabs detectors DET10A/M. The operating conditions were: a repetition rate of 1 kHz, 120 W pump power at 50% duty-cycle for a build-up time of 804 µs for CD operation and 640 µs for regenerative amplifier operation seeded with 0.6 nJ energy.

centered at 1030 nm were amplified to 3 mJ. This was the first report on Yb:CALGO used in a cavity dumped laser head and in a regenerative amplifier achieving both the broadest tunability as well as the highest CW output power reported from this material. Considering the CW output power of 23 W and the lifetime of the ytterbium ions in the CALGO host, potentially 10-mJ pulses at 1 kHz repetition rate could be extracted using low loss switching elements, however seeded at 1040 nm to 1045 nm. Even though a not yet fully mature material, the good thermal properties of Yb:CALGO make it very promising for a high energy, ultrashort pulses, regenerative amplifier [109].

With the Yb:KYW crystals, a regenerative amplifier delivering 6.5 mJ at 1 kHz repetition rate before compression with a beam quality parameter better than 1.1 was demonstrated. This was at the date of publication the highest reported pulse energy generated from a bulk Yb:KYW regenerative amplifier. The pulses stretched to 2.35 ns can be compressed to 615 fs with a multi-layer dielectric grating compressor with 81% efficiency. When operated continuous-wave, a maximum output power of 19.4 W was achieved with 40.3% slope efficiency and $M^2 < 1.1$ with 15% output coupling; the laserhead was tunable from 1021 nm to 1033 nm. The experimental results were in good agreement with numerical simulations of the laser dynamics.

The output of this laser was divided into two arms: after compression presented in the chapter 5, the first one was used as driving laser for a CEP stable front-end (*cf.* chapter 6); the second output, uncompressed, seeded a high energy pump line, presented in the next chapter, to pump the parametric amplifiers (*cf.* chapter 7).

4 Cryogenic composite thin-disc power amplifier

To boost the pump energy of the pump line to the 100 mJ level, ytterbium based cryogenically cooled amplifiers are employed. This technology, pioneered by T. Y. Fan [79], features high energies at high average powers, making it the ideal candidate for the booster stages in the pump line to drive few cycle OPCPAs at high repetition rates. The multipass amplifier described here corresponds to the first stage of the module *Yb-Cryo Amp* on figure 2.7. It is a cryogenically cooled ytterbium amplifier and is seeded with a fraction of the output of the regenerative amplifier described in chapter 3.

After the description of the state of the art in high energy amplifiers, the multipass amplifier with cryogenic composite thin-disk will be presented. Experimentally 72 mJ have been extracted with 5.1 mJ seed and 18.5% extraction efficiency; the 0.4 nm wide pulses are recompressible to 2.8 ps.

4.1 State of the art

Between 100 Hz and 1 kHz repetion rate, pulse energies as high as 1 J lead simultaneously to high power amplification, because the average power reaches then 100 W to 1 kW. High energy amplifiers at high repetition rates combine the challenges of high energy amplification and high power operation: specifically, avoiding damage and accumulation of nonlinearities for the high energy amplifiers and removal of the heat load from the laser medium for the high power amplifiers. The heat load needs to be removed from the laser medium to avoid distortions of the beam. Thoughtfully engineered heat management in design involving homogeneous pumping and aggressive but homogeneous cooling then minimizes thermally induced distortions and depolarization (*cf.* chapter 3.4.4). These distorsions lead to spatial aberrations in the laser beam, *e.g.* to a degradation of the beam quality, and to depolarization due to the stress generated in the medium. To minimize these effects an effective cooling of the laser medium has to be designed and implemented according to the thermal load to be removed from the gain medium.

Compared to traditional rod amplifiers improved cooling is possible by increasing the interaction surface between the laser medium and the cooler [45]. Fiber lasers scale up the length of the laser medium [45, 113], slabs scale the longitudinal cooled surfaces of the slab [45, 114] and thin-disk lasers increase the transverse dimension of the medium keeping the thickness very thin [45, 53].

High power, ultrashort pulses can be obtained with fiber amplifiers as demonstrated by Eidam *et al.* in [115] with 830 W and a beam quality parameter better than 1.4, but

the long interaction of the beam with the fiber limits the energy: the repetition rate in that work is 78 MHz and the pulse duration 640 fs, *i.e.* the peak power attains only 12 MW. The fiber laser with the highest energy demonstrated to date is reported as 1 mJ pulses from a fiber CPA system with bulk recompression [116]. The limitation in energy scalability is set by self-focusing inside the fiber material causing damage [50, 113, 117]. The self-focusing limit occurs at ∼4 MW peak power.

In a bulk multi-pass amplifier, the spot sizes are scalable; this kind of geometry, in contrary to the fiber geometry discussed above, minimizes hence the accumulation of nonlinearities and the beam paths for a timing stability adequate to the pump line of a waveform synthesizer (*cf.* section 8.1). Two geometries have been developed and are nowadays widely adopted to achieve 100 W power levels: the slab and the thin-disk geometry.

Among the slab lasers, one particular geometry is called "Innoslab". It was developed by Peter Rußbüldt and Thorsten Mans in 2000 for Neodymium doped laser media [114] and extended in 2009 to ytterbium doped media [118]. A slab is defined as a crystal thin in one dimension; the "Innoslab" is edge-pumped in the longitudinal direction, and the seed is amplified with several zigzag passes accross it, as shown in figure 4.1b. The thinness of the crystal and a good contact between both upper and lower faces to the cooler are key for very efficient cooling and low thermal lensing. The heat removal is increased by the short distance between pump beam and mounting surfaces. Thanks to the zigzag path of the beam through the slab, the thermal distortions on the wavefront are averaged during propagation. The alignment of the beam to amplify in the pumped part of the crystal is critical to keep a high beam quality.

Innoslab based laser systems are limited in the extractable energy by the nonlinearities accumulated during propagation through the long crystal. In view of the geometry of the pump and laser beams, reaching a high quality beam profile is challenging: the excited volume is much larger than the laser beam volume and the lack of guiding prevents higher order modes from transverse lasing.

The thin-disk, developed by Giesen in 1994 [53], relies on a very thin but wide crystal, typically <100 µm and up to 1 cm in diameter. The thermal lensing is reduced by removing the heat in the longitudinal direction as shown in figure 4.1a. A highly doped thin-disk, *e.g.* 10% for Yb:YAG, compensates for the thinness of the crystal and absorbs efficiently the pump, but a recycling of the latter and the implementation of multi-passes is often required to enhance the absorption. The extraction of the stored energy in the crystal is realized in a similar way via multi-passes of the laser beam. The number of passes through the crystal was increased to 13 passes by Neuhaus *et al.* in [51] to achieve 25.9 µJ at 2.93 MHz repetition rate, corresponding to 76 W of average power. With the increasing number of passes, the mechanical stability of the system is compromised, and consequently the long term operation of the laserhead. The cited 13-pass cavity is therefore actively stabilized. At ETH in Zürich, 242 W were demonstrated from an Yb:YAG oscillator at 3.03 MHz repetition rate [119]. In the summary of the 15 year development of thin-disk lasers from Giesen [120], the scalability to high power and energy is discussed; Trumpf GmbH produces for machining applications (welding, cutting) a 5 kW

thin-disk laser pumped with 8 kW optical power, albeit without diffraction-limited beam profile. Overall, thin-disk lasers proved their scalability to high power.

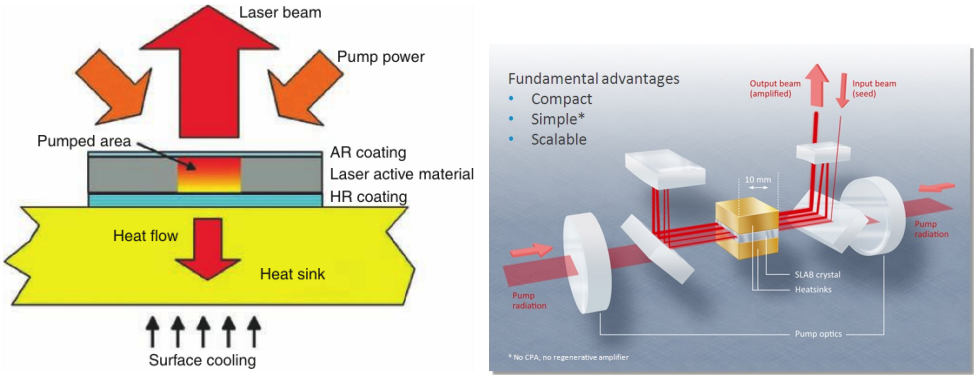

(a) Thin-disk **(b)** Innoslab

Figure 4.1: Schematic representation of the (a) thin-disk [45] and (b) Innoslab [121] geometries.

Thin-disk lasers are limited by amplified spontaneous emission (ASE), which growths transversally saturating and limiting the gain. When ASE is reflected at the edges of the disk, it crosses several times the pumped area, being amplified with the small-signal gain at each pass; that can lead to parasitic lasing. The highly doped thin-disk has a high small-signal gain. In the absence of a laser power extracting the energy, the transverse amplification of ASE depletes the stored energy and lowers the gain available for laser pulse amplification. Another limitation of the thin-disk is the small gain per pass: the thinness of the disk limits on one hand thermal effects like bulging and ensures a good heat transfer in the longitudinal direction, but on the other hand it also limits the available gain. Several passes have to be implemented for efficient extraction of the stored energy, increasing the complexity of the system and the overall length.

Scaling towards high power and high energy is conceivable not only with amplifier geometry but also with adequate choice of the material: the relevant parameters concern mechanical and optical properties. Laser hosts suitable for high energy are able to store the energy, *i.e.* a long lifetime of the doping ion in the host is advantageous. Besides, high emission cross-section is suitable for high power; mechanically, the main characteristic is the capacity of the host to remove the heat and minimize the deformations due to heat load, *i.e.* thermal properties like thermal conductivity, thermal expansion and change of refractive index with temperature gradients have to be taken into account. Thermo-mechanical and thermo-optical properties vary with temperature of the host and improve substantially at cryogenic temperature. A commonly used and extensively studied material is Yb:YAG [79, 122]: at 100 K the emission cross-section increases by a factor of 4.5 compared to room temperature, while the emission banwidth decreases accordingly. At 100 K the thermal conductivity increases by a factor of 4 reaching 49 $^{\mathrm{W}}/_{\mathrm{m\,K}}$, whereas the variations of the refractive index with temperature $^{dn}/_{dT}$ and the coefficient of thermal expansion decrease by a factor of 8 and 3 reaching respectively 1 and 2 $^{\mathrm{ppm}}/_{\mathrm{K}}$. Moreover, the small quantum defect between 5% and 10% is crucial to reduce the heat load in the crystal. Finally, direct diode pumping in the upper manifold of the ytterbium ion

is highly efficient. This reduces thermal lensing and consequently the aberrations during amplification.

The enhancement of the optical and thermo-mechanical properties of Yb:YAG at cryogenic temperatures leads to amplifiers with an average power in the multi-kW, like the one delivering 963 W average power reported in [123], or with energies beyond the Joule level, *e.g.* 10.1 J at 1 Hz repetition rate or 6.3 J at 10 Hz demonstrated by Mason *et al.* in [124]. Ultrafast amplifiers already reaches tens of mJ, *e.g.* 56 mJ at 1 kHz repetition rate as in [125].

The concept implemented in this laser system is based on a cryogenically cooled composite thin-disk (CTD) with a relay imaging architecture, as first described by Luis Zapata in "Methods, systems, and apparatus for high energy optical-pulse amplification at high average power" [126]: the laser medium is a disk thicker than in a usual thin-disk laser and the thermal bulging is reduced with an undoped-cap with fashioned edges rejecting the ASE. Two-stages will boost the energy from a few mJ up to the 1 J level. The next section presents this multi-pass architecture in detail.

4.2 Cryogenic composite thin-disk multi-pass amplifier

The multi-pass amplifier, as described in [127] and shown in figure 4.2, is based on strict relay-imaging for a good beam quality and a gain-medium shaped to reject ASE.

The cryogenic composite thin-disk is composed of a 1 mm-thick, 10% doped Yb:YAG disk bonded to a 4 mm thick index-matched YAG undoped cap, fashioned with a parabolic shape. The fashion of the undoped cap reflects ASE out of the gain module to avoid recirculation of ASE. The second role of the undoped cap is the limitation of thermal lensing: only the doped thick-disk is thermally loaded, and the stiffness of the undoped cap prevents thermal bulging. The other side of the thick-disk is soldered to a heat-spreader cooled down to cryogenic temperature.

A 500 W fiber-coupled laser diode (Laserline GmbH) provides the energy to the disk. A customized telescope demagnefies the output of the 1000 µm mode-field diameter fiber to 4.4 mm onto the disk, with a super-Gaussian higher order spatial profile. The super-Gaussian spatial beam profile can be imaged to a flat-top beam in the focus. The distance between the telescope and the CTD is 180 mm; the image is projected onto the CTD with a small reflective prism at the top of the angled kaleidoscope assembly, shown in figure 4.2b. On the opposite side of the kaleidoscope, another prism collects the unabsorbed pump light for measurement or possible recirculation of the pump. Two further prisms on the top of the angled kaleidoscope assembly are used for looking at the disk with a camera: the alignment of the pump beam in the center of the disk and its overlap with the laser beam is eased. The wavelength of the laser diode was tuned with temperature control of the cooling water to the highest absorption of Yb:YAG, which is located at 940 nm wavelength. This leads to 90% absorption of the pump light.

To seed the amplifier in parallel to the front-end (*cf.* 2.7), the output beam of the regenerative amplifier is split with a half-waveveplate and a TFP. The seed beam is coupled in and out of the cryogenic multi-pass amplifier through a TFP and passive polarization switching: at each passage in the mirror switchyard, the polarization is rotated by 120°.

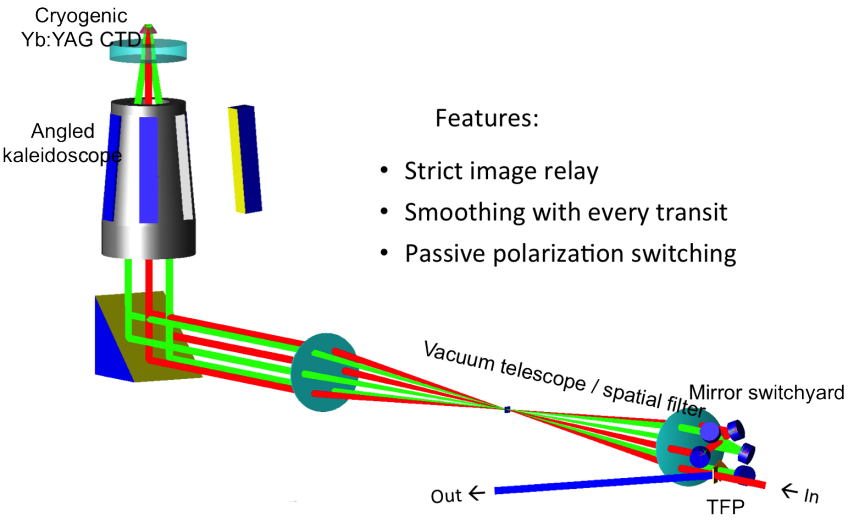

(a)

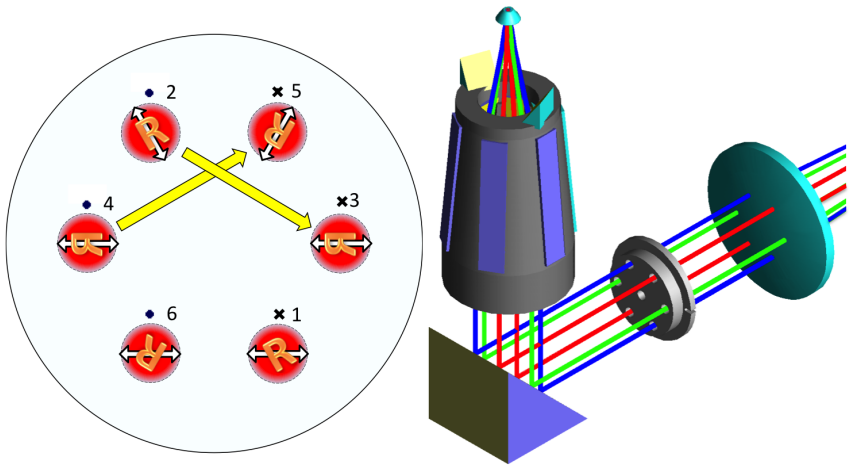

(b)

Figure 4.2: Setup of the cryogenically cooled multi-pass amplifier. (a) Schematic 3D view of the amplifier with the vacuum telescope for relay-imaging, the mirror switchyard to separate the passes, the angled kaleidoscope directing the amplified beam to and from the crystal, and the gain module assembly. (b) Zoom on the top of the kaleisdoscope with detail on the polarization switching.

After 6 passes through the crystal, the beam, reaching the last mirror of the switchyard, is sent back on itself. A quarter-waveplate is inserted before it to rotate the polarization into the orthogonal one. The input and output beams with polarization parallel and perpendicular to the optical table, respectively, are separated with a TFP. For efficient gain extraction 12 passes are necessary. The relaying architecture is made with a 1:1 vacuum telescope composed of two identical 3 inches diameter lenses with 300 mm focal length, set at the afocal distance. The collimation of the incoming beam and the exact alignment of the telescope are verified with a CW beam and a shear-plate. The beam path is folded between the telescope and the crystal with the angled kaleidoscope: the 85°

angle on incidence on the mirrors in combination with the polarization switching strongly limits the use of dielectric mirrors, and protected silver mirrors are used. The drawback of silver mirrors, even with a protective coating, is in their degradation in contact with the humidity of the air.

Two systems were built in parallel: one was in the part of the group located at MIT [128], and one in CFEL in this work. In [128] the repetition rate was 100 Hz to 300 Hz, corresponding to a heat load of 5 W to 15 W during pumping from the quantum defect. In this work the intended repetition rate was >100 Hz meaning that the thermal load to remove from the crystal was >5 W in average with 10% duty-cycle. Further heat load estimated to 10% originates from the reflected fluorescence. The total heat load at the goal repetition rate of 1 kHz amounts then to 50 W from the quantum defect and 50 W from the fluorescence. The cryogenic cooling was designed for removing this heat load. The bottleneck was however the crystal itself and the heat passing through the soldered high reflecting (HR) side: a larger crystal diameter would increase the heat flow and removal. A further improvement compared with [128] concerned the temperature control of the cold-head: as the bandwidth of YAG is strongly depending on the temperature, as well as the thermal coefficient and cross-sections [79], temperature control is equivalent to the control of the amplified bandwidth. For the intended OPCPA pumping, a compromise between high efficiency and bandwidth (*i.e.* pump pulse duration) was interesting to be investigated in detail. For this reason, the cold-head was equipped with a temperature control system, as shown in figure 4.3.

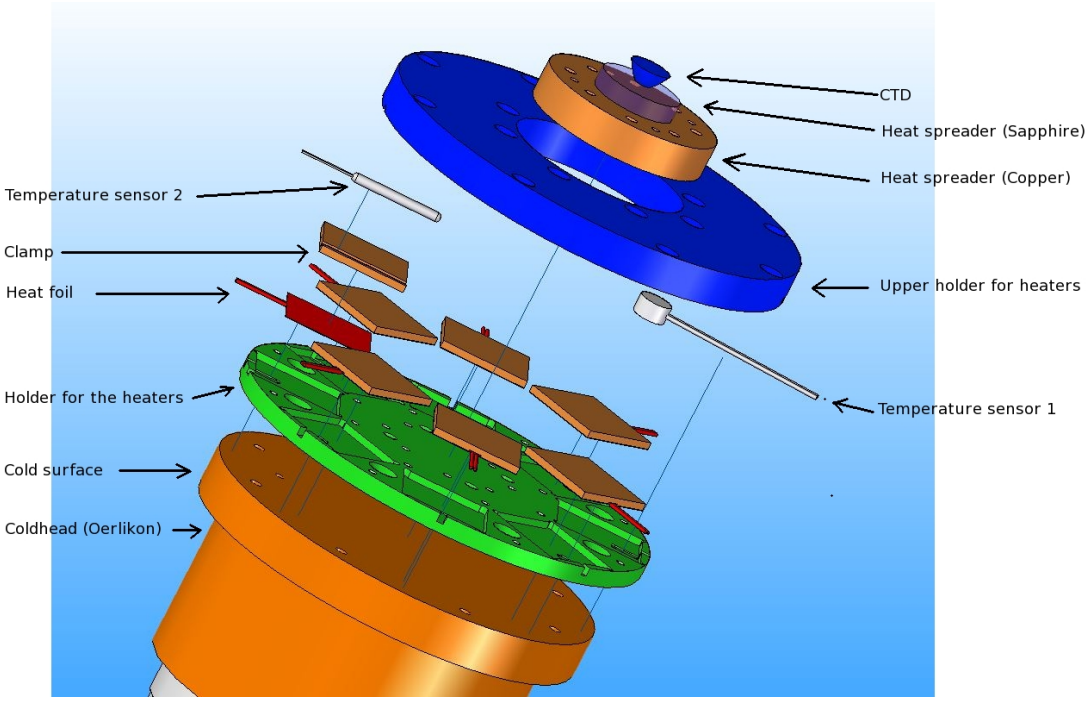

Figure 4.3: Heating system for temperature control of the cold head based on recirculating liquid helium. The crystal is mounted as close as possible to the cooling surface, whereas the heat foils to stabilize the temperature to the desired value are placed around it.

The mounting of the heat foils is illustrated in figure 4.3: a copper plate (*Holder for heaters* on the figure) with milled-out portions for the heat foils is screwed on the cold surface (*Cold surface*) of the cryogenic cooler (*Coldhead (Oerlikon)*). Precisely manufactured copper blocks (*Clamp*) press each heat foil (*Heat foil*) for an optimum thermal contact. A copper plate (*Upper holder for heaters*), with a hole in the middle for the crystal heat spreader (*Heat spreader (Copper)*), is used to clamp the heaters. The crystal heat spreader is mounted in the middle of the cold surface and of the heat foils: the foils are used to increase the heat load on the cryogenic cooler, so that it quenches and stabilizes at the desired temperature. The crystal heat spreader needs to be mounted with the least thermal resistance to the cold head. Two temperature sensors, a photo-thermistor (*Temperature sensor 1*) and one silicon diode (*Temperature sensor 2*), measure the temperature. The Si diode is mounted as close as possible to the crystal heat spreader.

The coldhead CoolPower 10 250 MD from Oerlikon, able to remove close to 300 W at 130 K, is based on a Griffith-MacMahon compressor for the circulation of liquid helium. The lowest temperature achievable on the cold surface was 25 K. By quenching the cooler the temperature could be adjusted. The clamped heat foils brought up to 300 W heat load; a power supply and temperature was monitored by a control software written in LabView(TM) that adjusted the current through the heating elements. The heat foils were mounted around the heat sink of the crystal, to ensure the best thermal contact between the crystal and the cold head. The temperature measurement was set-up as close as possible to the heat sink of the crystal. The disadvantage of this complex temperature control over a simple Dewar lies in the movements of the compressor for the Helium circulation which induce vibrations of the cold head propagating to the vacuum chamber and coupling into the optical table. These vibrations might disturb the CEP stability required by the synthesizer. A detailed analysis of the mechanical vibrations and their influence on other parts of the system is however beyond the scope of this thesis.

With this system, only preliminary temperature dependent measurements have been realized: a communication failure during temperature measurement caused an accident leading to full damage of the cooler and crystal.

For further experiments, this complex cold-head has been replaced with a simple Dewar without temperature monitoring as shown in figure 4.4. The crystal heat spreader is mounted directly to the cold surface (*Cold surface*) of the Dewar. The liquid nitrogen contained inside the Dewar boils due to the thermal load in the crystal and evaporates through the three pipes at the top of the Dewar (*Pipes for evaporation*). The Dewar is mounted directly onto the flange closing the chamber. To minimize the thermal resistivity the cold surface of the Dewar is made of copper and the gaps between the surfaces of the heat spreader and of the cold surface are filled with 0.5 mm indium foil.

The vacuum chamber was designed to accomodate 6 flanges: one for mounting the cryogenic cooler or the Dewar and opposite to it one with a window for the beams. On the sides a turbo pump HiPace from Pfeiffer and a vacuum gauge were mounted on two flanges. One flange had a feed-through for the connectors of the measurement diodes and the last one was unused. The pressure in the chamber was typically 10^{-6} mbar at room temperature and 10^{-7} mbar at cryogenic temperature.

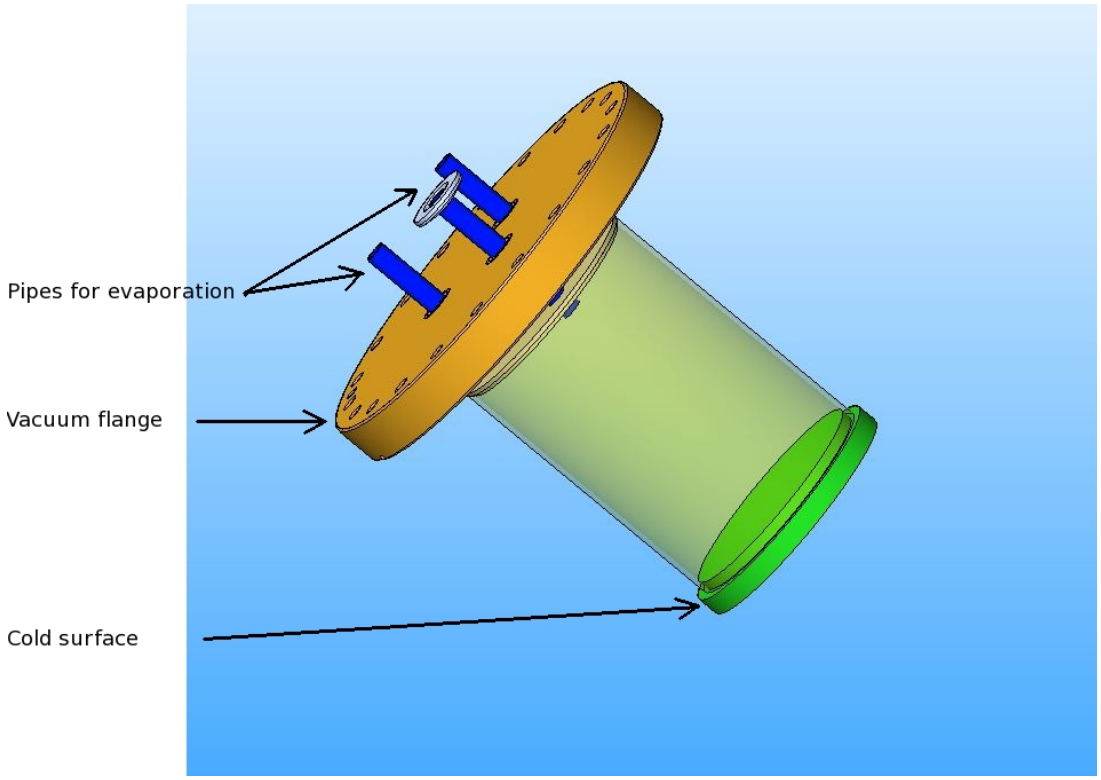

Figure 4.4: Dewar replacing the cold head from Oerlikon. The crystal is mounted directly on the cold surface, and the temperature is set by the boiling temperature of the liquid nitrogen – 77 K.

Measurements of the spectral properties of Yb:YAG have been taken with the temperature controlled cold-head and are presented in the next section. The last section describes the experimental results obtained with both cold-heads in continuous-wave regime and as multi-pass amplifiers.

4.3 Properties of Yb:YAG at cryogenic temperatures

At cryogenic temperatures the optical and thermo-mechanical properties of the material strongly depend on the exact temperature inside the crystal. The width of the absorption line is of importance for the absorption of the pump, whereas the emission linewidth determines the maximum spectral width of the amplified pulse. The spectral width is measured with the spectrum of the fluorescence, which is equivalent to the measurement of the gain.

In the context of the pump line of the ytterbium based waveform synthesizer, the spectral width of the emission line is important to determine the available bandwidth during amplification of the laser pulses. The spectral bandwidth was then measured versus temperature. The temperature measurement was not performed directly inside the crystal but between the cold head and the heat spreader: the effective temperature inside the crystal is slightly higher. With the heaters controlling the temperature of the crystal the fluorescence bandwidth was measured versus temperature of the cold-head.

The spectral width was resolved with the spectrometer ANDO AQ6315 with 0.05 nm resolution. From 0.8 nm at 80 K, the bandwidth increased to 1.3 nm at 130 K, as shown in figure 4.5. The central wavelength remained located at 1028.9 nm.

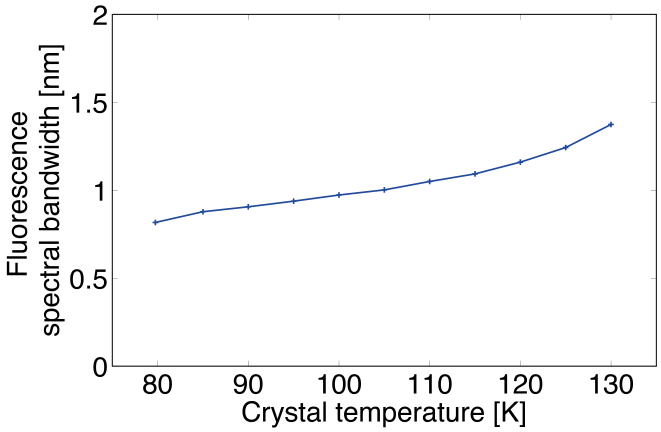

Figure 4.5: Evolution of the spectral bandwidth of the fluorescence as a function of the temperature of the Yb:YAG crystal.

4.4 Experimental results

4.4.1 Continuous-wave operation

The composite thin-disk was first tested in a multi-mode cavity composed of the disk, a 300 mm focal length lens and an output coupler. The extracted power is shown in figure 4.6. In figure 4.6a, the output coupling was varied between 7.5% and 15%. A maximum efficiency of 52.1% was reached with 10% output coupling. The efficiency curves are linear and show no sign of saturation, even when the disk is pumped with 150 W CW pump power. The maximal CW-power was 80 W.

The temperature dependency of the extracted power was also measured and the results are shown in figure 4.6b. From 80 W output power at 80 K heat sink temperature, the power dropped to 24 W at 158 K. This is due to the decrease of the emission and absorption cross-sections of Yb:YAG with increasing temperature.

The extraction measurements in QCW pumping regime with a maximum average pump power kept to 150 W are shown in figures 4.6c and 4.6d. The former illustrates the burst energy versus pump power: up to 250 mJ are extracted from the disk in 1 ms at 20 Hz repetition rate. The latter displays the average output power versus pump pulse duration at 10 Hz. 80 W are extracted at 30 ms, corresponding to 150 W average pump power. All these measurements show no roll-over in the extracted power and energy; the extraction is limited by the pump power and not by thermal effects.

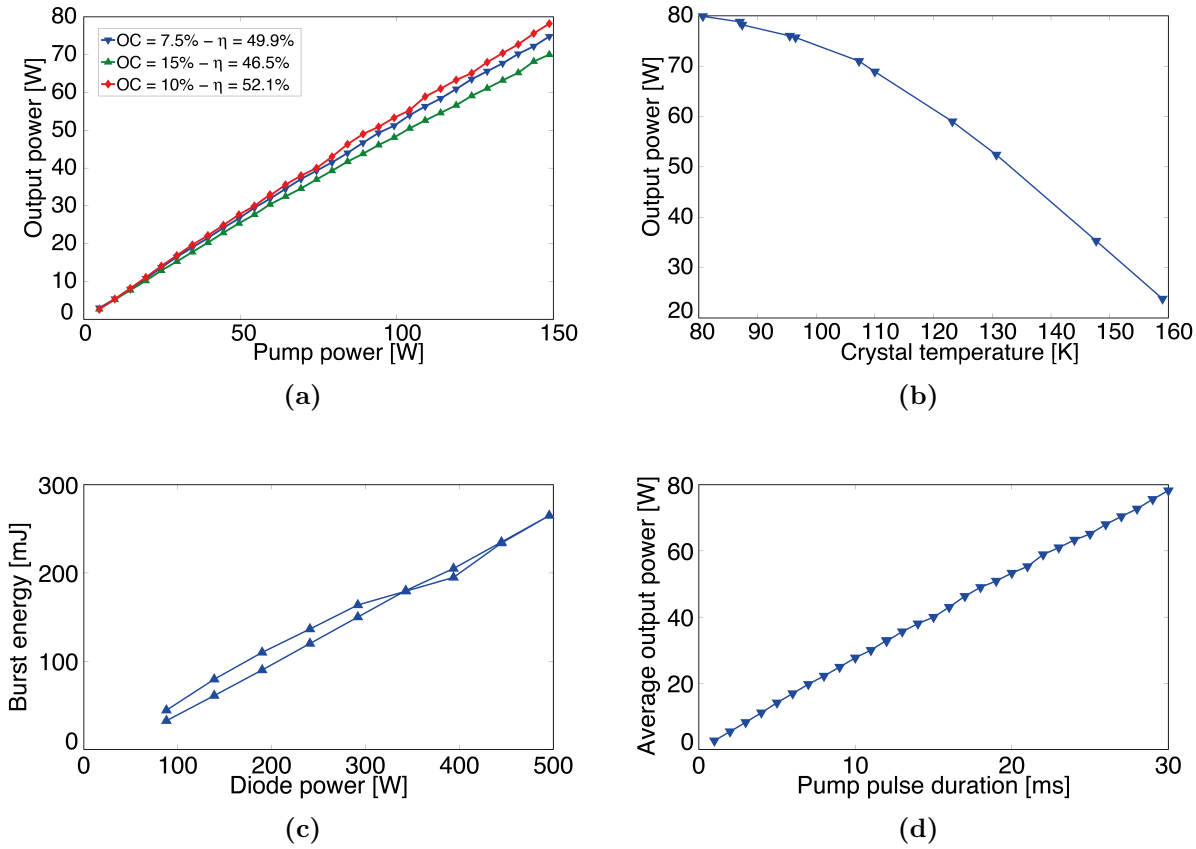

Figure 4.6: Characterization of the composite thin-disk CTD1 in a multi-mode cavity. In continuous-wave pumping: (a) Efficiency curves for 7.5%, 10% and 20% output coupling. (b) Output power versus temperature of the heatspreader. In QCW pumping: (c) Burst energy vs. burst pump power at 20 Hz repetition rate. The burst duration is 1 ms, *i.e.* approximately the life-time of Yb:YAG. (d) Average output power measured at 10 Hz repetition rate with increasing pulse duration.

4.4.2 Power amplification

After the characterization of the stored energy in the disk, it was used as the gain medium of the multi-pass amplifier and seeded with the output of the regenerative amplifier. The power amplification was measured for two different seed values of 1.35 mJ and 5.1 mJ. The former corresponds to the effective seed for the multi-pass amplifier when operating in parallel to the front-end in the ytterbium-based frequency synthesizer. The latter corresponds to the maximal seed energy available from the regenerative amplifier to test the multi-pass amplifier.

Figure 4.7 shows the amplification for 6 and 12 passes through the disk. The repetition rate set for this measurement is 100 Hz; the laser diode operated in QCW regime with 10% duty-cycle. At full burst power this corresponds to 49.5 W average power onto the disk, 92 % of which is absorbed. After 6 passes 12.9 mJ and 34 mJ respectively were extracted with the low and high energy seeds, whereas 63 mJ and 72 mJ were extracted

with 12 passes. The corresponding gain per round-trip defined as $g = \left(\ln \frac{E_{out}}{E_{in}}\right)^{1/n}$ with n the number of passes was 1.14 for 6 passes with low seed energy, and 1.1 with high energy seed. The linear amplification is a sign that the amplifier is not yet saturated. The gain per pass decreased with 12 passes to 1.12 and 1.08 respectively, indicating that the extraction is better saturated than with 6 passes. The increase of the output energy from 63 mJ to 72 mJ with an increase of the seed from 1.35 mJ to 5.1 mJ means that the amplifier was not saturated with the low energy seed.

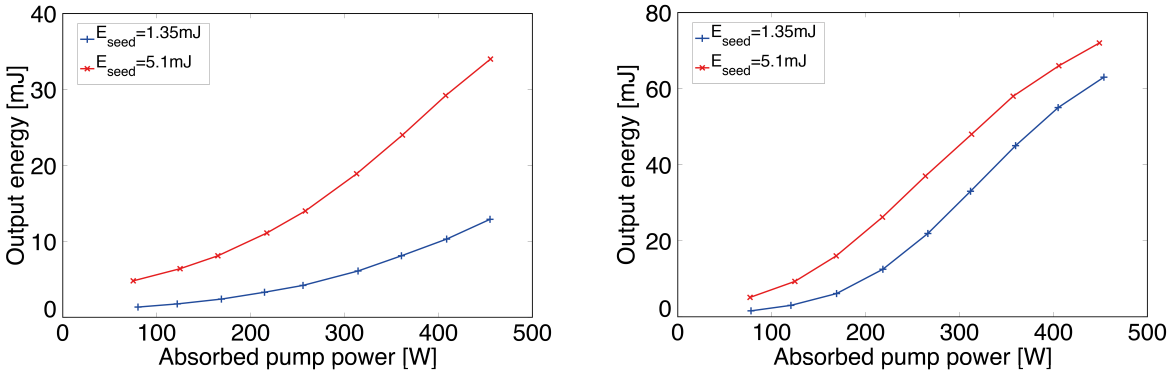

(a) 6 round-trips **(b)** 12 round-trips

Figure 4.7: Pulse energy after 6 and 12 amplification round-trips for low and high seed energy.

The effective seed energy is actually dependent on the spectral overlap between seed and gain line-shape. The spectral width of the input pulses is 3.6 nm centered at 1028.2 nm, but the width of the fluorescence spectrum at 80 K was 0.8 nm centered at 1028.9 nm: effectively, only the energy contained in the overlapping region is used for seeding. Figure 4.8 illustrates the evolution of the spectrum after amplification in the four cases (6-12 passes, low and high seed energy). Experimentally, the central wavelength of the amplified pulse shifts from 1029.1 nm to 1029.4 nm. The bandwidth decreased down to 0.5 nm after 6 passes and 0.4 nm after 12 passes amplification, because of gain narrowing.

As a comparison, in the twin-system built at MIT 23 mJ and 68 mJ are extracted for 6 and 12 passes respectively, limited by the energy and stretching of the seed, as reported in [127].

To understand the limitation of the extracted energy in the system at MIT compared to the one in this experiment, let us calculate the nonlinear phase accumulated through the multi-pass amplifier by the pulses from both seeds. The pulse used in the MIT system comes from an Yb:KYW commercial regenerative amplifier delivering 1.5 mJ per pulse, stretched to 300 ps. The pulse bandwidth is 3.5 nm, meaning that the seeding is actually realized with 0.4 mJ in the amplified 0.8 nm. After amplification and gain narrowing, the pulse duration decreases to 70 ps. For comparison, my system uses pulses stretched to 2.35 ns and with 3.6 nm spectral width; the pulse duration is reduced to 390 ps after gain narrowing to 0.6 nm. The accumulation of nonlinear phase is calculated with the formula 3.5, taking the values of the nonlinear refractive index coefficient of YAG as 7.3×10^{-16} cm^2/w at 94 K and 6.5×10^{-16} cm^2/w at room temperature [129]. The nonlinear

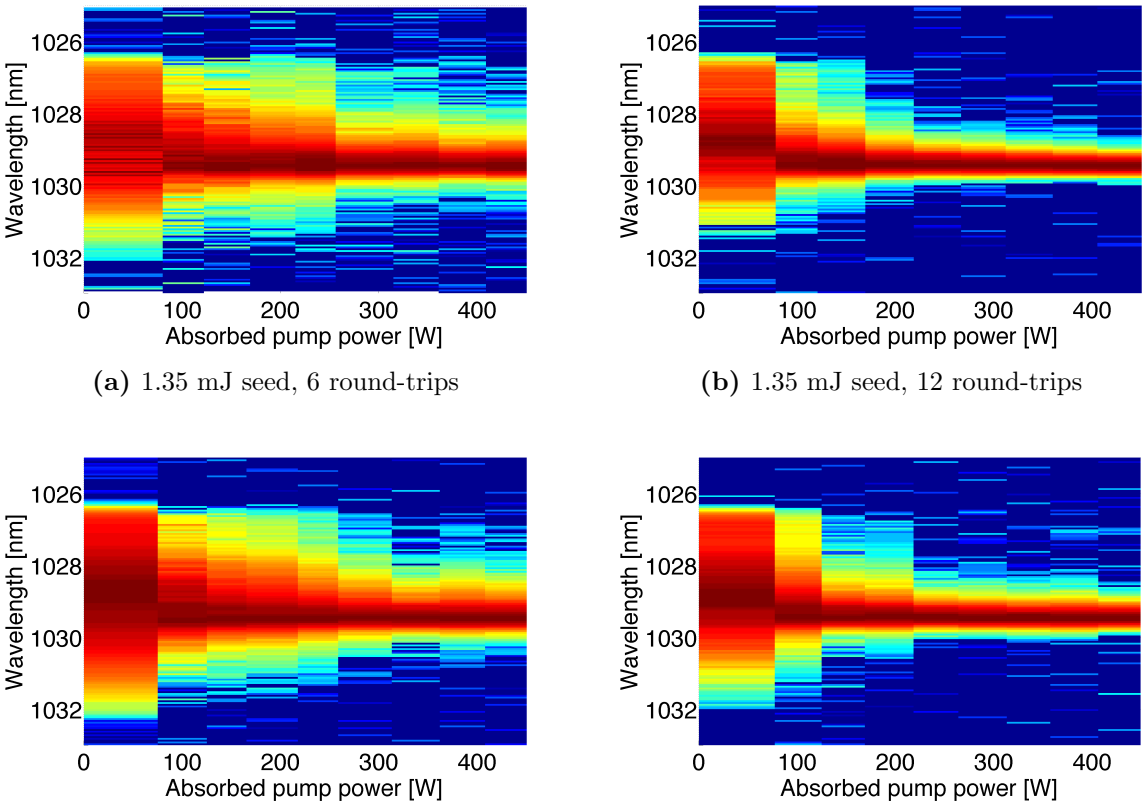

(a) 1.35 mJ seed, 6 round-trips

(b) 1.35 mJ seed, 12 round-trips

(c) 5.1 mJ seed, 6 round-trips

(d) 5.1 mJ seed, 12 round-trips

Figure 4.8: Spectra after 6 and 12 amplification round-trips: the spectra have been taken for different pump powers, for 2 seed energies and for 6 and 12 passes through the amplifying medium. The spectra narrows down to 0.4 nm due to gain narrowing.

phase after 12 round-trips in the multi-pass amplifier amounts then to 1.5 rad and 0.32 rad for both MIT and CFEL systems, respectively.

The energy fluctuations were measured with the energy meter set to record 10000 consecutive pulses and were 0.75% and 0.52% with respectively 496 W and 190 W incident burst pump power. At higher repetition rates, a similar energy was extracted from the disk. With 190 W burst pumping power, the pulse energy after 12 passes in the disk decreased slightly from 16 mJ at 100 Hz to 14 mJ at 500 Hz.

The beam profiles in the near and far-fields are shown in 4.9. The rows show the beam profile after 6 and 12 passes through the disk and the columns the far-field and near-field of the 5 mJ seed and 72 mJ amplified beams. The far- and near fields are similar for the seed and amplified beam, *e.g.* no distortions were attributable to the amplification itself. The degradation of the gaussian input beam profile is due to the CTD used in the experiment: it was damaged in the center during previous experiments as illustrated by the strong scattering in figure 4.10. As a comparison, figure 4.10b shows the disk under operation as it should look like.

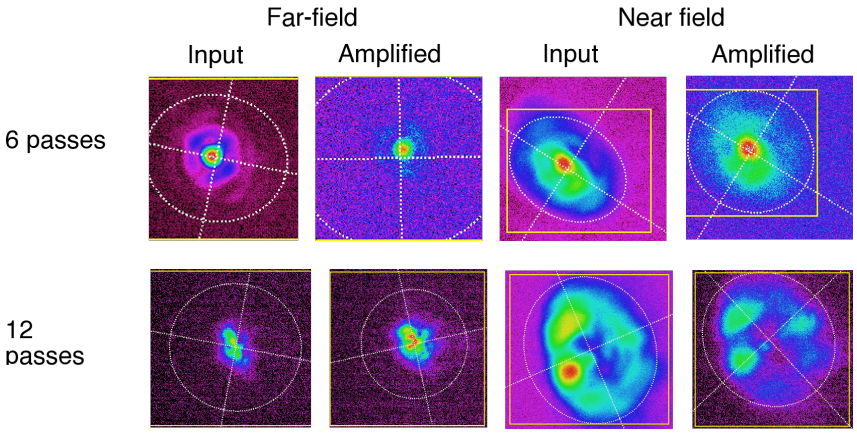

Figure 4.9: Beam profiles: the beam profiles after 6 and 12 passes through the disk are displayed in rows; the first two columns show the far filed of the input and amplified beam, and the last two colums the far-field of the input and amplified beam. The Gaussian input beam from the regenerative amplifier is distorted due to a previous damage in the disk, but no change in the spatial profile is observed during amplification.

4.5 Summary

In this chapter, a multipass amplifier based on a cryogenically cooled composite thin-disk delivering 72 mJ is demonstrated as part of the high energy pump line for OPCPA pumping. The design of the gain medium [126] allows a reduction of the parasitic lasing limiting the gain in traditional thin-disks, *e.g.* an increase in the gain, via an undoped end-cap with fashioned edges bonded to the disk. Cooling to cryogenic temperatures increases material characteristics such as thermal conductivity, emission and absorption cross-sections and decreases the change of the refractive index with temperature gradients. Yb:YAG has been chosen as gain medium for its high reliability, manufacturing reproducibility and good thermal properties.

The cooling of the crystal has been realized first with a closed circuit of liquid helium recirculated with a compressor, then with a Dewar filled with liquid nitrogen. The first had the advantages of standing alone and long-term operation, but caused strong vibrations over the full table. The second one prevented the vibrations which might disturb the CEP stability of the front-end and the pointing stabilizers but allows an operation over only a few hours.

With this amplifier, up to 80 W have been extracted from one disk with 52.1% optical-to-optical efficiency. Seeded with 1.35 mJ and 5.1 mJ, the pulses were respectively amplified to 63 mJ and 72 mJ with 12 passes in the multi-pass amplifier. The pulse spectral bandwidth decreases from 3.6 nm to 0.4 nm, because of the emission bandwidth of Yb:YAG at cryogenic temperature and gain narrowing.

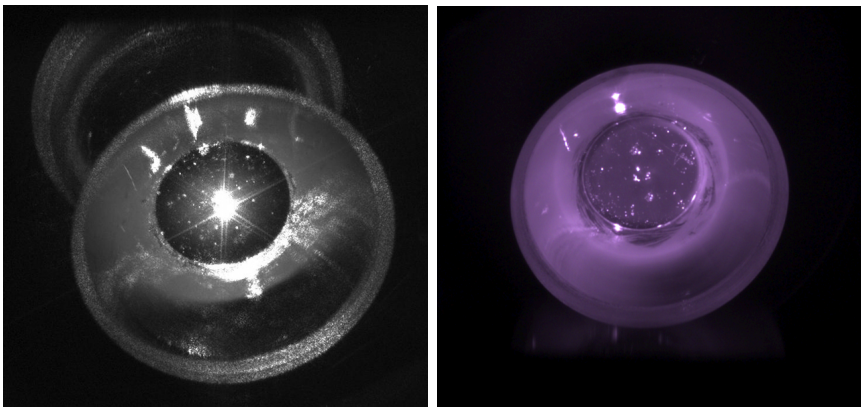

(a) **(b)**

Figure 4.10: Photo of the composite thin-disk during operation: (a) with and (b) without damage.

5 Pump line stretcher and compressor

This chapter discusses the stretcher and compressors used in the pump line of the frequency synthesizer before and after the successive high-energy amplifiers. On figure 2.7 this corresponds to the modules *Stretcher* and *Compressor*.

The spectral gain of the amplifiers influences the amplified pulse spectrum. During amplification of a laser pulse, the spectrum is multiplied on every passage through the amplifying medium with the spectral shape of the gain. In the case of non-uniform gain some spectral components are amplified differently depending on the spectral shape and the overlap with the gain peak. If the spectrum and gain are centered at the same wavelength, the center of the spectrum is more amplified than the wings, due to the limited bandwidth of the gain material. This leads to a spectral narrowing and is called "gain narrowing". For highly chirped pulse amplification, the stretched pulses are also shortened in time, while transform limited pulses would become longer. Chirped pulse amplification (CPA) is required as ultrashort pulses (∼ps time scale) are needed for the OPCPAs. High energy, shorter pulses accumulate during propagation in the amplifying media more nonlinear distortions than longer pulses: during the amplification two factors contribute to the increase of the nonlinear phase, the increase in energy and the shortening in time of the stretched pulses.

In this chapter available solutions for the stretcher and compressor, based on chirped volume or fiber Bragg gratings or on bulk gratings, are discussed in detail. Afterwards the solutions are compared, justifying the choices of chirped fiber Bragg grating (CFBG) stretcher and bulk grating compressor made to reach the large stretching factor of $\sim 0.8\ ^{\mathrm{ns}}/_{\mathrm{nm}}$ required by this system, before presenting the experimental results. Their design is compatible with both versions of the Yb frequency synthesizer, either based on a Ti:sapphire oscillator or on an Yb one.

5.1 Gain narrowing and stretching ratio

When a pulse propagates over a distance z in a dispersive medium, the spectral components undergo a different velocity and are spread in time. For a Gaussian pulse with initial Fourier-transform pulse duration $\Delta\tau_0$ at FWHM, centered at the frequency $\omega_L = {}^{2\pi c}/_{\lambda_L}$, the complex electric field $\widetilde{E}(x, y, z, \omega)$ is written as [130]:

$$\widetilde{E}(x, y, z, \omega) = E(x, y)\widetilde{B}(z, \omega)\mathrm{e}^{i\beta z} \tag{5.1}$$

where x and y are the transverse directions, z the propagation direction, ω each frequency component of the optical field. $\widetilde{B}(z, \omega)$ is the spectral amplitude and β the propagation constant.

In the time domain, the amplitude is given by the inverse Fourier transform of $\widetilde{B}(z,\omega)$:

$$B(z,t) = \frac{1}{2\pi}\int_{-\infty}^{\infty} \widetilde{B}\mathrm{e}^{-i\omega t}\mathrm{d}\omega \tag{5.2}$$

The propagation constant β is frequency dependent, and $\beta(\omega)$ can be expanded in a Taylor series around the carrier frequency ω_L for pulses with a spectral width $\Delta\omega$ respecting the relationship $\Delta\omega << \omega_L$ and propagating in a media with refraction index $n(\omega)$:

$$\beta(\omega) = n(\omega)\frac{\omega}{c} \approx \beta_0 + \beta_1(\omega-\omega_L) + \frac{\beta_2}{2}(\omega-\omega_L)^2 + \frac{\beta_3}{6}(\omega-\omega_L)^3 + ... \tag{5.3}$$

where $\beta_m = (\mathrm{d}^m\beta/\mathrm{d}\omega^m)_{\omega=\omega_L}$. β_0 is the absolute phase delay; $\beta_1 = 1/v_g$ with v_g the group velocity is the group velocity; β_2 is the group velocity dispersion.

The propagation in the dispersive medium adds a dispersion β_2 written for the second order:

$$\beta_2 = \frac{\lambda_0^3 z}{2\pi c^2}\frac{d^2n(\lambda)}{d\lambda^2} \tag{5.4}$$

This linear phase results in a stretching of the pulse and the new pulse duration $\Delta\tau_{out}$ is given for a Gaussian pulse by:

$$\Delta\tau_{out} = \Delta\tau_0\sqrt{1+\frac{\beta_2^2}{\Delta\tau_0^4}16(\ln 2)^2} \tag{5.5}$$

In the chirped pulse amplification scheme, positive dispersion is introduced to stretch the pulses, then the compressor adds negative dispersion to recompress the pulses. For a full recompression of the pulses, not only the second order of the introduced dispersion has to be matched but also the higher orders. For the compressed pulse duration of this pump line of ∼500 fs, only the compensation up to the third order is relevant.

Not only material but also geometrical arrangements and interferometric structures change the spectral phase of a pulse, as detailed in section 5.2.

The necessary stretching ratio to minimize the accumulation of nonlinearities during amplification is determined by the amplification stage which is the most susceptible to add nonlinear distorsions. From formula 3.5 this concerns the pulses with the highest energy or the shortest pulse duration. Considering the gain narrowing, *i.e.* pulse shortening occurring in the amplification stages of this system, the highest energy and shortest pulse duration are likely reached in the last stage. Estimates of the resulting bandwidth after each amplification stage will be presented in the following discussion.

As derived by Rouyer *et al.* in [131], the gain narrowing during amplification can be estimated by the formula:

$$\Delta\lambda = \Delta\lambda_0\left(1+\beta lnG\left(\frac{\Delta\lambda_0}{\Delta\lambda_{fluo}}\right)^2\right)^{-1/2} \tag{5.6}$$

with $\Delta\lambda_0$, $\Delta\lambda$, $\Delta\lambda_{fluo}$ the input, output and fluorescence spectral bandwidths, G the gain and β the relative position of the peaks of the gain and input pulse spectrum:

$$\beta = 2\left(\frac{\lambda_0-\lambda_{fluo}}{\Delta\lambda_{fluo}}\right)^2 - 1 \approx 1 \tag{5.7}$$

Table 5.1 summarizes the different spectral bandwidths inside the pump line calculated according to Rouyer's formula.

Module	Parameter	Unit	Value
Regen	E_{in}	nJ	0.6
	E_{out}	mJ	6.5
	$\Delta\lambda_{fluo}$	nm	24
	$\Delta\lambda_{in}$	nm	5.7
	λ_0	nm	1030
	λ_{fluo}	nm	1023
	$Gain$	dB	70.3
	$\Delta\lambda_{out}$	nm	5.4
Cryo 1	E_{in}	mJ	1.5
	E_{out}	mJ	100
	$\Delta\lambda_{fluo}$	nm	0.8
	$\Delta\lambda_{in}$	nm	5.4
	λ_0	nm	1030
	λ_{fluo}	nm	1030
	$Gain$	dB	18
	$\Delta\lambda_{out}$	nm	0.7
Cryo 2	E_{in}	mJ	100
	E_{out}	mJ	500
	$\Delta\lambda_{fluo}$	nm	0.8
	$\Delta\lambda_{in}$	nm	0.7
	λ_0	nm	1030
	λ_{fluo}	nm	1030
	$Gain$	dB	7
	$\Delta\lambda_{out}$	nm	0.5

Table 5.1: Calculation of the spectral bandwidth after each amplification stage, according to the formula from Rouyer *et al.* [131].

The discrepancy of the spectral width after the regenerative amplifier between calculation and measurement (*cf.* figure 3.17 in chapter 3) is most likely due to the fact that the formula does not take into account the exact shapes of the gain and pulse: the gain shape as obtained during Q-switched operation presents a double-peak which . In this experimentally implemented laser system, the stretched pulse and the free-running spectrum of the regenerative amplifier working in cavity dumping operation were not completely overlapping. The spectral components with low power density are less amplified and finally cut down due to gain narrowing. Overall the spectrally limiting module is the cryogenically cooled Yb:YAG multi-pass amplifier.

The power amplifier to reach 500 mJ to 1 J output energy is intended to be built on an extended thin-disk design with 17 to 20 mm disk diameter. To minimize the nonlinearities in this stage and in the last round-trips of the 100 mJ amplifier, a pulse duration of ∼500 ps in the high energy amplifiers is required. Considering the limited spectral width of 0.6 nm after amplification, this corresponds to a stretching ratio of 0.8 $^{\mathrm{ns}}/_{\mathrm{nm}}$.

In view of the high stretching ratio, the narrowing of the spectrum during amplification to high energies translates one-to-one to a shortening in time. In the high energy stages, susceptible to add nonlinear phase shift to the pulse, the pulses are then also shortened, increasing further the nonlinear phase-shift.

In a CPA scheme, the dispersion of the stretcher and compressor have opposite signs. It also has to be considered that the optical components between stretcher and compressor introduce additional dispersion. The second-order dispersion can be compensated but the compression is limited by the third-order dispersion: usually the third-order dispersion originating from the compressor and from the material have the same sign at 1 µm and add up (*cf.* section 5.3).

The next section describes the possible stretcher and compressor solutions before justifying the choice of the implemented one. The last section concerns the experimental realization of the stretcher and both compressors for the regenerative amplifier output and the high energy booster amplifier.

5.2 Stretchers and compressors

Different stretchers have been developed over the last decades. Stretchers based on geometrical arrangements are either based on gratings or on prisms [132]. The grating stretcher from Martinez [133] relies on a Newton telescope and the one from Offner [134] on a Galilean telescope. Grating based stretcher and compressor differ from the prism based ones by the amount of dispersion introduced for a given distance between gratings or prisms respectively, where the grating method allows significantly higher dispersion. For this reason, the prism based stretcher and compressor are not detailed here. Chirped Bragg gratings bring less stretching than a grating or prism stretcher, but enable very compact setups.

These solutions are presented and discussed below for stretchers and compressors. The last section details different solutions and justifies the implemented one.

5.2.1 Chirped Bragg Gratings

The Bragg grating [135] is a periodic variation of the refractive index in the material, creating interferences between forward and backward propagating modes; by adjusting the grating parameters, constructive interferences highly reflect some given wavelengths, acting as a spectral filter. This is used *e.g.* for wavelength stabilization in laser diodes. By chirping the grating period, different wavelengths are reflected at different positions in the material. The difference in the optical paths undergone by each wavelength adds positive or negative dispersion to an optical pulse. The principle of a chirped Bragg grating is shown in figure 5.1 with an example of a grating written in bulk and in fiber as inset.

The first chirped fiber Bragg grating was developed in 1978 by Hill *et al.* [136], and further developed in the 80's and 90's [137, 138], originally for optical fiber communication systems. Bragg gratings can be written with phase mask techniques in bulk (VBG) [139] or in fiber (FBG) [138], or with a transverse holographic method [137, 140], which is now wide-spread. The phase-mask technique is attractive because of its repeatability. The grating length, hence the maximum achievable dispersion, is limited by the writing setup of the phase mask.

The stretching factor seen by the pulse depends on the wavelength, the spectral bandwidth and the grating length. The dispersion D in $^{\mathrm{fs}}/_{\mathrm{nm}}$, the spectral bandwidth $\Delta\lambda_{CBG}$ of the filter and the maximum stretching factor τ_{max} are related by: $D \cdot \Delta\lambda_{CBG} = \tau_{max}$

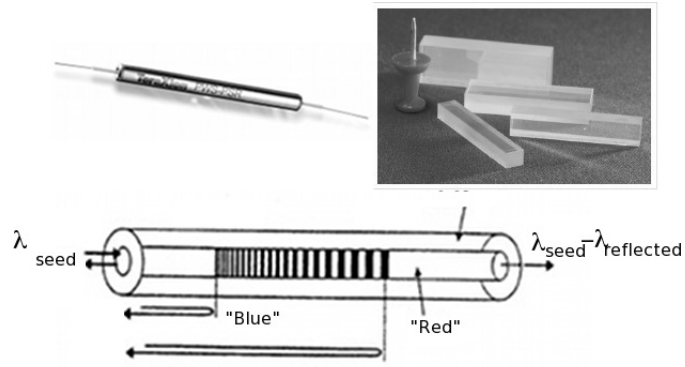

Figure 5.1: Working principle of a Bragg grating: in light of interferences between the forward and the backward propagating waves, the different wavelengths are reflected at different positions inside the material. In this example, the shorter wavelength (bluest) are reflected before the longer ones (redest), introducing negative dispersion. The insets show chirped fiber and volume Bragg gratings.

(*cf.* equation 5.5). τ_{max} corresponds to the maximum delay which might be written inside the material, to delay the extreme wavelengths of the spectral width $\Delta\lambda_{CBG}$ from each other.

As the spectral shape of the filter can be first approximated with a rectangular shape, the spectral bandwidth of the pulse needs to be at least a factor of two narrower than the filter bandwidth to limit spectral clipping during the passage through the CBG. For a Gaussian pulse, a factor of three between the FWHM of the quasi-flat-top filter and the one of the pulse would actually cover the whole spectrum, even the components with very low spectral density, *i.e.* $\Delta\lambda_{CBG} \approx 3\Delta\lambda_{FWHM}$. The consideration of only a factor of two for the ratio between both spectral FWHM implies thus that the spectral components with low energy are filtered out, which can be accepted in this specific design because of the gain narrowing encountered during later amplification, narrowing the edges of the spectrum, too. The filtering by the CBG means that the pulse is only lengthened according to the dispersion seen by its spectral bandwidth.

One problem of Bragg gratings, either in bulk or in fiber, is the appearance of side lobes in the reflected spectrum if the strength of the index modulation is constant over a certain length and suddenly drops to zero. In order to avoid this, a technique called apodization is used: the change in the refractive index is slowly ramped up and down over a certain length. This decreases the reflectivity of the filter, which can be compensated with an increased grating length. There is consequently a trade-off in the CBG design between filter reflectivity and side-lobes suppression. Group-delay ripple may be present even with apodization *e.g.* due to phase error of the phase mask [141].

Chirped volume Bragg gratings

The chirped volume Bragg gratings (CVBG), initially developed by Efimov *et al.* [142] at the turn of the millenium, are now commercially available; their current maximum delay is about 450 ps for a flat-top bandwidth of 7 nm, limiting the pulse bandwidth to ∼3 nm, hence the stretching factor is quite low. In order to achieve 1 to 2 ns stretching, it would

be necessary to have at least 4 CVBG in series [143]. As each of them has a reflectivity of ∼75%, the total reflectivity of the stretcher would be 31%. To obtain 0.8 $^{ns}/_{nm}$ over 5 nm, a design with 16 passes through the CVBGs could be a solution. Such an experimental setup might introduce instabilities and issues during the recompression: to recompress with a grating pair, the dispersion curves of both stretcher and compressor need to exactly compensate each other, but a high number of CVBGs multiplies the production tolerances and errors in the dispersion curve, thus endangers the recompression to a transform limited pulse, and might lead to the appearence of unwanted satellite pulses.

Chirped fiber Bragg gratings

The commercially available chirped fiber Bragg gratings (CFBGs) are written in a similar way to the CVBG, and encounter similar limitations as the CVBG, but their writing process makes a longer grating possible. CFBGs were first developed for dispersion compensation in optical fiber communication systems, then extended to stretch and compress the pulses in ultrafast laser systems.

The maximum stretching factor which can be written in one grating is 1100 ps for CFBGs written by the company Teraxion in Québec. Some other possible sources for CFBGs are the research group of Prof. Ben Eggleton in Australia, and the company Idil in France, among others.

It seems logical to use several CFBGs in series to increase the stretching factor, which is only practicable if the dispersion is very well controlled. During the writing process, some delay ripples appear however on the dispersion filter as shown in figure 5.2. Their period is about a few picometers. The delay ripples stem from random and systematic errors during fiber manufacturing. They represent the deviation between the written filter and the targeted one. Delay ripples distort the spectral phase of the pulses and result in incompressible pedestals in the time domain. A correction of low frequency delay ripples based on iterative measurements of the group delay (GD) curve and UV illumination of the grating was demonstrated in [144]; the curve calculated for the new illumination is obtained by using a simple solution of the inverse problem for the coupled-wave equation. In that work, the low-frequency group-delay ripples have been reduced from ±15 ps to ±2 ps. According to the manufacturer TeraXion, the amplitude of the delay ripple is reduced from 150 ps to 40 ps peak-to-peak after correction. During the writing-process of a CFBG for 1550 nm, it is already possible to measure the delay ripples and to reduce them with an adequate choice of parameters; at the time of designing and ordering, this was not yet implemented for the writing setup of the 1 µm centered gratings, representing a risk for the pulse compression when selecting this stretching method.

As a result, if the compressibility needs to be optimized so that the recompressed pulses achieve a nearly transform limited pulse length, the number of CFBGs in series for stretching the pulse should be minimized. It is besides possible to write a nonlinear dispersion curve in the CFBGs to compensate higher order dispersion.

CVBG and CFBG as compressors

Passing backwards through a CVBG adds the opposite dispersion than the forward pass, hence compresses the pulses up to the dispersion added between stretcher and compressor.

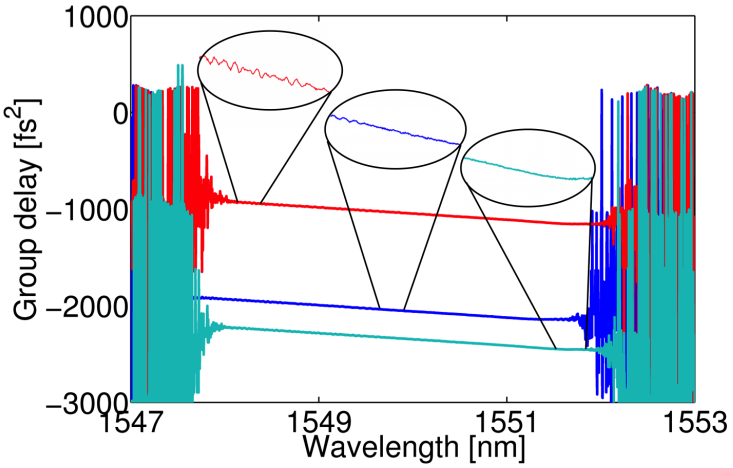

Figure 5.2: Example of delay ripples on the GD of 3 CFBGs with 3.5 nm filter bandwidth centred at 1550 nm, and with a stretching of 62.5 ps. Data: Courtesy of TeraXion.

Unfortunately the high energies in the compressor require large apertures which are not yet available. To date up to 8×5 mm^2 grating aperture can be written, limiting the beam diameter to $\sim$ 2 mm, which can sustain only mJ level energies for sub-picosecond pulses. The passage through the glass also adds nonlinearities to the beam. This solution has been discarded for all these reasons.

CFBGs are not an option as a compressor for mJ energy level with sub-picosecond pulse duration, beause they are written in single-mode fused silica fiber: the maximum peak power inside the fiber shoud not exceed a few kW to minimize nonlinearities.

5.2.2 Bulk grating stretcher and compressor

Grating and prism stretchers and compressors use angular dispersion and a geometric arrangement to introduce dispersion on a pulse. When the low frequency spectral component of the pulse (reddest) undergoes a shorter optical path than the high frequency ones (bluest), positive dispersion is introduced.

In figure 5.3, the principle layouts of a stretcher and a compressor are shown. Both differentiate from each other by the distance between the gratings: in the case of a compressor, the optical distance L_{comp} is positive and negative in the case of the stretcher. For this, the image of the grating G_1 is placed as a virtual image by the telescope after G_2: on the figure G_2 is located between the telescope and F_2' focal point of the telescope, whereas the image of G_1 would be located after. The incident γ and diffracted γ_{diff} angles are defined in the layout of the compressor, and are correspondingly defined in the stretcher. The stretching factor depends on the parameter L_{comp}. According to the formula for a grating pair derived by Fork *et al.* in [146], the second (GDD) and third order (TOD) dispersion for a grating pair are given by:

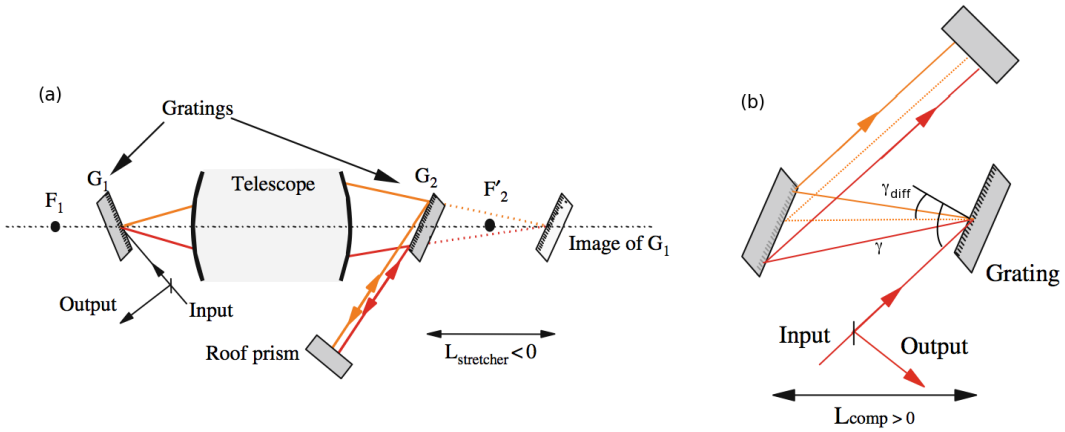

Figure 5.3: General scheme of a grating stretcher (a) and compressor (b). Schema adapted from [145].

$$\frac{d^2\beta_g}{d\omega^2} = \frac{\lambda^3 l_g}{\pi c^2 d^2}\left(1-\left(\frac{\lambda}{d}-\sin(\gamma)\right)^2\right)^{-3/2} \tag{5.8a}$$

$$\frac{d^3\beta_g}{d\omega^3} = -\frac{d^2\beta_g}{d\omega^2}\frac{6\pi\lambda}{c}\times\frac{1+\frac{\lambda}{d}\sin\gamma-\sin^2\gamma}{1-\left(\frac{\lambda}{d}-\sin\gamma\right)^2} \tag{5.8b}$$

where l_g is the perpendicular distance between the gratings and d the spacing of the grooves of the grating.

According to the dispersion formula for a stretcher or compressor, the introduced GDD and TOD depend on the line density of the grating and on the distance of the focus to the grating.

In this experiment, in order to stretch the assumed 10 nm wide pulses up to 0.8 $^{\text{ns}}/_{\text{nm}}$ while minimizing the footprint, the grating would need the highest possible number of lines per mm. Currently 1740 $^{\text{lines}}/_{\text{mm}}$ are achievable while not introducing distorsions due to TOD. Some companies like Richardson Gratings can increase it up to 2400 $^{\text{lines}}/_{\text{mm}}$, however with too small an aperture for this system. The corresponding Littrow angle for a given groove density is: $2d \cdot \sin(\gamma) = m \cdot \lambda_L$, where d is the distance between the grooves, γ the incident angle and m the diffraction order.

In the case of a grating with 1760 $^{\text{lines}}/_{\text{mm}}$ and using the first diffraction order, γ equals 64.9° at 1029 nm. The extreme wavelengths of the pulse spectrum $\lambda_{\text{min}} = 1026$ nm, $\lambda_{\text{max}} = 1032$ nm are diffracted into the angles γ_{min}, γ_{max} according to the grating condition $d \cdot (\sin\gamma_{min,max} + \sin\gamma) = m \cdot \lambda_{min,max}$ to 65.6° and 64.2°, respectively.

Figure 5.4 shows a detail of the grooves of the gratings with 1760 $^{\text{lines}}/_{\text{mm}}$ groove density from Plymouth Grating Laboratory. The design of the grooves allows a high diffraction efficiency >97.5%, as illustrated in figure 5.5: the diffraction efficiency in the first order is given vs. wavelength and angle of incidence on the grating; the maximum diffraction efficiency is represented in the yellow zone. In this grating design, the further away from

Littrow angle, the least efficiency and the more narrowband. For a detuned wavelength, the efficiency decreases as well. From this graph a pulse centered at 1030 nm with 10 nm full spectral bandwidth incoming with an angle of incidence of 60° would be diffracted with the maximum efficiency.

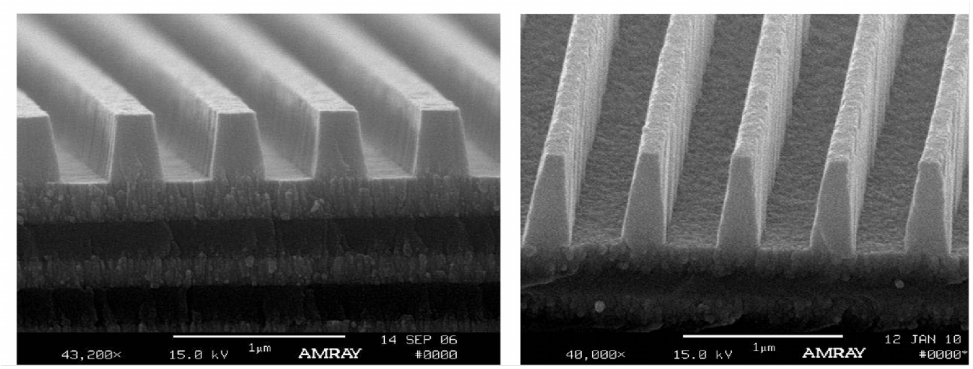

Figure 5.4: Details of the grooves of the grating from Plymouth Laboratory Grating. Photo from the quotation of the gratings.

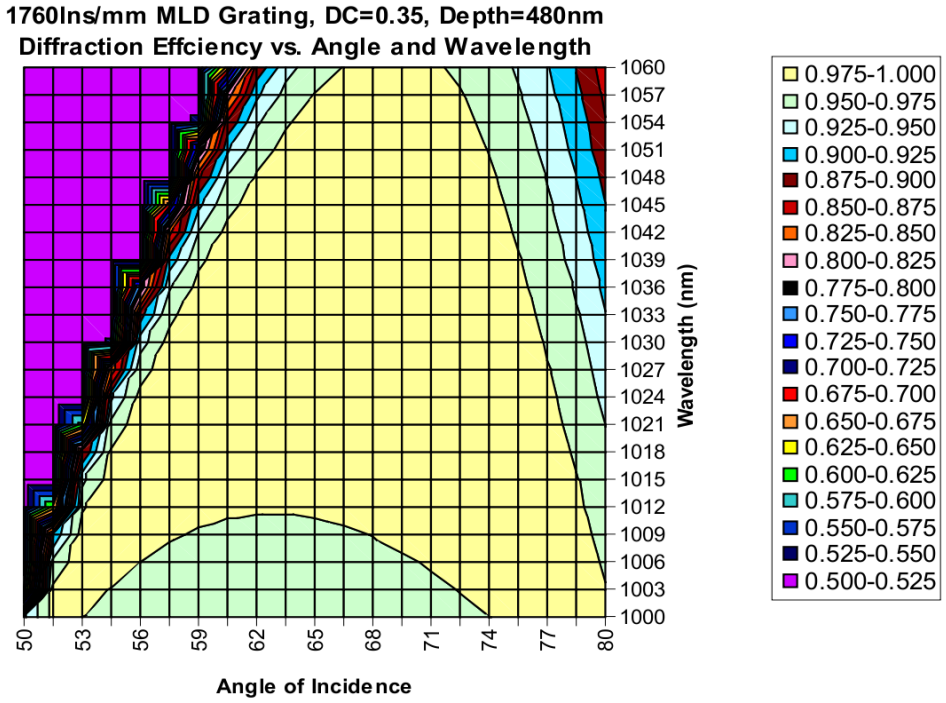

Figure 5.5: Efficiency curve of a grating from Plymouth Laboratory Grating optimized for 1030 nm central wavelength. Graph from the quotation of the gratings.

Stretcher geometries

Several configurations of grating stretchers were demonstrated. For this system, two configurations have been examined: Offner [134, 147] and Martinez [148, 133]. The Martinez

stretcher is presented in the following, whereas the calculations for the Offner stretcher are in appendix 10C.

The scheme of a Martinez stretcher is shown in figure 5.6a. These figures show the ray tracing of the beam inside the stretcher: the single-deck stretcher is shown from the top and, as inset, from a different angle showing the input and output beams. The lens is located 1 m after the grating. In the double-deck shown in figure 5.6b, the stretcher is folded in the middle: 4 passes are done on each grating instead of 2 in a conventional, single-deck stretcher. The advantage of this folding is the smaller footprint compared to the unfolded version, but the alignment of the lenses would be complex from the point of view of space, holders, and required precision. Each pass on the grating induces however losses, and a small amplifier or a stronger oscillator would be necessary to compensate for these losses. In order to reach the required 0.8 $^{ns}/_{nm}$ stretching ratio, two double-deck Martinez stretchers in series would be required.

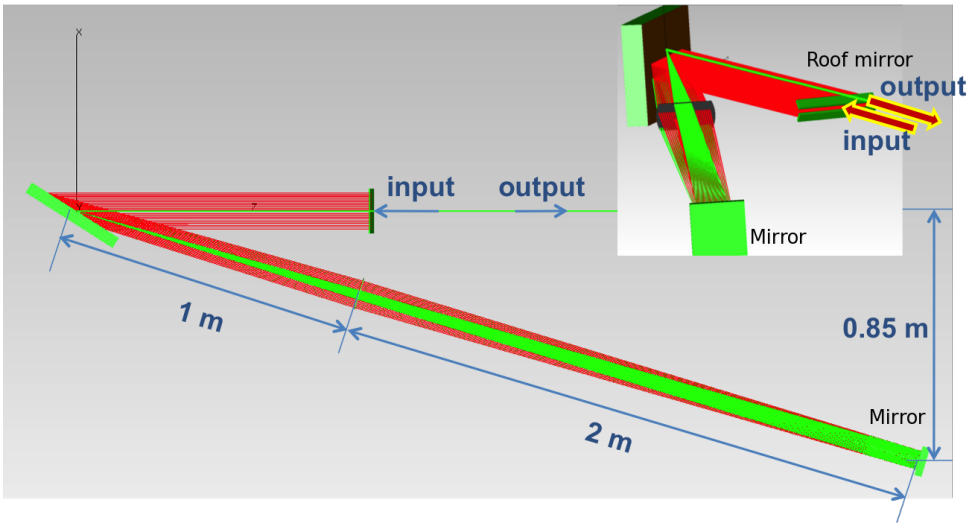

(a) One-Deck Martinez stretcher

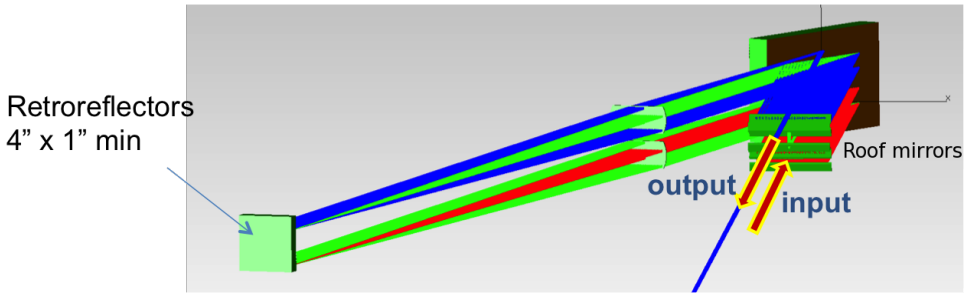

(b) Double-Deck Martinez stretcher

Figure 5.6: Martinez stretcher to reach the required 0.8 $^{ns}/_{nm}$ stretching ratio for high energy amplification, traditional and double-deck. Design by Eduardo Granados.

The grating of the Martinez stretcher can be chosen as multi-dielectric to be completely symmetric with the compressor grating or gold coated. The manufacturers typically offer 1740 $^{lines}/_{mm}$ for gold coated ones (Horiba Jobin-Yvon), whereas the multi-dielectric ones have 1760 $^{lines}/_{mm}$ (Plymouth Laboratories Gratings). The difference in the dispersion due

to the line difference could be compensated with an adaptation of the angle of incidence on the gratings without endangering the compression.

Another problem of this solution resides in the stability of the whole system. On such large distances a small variation of the alignment of one optical component has a large influence. The gratings and mirrors have to be thick enough to avoid distortions of the surface and therefore of the wavefront.

Compressor geometry

As explained in figure 5.3 (b) the Treacy compressor [149] consists of 2 gratings placed at or close to Littrow angle; the beam makes a double pass on both gratings. The spectral components are diffracted under different angles and thus see different path lengths. After the first pass, the beam is spatially chirped. A second passage through the compressor overlays the individual spectral components in space. In order to obtain at the output a not only spatially compressed but also temporally compressed beam, half of the total dispersion is introduced by a single-pass. This makes it possible to reduce the required distance between both gratings. The grating pair dispersion formula given in equation 5.8 covers the case of the compressor geometry: the distance between the gratings is negative in the case of a stretcher and positive in the case of a compressor; this induces a change of the dispersion sign.

In case of a transmission grating compressor, by passing through the gratings, the beam will encounter self-phase modulation if the intensity is too high. As the damage threshold of silica is 1.15 $^{J}/_{cm^2}$ for 1 ps long pulses [150] and the nonlinearity threshold determined by the critical power 3.5 MW, the maximum intensity on the grating imposes a minimum waist radius of 4.6 mm, which should be increased to 6-10 mm for safety reasons. Reflection gratings will be used to avoid this issue.

With 1740 $^{1}/_{mm}$ and 1 m separation between the mirrors, under Littrow angle, a dispersion of -1.319×10^8 fs^2 is coupled to a third order dispersion about 1.959×10^9 fs^3; this dispersion corresponds to the one needed to stretch the seed pulses to 0.65 $^{ns}/_{nm}$.

A grating stretcher followed by a grating compressor has the advantage of completely eliminating the higher order dispersion after recompression if their dispersion curves are opposite, but the sizes of the gratings lead to high costs and the long beam paths to an increased mechanical instability. The presented double-deck double Martinez stretcher is quite compact though it still needs close to 30 m free space propagation. Therefore, in this work, the combination of CFBG and double-deck compressor is pursued.

5.3 Dispersion analysis and comparison of the solutions

A twin-system of the high energy booster was developed in parallel in the group of Prof. Franz X. Kärtner at MIT; this system required as well stretcher and compressor. The stretcher at MIT was designed as a double-deck double-Martinez stretcher shown in figure 5.6b, which fixes the design of the compressor. To reduce the development effort both systems should receive the same compressor, *i.e.* the compressor designed in this work

had to be compatible with the double-deck double-Martinez stretcher. The stretcher was then designed to match the compressor.

The resulting compressor design compensates exactly the dispersion introduced by the gratings ordered at MIT for the double-deck double-Martinez stretcher, though the groove density is slightly different: by adapting the angle of incidence of the 1760 $^{\text{line}}/_{\text{mm}}$ gratings to 59.85° instead of 60°, the TOD/GDD ratio is equal to the one of the stretcher with 57.5° and 1740 $^{\text{line}}/_{\text{mm}}$. This means that at least the GVD and TOD could be exactly compensated between the grating stretcher and the grating compressor. The CFBGs are however designed to compensate a grating compressor with 60° angle of incidence upon the first grating, which is the main design of the compressor. The dimensions of the gratings and of the roof mirrors are calculated through geometric raytracing and angle considerations with Mathcad. A simulation with TracePro confirms these dimensions and allows for a more detailed sensitivity analysis.

The compressor after the regenerative amplifier (*cf.* figure 2.7) is illustrated in figure 5.7. Figure 5.7a represents the implementation of the compressor, folded between both gratings *G1* and *G2* with the mirrors *RM6* and *RM7* to decrease the foot-print, and figure 5.7b the so-called "double deck" compressor: the compressor of figure 5.7a can be folded with the roof mirrors *RM4* and *RM5* in a double pass compressor, to reduce the footprint by half. The double-deck can be implemented after the cryogenic amplifier, depending on the grating efficiency, as the losses have to be minimized after amplification to high energies.

The sensitivity analysis is performed with TracePro by tilting one mirror or grating and observing the pointing difference on a screen 5 m away from the first grating. As a result, the gratings as well as the roof mirror consisting of RM1 and RM2 have to be aligned with a precision of <1' around the X-axis to meet the clear aperture of the optics and to minimize distorsions due to the gratings. RM3, RM5 and RM6 are introduced in the beam path if the double-deck is needed. RM5 and RM6 are mounted on a periscope with fine adjustable mirrors. Both mirrors could also be rectangular and optically contacted orthogonally to each other, forming one unit with a tolerance on the angle about 1.5'. This solution was discarded due to its cost.

In this work, the implemented solution for the stretcher is the one based on CFBG, presented in detail hereafter. The grating-based stretcher was not the preferred solution due to its high cost and space requirements, but the implemented CFBG stretcher and bulk grating compressor were designed to be compatible with this back-up solution.

Here, only a recompressibility to pulse length below 1 ps after the regenerative amplifier is aimed at and a stretching ratio of ∼0.8 $^{\text{ns}}/_{\text{nm}}$ is the main goal. The scheme of the stretcher is shown in figure 5.8. The oscillator (not represented) is coupled in a custom-made, commercial fiber amplifier, which has three outputs: the outputs *For Super-continuum* and *For DFG for Tm Amplifier* are for the actively CEP-stabilized front-end of the synthesizer (*cf.* 2.5) and the third output is the one for seeding the regenerative amplifier. This low energy arm is stretched through one CFBG with a FWHM bandwidth of 6 nm, then amplified, thus avoiding the accumulation of nonlinearities during the propagation of ultrashort-pulses in fibers. A second CFBG preceeds a last fiber amplifier followed by two CFBGs located on a four port circulator. Both fiber amplifiers are single-mode, co-propagating core pumped, polarization maintaining amplifiers. The

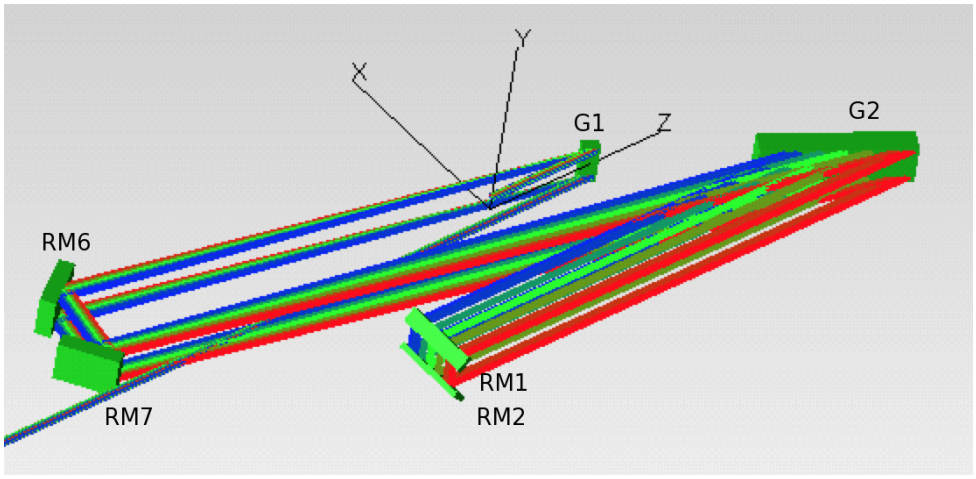

(a) One-Deck Compressor

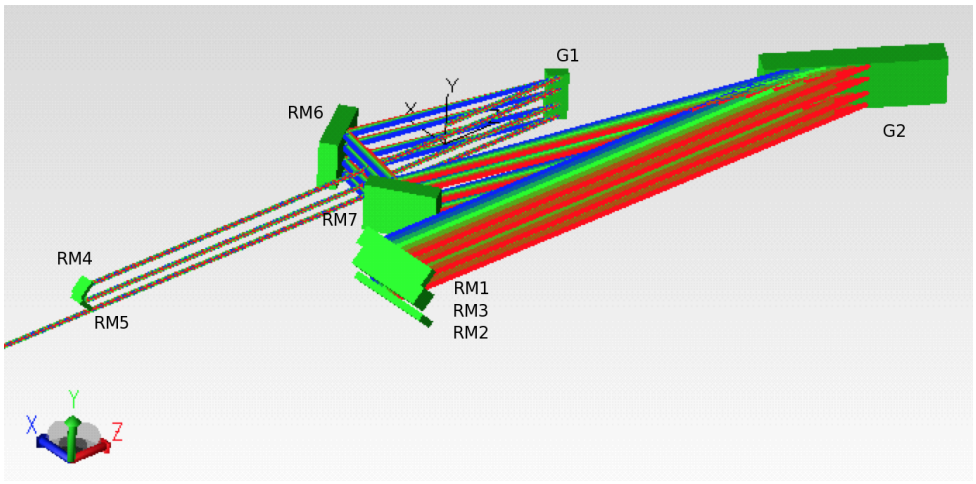

(b) Double-Deck Compressor

Figure 5.7: TracePro simulation of the compressor after the regenerative amplifier. On the top, the single deck version is represented, whereas the double-deck version is on the bottom.

chosen fibers are highly doped and absorb the 700 mW pump power with 140 $^{\mathrm{dB}}/_{\mathrm{m}}$; the pump wavelength is centered at 975 nm. The gain is calculated to be 16 dB per amplifier with derated pumps: on one hand, using only one amplifier would have been on the achievable limit, but would result in the loss of scalability; on the other hand, there is still some spare pump power to increase the output power if necessary.

At the entrance of the custom-made, commercial fiber amplifier, the pulse from the oscillator is assumed to be an ideal $sech^2$ unchirped pulse. It leaves Amp2 and Amp3 with an estimated duration of 1.7 ps and Amp1 with ∼750 fs duration due the dispersion (GDD and higher orders) introduced by the fibers. From this point, several stretcher concepts based on CFBGs have been compared: different spectral widths of the CFBG (3, 5, 6, 7 and 15 nm) and the losses of the assembly due to circulator and CFBG have been considered.

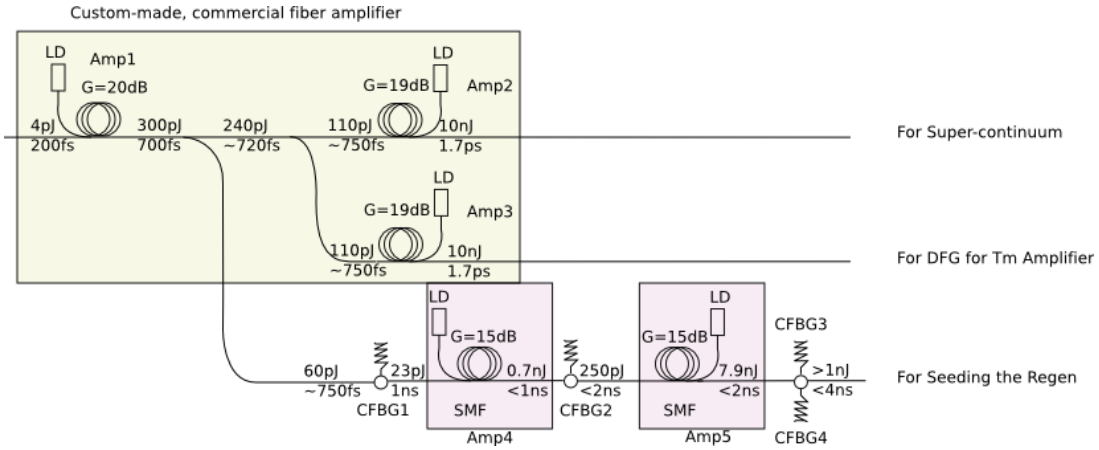

Figure 5.8: Scheme of the fiber amplifier with three outputs: one to seed the regenerative amplifier with its stretcher, one for the super continuum and a spare one. Amp1, Amp2 and Amp3 are parts of a custom-made, commercial fiber amplifier, whereas Amp4 and Amp5 have been built within the stretcher. The energies and pulse durations after each stage and split are indicated on the drawing.

- The losses are mainly caused by the circulators (3 dB losses), whereas the reflection of the CFBG is specified to be better than 80% by Teraxion. Adding the losses of the splices, the losses of each assembly can be estimated to 4.5 dB. Fiber amplifiers compensate for these losses.

- CFBGs with 15 nm bandwidth would avoid cutting down the input spectrum, thus they would keep a Gaussian spectrum. The number of CFBGs to reach the required stretching ratio would however be too large considering the delay ripples and the losses.

- Two CFBGs with 3 nm bandwidth on the contrary would stretch the pulse to the required stretching ratio but drastically narrow down the spectrum, preventing a recompression below a picosecond after the regenerative amplifier.

- The main problem of the delay ripples is their amplification through all the stages [46]: in the last stage, at the Joule level, the spectrum could then be very sharply structured. The difference between this solution and one based on CVBG as in [46] mostly relies on the manufacturer's know-how, and the confidence that the delay-ripple are well-controlled by Teraxion and the manufacturing process regularly improved.

Four CFBGs with 6 nm bandwidth represent the best compromise to reach the required spectral width at the output of the stretcher, while limiting the influence of the delay ripples. To compensate for the losses, two fiber amplifiers are added after the first and second CFBGs.

The spectrum of the stretched pulses, narrowed down to the filter width of the CFBGs, is reshaped by the amplification in the fiber amplifiers and in the regenerative amplifier.

An estimation of the maximal spectral width after the latter is given by a wavelength dependent Franz-Nodvik simulation; this only takes into account the available stored energy for each wavelength, calculated from the emission and absorption cross-sections of the material, and neglects the homogenization of the upper and lower laser levels. With this simplified calculation and from the estimation of the gain narrowing from Rouyer's formula, the pulse duration after recompression is expected to be between 400 fs and 1 ps.

In conclusion it is interesting to test the CFBGs, but one should keep in mind the potential issue of the delay ripples. The double-grating solution should work in all cases and is kept as a back-up option. The CFBGs are more elegant and the "all-fiber" concept is then fully utilized; for this reason this solution will be first implemented. As for the compressor, the Treacy grating compressor is implemented after the regenerative amplifier and after the cryogenic amplifier.

5.4 Experimental results

5.4.1 Stretcher

The implemented fiber stretcher with the necessary intermediate fiber amplifiers are represented on figure 5.9. The first 3-port circulator and apodized CFBG are spliced directly to the split output from the commercial fiber amplifier, in order to minimize the nonlinearities accumulating through propagation in the fibers. The pulse is thus at least 1 ns long and the peak power is low enough to neglect the nonlinearities, even after the amplification stages. A second 3-port circulator and CFBG follow the amplifier (Amp4 on figure 5.9). After the second amplifier (Amp 5 on figure 5.9), a 4-port circulator with two CFBGs terminates the stretcher setup. The intermediate amplifiers are pumped with an Oclaro diode centered at 974 nm and with a JDSU diode centered at 976 nm delivering both more than 600 mW power. They consist of a high-absorption (140 dB/m at 915 nm) single-mode fiber from CorActiv (Yb 401-PM, photodarkening resistant). The whole setup is polarization maintaining and all splices were made with an Ericsson splicer FSU995PM. As the fiber PMCMS1060 for the CFBGs from Teraxion are specially made by Nufern, the parameters of the splicers had to be adapted from the ones for splicing standard fibers; they were tested and improved to optimize the transmission. From an average of 0.4 dB measured losses, splices to PM980 fiber were improved to less than 0.2 dB measured losses on average.

First, the commercial fiber amplifier from figure 5.8 and the stretcher were characterized by coupling a transform-limited 200 fs Gaussian pulse coming from the output of the seed oscillator model T-Pulse manufactured by Amplitude Systèmes, attenuated to achieve an input energy level between 2 and 8 pJ, corresponding to the expected available energy from the Ti:sapphire oscillator in a 10 nm spectral bandwidth centered around 1030 nm. The repetition rate is with 42.5 MHz half the one of the Ti:sapphire oscillator. This allows a compatibility with both versions of the Yb frequency synthesizer shown in figures 2.5 and 2.6.

The commercial fiber laser delivers 600 µW with 17.2 nm bandwidth on the split output after the first amplification stage. As the first CFBG cuts the spectrum to its own spectral

width, less than 100 µW seeds Amp4. The latter is set up to deliver 140 mW with 400 mA pump current. At the output of the stretcher, both Amp4 and Amp5 are configured to have 48 mW average power, corresponding to 1.13 nJ pulse energy.

The pulse train of the stretched pulses (a), the seed spectrum (b) and the output spectrum (c) are displayed in figure 5.10. The measurements of the stretched pulse train were acquired with a fast oscilloscope (Agilent 8GHz 80804B/001) and the spectra with a high resolution spectrometer from OceanOptics (HR4000).

The reflection bandwidth of each of the four CFBGs is centered at the wavelength 1029 nm ±0.1 nm, hence no spectral cut was observed in addition to the one expected from the nominal bandwidth of the filters. This has been measured with an ANDO AQ-6315 spectrometer with 0.05 nm resolution. The effective stretching ratio of the pulses can be obtained from the measurement of the temporal and spectral widths and is equal to 0.65 $^{ns}/_{nm}$.

The spectral and temporal resolutions are not high enough to resolve the possible delay ripples. These would have been experimentally observed after compression of the pulse, because they would have caused a long pedestal in the time domain. The spectral modulations on figure 5.10 originate from SPM in the fiber pre-amplifier.

5.4.2 Compressor

The compressors are mechanically engineered because of the extra-large size of the mirrors and gratings. The first compressor refers to the one after the regenerative amplifier and the second compressor to the one after the cryogenically cooled booster, set up in this work after the 100 mJ booster stage, but compatible with the booster stage toward the Joule level. A first version of the holders was designed by the DESY and CFEL engineering teams for the compressor after the regenerative amplifier, and the later experimental discoveries were used as input for the mechanical design of the compressor after the cryogenically cooled amplifier. Figure 5.11 shows the holder of the second grating and an overview of the folded compressor, while the one after the cryogenically cooled amplifier is shown in figure 5.12.

In order to reduce the footprint the compressor is folded horizontally and vertically with a double-deck. Thanks to the high first order diffraction efficiency of the gratings, the overall efficiency of the compressor after the regenerative amplifier is 81%, corresponding

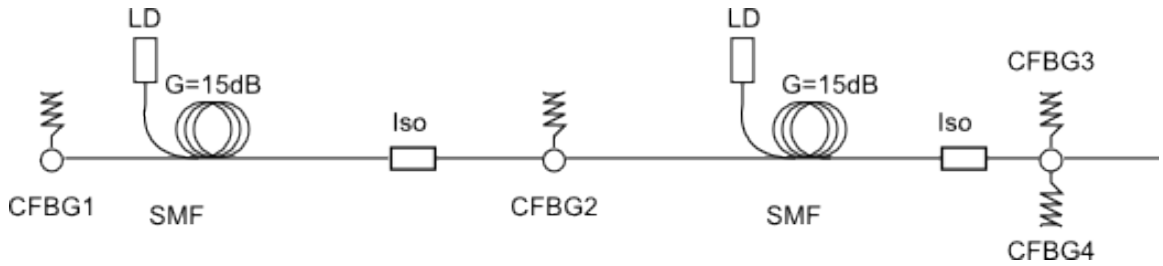

Figure 5.9: Experimental setup of the CFBG stretcher: two isolators *Iso* have been added to the prepared layout shown in figure 5.8. A 2 ps long pulse with more than 6 nm bandwidth is stretched up to 4 ns; its spectral bandwidth is narrowed to 5.5 nm.

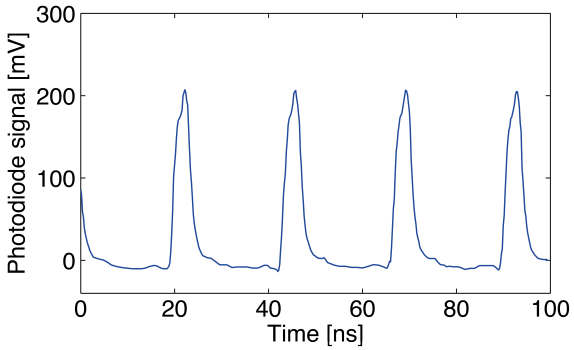

(a) Pulse train after stretching

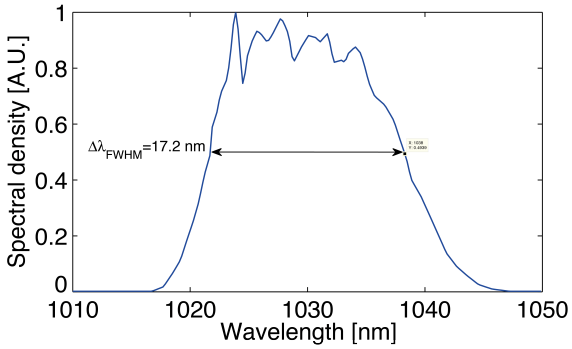

(b) Spectrum before stretching

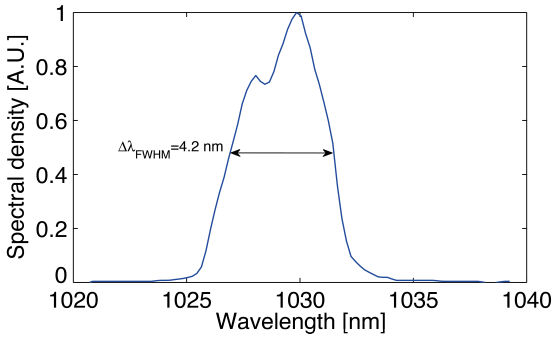

(c) Spectrum after stretching

Figure 5.10: (a) representation of the stretched pulse train on the oscilloscope. The spectral modulations can be seen in the time domain. The spectra before and after the stretcher are displayed in (b) and (c). The modulations orginate from SPM in the first fiber amplifier.

to 97.5% per pass on the gratings. For this reason, the second compressor has been also designed with a double-deck. In light of the size of the beam after the 1 J amplifier and the narrower bandwidth, the optics of the second compressor are much higher and narrower (*cf.* table 5.2). The degrees of freedom have been chosen to allow an easy alignment: in the second version the vertical alignment screw of the roof mirror has been removed, as well as one of the three alignment screws of the baseplate of the gratings. The other two screws of these baseplates have been kept to fine tune the parallelism of the lines with the beam polarization and the vertical tilt alignment. The angle of incidence can be finely aligned with an adjustable screw; in the first version the location below the mid-point of the grating led to a vertical shift while aligning the angle, that is why it has been shifted in the second one to the middle of the grating. Table 5.2 summarizes the dimensions of the mirrors and gratings used in both compressors as well as the degrees of freedom for the alignment.

In the second version, the alignment screws have been redesigned to ensure a longer travel range with a finer step size via a double differential screw. The alignment of the folding mirror was limited to vertical alignment for one mirror and horizontal alignment

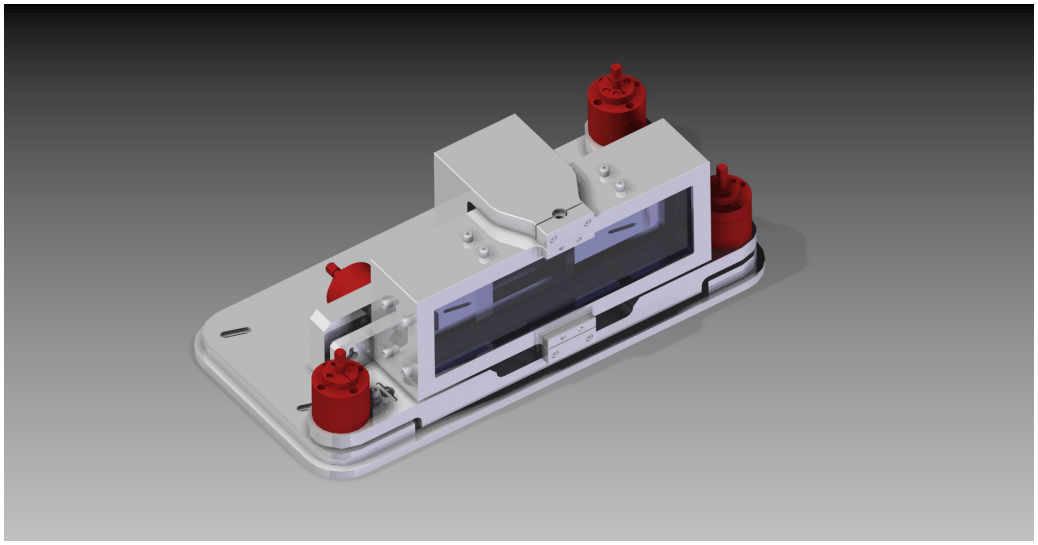

(a) Holder of the grating G2

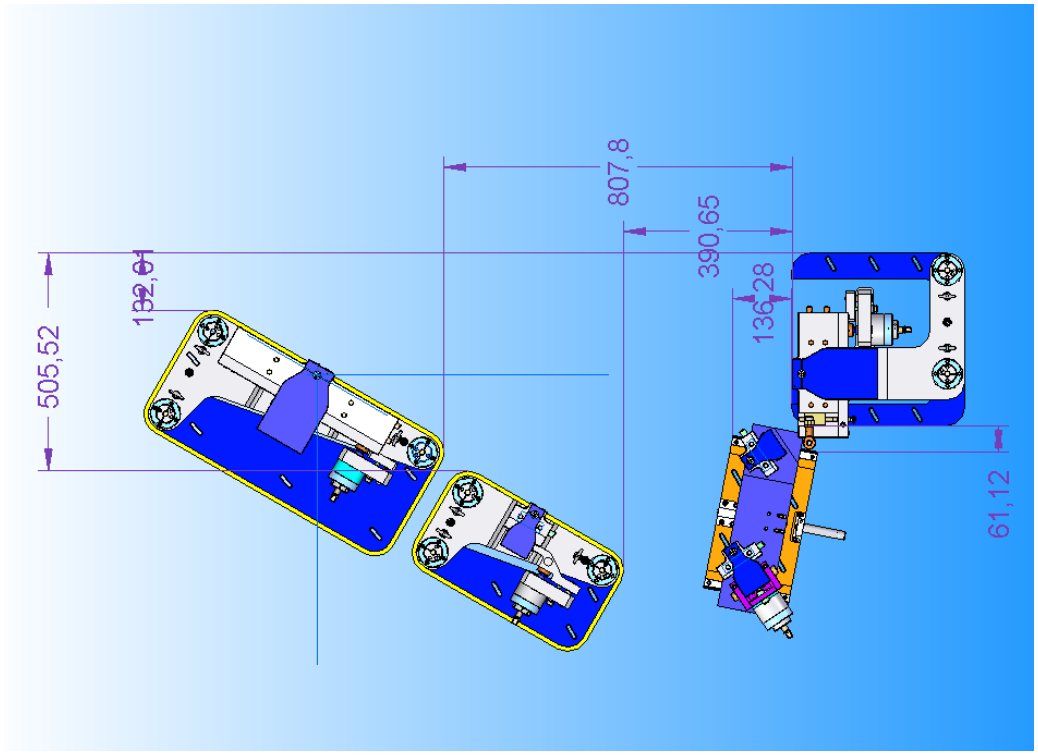

(b) Compressor layout

Figure 5.11: Mechanical design of the compressor after the regenerative amplifier. (a) Holder of the big grating G2. (b) Layout with holders and beam path. The adjustment screws are shown in red.

for both, though not as fine as with the differential screw. The translation stage was modified to improve the stability. A photograph in figure 5.13 illustrates the compressor after the regenerative amplifier.

The alignment of the compressor started by placing the optics according to the calculated distances and angles. The precision of this alignment was verified with references

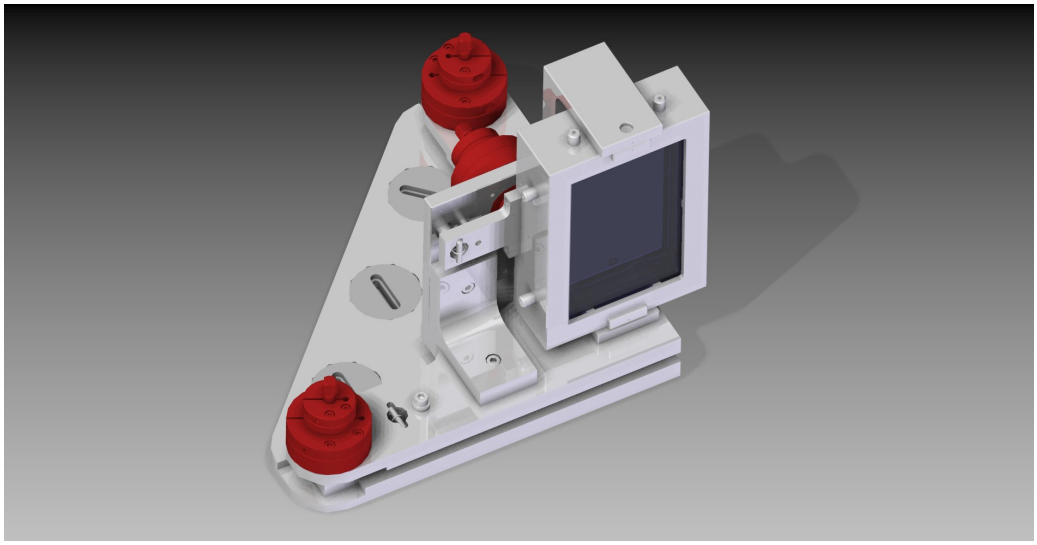

(a) Holder of the grating G2

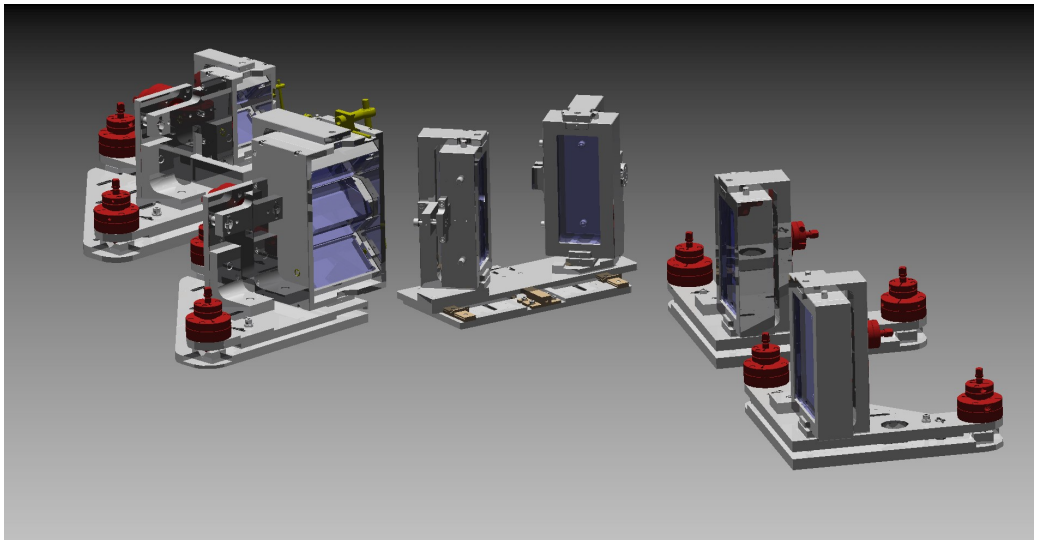

(b) Compressor layout

Figure 5.12: Mechanical design of the compressor after the cryogenic amplifier. (a) Holder of the big grating G2, with dimensions. (b) General view of the compressor. The adjustment screws are shown in red.

at very long distances: for example, the vertical alignment of a component was confirmed over 4 to 5 m before placing the next component. For the fine adjustment of the folding mirrors along the Y-axis, this alignment distance has been increased to 7 m. The alignment of the optics along the X-axis has been verified in a similar way.

After setting the optics the fine-tuning of the pulse compression is performed with the angle of incidence onto the first grating, the parallelism of the two gratings and the distance between them. The pulse duration was measured first with a fast photodiode (EOT3500) and an oscilloscope (Lecroy WaveRunner 640 Zi); the oscilloscope was then replaced with a sampling scope (Agilent). The bandwidth of the oscilloscope was 4 GHz and the one of the photodiode 12.5 GHz, meaning that the total bandwidth of the chain

		Regen.			Cryo.		
Optic	Abbr.	Dim.	Clear ap.	Align	Dim.	Clear ap.	Align
		$[mm^2]$	$[mm^2]$		$[mm^2]$	$[mm^2]$	
Grating	G1	$60 \times 120 \times 25$	45×105	$\theta_y, \theta_x, \theta_z, y$	$130 \times 210 \times 40$	105×195	$\theta_y, \theta_x, \theta_z$
	G2	$390 \times 120 \times 60$	375×105	$\theta_y, \theta_x, \theta_z, y$	$160 \times 210 \times 40$	145×195	$\theta_y, \theta_x, \theta_z$
Folding mirror	FM1	$80 \times 120 \times 25$	70×105	θ_x, θ_y	$85 \times 210 \times 30$	80×195	θ_x, θ_y
	FM2	$80 \times 120 \times 25$	70×105	θ_y	$85 \times 210 \times 30$	80×195	θ_y
Roof mirror	RM1	$200 \times 40 \times 15$	190×35	θ_y	$140 \times 75 \times 24$	135×70	θ_y
	RM2	$200 \times 40 \times 15$	190×35	θ_x, θ_y	$140 \times 75 \times 24$	135×70	θ_x, θ_y
	RM3	$200 \times 40 \times 40$	$2 \cdot 190 \times 35$	θ_y	$140 \times 75 \times 75$	$2 \cdot 135 \times 75$	θ_y

Table 5.2: Dimensions of the optics in the compressors with degrees of freedom in the alignement. Dim. dimensions, Clear ap. clear aperture, Align alignment degrees.

Parameter	Unit	Regen	Cryo
$w_{0,max}$	mm	4	20
l_g	m	1.109	1.109
AOI	$^\circ$	60	60
$\tau_{in,FWHM}$	ns	2.35	0.26
$\tau_{out,FWHM}$	ps	0.650	*2.45*
$\Delta\lambda_{FWHM}$	nm	3.6	0.4

Table 5.3: Parameters of both compressors. The given pulse duration of the pulses after the cryogenically cooled amplifier is the expected one.

was limited to 3.8 GHz, corresponding to 260 ps resolution; with the sampling scope, the minimum pulse duration measurable was 140 ps. The grating separation was set up in the center of the range measuring the shortest electrical pulse duration of 140 ps. The autocorrelation was then measured with an autocorrelator with 50 ps scan range (APE PulseCheck 50) and the alignment of the compressor optimized iteratively. Further diagnosis of the proper alignment was the beam profile after the compressor: remaining spatial chirp, due to non-parallel gratings, leads to horizontal ellipticity of the beam. The angle of incidence on G1 and G2, their parallelism and the distance in-between were scanned systematically to achieved the best pulse compression.

After the regenerative amplifier, the pulse duration reaches a minimum of 615 fs, assuming a Gaussian fit and deconvolution, as shown in figure 5.14. 15% of the energy is estimated to be in the pedestals by substracting the energy in an ideal Gaussian pulse and in the real pulse. On the autocorrelation trace, there is no sign of an uncompressed background; this indication is however strongly limited by the sensitivity of the autocorrelator. The absence of an uncompressed background was double-checked with SHG of the compressed pulses. The efficiency of 45 % confirms that the main energy is located in the compressed pulse. By taking the Fourier-transform of the spectrum, the pulses from the cryogenically cooled amplifier are expected to be compressible in a similar way to 2.45 ps.

After the compressor, the beam profile is elliptical, with a ratio of ²/₃. This might originate from the inherent divergence of the beam inside the compressor competing with the angular dispersion, even if the Rayleigh length of 48 m is longer than the total compressor length. Therefore, the beam diameter at the input of the compressor has been increased by a factor of 1.5 by changing the telescope located between the regenerative amplifier

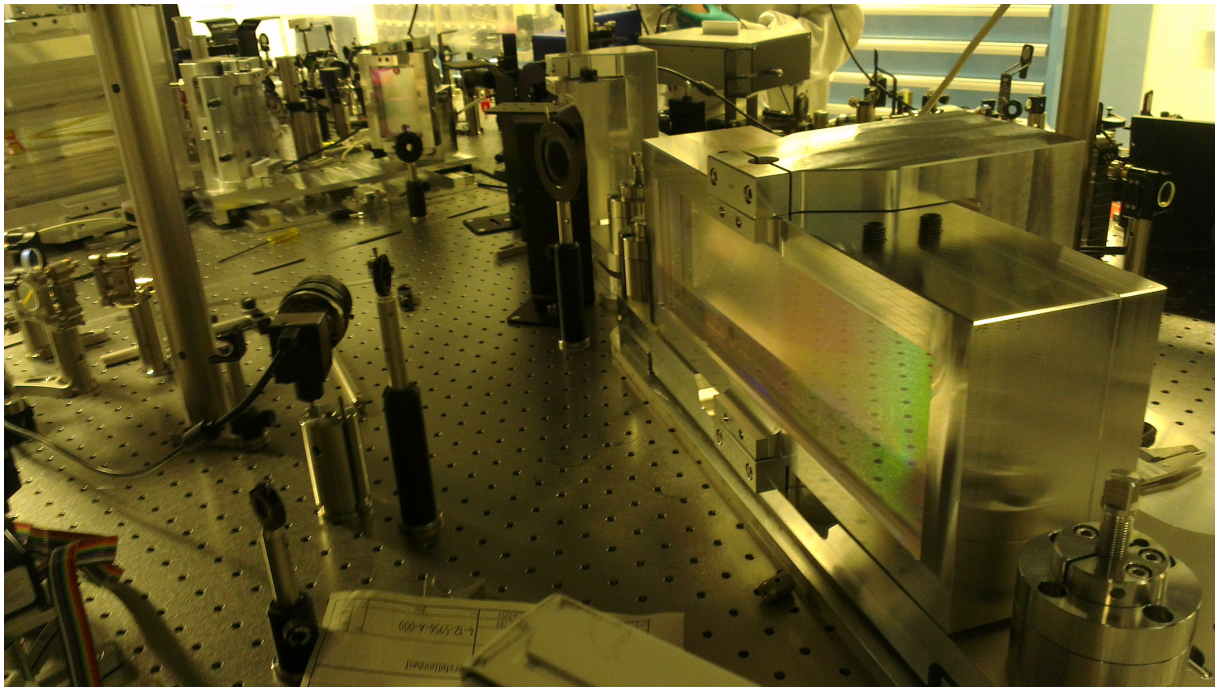

Figure 5.13: Photograph of the compressor after the regenerative amplifier: the gratings are located on the right, the roof mirror and folding mirror on the translation stage on the left.

and the compressor. The increase of the beam diameter is limited by the clear aperture of the gratings. The divergence of the collimated beam, with collimation verified with a shear-plate, has been reduced from 0.2 mrad to 0.13 mrad, however without noticeable improvement of the output beam. A cylindrical telescope with 200 mm and −150 fs sagittal focal lengths compensates for the ellipticity.

During operation over several days, some changes in the stretched spectrum, monitored with a fast photodiode at the output of the regenerative amplifier, have been correlated with variations of the compressed pulse duration. These variations were originating from temperature and humidity variations in the stretcher box. Water cooling stabilizes since partly the temperature inside the box, and nitrogen flooding controls the humidity. With a controlled environment around the fiber based stretcher, the spectral shape of the pulses and consequently the compression remain constant over time.

5.5 Summary

In this chapter, concepts for stretching and compressing the pump line pulses have been examined and compared. Their design is compatible with both versions of the Yb frequency synthesizer: the actively CEP stable one starting with a Ti:sapphire oscillator and the passively CEP stable one based on ytterbium oscillator. The implemented stretcher consists in four CFBG with two intermediate fiber amplifiers compensating for the losses. The stretching ratio of 0.65 $^{\mathrm{ns}}/_{\mathrm{nm}}$ is close to the estimated one of 0.8 $^{\mathrm{ns}}/_{\mathrm{nm}}$, meaning that the gain narrowing in the fiber amplifiers and the spectral cut in the CFBG has been

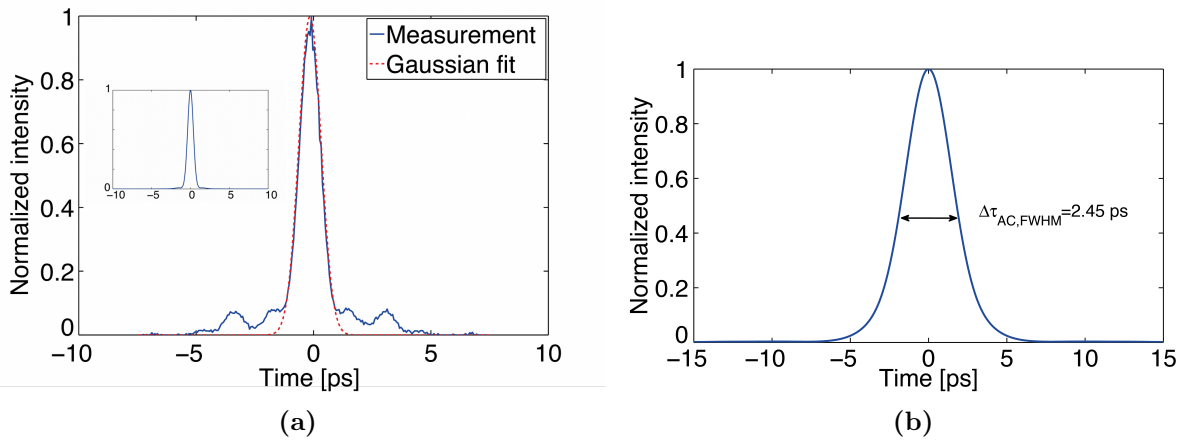

Figure 5.14: (a) Autocorrelation of the pulses compressed at the output of the regenerative amplifier and (b) expected autocorrelation at the output of the cryogenically cooled booster.

correctly estimated. The compression is achieved with a bulk grating compressor; the 1740 $^{\text{lines}}/_{\text{mm}}$ gratings are separated with a perpendicular distance of 1.109 m. The pulse compression of the regenerative amplifier output delivers pulses as short as 615 fs, close to the Fourier-transform limit of 612 fs, with ∼15% energy spread in the pedestals.

The pulses compressed after the regenerative amplifier drive the front-end presented in the next chapter and pump a first amplification stage of the CEP stable generated pulses (*cf.* chapter 7), whereas the compressed pulses from the power amplifier will be used in the future for other experiments.

6 CEP stable front-end

The intended experiments in strong-field physics driven with the Yb based waveform synthesizer depend on the strength of the electric field. The latter varies with the CEP of the single to few-cycle pulses, hence CEP stability is required.

The CEP-stable front-end, *Front-end* in figure 2.2 is based on the scheme described in section 2.2.2 and consists of a first white-light (WL) continuum stage followed by two parametric amplifiers, whose idler is CEP stable and used to generate a second white-light supercontinuum. The driver pulse of the first WL stage is here the compressed output of the regenerative amplifier described in chapters 3 and 5. Two versions of the front-end were implemented, differing in the central wavelength of the amplified spectral region of the first white-light stage: with the first one, the proof-of-principle of the CEP stability was demonstrated, and the central wavelength of the second one is located in a spectral region not amplified by the frequency synthesizer, in order to ensure a smooth and compressible phase of the later-on amplified spectra.

White-light generation (WLG) is a complexe process involving several nonlinear mechanisms and was demonstrated in previous works in bulk with pulses shorter than half a picosecond or several tens of picoseconds long; the shorter ones generate a coherent white-light whereas the longer ones lead to incoherent broadening. There was thus an uncertainty on the coherence of the WL generated with sub-picosecond pulses as in this work. The questions to answer concerns the coherence of the WL spectrum, required for generating a second WL stage with passive CEP stability, and its shot-to-shot stability, to ensure constant conditions for the second WL stage. The WLG with sub-picosecond pulses is thus experimentally investigated prior to the implementation of the CEP-stable front-end. A further numerical analysis would be necessary for an in-depth understanding of the white-light broadening.

The experimental realization of the front-end is discussed in the following sections. The first section details the white-light generation with sub-picosecond pulses and the optimization of experimental parameters. The second section describes the OPAs and the second WL stage. Finally, the reconstruction of the complete electric field of the amplified signal and the measurement of the CEP stability are presented.

6.1 White-light generation with sub-ps pulses

After the presentation of the mechanisms underlying WLG and of the state of the art, the experimental setup for the WL study is discussed. The experiments investigate the influence of the materials, of their length, and of the pump pulse duration.

6.1.1 State of the art

White-light generation in bulk materials was first demonstrated in the NIR in 1970 [151]. Extension to the mid-infrared and the visible was previously demonstrated in [152]. White-light generation in bulk is an extremely complex process and still requires a deeper understanding, even if the experimental implementation seems trivial. Several theories were developed over the last decades, and the most accepted one was proposed by Bergé in [153] and Chin in [154]. The spectral broadening results from the interplay of nonlinear effects during propagation through a medium: the driver laser is focused inside a crystal at intensities leading to strong nonlinear interactions with the material. With spectral broadening the pulse shortens in time due to self-steepening. This increases the intensity up to the level required for self-collapse of the beam in space, increasing the intensity even further: self-collapse happens when the nonlinear phase overcomes diffraction. This process ultimately results in plasma generation by freeing electrons; the plasma defocuses the beam. When the plasma defocusing compensates the self-focusing, a filament is created. This ensures a long interaction length for the formation of all spectral components. During propagation other nonlinear effects contribute to the broadening: self-steepening shortens the trailing edge of the pulse in time and leads to a broadening toward shorter wavelengths; four-wave mixing between all the frequency components contributes to the spectral broadening. The material dispersion plays an important role on the temporal overlap of the different frequencies, *i.e.* it influences the frequency mixing.

Self-focusing would lead to catastrophic damage if not stopped by the plasma defocusing of the beam. For sub-hundred femtosecond pulses this plasma is created by multiphoton excitation (MPE) [37], whereas for longer pulses it is generated by avalanche ionization [37, 155]. Pulses with picosecond duration belong to the intermediate region and stable white-light continuum was not previously demonstrated with this pulse duration. It is consequently of great interest to understand whether a stable, reproducible and smooth spectrum can be generated from these pulses and what mechanism underlies the supercontinuum generation (SCG). In the case of avalanche ionization stopping the SPM, the energy loss of the driving pulse should be noticeable and the spatial characteristics of the beam modified. In the case of MPE, a bandgap dependence of the medium on the WLG should be observed [156].

The broadening is limited on the short wavelength side by the material bandgap, as discovered by Brodeur *et al.* in 1998 [157, 158, 159]: if the ratio between the photon energy of the driving laser and the material bandgap is less than a threshold equal to 2, no supercontinuum is created. The created spectral components are absorbed instead by two-photon absorption; the generation through SPM competes with this process. As the broadening begins by the extreme wavelengths the absorption prevents any further broadening. This plays a role *e.g.* in the choice of the material for WLG and is particularly critical for WL driven in the visible. Once this condition is fulfilled, the bandwidth of the blue wing of the WL increases with the material bandgap, as demonstrated experimentally in condensed materials for a fixed driving wavelength by Nagura *et al.* [159]. The influence of the driving wavelength on the blue shifted wave and its width was studied by Smetanina *et al.* in [160]: increasing the driving wavelength leads to a blue-shift and to a narrowing of the spectrum.

The influence of the divergence of the driver laser was studied in [161]: the numerical aperture of the focusing lens is important to couple the maximum energy into the filament. The separation of both spatial beam parameters – beam diameter and divergence – is possible by introducing an iris before the focusing lens reducing the beam diameter.

WLG driven with a 2-µm laser was demonstrated in 2013 by Malevich *et al.* [162]: a Ho:YAG regenerative amplifier delivering 550 fs long 3 mJ pulses drove WLG in 8-mm long sapphire and 6-mm YAG. The spectra from the sapphire plate extended from 500 nm to more than 2.5 µm, with a strong dynamic in the spectral amplitude. For longer pulse durations, WLG was demonstrated in fibers with 60 ps [163] and 600 ps [164] long pulses. It is believed that no generation with pulse duration close to a picosecond has been previously reported. Generating WL with this pulse duration represents a challenge for finding the right parameters, between peak power and medium length: long pulses may acquire nonlinearities over the material length, such as in a fiber, however with a limitation to a few kW peak power. In the case of a pulse with duration close to a picosecond, the input and output energy of the WL is limited by the interaction length. The exact parameters to generate a stable filament in bulk, delivering several nJ output energy, will be examined carefully and reported in the following.

The filament formation is influenced by several parameters, such as the focusing of the driving beam and the peak power, as Ashcom *et al.* have reported in [161]. The peak power is the key for self-phase modulation and self-steepening leading to collapse of the beam in time and space. The critical peak power for self-focusing grows quadratically with wavelength and inversely with the refractive and nonlinear index coefficients $n_{0,mat}$, $n_{2,mat}$:

$$P_{Crit} = \alpha \frac{\lambda^2}{4\pi n_{0,mat} n_{2,mat}} \tag{6.1}$$

where α depends on the spatial distribution of the beam and equals 1.8962 for Gaussian beams. From the material parameters given in table 6.1, the critical powers for YAG (respectively sapphire) become then 1.36 MW (3.26 MW) for 1 µm wavelength and 0.22 MW (0.68 MW) for 515 nm wavelength.

	λ	n_0	n_2	E_{gap}	ZDW
	nm	[]	10^{-16}cm^2/W	eV	nm
YAG	1030	1.8153	6.5	6.3	1.6
YAG	515	1.84	10	6.3	1.6
Sapphire	1030	1.7552	3.06	9.9	1.315
Sapphire	515	1.7731	3.3	9.9	1.315

Table 6.1: Comparison of the material parameters important for WLG, from [165, 166, 167, 168, 169, 97].

The ratio between peak power and critical power for self-focusing has been mentioned in [158, 155] to characterize the operating piont. Kandidov *et al.* report a ratio P_{peak}/P_{crit} of ∼5 [170]. The same group reported a ratio close to 1 for SCG in transparent condensed media in [155]. The parameters of these experiments are close to the ones of this study.

The optimum experimental parameters for WLG with sub-picosecond pulses such as the ratio P_{peak}/P_{crit} are determined in this experimental study. Its setup is presented in the following sections, then the results obtained for 1030 nm and 515 nm driven WL are

described. Parameters to optimize during SCG are the reproducibility of the spectrum and the stability of the energy of the supercontinuum from shot to shot and over a long operation time. A detailed study of WL continuum with long pulse duration is thus performed, in which pulse duration, material and central wavelength are varied.

The complexity of the WLG process raises the question of the compressibility of the pulses, *i.e.* of the behaviour of their phase, and of their coherence. The experiment of Bellini *et al.* in 2000 with 100 fs long pulses from a Ti:sapphire laser demonstrates that the supercontinua generated by two phase-locked lasers are coherent and that random phase jitter is negligible [171]. The phase of super-continua was characterized in [159], but for shorter driver pulses.

6.1.2 Experimental setup

The experimental setup of the WLG study, shown in figure 6.1, is composed of a telescope to demagnify the incoming beam (*Tel* in the figure), of the setup for white-light generation itself, including a focusing lens (*L*) and a crystal for WLG (*X1*) and of the diagnostics setup. Be fore the focusing lens a variable attenuator is used to vary the intensity at the crystal entrance. The numerical aperture at the entrance of the filament is varied with a set of BK7 lenses with focal lengths ranging from 50 mm to 200 mm. An iris (not shown) located before the focusing lens allows a slight change of the input beam diameter, hence of the focused beam diameter, as described in [161]. This variation is kept to the minimum to avoid diffraction effects in the focus.

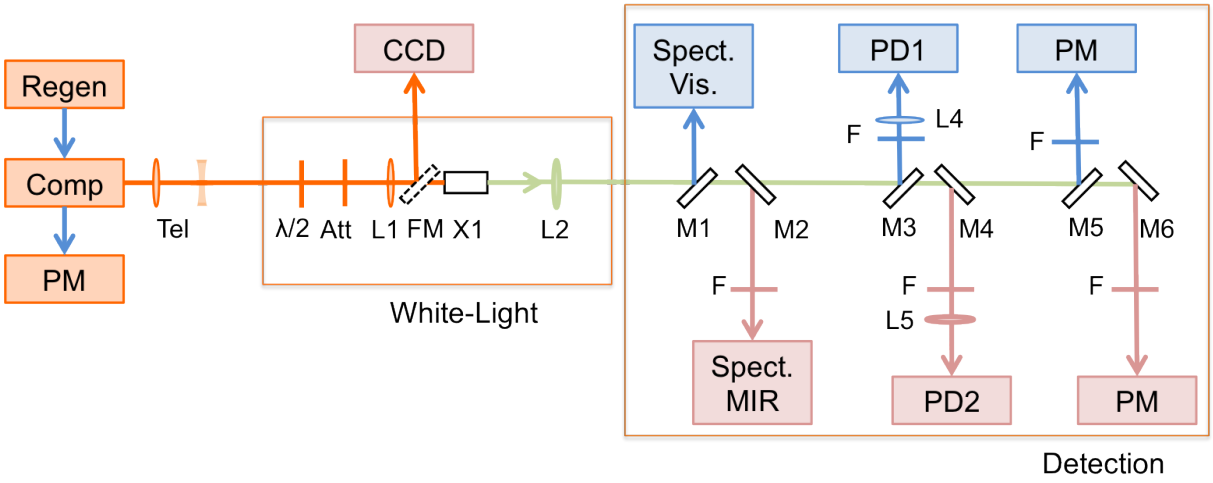

Figure 6.1: Layout of the experimental setup of the white-light generation study. *SHG* stands for second-harmonic stage, *L1-L4* focusing and collimating lenses, *I* iris, $\lambda/2$ half-waveplate, *Att* attenuator, *WLXtal* WL crystal, *PD1-PD2* photodiodes, *PM* powermeters, and *Spect. Vis.* and *Spect. MIR* spectrometers for visible and MIR. Filter sets cut the pump wavelength to avoid saturation of the detectors.

For the measurements of the WL generated with 515 nm driving wavelength, a supplementary SHG stage (*SHG*) is added after the compressor. The SH is generated with a 1.5 mm long BBO crystal and 3 separators, which are high reflectors for 515 nm and

anti-reflectors for the fundamental wavelength, isolate the frequency doubled pulses from the fundamental ones. The energy after the SHG stage was 1 mJ, from which only a few µJ were used for this experiment.

The diagnostics setup needs to cover the broadest possible wavelength region, ideally from the visible to the mid-infrared. For this reason, two spectrometers and two photodiodes were employed: the detection in the visible was performed with an HR4000 spectrometer from OceanOptics covering the range from 200 nm to 1100 nm and with an InGaAs photodiode EOT4000; in the IR, the spectrometer used was a NIRQuest 256 from OceanOptics ranging from 1100 nm to 2500 nm and a detector Det10D/M from Thorlabs. A set of filters cut the fundamental spectrum before the detection with photodiodes as well as in the measurement with the IR spectrometer. In the visible, the spectrometer was saturated at the pump wavelength, because the saturation induces an artificial broadening toward the red. This has the advantage of resolving the supercontinuum without introducing the ripples of short or long pass filters. The filtering of the pump before the IR spectrometer was necessary to avoid the saturation of the instrument, but reduced the signal level of the continuum and prevented to record the whole broadened spectrum.

The materials for WLG used in this study are YAG with 6 and 10 mm length, sapphire with 6 mm length and CaF_2 with a thickness of 6.35 mm. As sapphire is birefringent, the broadening depends on the orientation of the polarization with respect to the crystallographic axes and a half-waveplate is added in the input beam path to rotate the polarization. The intensities are calculated in the focii, taking into account the Fresnel losses for an angle of incidence of 0° on the crystals.

The criterion for the optimization is the generation of the broadest spectra with less than 5% fluctuations in the two spectral regions below and above the pump wavelength. The filters used to cut the pump determine the lower and upper wavelength regions. During the formation of the blue wing, third harmonic is generated, which mixes with the input beam via four-wave mixing to extend the broadening toward the driver pulse; the THG is a decisive step in the WLG, even though its efficiency remains as low as 10^{-6} to 10^{-4} [172]. The wavelengths of the broadened wing which exhibits a smooth spectrum and is closest to the driving pulse are generated last. Directly around the driver pulse self-phase modulation broadens the spectrum. In these experiments, this broadening around the driver extended maximum to 200 GHz bandwidth. The WL spectrum shows thus a dip with low spectral density and it is convenient to define the lower spectral region up to this wavelength. In the following measurements this dip was located at 900 nm.

In the analysis, the response function of the filters, lens coatings, silver mirrors and powermeters have been taken into account to rescale the energies and the spectra.

A measurement with one configuration (10 mm YAG-crystal and 100 mm focal length lens) has been repeated 10 times for the calculation of the error bars. During each measurement, the lens was removed and the incoming beam misaligned; realigning the WL shows then the influence and reproducibility of the position of the lens and the angle of incidence on the crystal. The error is calculated from the standard deviation σ with the formula: $Err = \sigma/\sqrt{N}$, N being the number of measurements. The measurement of the beam diameter in the focus of the lens with the CCD is not limited by the resolution of the camera and had a precision of less than 1 µm. For further analysis, the contribution

of each term in the expression of the intensity, peak power, and fluence (input power, beam diameter) is taken into account with the geometrical mean.

6.1.3 Influence of material

This section will compare first the results obtained for 1030 nm driven WL with 6-mm long sapphire and YAG crystals, then focus on the differences in the continuum for 6 mm and 10 mm long YAG crystals. These thicknesses and crystals corresponded to the best results obtained for different focusing conditions. At the end, the results obtained with a 515 nm driving laser will be presented.

The first measurement set was acquired by varying the WLG crystal and its thickness. The setup was optimized for each crystal: the focusing lens was exchanged, its position varied and the variable attenuator adjusted to find the optimum numerical aperture, start position of the filament and intensity.

Comparison of the materials: sapphire and YAG

Stable WL supercontinuum is generated at 1030 nm with all three materials. The WLG induced in CaF_2 crystal led to rapid degradation of the crystal; techniques such as rotating or moving the CaF_2 plate are well developed, but lead to disturbances on the pulses. For the application in a CEP-stable front-end, this is not suitable and CaF_2 was discarded. The setup with a 100 mm focusing lens, the 10 mm long YAG and 2.7 mm input beam diameter presented the lowest sensitivity to experimental variations such as crystal position and intensity.

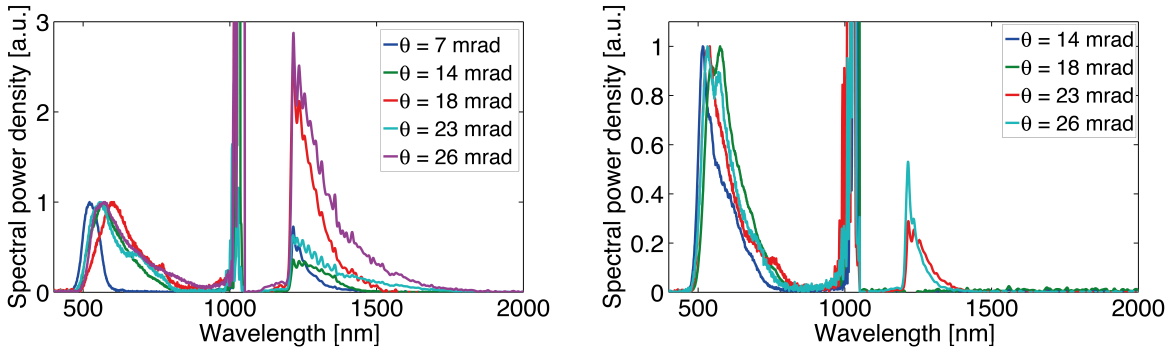

Figure 6.2: Spectra of the white-light supercontinua obtained with (a) 6 mm YAG and (b) 6 mm sapphire under different focusing conditions.

Figure 6.2 shows the measured spectra for the 6-mm long YAG and sapphire crystals, rescaled so that the area corresponds to the measured energy for the blue and red shifted waves. The normalization of the spectra is performed for the blue wing, to clearly show the change in spectral density between both spectral domains with the different configurations.

Figure 6.3 shows the evolution of the FWHM spectral width with the focal length, whereas figure 6.4 displays the evolution of the power vs. intensity and normalized peak

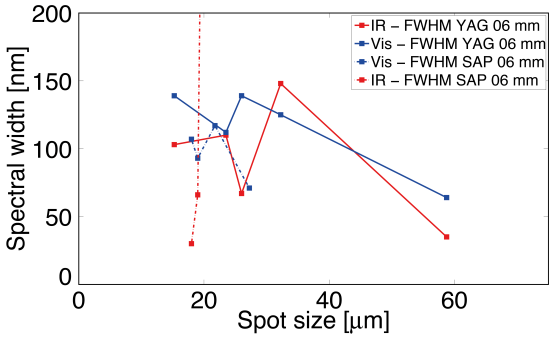

Figure 6.3: Spectral width of the blue and red waves of the supercontinua obtained with 6 mm YAG and 6 mm sapphire. The full spectral width is taken at 5% from the maximum amplitude of each wing.

power. In all graphs showing the characteristics of both blue and red broadened waves, the IR power is shown with the red line, the visible one with the blue line.

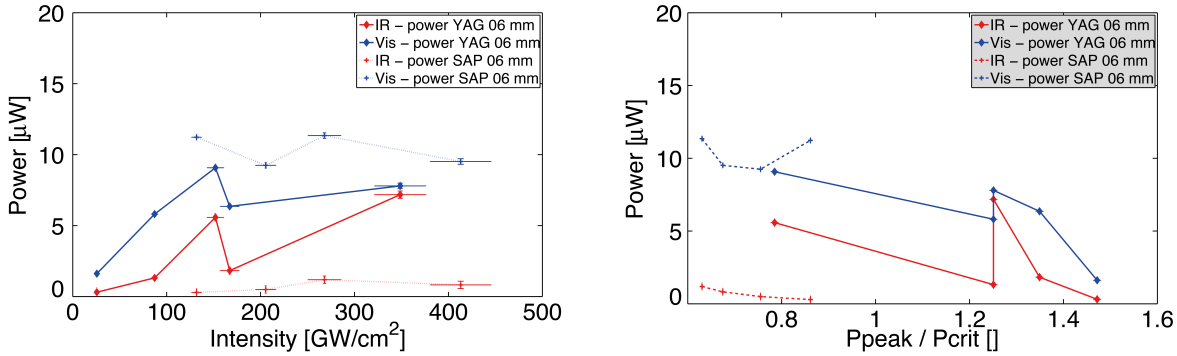

(a) **(b)**

Figure 6.4: Power contained in the blue wing and red wing of the supercontinua, vs. intensity (a) and normalized peak power (b) of the input beam.

The intensity in the focus of the crystal is here calculated with the diameter of the collimated input beam in x and y, propagated with ABCD formulas through the focusing lens and with the measured distance between the center of the thin lens and the surface of the crystal. The precision of the distance measurement is taken into account in the calculation of the error bars of the intensity. The super-continuum is generated for peak powers close to the critical power, which is in agreement with previous observations [173].

One can see a trend on these graphs in the broadening of the driving pulses: the power is slightly lower in the visible, but higher in the IR with YAG than with sapphire. The broadening in sapphire is difficult to extend towards the IR, and even not measurable with this experimental setup in the configurations with the 75 mm and 100 mm lenses, corresponding to divergences of 14 mrad and 18 mrad, the energy of the red broadened wave being below the sensitivity of the detection apparatus. The power measured in the filaments created in YAG or sapphire is similar in the visible region but differs in the

IR. This different behavior, which was also reported in [173], might originate from a too short filament in the 6 mm long sapphire compared with the 6 mm long YAG crystals, considering the long pulse duration, and narrow-band input spectrum, of the driving laser. In case of sapphire no broadening is observed for the largest spot sizes: in this case the focusing was probably too loose to start accumulating nonlinearities via self-phase modulation and to shorten the pulse in time with self-steepening.

The conversion efficiency from the driving laser into the supercontinuum is less than 5%. This is an indication that avalanche ionization is probably not the ionization mechanism, but multi-photon ionization [154].

Influence of the material length: case of YAG

Figure 6.5 shows the spectra obtained for the 10 mm long YAG. In a similar way as in the previous section, figure 6.6 and 6.7 show the evolution of the spectral bandwidth and of the power of the red and blue broadened waves vs. intensity and peak power, comparing the 6 mm and 10 mm long YAG crystals.

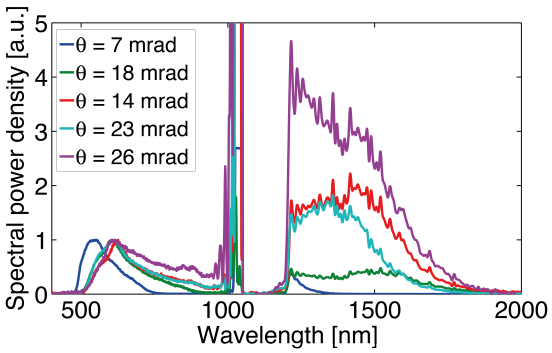

Figure 6.5: Spectra of the white-light supercontinua obtained with 10 mm YAG for different focusing conditions of the driver pulses.

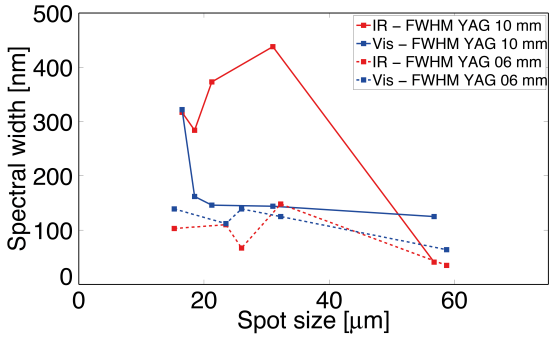

Figure 6.6: Spectral width of the blue and red waves of the supercontinua obtained with 6 mm and 10 mm YAG.

With the short YAG crystal of 6 mm, the IR power is lower than with the longer YAG crystal. The spectral width of the filaments created in the 6 and 10 mm long YAG crystals

can be compared in a similar way: the spectral width achievable from the longer crystal is constant over the different experimental configurations, but varies strongly in the case of the shorter crystal.

The spectra obtained with both the 6 mm and 10 mm YAG crystals are narrower in the configuration with the smallest spot size than with larger spot sizes. The powers contained into both IR and visible wings seem to increase with the intensity and to decrease with the peak power in the case of the shorter crystal, which is related to the accumulation of nonlinearities along propagation in the material.

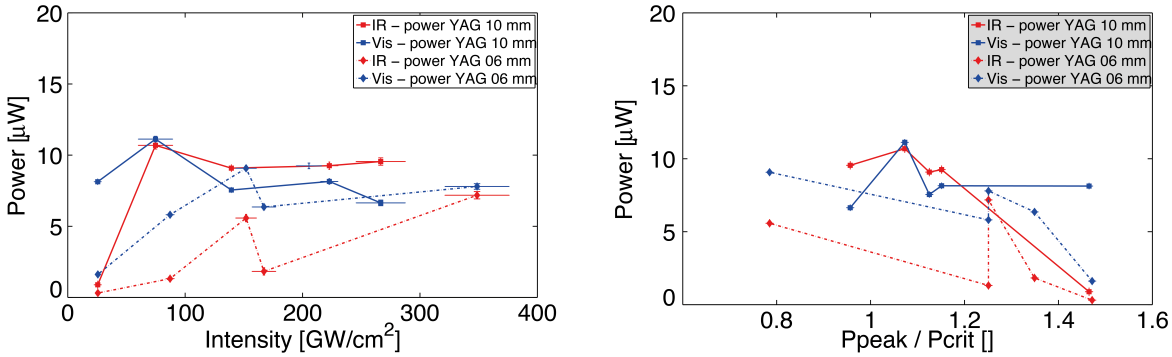

Figure 6.7: Power contained in the blue wing and red wing of the supercontinua, vs. intensity (a) and normalized peak power (b) of the input beam for 6 and 10 mm YAG crystals.

This might correspond to a saturated and a transient filament in the 10 mm YAG crystal and in the 6 mm YAG or sapphire crystals, respectively. A long crystal and a loose focus care for accumulating nonlinearities over the propagation length, generating new spectral components around the input spectrum and shortening the pulse in time.

Observations on the spatial profile of the filament

For the long YAG crystal, two domains of WLG exist with the following, different characteristics depending on the lens position. If one progressively increases the distance between lens and crystal, *i.e.* the crystal is shifted through the focus, a filament appears, then splits up, then another, stable filament forms. In the first filament the broadening is mainly toward the visible; neither the IR power nor the IR spectrum are measurable with this detection setup.

The second filament extends significantly further, from the visible to the mid-IR. The root-mean-square (rms) stability is different in both domains: a low amplitude noise in the lower wavelength region is typically obtained in the first configuration, whereas the long wavelength part is usually optimized to reach a low noise in the second domain. The minimization of amplitude fluctuations for both spectral regions simultaneously is only possible in the second filament position, however the complexity of the alignment and its robustness against external influences are greatly depending on the exact experimental parameters (lens, E_P).

Both filaments present further distinguishable characteristics: in the first domain, the edges of the filament are visually extremely sharp, without halo, and the filament presented a low divergence. In the second one, the divergence increases, and a halo appears, containing nearly all the spectral components present in the filament, the IR being proportionally stronger.

The exact behavior of the filament between both domains strongly depends on the exact focusing conditions and input energy: either the transition between both domains is smooth, or there might be a transition with multi-filamentation. The behavior of the divergence of the filament can be explained by the guiding of the filament over different lengths: the first domain corresponds to a focus position further inside the crystal than in the case of the second domain [155]. This matches the observation that the continuum is starting very close to the surface of the crystal in the case of a 6 mm crystal; the focusing of the input beam onto the surface during the optimization of the alignment repeatedly led to damages of the crystal in this configuration.

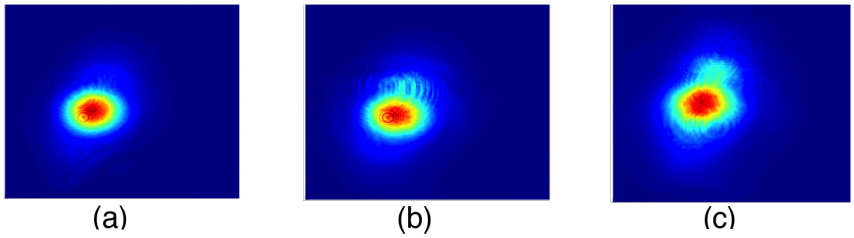

Figure 6.8: CCD acquisition of the driving beam for three energies: (a) below threshold of WLG, (b) at threshold, and (c) when the filament is well-established.

The pump profile is measured with a CCD camera after the crystal, with and without the filament, as shown in figure 6.8. There is a clear change in the beam profile. The filament is here filtered out to isolate the pump. When the filament appears, the beam profile of the infrared beam is modified and a weak side-lobe appears, at the same position than the filament. A change in the beam profile is typically correlated with an avalanche process of the ionization [155].

As avalanche ionization typically starts from a defect in the crystal, the crystal has been translated transversally to the propagation direction : this verified that this change is actually independent of the beam position on the crystal. A possible explanation of the change in the beam profile might then be the influence on the filament formation of the spatial characteristics of the beam, which is slightly astigmatic.

Results for 515 nm driving pulses

For a pump wavelength of 515 nm, broadening has also been observed. The broadening is limited toward the UV by the absorption edge of the material. The spectra obtained with compressed pulses, 450 fs long after doubling, are shown in figure 6.9.

Strongly different behaviors have been observed in both cases. In the case of 515 nm central pump wavelength, spectral broadening could be obtained with the YAG and sapphire crystals, but only for a limited range of focusing conditions, indicated in figure 6.9. The broadening was significant with CaF_2, but the crystal degraded immediately. This

different behavior is due to the material bandgap, as explained in [157]: for CaF_2, the absorption edge is lower than for sapphire and YAG. In the WLG process, the extreme wavelengths are generated first and their absorption prevents the spectrum to broaden towards the pump wavelength. A strong absorption in the UV leads to damages of the material.

During the spectral measurements of white-light driven with 515 nm or 1030 nm pulses, a bandgap dependency of the blue-shifted spectrum was noticeable. This dependency on the material bandgap is a sign of multi-photon excitation intervening in the filamentation process.

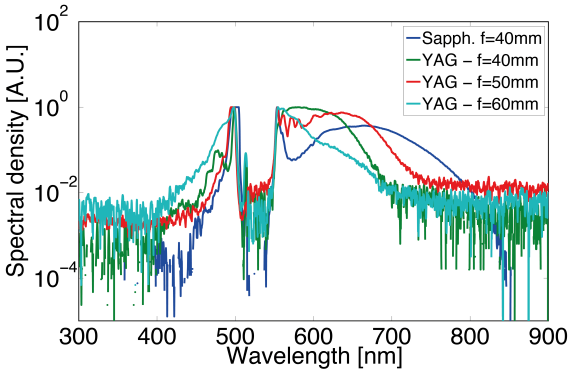

Figure 6.9: Spectra obtained with 515 nm driving wavelength. The two materials are 6 mm sapphire and 6 mm YAG crystals. Three focusing configurations lead to a spectral broadening in YAG.

6.1.4 Influence of pulse duration

After studying the influence of the material on the white-light continuum the influence of the pulse duration has been investigated in two ways: first by changing the compression of the driving pulses, second by narrowing down their spectrum.

For this set of measurements the setup chosen after trying different lenses was the 10 mm long YAG crystal with a lens of 75 mm focal length. The distance between the two gratings of the compressor was changed to vary the pulse duration, while keeping the full spectrum delivered by the regenerative amplifier. The pulse duration was monitored with a PulseCheck50 autocorrelator from APE. The autocorrelation was fitted with Matlab with a Gaussian pulse shape to obtain the pulse duration. The pulse durations were varied between 615 fs, 1030 fs and 1070 fs corresponding to the compressed, and most positively and negatively chirped pulses, respectively.

Figure 6.10 shows the obtained spectra, spectral width and power of the blue and red broadened waves. The shape of the spectra remained similar for all measurements. The power however tends to depend on the pulse duration: the power in the visible domain increases slightly for long pulses, either positively or negatively chirped, whereas the one in the IR tends to decrease. The minimum fluctuations are obtained with the shortest, transform-limited pulse duration. The spectral width remains constant for negatively chirped pulses, but tends to decrease in the visible for positively chirped pulses.

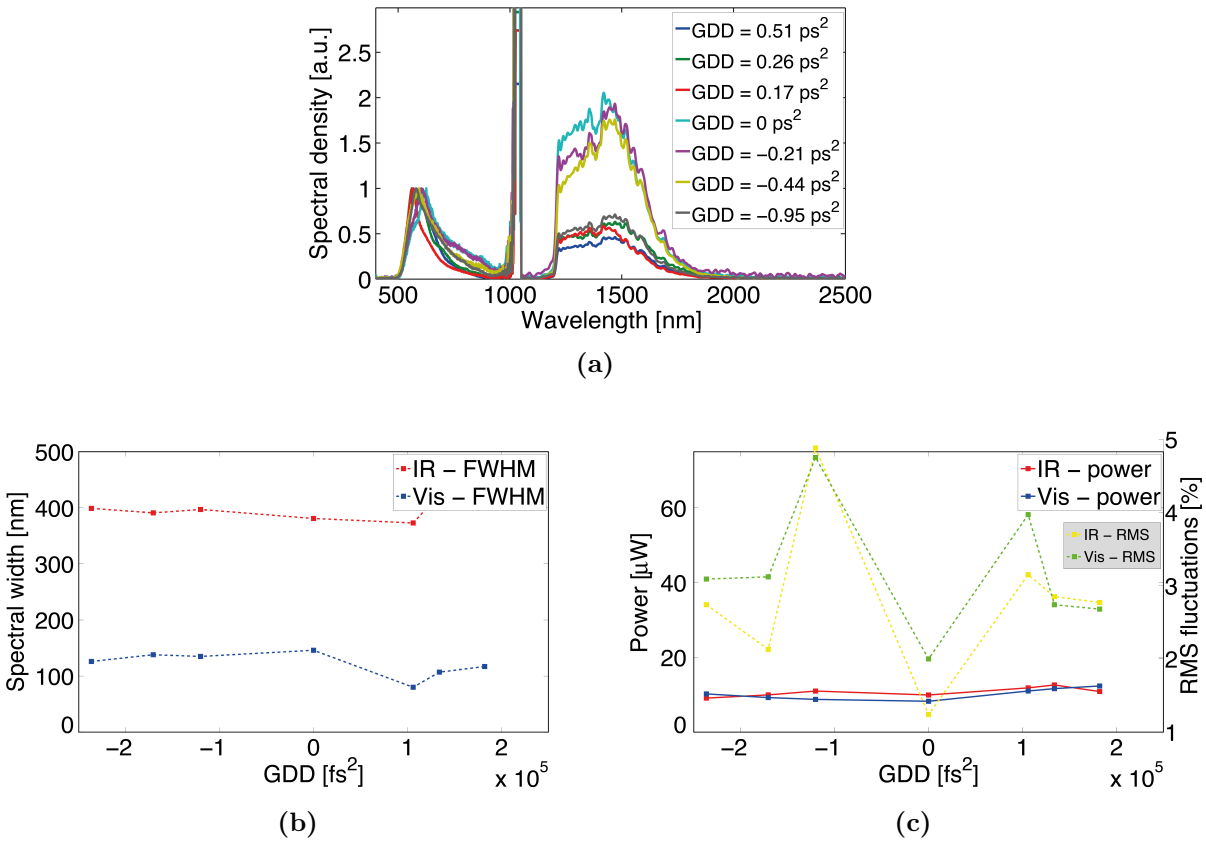

Figure 6.10: Influence of the chirp on the supercontinuum generation. The spectra are plotted in (a), the evolution of the spectral width in (b) and the power and rms stability as a function of group delay dispersion in (c). In (c), the solid lines show the power evolution whereas the dashed curve displays the rms stability.

The WL obtained with transform limited pulse durations is more robust against environmental disturbances than the one obtained with stretched pulses. This might be compensated with a longer crystal to saturate the filament generated with longer pulses, in a way similar to the demonstration in the previous section showing the scaling from more traditional, few 100 fs long pulses to sub-picosecond pulses.

When the pulse duration was increased while keeping the pulses transform-limited, a similar trend was observed, as shown in figure 6.15: The spectral shape remains similar, the power in the visible tends to decrease while the IR one increases slightly. The filament was however difficult to stabilize for narrowband, long pulses, and a longer crystal would probably have been necessary to reach saturation. This is correlated with the increase of the rms fluctuations with the narrowing of the spectral width. This behaviour differs from the one of the filament generated with ∼100 fs long pulses, where a pre-chirp helps to increase the spectral width and stability: the pulses are effectively compressed during propagation in the material, which increases the accumulation of nonlinearities at the beginning of the filament formation. In the case of sub-picosecond pulses though, the

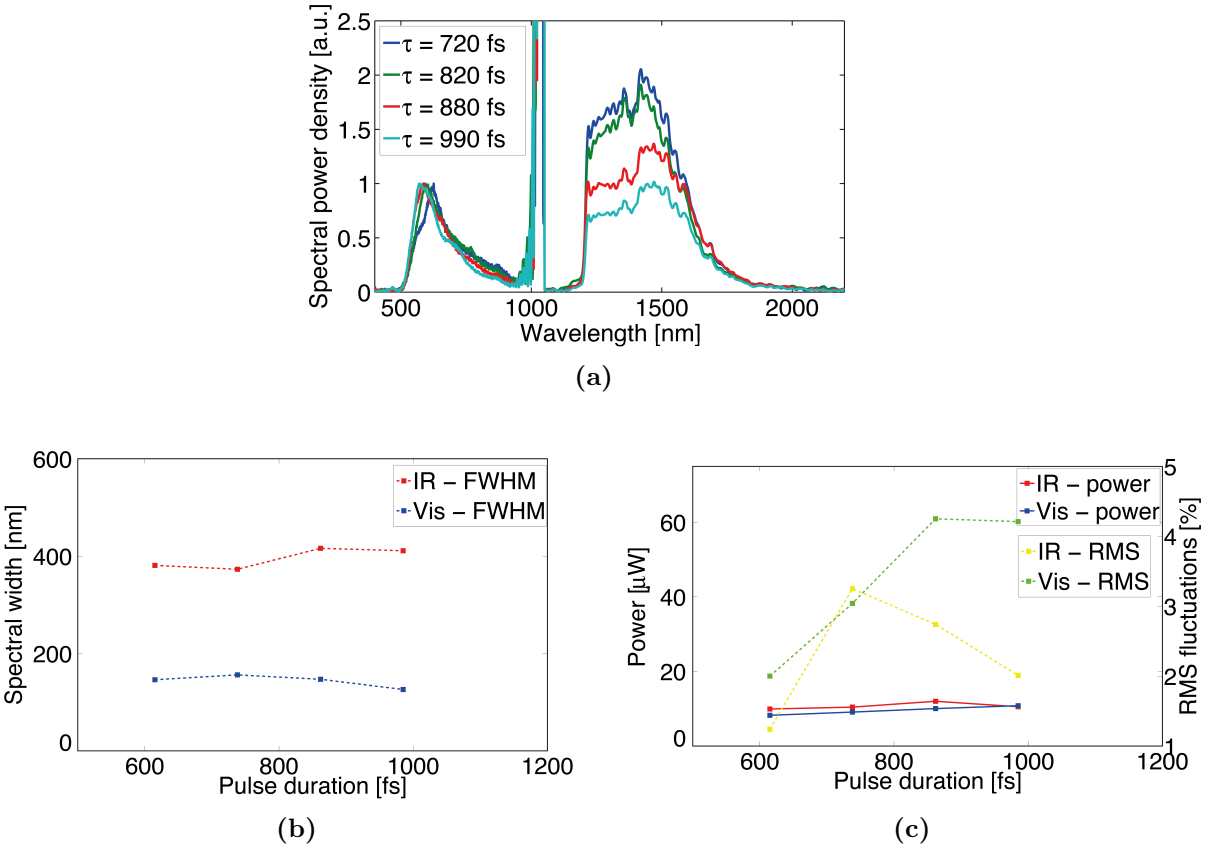

Figure 6.11: Influence of the transform-limited pulse duration on the supercontinuum generation. The spectra are plotted in (a), the evolution of the spectral width in (b), and the power and rms stability vs. transform limited pulse duration in (c). In (c) the solid lines show the power evolution whereas the dashed curve displays the rms stability.

dispersion of the material is not high enough to change significantly the pulse duration over the relatively short propagation length.

In this study with narrower spectra and transform limited pulses, a narrowing of the bluest wing is observed, in a way similar to the previous case with stretched driver pulses. The red spectral wing tends to broaden slightly.

From this study, the best parameters to generate a stable, broadband white-light supercontinuum correspond to an intensity of $\sim 8\ ^{\mathrm{GW}}/_{\mathrm{cm}^2}$, a numerical aperture of 0.015 with the 100 mm focal length lens and compressed pump pulses. The rest of the front-end for the frequency synthesizer is now described and builds on this WL stage.

6.2 Two-stage amplification and CEP-stable WLG

Two parametric amplification stages amplify a narrow spectral band of the optimized first WL stage; the spectral bandwidth corresponds to <100 fs pulse duration. This is

important for the stability of the second WL stage. To demonstrate the CEP stability, the OPAs have first been tuned to amplify at 2 µm, then at 2.45 µm. The results at 2 µm, previously published in [174], are detailed in this section. As the phase around the driver is not well-preserved during supercontinuum generation and cannot be amplified for frequency synthesis, tuning the OPA from nearly degenerated 2 µm to 1.7 µm was necessary. This way, the spectral domain around the central frequency of the driving pulses for the second WL stage is not included in the spectral regions amplified in each parallel channel of the waveform synthesizer.

Figure 6.12 describes the experimental layout of the front-end including the interferometric measurement of the CEP stability. From the high-energy Yb:KYW regenerative amplifier, a minor portion of 0.65 mJ energy is used in the front-end. After the generation of white-light with sub-picosecond pulses, optimized with µJ input energy, 10 mm YAG, two quasi-degenerate OPA stages amplify a spectral bandwidth of 200 nm centered at 2.18 µm to 7 µJ. Experimentally the optimum length of the BBO crystals (X2 and X3) is found to be 6 mm and 5 mm. The passive CEP stable idler of the second OPA, centered at 1.96 µm, is then used to generate white-light in a 3 mm long YAG crystal (X4).

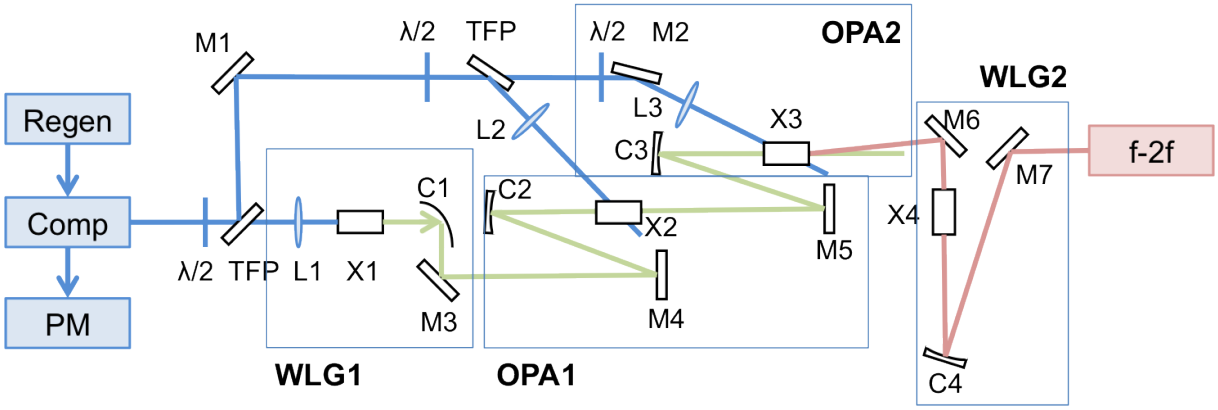

Figure 6.12: Layout of the experimental setup of the front end, consisting of two white-light generation stages WLG1 and WLG2, OPAs and f-2f measurement. TFP stands for thin-film polarizer, M1-M7 flat mirrors (dielectric high reflectors for the pump and silver mirrors for the broadband pulses), X1-X4 nonlinear crystals, L1-L6 focusing and collimating lenses, $\lambda/2$ half-waveplate, Att attenuator, Spect. spectrometer, D1 dichroic mirror, and BS beam combiner. L1-L3 are focusing lenses for the 1 µm beams, respectively, whereas the broadband pulses are collimated and focused with the parabolic mirror C1 and curved mirrors C2-C4.

In this configuration the pulse-to-pulse fluctuations of the second WLG are 3.4% and 2.8% for the spectral regions below and above the driver wavelength, respectively. The spectra of the signal and idler after the second OPA stage are shown in figure 6.13. The signal is centered at 2178 nm with 210 nm spectral bandwidth (FWHM), while the idler spectrum has 153 nm bandwidth centered at 1956 nm, corresponding to 26 fs transform limited pulses.

The amplitude fluctuations of the signal after the second OPA are measured to be less than 2% rms, enabling stable WLG. The second WLG stage is driven by 7 µJ pump

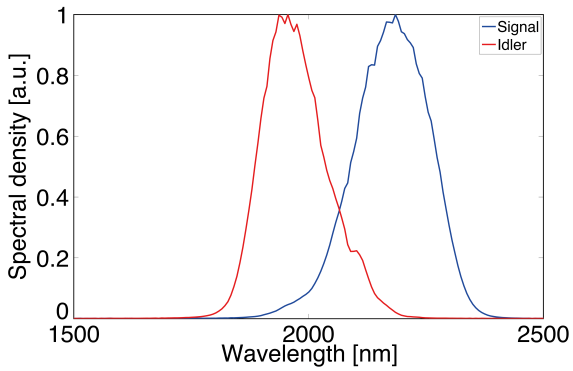

Figure 6.13: Spectra of the signal and idler out of the second OPA in the front-end.

pulses. The pulse duration has been estimated to be 43 fs at the entrance of the second WL stage: this estimation assumes that the WL is formed close to the entrance of the crystal, and that the pulse is stretched by the material dispersion. No stretching has been used to match the signal and pump duration in the OPAs, explaining the low efficiency of the parametric amplification. Matching the durations would have required 4700 fs^2 second-order dispersion; at 2 µm central wavelength, this represents a high dispersion, reachable either with extremely long propagation through material, or more conveniently for example with a prism pair. The losses would have reduced the seed energy for the first OPA, yet superfluorescence appears at too low power density of the signal. The stretched pulses should have been recompressed before WLG, for example with DCMs.

In the WL spectrum generated with 2 µm driving pulses shown in figure 6.14, the broadband minimum between the anti-Stokes spectrum and the driving wavelength results from destructive interferences, as demonstrated in [160]. Even though the spectral density is low in this spectral region and not visible on a linear scale, it is sufficient to seed an OPA stage.

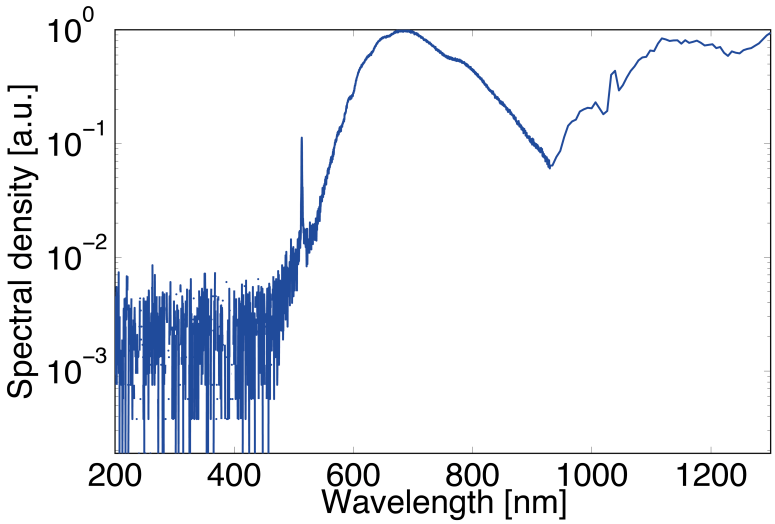

Figure 6.14: Spectrum of the CEP-stable white-light, generated with the 1.956 µm centered idler in 3 mm YAG represented on logarithmic scale.

The disadvantage of a nearly degenerate OPA stage is that the driver pulses of the CEP stable WLG overlap with the MIR amplification region of the waveform synthesizer. By shifting the central wavelength of the signal of the BBO-based OPA at 1.7 µm, the idler is generated at 2.48 µm, which is then frequency doubled to 1.24 µm. The idler wavelength is thus located at a local maximum of the transmission of BBO: the absorption is minimized at this wavelength compared with 2.45 µm or 2.5 µm. 1.27 µm corresponds experimentally to the easiest reachable wavelength to drive the CEP-stable WL. Ideally though, the driver would be located between 1.4 µm and 1.6 µm, because the 515 nm pumped noncollinear OPA and the 1030 nm pumped degenerate OPA are computed to extend respectively up to 1150 nm and down to 1.8 µm. This might be achieved with KTP or $LiNbO_3$ based OPAs, but is out of the scope of this thesis, as the results with 2.45 µm presented below are fulfilling the requirements for the front-end.

The shift of the OPA signal to 2.4 µm has been implemented experimentally. Two filters were needed to suppress the remaining fundamental at 2.45 µm. With only one filter, cutting 85% of the fundamental, the remaining 2.45 µm pulses competed with the 1.25 µm second-harmonic, leading to a WL with >4% noise. The spectra of the signal, idler and its second harmonic are shown in figure 6.15a and the spectrum of the blue-shifted wing of the white-light in figure 6.15b. The 35 nm wide signal pulses centered at 1758 nm have a transform-limit duration of 93 fs assuming a $sech^2$ fit. The corresponding idler pulses are centered at 2457 nm and 55 nm wide, corresponding to 115 fs assuming a $sech^2$ fit.

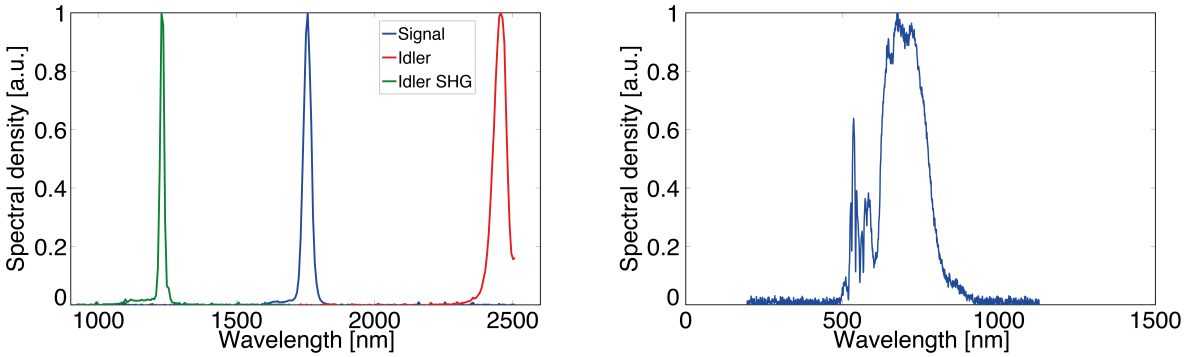

Figure 6.15: (a) Spectra of the signal centered at 1.7 µm (blue curve) and the corresponding idler at 2.4 µm (red curve). The SHG of the idler (green curve) is obtained by conversion in a 3 mm long BBO crystal. (b) Spectrum of the visible broadening of the WL generated by the frequency doubled idler in 6 mm YAG. As the idler is passively CEP stable, its SHG and the generated WL are CEP stable, too.

An uncertainty remains whether the spectral phase of the super-continuum is continuous or shows jumps which would prevent compression to transform-limit of the spectrum. This uncertainty arises with the use of long driving pulses for the first WLG. A knowledge of the pulses including spectrum, electric field, spectral and temporal phases is then required to

remove it. The low energy of the generated white-light makes this measurement difficult without prior amplification of the spectrum. For this reason, the amplified signal of the second OPA of the front-end was measured, even though its spectrum is only 35 nm wide.

The signal pulse characteristics were measured with second-harmonic frequency resolved optical gating (SH-FROG). The FROG setup is similar as the one of an intensity autocorrelator [175], but the spectrum of the sum-frequency between the delayed pulses is measured versus the delay [176].

The results are shown in figure 6.16. The retrieved 33.2 nm wide pulses are 197 fs long. The measured spectrum and the reconstructed one agree very well with each other after marginals correction. The spectral phase is well-behaved and compressible. The Fourier-transform of the measured spectrum is 53 fs long.

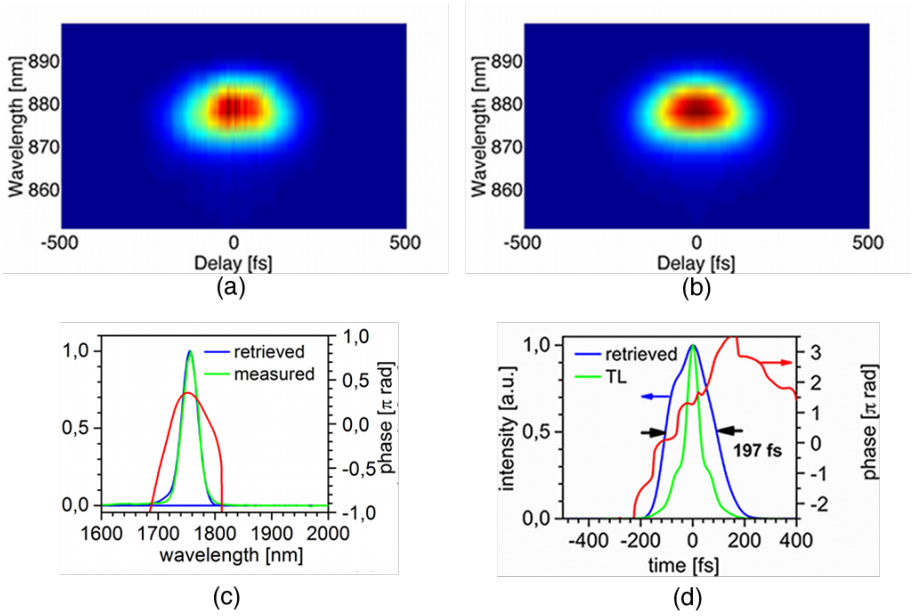

Figure 6.16: FROG measurement of the signal pulses after the second OPA in the front-end. The measured (a) and retrieved (b) traces are shown in the first row and the retrived spectral (c) and intensity (d) profiles in the second row. In (c), the retrieved spectrum is the blue line and the measured one the green line. The phases are displayed in red.

6.3 CEP stability

In a passively CEP-stable front-end, the pulse generating white-light (WL) and the pump pulse for the OPA have to originate from the same pulse to cancel the component of the CEP varying from pulse to pulse (*cf.* chapter2.2.1). This is realized in this setup and the CEP stability is verified.

The CEP stability of the 2 µm driven WL was confirmed by interfering the fundamental spectrum at 960 nm with the SHG of the remaining idler in an f-2f setup. Figure 6.17 shows the CEP stability over more than 11 h. This measurement was taken for the WL generated with 2 µm idler.

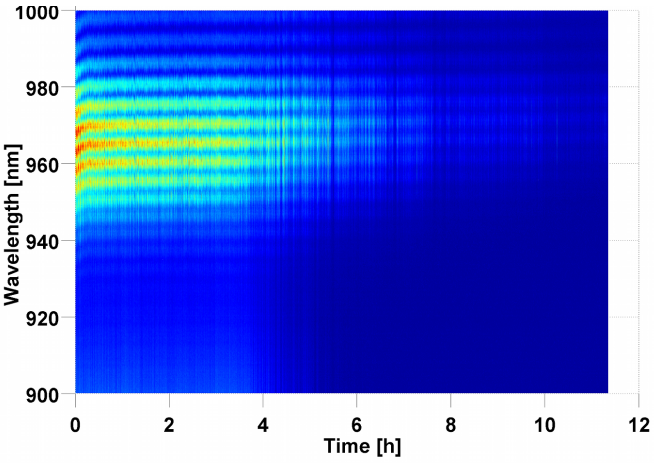

(a) f-2f measurement

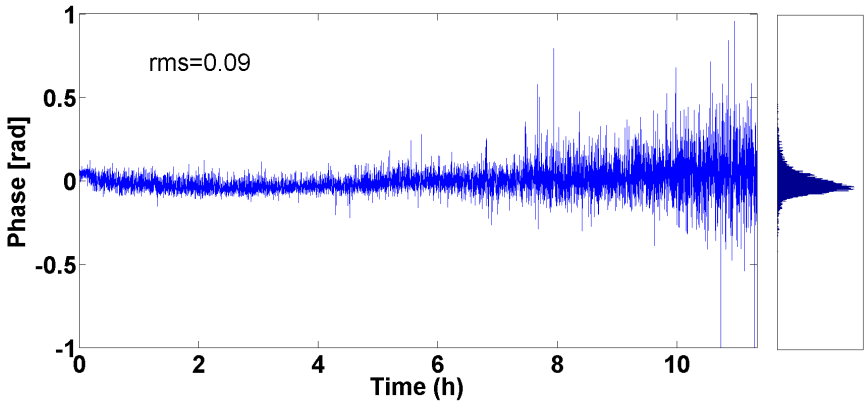

(b) Data analysis

Figure 6.17: CEP stability measured with f-2f setup over 11 h (a) and its analysis to extract the phase (b). The variations of the CEP are better than 90 µrad measured over 11 h. The total acquisition lasted 11h, with a spectrum taken every 5 s by averaging the spectrometer signal over 100 ms. The fringes faded away with the pointing drift of the driving laser caused by the environmental changes.

The fringed spectrum was acquired with the spectrometer HR4000 from OceanOptics with 10 ms integration time every 10 s. The spectral position of the fringes reflects the change in the CEP: if the CEP is stable, then the fringes remain constant from shot to shot. Some tests on the f-2f interferometer confirmed the correctness of this measurement: *e.g.*, the fringes widened spectrally and disappeared with a non-zero delay in both arms of the interferometer; they shifted with the phase-matching angle of the BBO which changed the central wavelength of the SHG; the contrast decreased when rotating the polarisation in one of the interferometer's arm.

The fringes slowly drifted away during the acquisition because of the pointing drift of the driving laser; this can be stabilized with a slow feedback loop compensating the environmental drifts. Previous works have demonstrated the phase stability of WLG for pulses shorter than 550 fs [23, 173]. The CEP of the WL has been confirmed to be preserved for both short and long driving pulses for the first time. The analysis of the spectral position of the fringes shows rms fluctuations of 90 mrad over 11 h.

6.4 Summary

A passively CEP-stable front-end based on white-light generation has been demonstrated. WLG with 700 fs driver pulse duration has been reported for the first time. A detailed study of the reproducibility of the WLG and of its stability has been conducted. From the experimental observations, compared to the widely accepted WLG theory of Chin and Bergé, multi-photon ionization seems to be the dominant mechanism defocusing the beam after the time-space collapse. This study shows that the well-known white-light generation in bulk with ∼100 fs long pulses is scalable to sub-picosecond driving pulses by adapting focusing conditions and material length; one major difference lies in the need to compress the pulses at the input of the crystal to ensure accumulation of nonlinearities for starting the filament. From the broadening of the 700 fs long, 1030 nm centered pulses, 200 nm at 2 µm were amplified in a two-stage parametric amplifier. The CEP of the spectrally broadened pulse and of the pump pulse cancel out in the generated idler pulse. This CEP-stable idler is then used for generating CEP-stable WL in another YAG crystal. The CEP stability is measured with an f-2f interferometer over 11 h with 90 mrad rms fluctuations. These fluctuations could be decreased with a slow feed-back loop stabilizing the input pulse and its pointing.

In order to amplify the spectral bandwidth 1.8 µm – 2.4 µm in one of the channels of the waveform synthesizer, the OPAs in the front-end have been detuned to 2.45 µm and frequency doubled to 1.27 µm. The generated WL is stable after cutting the fundamental pulses at 2.45 µm with two 1.3 µm short-pass filters. The spectral phase retrieved from a FROG measurement of the signal is well-behaved and compressible.

7 Amplification of the different spectral bands

This chapter will give an overview of the amplification of the different spectral channels of the Yb:frequency synthesizer, shown in figure 2.4. One application of the whole system is the generation of attosecond pulses which is a process needing at least hundreds of µJ-level pulses to be efficient. At a µJ energy level sub-cycle or few cycle pulses might be used for other experiments, such as field-emission [177].

The channels of the synthesizer cover the spectral domains 440-650 nm, 670-1180 nm, and 1.8-2.4 µm, as shown in figure 2.4. They correspond to parametric amplification of the phase-matched bandwidths for 1030 nm, 515 nm and 343 nm pump with the well-developed, commercially available and high energy compatible BBO crystal.

As discussed previously, from the 6.5 mJ out of the regenerative amplifier, 1.35 mJ seeds the cryogenically cooled multipass amplifier, the residual energy is compressed to ∼700 fs long, 4.2 mJ pulses. Substracting the 650 µJ for the front-end as demonstrated in chapter 6, 3.5 mJ, 700 fs long pulses remain for OPA pumping. 700 fs pulse duration in the first amplification stages is of advantage, compared to 2 ps long pulses such as after the multi-pass amplifier, for minimizing the superfluorescence coming from OPCPAs. The amplification design will hence consist in amplifying the spectral domain covering 550 nm to 2.4 µm first with the regenerative amplifier pulses, then to higher energies with the pulses amplified in the cryogenically multipass amplifier. The visible noncollinear OPA (NOPA) will be discussed for the sake of compatibility with potential further extension.

The split of the energy output from the regenerative ampifier is represented in figure 7.1 in the two amplification cases of two and three OPCPA channels. The pumps for amplifying the visible part and the NIR region are the 2nd and 3rd harmonics of the fundamental pulses at 1030 nm. The assumption for the energy split was to pump all OPCPA stages with the same number of photons, in such a way that the three amplified pulses have an equal amount of photons, which corresponds in a first approximation to the shortest possible transform limited pulse, as shown in chapter 8. The conversion effiencies assumed for splitting the IR were 50% for the doubling and for the sum between green and IR. With these pump levels, the OPAs can reach the µJ level.

After a presentation of the theory and state of the art of the OP(CP)As, the calculations and experiments for the SHG and THG of the fundamental frequency will be presented. The design of the OP(CP)A stages will then be explained. The chapter will close with the first experimental results.

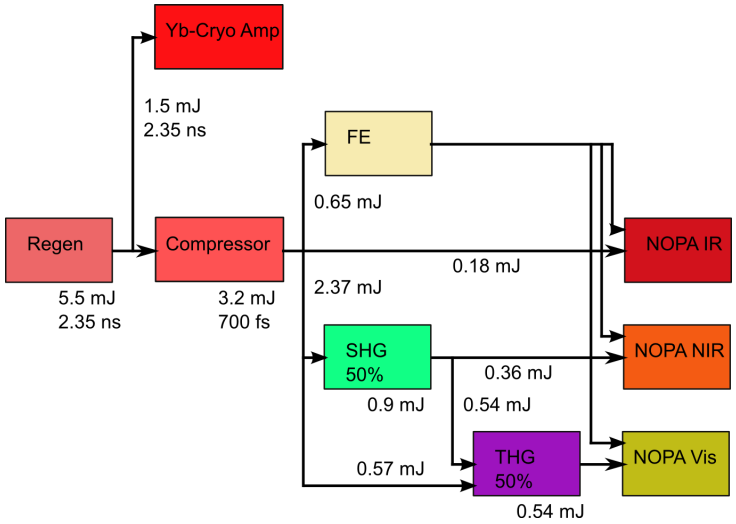

(a) Split of the regenerative amplifier for three OPCPA channels

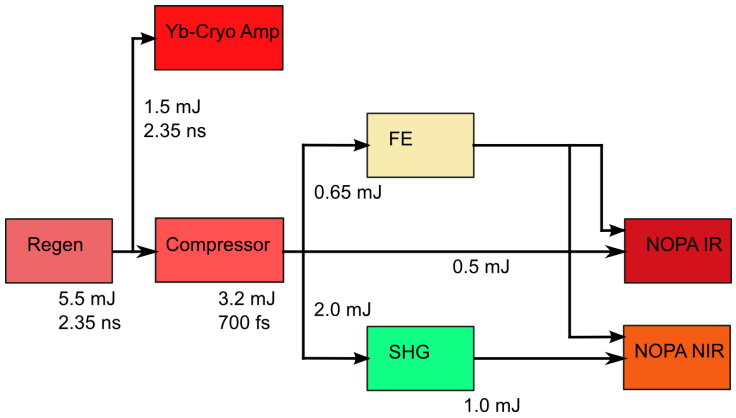

(b) Split of the regenerative amplifer for two OPCPA channels

Figure 7.1: Splitting of the output of the regenerative amplifier for seeding the multipass cryogenic amplifier and pumping the first stage of OPCPAs. (a) and (b) correspond to the pumping of three or two amplification channels, respectively.

7.1 Fundamentals of frequency mixing

Frequency doubling, tripling and parametric amplification are three-wave mixing processes which can be represented with two photon interaction between two virtual energy levels, as indicated in figure 7.2 and governed by the interaction equations between the three fields [96].

The case of parametric amplification is represented in figure 7.3. A strong pump p interacts with a signal pulse s, resulting in an amplified signal pulse at the output as well as the generation of an idler wave i, in agreement with the law of energy conservation.

The parametric gain decreases exponentially with the increase of the phase mismatch between pump, signal and idler. The phase mismatch parameter is defined as: $\Delta k = k_p - k_i - k_s$, where k_p, k_s and k_i are the wavevectors of the pump, signal and idler waves. The conversion is maximum when $\Delta k = 0$, and to amplify broadband pulses, a small phase-mismatch over a broad bandwidth is needed. The phase-matching bandwidth is

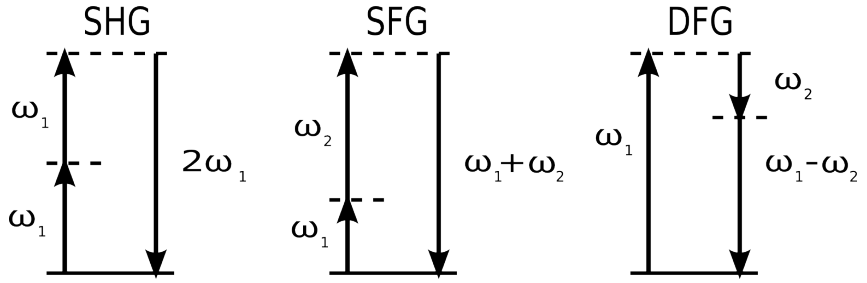

Figure 7.2: Energy diagrams of three-wave mixing processes: second harmonic generation (SHG), sum frequency generation (SFG) and difference frequency generation (DFG).

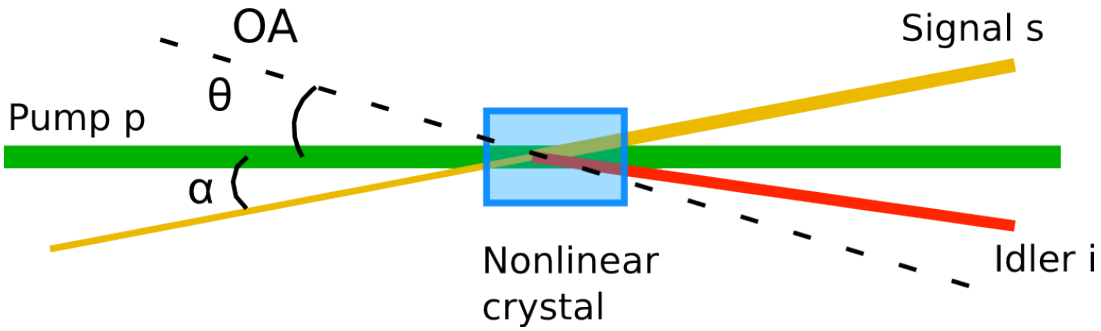

Figure 7.3: Scheme of parametric amplification: the pump p and signal s enter the frequency mixing crystal with the non-collinear angle α. The pump is set at the angle θ from the axis OA of the crystal. The idler i is generated as the pump and signal interact.

determined by the group-velocity mismatch (GVM) between signal and idler pulses; the larger the GVM, the narrower the phase-matching. Large gain bandwidth is thus expected close to degeneracy ($\omega_i = \omega_s$) in type 1 phase-matching and when the group-velocity of the signal matches the one of the idler. This condition can be obtained geometrically in a NOPA, as shown in figure 7.3. The broadband phase-matching is reached with an appropriate choice of the angle θ between pump and signal. In this configuration, the signal and the projection of the idler on the signal wavevector propagate at the same speed inside the crystal, ensuring their temporal overlap. The group-velocities of signal and idler are thus related with: $v_{gs} = v_{gi} \cos\Omega$, with Ω the angle between signal and idler [178].

7.2 State of the art

Nonlinear frequency conversion, experimentally demonstrated first in 1961 [179] and theoretically studied since 1962 [180], has been further investigated during the last decades. The increase in average power and pulse energy of the laser systems have set a challenge to the implementation of frequency conversion, but are also a great opportunity. This includes crystal quality, beam quality and thermal management.

7.2.1 Frequency doubling and tripling

Very high energy, nanosecond pulse duration laser systems, like NIF, use KTP crystals; for NIF, large aperture crystals (40×40 cm^2 aperture) were developed [45], but this laser operates single-shot. In longer operation, KTP crystals degrade due to gray-tracking [181]. For long-term operation, borate crystals like BBO, LBO, C-LBO or BiBO show no degradation due to gray-tracking. Their lower effective nonlinear coefficient has to be compensated by adjusting the crystal length. BBO crystals were first grown in 1984 [182], whereas lithium tri-borate (LBO) crystals were manufactured in 1989 [183]. With very broadband phase-matching and a transmission up to 2.4 µm for BBO and 2.6 µm for LBO, they were applied for SHG, THG and also for parametric amplification.

The frequency doubling and tripling of ultrafast, mJ level lasers is highly efficient, as the conversion efficiency increases with the intensity, but unwanted nonlinear processes, like SPM, appear. They lead to spectral and spatial distortions of the pulses. There is therefore a trade-off between beam quality and high conversion efficiency. In 1992, Brown *et al.* demonstrated 80% SH conversion efficiency of 900 mJ Q-switched Nd:YAG laser; the beam profile was a super-Gaussian 6^{th} order [184]. Akahane *et al.* reached in 2007 25% SHG conversion efficiency of 35 ps long, 8 mJ pulses, with a beam profile suitable for OPCPA [185]. In 2010, Hermann *et al.* generated 7 mJ UV with 40% conversion efficiency from a 78 ps Nd:YAG laser [186]. To overcome the limitations in conversion efficiency, some strategies have been developed, as in [187], where the pulses are converted when stretched, and compressed after conversion. For future conversion of high peak power pulses, one could imagine a similar scheme as this demonstration [187].

7.2.2 Broadband parametric amplification

Broadband parametric amplification in the MIR and in the NIR has been demonstrated by [188, 32, 20]. In [188, 32], the wavelength of a neodymium doped pump laser was 1 µm, and in [20] the pump lasers are a Ti:Sapphire amplifier operating at 800 nm and its second harmonic. Matyschok *et al.* have amplified a broadband spectrum covering the range 650-1100 nm to 10 µJ level with an ytterbium doped pump [189].

Broadband amplification up to levels higher than hundreds of µJ was implemented with non-collinear OPAs. The visible part of a white-light super-continuum was amplified to 300 µJ by Tzankov *et al.* and recompressed to sub-25 fs [190]. Pergament *et al.* demonstrated a 180 µJ OPA; the pulses centered at 810 nm were compressible to 15 fs. These results obtained with BBO based OPA were reproducible with LBO crystals [191]. In [192] Stanislauskas *et al.* amplified an 800 nm signal generated with WL up to 35 mJ and compressed the pulses to 9 fs. 90 mJ have been reached with 10 fs long pulses by Tavella *et al.* in [193].

The most commonly used nonlinear crystal is BBO for its broad phase-matching and transmission up to 2.4 µm. In OPAs where the signal or idler is longer than 2.4 µm, absorption might be detrimental: at high energy levels, the latter generates heat in the crystal, which could lead to thermal aberrations, stress and depolarization.

7.2.3 Crystal quality

During propagation in the crystals the pulses accumulate nonlinear phase shift, leading to distorsion in the spectrum and in the phase-front. Another effect related to the spatial intensity distribution is back-conversion: when the highest conversion has been reached, the pump is depleted and back-conversion occurs. For Gaussian beams the highest intensity is spatially in the center. For limiting both effects as well as the risks of damages, the aperture of the crystals has to be scaled up. The homogeneity and quality of the crystals had consequently to be improved. A bubble, inclusion, defect or impurity leads to local absorption and to light scattering. The crystals heat up locally with absorption, inducing some stress which might lead to damage of the crystal [45]. Single or multi-photon absorption in the crystals might induce bond-breaking, *i.e.* a local damage of the crystal. This phenomenon, also called gray-tracking because of the gray track visible at the irradiated location in the crystal is reversible depending on the illumination conditions (duration and intensity) [194]. This occurs for example in KTP crystals. A long and intense illumination leads to catastrophic damage. Absorption as driving force of gray-tracking depends on the difference between bandgap and photon energies. The material bandgap is generally located in the UV, for example 350 nm for KTP, 189 nm for BBO and 160 nm for LBO. In the case of THG, the generated wavelength is in or close to the UV-region and single-photon absorption leads to damage. In this respect, LBO is a perfect material for SHG: the photon energy of the frequency doubled pulses lies a factor of three lower than the material bandgap.

Several techniques have been developed for optimizing the crystal quality and minimizing its absorption. The inclusions and bubbles depend on the growing process and on the materials used for the crucible [195]. Absorption has been related to the presence of O-H bonds in the material, for example in lithium niobate; adding dopants such as manganese into the stoechiometric material prevents the formation of these bonds [196].

The optical properties (absorption and nonlinear refractive index coefficient) of BBO were studied for different crystal manufacturers at DESY [197]. The results confirmed the practical experience, that the crystal quality strongly depends on the manufacturing company and their manufacturing process. The residual absorption of the nonlinear crystals in the UV and in the green is responsible for a decrease in the lifetime of the crystal: when a UV photon with 5-7 eV energy is absorbed, its energy is high enough to break bonds in the crystal, inducing damage. In the green, the two-photon absorption of photons with ∼2-3 eV energy leads in a similar way to damages. This microscopic local break acts as a center for further damage in the material inducing macroscopic damage. The homogeneity of the crystals is relevant for high energy conversion because of the increase in the beam sizes: the probability for the beam to hit a defect in the crystal leading to damage is higher than for small beam diameters. These damages are a question of time.

Even though the following experiments are realized with the conversion of the remaining energy of the regenerative amplifier and the average power is thus kept low, the crystal quality is of high importance for a long life-time of the synthesizer. Thermal management of the crystals for frequency conversion will be an issue during the amplification with the output of the cryogenically cooled amplifier, but its detailed study is outside the scope of this thesis.

7.3 Frequency doubling and tripling

Harmonic generation from the fundamental was simulated with SNLO [198, 199, 200], then implemented experimentally.

7.3.1 Simulations

Two crystals were investigated because of their different optical properties: BBO and LBO. SNLO performs simulations based on plane-wave mixing or two-dimensional model; here the 2D-mix-SP module was used, including diffraction, birefringent walk-off, group-velocity walk-off and group-velocity dispersion. The Maxwell differential equations are integrated using the split-step fast Fourier transform (FFT) method, as described in [198, 199, 200]: the equations are integrated over z for constant time step t and the transformation occurs between z and $k = {}^{n\omega}/_{c}$. For this project, the optimum conversion was defined to be the highest efficiency reachable with temporally transform-limited and spatially Gaussian pulses. In table 7.1, the parameters of the materials and their cuts for converting 1030 nm to 515 nm and 1030 nm mixed with 515 nm to 343 nm are shown.

		SHG		THG	
Parameter	Unit	BBO	LBO	BBO	LBO
$Walk-off$	$mrad$	56.98	8.16	74.1	18.72
θ	°	23.4	90	32.5	90
ϕ	°	90	13.6	90	40.1
d_{eff}	pm/V	2.01	0.828	2.01	0.69

Table 7.1: Parameters of BBO and LBO for SHG and THG.

Table 7.2 shows the parameters of the simulation, with the expected output energies, pulse duration and spectrum. The output energy corresponds to the pump energy for OPA design, with equal photon amounts in each three pump beams, as shown in figure 7.1. This means that the 3 OPA pumps contained the same amount of photons per pulse, in order to have equally weighted amplified signals. The resulting energy in the UV was thus three times higher than in the IR.

		SHG		THG	
Parameter	Unit	SHG BBO	SHG LBO	THG BBO	THG LBO
w_0	mm	1.7	2	1.7	1.1
l_{Xtal}	mm	0.7	1.7	0.5	1
$E_{in,1030}$	mJ	2.4	2.4	0.45	0.45
$E_{in,515}$	mJ	0	0	0.9	0.9
E_{out}	mJ	1.8	1.6	0.84	0.86
τ_{in}	fs	700	700	700, 540	700, 530
τ_{out}	fs	540	530	470	430
$\Delta\lambda_{out}$	nm	0.53	0.51	0.66	0.64

Table 7.2: Parameters for SHG and THG with the compressed output of the regenerative amplifier.

These parameters reflect some assumptions: in the calculation for THG the pulse shortening during conversion into green has been taken into account, but the waists of the SHG

and IR beams were assumed to be equal. This would not be true without a telescope for matching the IR to the green. Experimentally working without a telescope simplifies the setup and avoids interfaces and losses. The THG efficiency would however be decreased.

The intensity on the crystal is 37.8 $^{GW}/_{cm^2}$ for SHG, which is close to the damage threshold of BBO. Increasing the spot size and compensating with longer crystals reduces the risk of damage. The maximum aperture for manufacturing the crystals is however 15 × 15 mm^2, hence the maximum beam diameter at $^1/_{e^2}$ is 5 mm for Gaussian beams. Testing experimentally with smaller beam diameters allows to explore the exact limitations for doubling the output of the cryogenic amplifier.

The B-integral expected during frequency doubling amounted to 0.34 for BBO and 0.13 for LBO, considering the full crystal length and the nonlinear refractive indexes $n_{2,BBO,515} = 10.9 \times 10^{-16} cm^2/W$ [94] and $n_{2,LBO,515} = 2.58 \times 10^{-16} cm^2/W$ [201].

7.3.2 Experiments

Figure 7.4 shows the experimental layout for SHG and THG: the compressed output of the regenerative amplifier is split between the front-end described in chapter 6 and the pumping of two OPCPA channels, as shown in figure 7.1. The goal of this setup was to verify the calculations and achievable conversion efficiencies with good beam quality before implementing the SHG for pumping the NOPA.

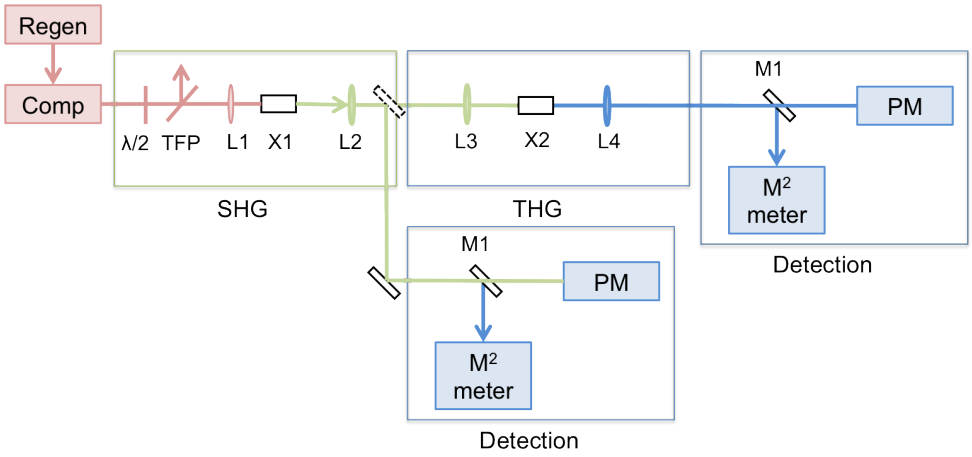

Figure 7.4: Frequency doubling and tripling setup. The crystals are named X1 and X2, the lenses for the mode-matching telescopes L1 to L4, the mirrors M1 to M3. For attenuating the beam, the quarter-waveplate $\lambda/2$ and the thin-film polarizer TFP were used. The measurements of the pulse energy and beam quality were taken with an energymeter and an M^2-meter, respectively.

Two different crystals have been compared: BBO and LBO. The lengths of the BBO crystals were 0.5, 0.7 and 1.0 mm, and the ones of the LBO crystals 1.5, 1.7 and 2 mm. Before the telescope the beam diameter was 4 mm at $^1/_{e^2}$. The telescopes reduced the beam by a factor of either 0.75 or 0.6 or 0.4. The smallest beam diameter was used with the thinnest crystals to reach the highest efficiency. In the optimization between conversion efficiency and beam quality, the goal was to keep the beam quality parameter

M^2 below 1.4 and mostly to have a circular, homogenous, Gaussian beam profile in the far field. This is important for pumping in an homogenous manner the NIR NOPA.

In view of nonlinearities in the crystals, the conversion efficiency was limited with the 0.7 mm long BBO crystal to 37% with a good beam quality ($M^2 < 1.3$), generating 0.28 mJ SH. With the 1 mm long crystal, the interaction length was increased and a larger beam diameter was possible, which reduced the peak intensity and hence the nonlinear phase accumulated in the crystal. The conversion efficiency has been increased up to ∼41% with a beam quality parameter of 1.4.

With LBO, a higher conversion effciency of 45% was obtained with the same beam quality. The optimum parameters were the 2 mm crystal with a collimated beam with 3.4 mm diameter. The efficiency curves obtained with 3.4 mm input beam diameter, for 1.5 mm long BBO and 2 mm long LBO respectively, are shown in figure 7.5a. A good operation point was found to be the conversion in BBO from 1.75 mJ infrared to 0.75 mJ green.

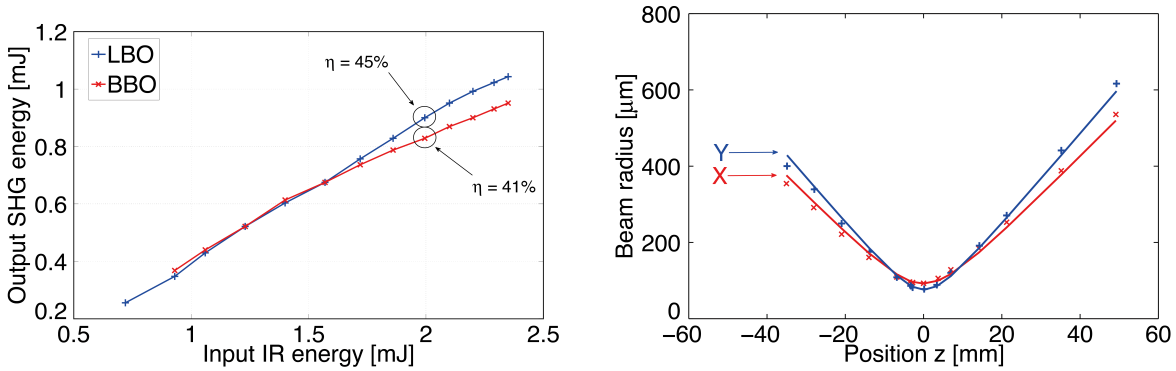

(a) Efficiency curves **(b)** Beam profile

Figure 7.5: Results of the frequency conversion: (a) efficiency curves of SHG obtained with BBO and LBO and (b) measurement of the caustic at the working point of 0.75 mJ green with 43% conversion efficiency.

The measurement of the caustic, acquired with the M^2-meter M200-s from Ophir-Spiricon Ltd., is displayed in figure 7.5b with the beam profile in the focus of the lens illustrated in the inset. The beam profile was similar with BBO and LBO, even though LBO introduced on the phase front less distortion caused by nonlinearities. The beam diameter was 3.2 mm and the divergence of 0.3 mrad corresponds to a well-collimated beam.

For pumping the NOPA the SHG was implemented with the BBO crystal. Further improvement will be done by encapsulating the SHG crystal in a small box flooded with nitrogen. The flooding is to avoid degradation of the crystal due to impurities and outgassing products originating from single or two photon-absorption of the scattered green light.

7.4 OPA and OPCPA calculations

For parametic amplification the pulse durations of signal and pump have to be matched to each other. In the case of an OPA, signal and pump pulses have the same duration, whereas in an OPCPA the signal is stretched. The approximate seed duration is typically a third of the pump pulse duration for optimizing gain and spectral bandwidth [202]. The following condition has to be fulfilled to respect the local approximation valid for OPCPA:

$$L_{c,OPA} < \frac{L_{GVM}}{3} = \frac{\Delta\tau_{chirped}}{3 \cdot |GVM|} \tag{7.1}$$

Here, $L_{c,OPA}$ is the length of the OPA crystal, $L_{GVM} = \frac{\Delta\tau_{chirped}}{|GVM|}$ the group velocity mismatch length. The parameters and the maximum crystal lengths for the amplification stages pumped with the regenerative amplifier and the cryogenic amplifier are given in table 7.3. The group velocity mismatch GVM_{1-2} is defined as the difference of the inverse of the group velocities at wavelengths $\lambda_{1,2}$ with $GVM_{1-2} = \frac{1}{v_{g,1}} - \frac{1}{v_{g,2}}$, where $v_g = {}^{c}/_{GVI}$ and GVI_λ the group velocity calculated for wavelength λ as $\mathrm{GVI}_\lambda = \frac{1}{n_\lambda - \lambda \frac{dn}{d\lambda}}$.

For uniaxial materials, the effective refractive index for a beam at an angle θ from the ordinary optical axis is calculated as:

$$\frac{1}{n_{eff}(\theta)^2} = \frac{cos^2\theta}{n_o^2} + \frac{sin^2\theta}{n_e^2} \tag{7.2}$$

Sellmeier coefficients for BBO were taken from Ref. [203].

Material	$\lambda_p, \lambda_s, \lambda_i$ µm	τ_p ps	α, θ °	d_{eff} ${}^{\mathrm{pm}}/_{\mathrm{V}}$	GVM_{s-p} ${}^{\mathrm{fs}}/_{\mathrm{mm}}$	GVM_{i-p} ${}^{\mathrm{fs}}/_{\mathrm{mm}}$	GVD_{λ_p} ${}^{\mathrm{fs}^2}/_{\mathrm{mm}}$	GVD_{λ_s} ${}^{\mathrm{fs}^2}/_{\mathrm{mm}}$	GVD_{λ_p} ${}^{\mathrm{fs}^2}/_{\mathrm{mm}}$	$L_{c,OPA,max}$ mm	Valid Approx?
Regen.	0.343, 0.55, 0.911	0.4	4.5, 37	1.98	-188	-316	250	130	60	0.4	×
	0.515, 0.85, 1.66	0.5	2.5, 24	2.02	-68	-101	134	68	-31	1.8	∨
	1.03, 2.06, 2.06	0.7	0, 21.6	1.84	60.8	60.8	42	-101	-101	3.8	∨
Cryo.	0.343, 0.55, 0.911	1.7	4.5, 37	1.98	-188	-316	250	130	60	1.8	∨
	0.515, 0.85, 1.66	2.1	2.5, 24	2.02	-68	-101	134	68	-31	7.5	∨
	1.03, 2.06, 2.06	3	0, 21.6	1.84	60.8	60.8	42	-101	-101	16.4	∨

Table 7.3: Verification of the validity of the local approximation for OPCPA in BBO for the regenerative amplifier (cryogenic amplifier) pump pulse durations of 700 fs (3 ps) in the IR and correspondingly 500 fs (2.1 ps) and 400 fs (1.7 ps) in the green and UV. The parameters are given for BBO typ 1 (psi = eoo).

The pulse duration after the regenerative amplifier of 700 fs determines the parametric amplifiers as inbetween OPA and OPCPAs. In the case of the amplification after the cryogenic amplifier, the pump pulses will be ∼3 ps in the IR, ∼2.1 ps in the green and ∼1.7 ps in the UV, corresponding to the OPCPA case.

With a computational code giving the phase-matching gain, starting parameters for crystal length, intensity and noncollinear angle have been found. In the case of the MIR degenerate OPA (DOPA) and NIR NOPA, the noncollinear angle inside the crystal is 0.6° and 2.4°, respectively, and the intensity is 50 ${}^{\mathrm{GW}}/_{\mathrm{cm}^2}$ for both.

The first stages of the DOPA pumped at 1 µm and NOPA, pumped at 515 nm, have been further simulated with Chi2D, a software written in the group of Prof. Morgner

by Tino Lang [204, 189]. This simulation software is based on a (2+1)D algorithm and encompasses the effects of dispersion, self-phase modulation and walk-off during the non-linear interaction of the pump and signal along the crystal. With these simulations, the mentioned starting parameters have been refined.

7.5 Experimental results

Figure 7.6 shows a schematic layout of the DOPA stages and dispersion management. The crystals of the three amplifying stages *X1-X3* are BBO cut at 21.8°; the crystal used in the first amplification stage was 4 mm long. The pump was split into three parts: 75 µJ powered the preamplifier stage, ∼100 µJ the stage after the Dazzler and the rest the last stage. The pump beam was focused with lenses into the crystals to 210 µm radius in the first stage. The signal was focused and collimated with curved mirrors to minimize the dispersion. The internal angle between pump and signal was 1.65°. The corresponding intensity in the first stage is thus 97 $^{GW}/_{cm^2}$.

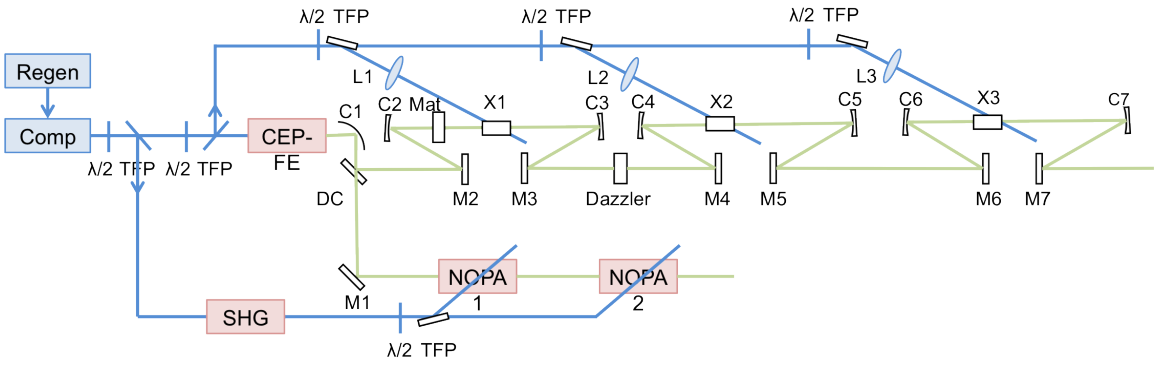

Figure 7.6: Schematic layout of the experimental setup of the DOPAs and dispersion compensation. The three stages are represented: stage 1 preamplifying before the Dazzler, stages 2 and 3 after the Dazzler. *L1-L3* lenses for mode-matching of the pump, *C1* parabolic mirror for collimation of the CEP stable white-light, *C2-C5* curved mirror for focusing and collimating the signal, *M1-M6* flat silver mirrors, *X1-X3* BBO crystals, *Mat* material for dispersion compensation, $\lambda/2$ half-waveplates and *TFP* thin-film polarizers. The separation of the short and long spectral components of the super-continuum is performed with the dichroic mirror *DC*. The short wavelengths will later be amplified in the stages *NOPA1* and *NOPA2*, which can be built in a similar way to the DOPA stages.

The spectra displayed in figure 7.7 correspond to different crystal lengths: the broadest spectrum was amplified with the 4 mm long BBO crystal. In longer crystals, the group-velocity mismatch limits the phase-matching bandwidth and leads to a narrowing of the amplified spectrum. The efficiency was limited by the mode-matching of the signal and the pump pulses: the diameter of the signal beam is much smaller than the pump beam.

The first stage amplifies the white-light by a factor of 575 measured with a photo-detector (Thorlabs Det10D/M). The spectrum covers the range 1800–2500 nm and extends beyond 2.5 µm as shown in figure 7.7: the measurement was limited by the range

900–2500 nm of the NIRQuest spectrometer from OceanOptics. Figure 7.7 illustrates the narrowing of the phase-matched spectral width with the length of the crystal. The broadest spectrum was achieved with the 4 mm long crystal and a gain higher than 550. This spectrum corresponds to a 23 fs long transform-limited pulse. Superfluorescence was measured with the photo-detector by blocking the signal; the superfluorescence background was 1.7% under these conditions. During amplification of the signal, less superfluorescence is however generated. The amplification factor increased to 3000 by increasing the pump energy to 100 µJ; the measured energy of the signal was ∼1 µJ.

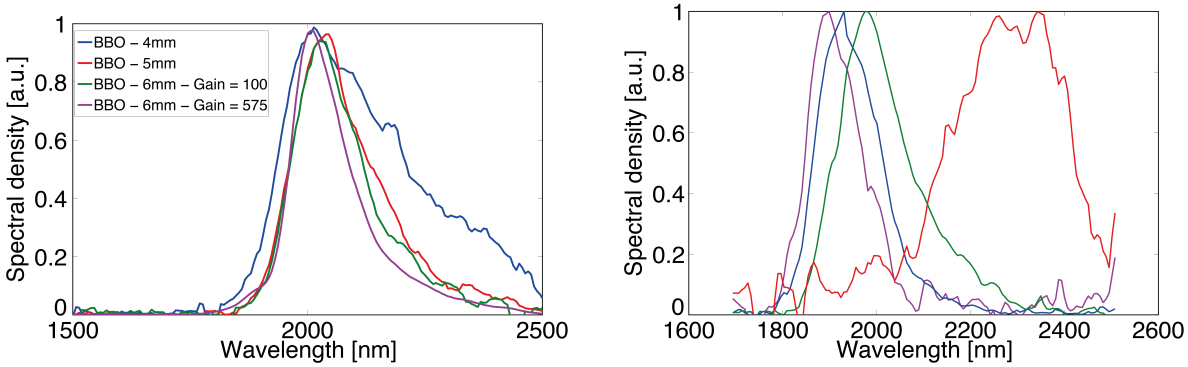

Figure 7.7: Spectra of the signal of the DOPA, (a) for different crystal lengths and (b) by varying the delay between pump and signal. In (b) the signal was stretched before amplification with 6 mm ZnSe; the spectra correspond to the amplification of different spectral regions.

The temporal overlap of signal and pump pulses was verified by introducing materials in the path of the signal. ZnSe adds positive second order dispersion, whereas materials with zero-dispersion wavelength below 1.8 µm add negative second order dispersion. In this experiment BK7 was used. From the starting parameter of the required chirp given by Chi2D and formula 5.5, between 6 mm and 10 mm ZnSe were estimated for matching the pump pulse duration. The amplification gain decreased however with 6 mm ZnSe and the chirp was noticeable when varying the delay between pump and signal pulses. The amplified spectra for several positions of the translation stage are shown in figure 7.7b. In order to understand whether this comes from the spectral phase of the super-continuum, this chirp measurement was repeated with a different signal seeding the OPA.

The crystal generating the CEP stable white-light was exchanged from 2 mm to 6 mm in order to test the following assumption. The chirp on the WL is estimated by the dispersion of the material, assuming a start of the filament at the entrance of the crystal. The pulse duration was estimated by taking the Fourier-transformation of the spectrum and by propagating the pulse through the materials. The red wing of the WL spectrum extends above 2.5 µm and was approximated by a super-Gaussian of the 3^{rd} order. The pulse duration was then expected to be ∼25 fs and ∼70 fs at the exit of the 2 mm and 6 mm long YAG crystals and 200 fs and 50 fs at the entrance of the DOPA crystal, respectively. If the assumption of the white-light phase by the material dispersion is correct, a different behavior should be noticeable during amplification with 700 fs long pump pulses. Though,

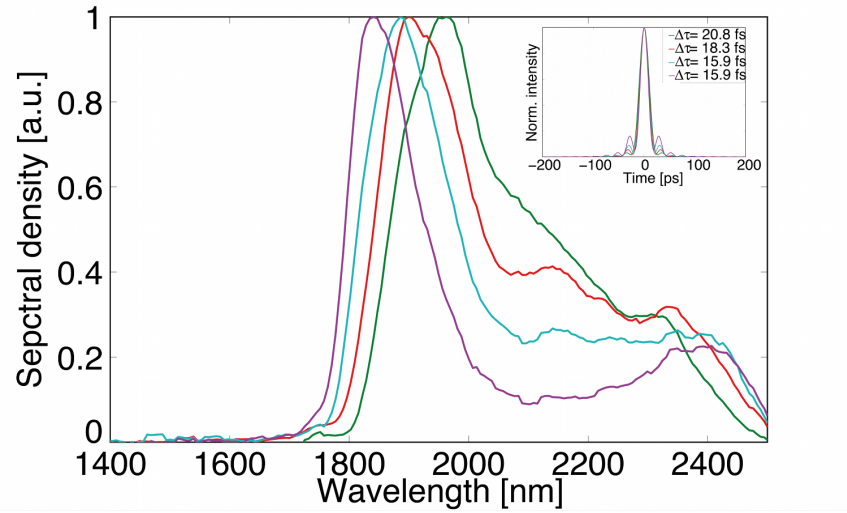

Figure 7.8: Spectra of the signal of the DOPA for different angles between the pump and the signal. The temporal intensity profile, calculated assuming a transform-limited pulse, is shown in the inset.

the same behavior of a strong chirp on the amplified spectrum was observed, meaning that the phase will have to be characterized thoroughly after amplification in future work.

7.6 Summary

The amplification of the spectral bands was rewieved in this chapter and preliminary experimental results given. The split of the remaining energy from the regenerative amplifier is detailed in light of the parametric amplification of the channels of the waveform synthesizer. In the case of amplifying two channels, which are the NIR NOPA and the MIR DOPA, the pump is experimentally split between 0.4 mJ at the fundamental and 0.75 mJ at the doubled frequency.

Calculations of the DOPA and NOPA were performed with the software published as "Chi2D" [204] as a starting point for the experiments. The first DOPA stage was implemented with a gain of 3000 and amplified signal pulses to the µJ level.

8 Recombination and compression of broadband pulses

The last part of the frequency synthesizer consists in the recombination (or synthesis) of the pulses amplified in the different channels and their compression. The combination of two or more ultrashort pulses to generate a single to sub-cycle pulse is a crucial step of the frequency synthesizer. Two major issues have to be studied: the timing stabilization of the individual pulses and the dispersion management for compressing the pulses. Timing stabilization in the parametric amplifiers is also a critical point to keep the temporal overlap of the pump and signal pulses. The required precision of the timing differs with the application: in the case of parametric amplification, a stabilization whithin a few tens of femtosecond suffices, whereas the waveform synthesis requires a stabilization more precise by three orders of magnitude.

In order to compress the pulses to the transform-limit, the dispersion management for stretching and recompressing the pulses needs to be examined carefully. In addition, the CEP stability is also of importance for strong-field experiments with single-cycle to few cycle pulses.

In this chapter only the concepts and preliminary work concerning timing stabilization, CEP stabilization and dispersion management will be presented.

8.1 Timing stabilization

Timing can be measured at the femtosecond to attesecond level only with optical means, since electronic synchronization cannot perform better than 100 fs. The balanced optical cross-correlator (BOC) has been shown to be suitable to measure timing with sub-femtosecond precision. It was developed for synchronization of two lasers in [205] and is now used for timing distribution between all the instruments in large facilities such as Fermi@Elettra (Italy) with 70 fs precision [206] or FLASH (Germany) with <10 fs precision [207]. In frequency synthesis of single to sub-cycle pulses, corresponding to <5 fs long pulses, BOCs require a precision of a few tens of attoseconds for an efficient combination as demonstrated in [208].

8.1.1 Balanced optical cross-correlators

The layout of the BOC is shown in figure 8.1. The experimental setup is slightly different whether the two pulses have the same wavelength or not. The principle of the BOC is to detect the signal of an optical cross-correlation between the two pulses, which is sensitive

to their delay. In practice, the energy of both pulses is split into two equal arms, to delay one arm to the other and to generate their sum-frequency. The timing jitter translates linearly into variations of the generated signal when the delay is close to zero [209].

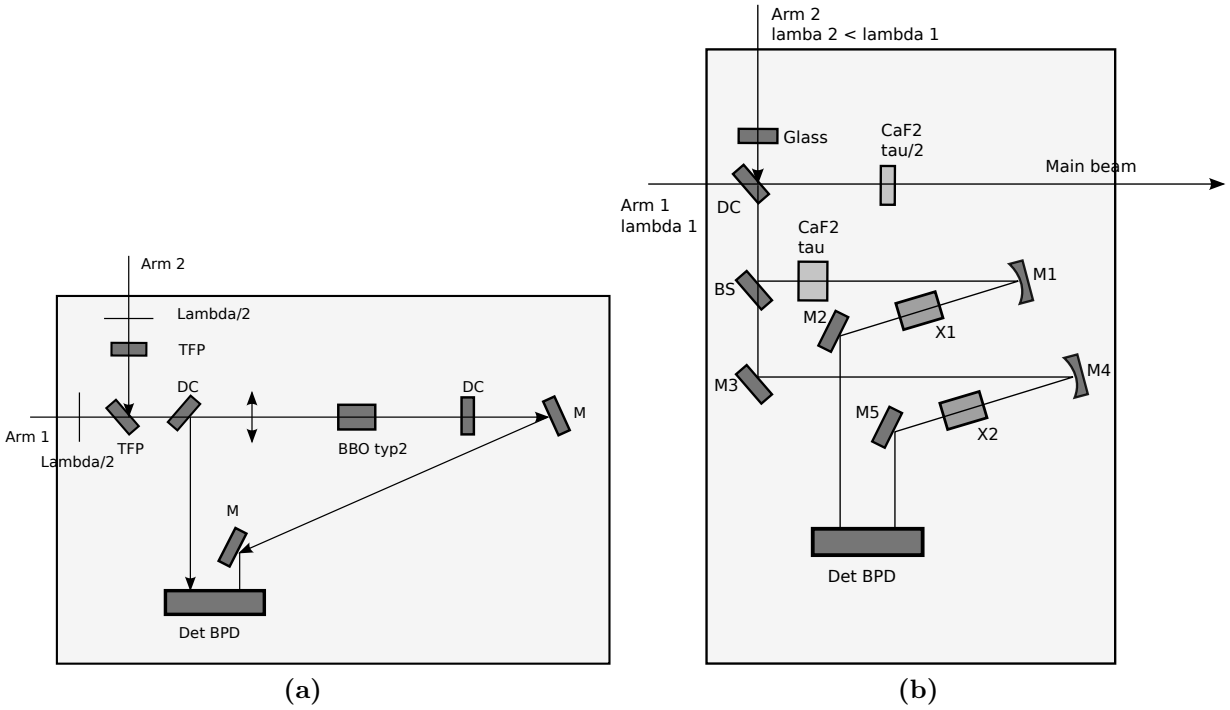

Figure 8.1: Scheme of a balanced optical cross-correlator: the two pulses have (a) the same and (b) two different wavelengths. *BS* beam splitter 50-50%, *M1* to *M5* flat or curved silver mirrors *X1* and *X2* BBO crystals cut for type 1 phase matching for SFG between the two branches of the BOC.

To stabilize the timing between the zwo pulses, a feedback loop (not shown) is implemented to control a piezo-transducer in one of the synthesizer channels. The two nonlinear crystals are BBO crystals, cut for type 1 phase-matching for sum frequency generation (SFG) between λ_1 and λ_2. In this scheme, delays $\tau/2$ and τ are introduced in the main beam and in one of the BOC arms respectively. One arm of the BOC is consequently delayed by τ and the other one not delayed. The substrates chosen for the delays τ and $\tau/2$ are CaF_2 ones, because its transmission extends up to 5 µm, as illustrated in figure 8.2; other possible materials, like undoped YAG, sapphire or infrasil, absorb above 4.3 µm, 4.2 µm and 3.4 µm, respectively. In the BOC scheme for pulses with the same wavelength, the SFG from the combined pulses is transmitted by the dichroic mirror and the remaining IR is reflected to generate the second sum-frequency signal. This supplementary path corresponds to the delay of τ.

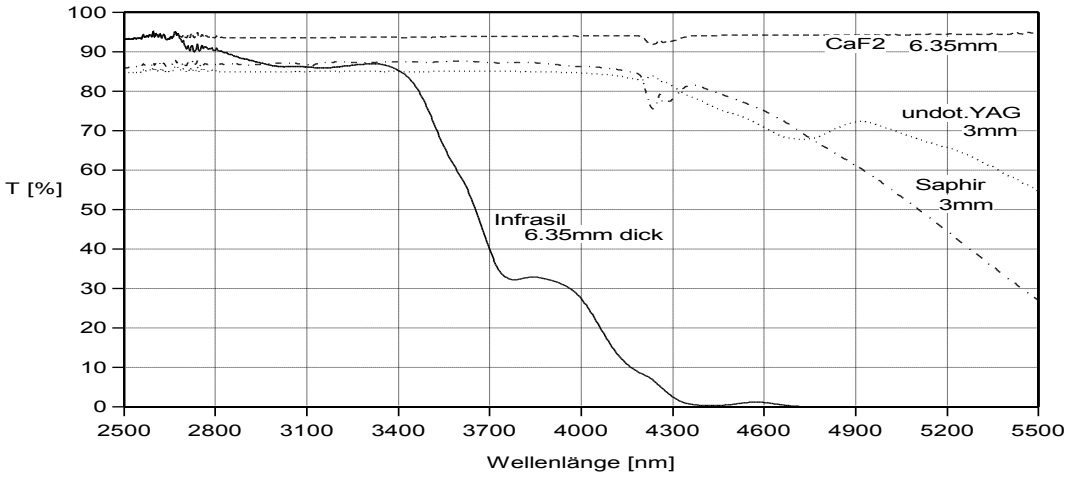

Figure 8.2: Transmission curve of standard substrates, like CaF_2, YAG, Infrasil and Fused Silica

8.1.2 Jitter in the pump line

The timing jitter between the pump pulses after the regenerative amplifier and the cryogenic multi-pass amplifier has also to be minimized, such that the signal pulses from the front-end and the pump pulses from the multi-pass amplifier arrive synchronously in the OPCPAs. A sub-femtosecond precision is necessary for recombining the pulses from the different channels. Moreover, the absolute timing is relevant for scientific experiments, requiring synchronization of the frequency syntheziser with an external clock or another laser system. The timing is influenced by thermal changes on a slow time scale and vibrations on a fast time scale.

Thermal drift is calculated as $\Delta l = \Delta T \cdot \alpha \cdot l$ with α the thermal expansion coefficient, ΔT the temperature difference and l and Δl the length and its variation, respectively.

The longest beam path occurs in the regenerative amplifier and in the following compressor and are estimated to be 195 m and 22 m. On a steel breadbord, considering an expansion coefficient of 12×10^{-6} K^{-1} and 40 round-trips in a 5 m single-pass cavity, the corresponding path difference for ±1 K is ±2.6 mm, or ±8.6 ps. The length of the cavity on an aluminium breadbord, whose temperature is stabilized to ±0.05 K by an open-bath chiller, varies only by ±250 µm, or ±800 fs. This is on the same order of magnitude as the pulse duration after compression. For this reason a detection of these fluctuations and their correction with a feedback loop is necessary.

Preliminary measurements of the timing jitter were performed with a commercial laser system. The regenerative amplifier s-Pulse HP2 from Amplitude Systèmes was seeded with a Yb:KYW oscillator (t-pulse). The implemented experimental setup for this measurement was a BOC detecting the timing-jitter between two pulses of the same wavelength, *cf.* figure 8.1. The difficulty originated in the highly different repetition rates (42.5 MHz for the Yb:KYW oscillator vs. 1 kHz for the regenerative amplifier), pulse durations (210 fs for the oscillator vs. 450 fs for the regenerative amplifier), and energies

(16 nJ for the oscillator vs. 1.8 mJ for the regenerative amplifier). The higher repetition rate of the oscillator caused a high background level: this was avoided by pulse-picking the output of the oscillator with a Pockels cell located before the BOC. The pulse duration difference was responsible for a short interaction time between both pulses; the head and tail of the pulses from the regenerative amplifier caused some background. The useful energy of the longer pulses has been equalized carefully to match the energy of the seed pulses for obtaining a symmetric signal.

The measurement showed a high jitter of 3 ps, partially even between successive pulses. This was at the time of the experiment not possible to compensate with the Labview control software and piezo driver: the jitter was faster than the bandwidth of the feedback loop. This strong jitter might originate from a change after delivery inside the compressor, which made the compressor be mechanically much less stable, and is therefore not representative of the jitter of these sources. This example still shows that the jitter inside a regenerative amplifier and compressor has to be carefully considered.

In future work, the jitter between the home-made regenerative amplifier and the cryogenically cooled multi-pass amplifier will be measured after the respective compressors. In this configuration enough energy is available and both pulse trains can be operated at the same repetition rate. Both pulses originated from the same oscillator pulse, hence only the jitter added by the compressor in one arm and the amplifier with its compressor on the other arm has to be compensated for.

8.2 CEP stabilization

A stable recombination of the pulses is only possible if the CEP is kept stable. With the passive CEP stabilization of the pulses in the front-end as demonstrated in section 6 only slow thermal drifts and some vibrations need to be compensated. The vibrations might come for example from the cryogenic cooler or the vacuum pumps used in the multipass amplifier.

8.3 Dispersion management

The generation of compressed single-cycle pulses requires a careful dispersion management, compensating not only for the second order but also for higher order dispersion of the material. In chapter 7, the pulses were assumed to be stretched to the optimum duration for maximizing the efficiency of the frequency conversion. After a general description of possible schemes for dispersion management, it will be here explained how this is realized in practice and how the pulses are recompressed to transform-limit duration.

The biggest challenge between stretching and compressing is the compression of the pulses: with an octave-spanning spectral width, it is not possible to use a grating or a prism compressor. Chirped mirrors or bulk materials are suitable alternatives. A recombination of the pulses might be implemented to attain compressed pulse duration at the exit of the combiner, but this leads to high intensities inside the combiners, thus to nonlinear effects. This method of combination is hence not suitable for high energy pulses.

This can be overcome by partly compressing the pulses before and during the combination, then having a final compression stage for the full-bandwidth, as it is implemented in [210].

In the case of full compression after the combination, a large stretching ratio, different in each arm, would need to be compensated for: designing several octave-spanning optics is extremely challenging. It is then strategically easier to precompensate the chirp before the combination. If the pulses are fully compressed directly after the last combination, the high intensity on the surface of the mirror could lead to damage, or to nonlinearities inside the material. For these reasons, the compression is partially realized before combination and finalized just before the actual experiment, in a vacuum chamber to avoid the dispersion and nonlinearities from the air. The final compression of the five octave spanning spectrum would be finalized after a piece of glass, with accordingly large beams to avoid SPM. This scheme is however not scalable to high energies. For compression of spectra of one up to two octaves, DCMs might be used, as demonstrated in [19].

For the first implementation of the Yb frequency synthesizer, the combination will extend from ∼500 nm up to 2.5 µm, spectral bandwidth which can be supported by double-chirped mirrors, as demonstrated in [19].

Stretching the pulses is relatively easier than compressing them: the optimum duration is between ∼200 fs and ∼300 fs for the first stages, and ∼1 ps and ∼2 ps for the last stages, as mentioned in chapter 7. This can be done with adapted material, or with a prism setup, or with adaptive optics such as Dazzlers and spatial light modulators (SLM).

The options for the stretching and compression are then the following: first bulk stretcher, DCM compressor, second DCM stretcher, bulk compressor, third prism + SLM stretcher, bulk compressor, and fourth prism or grism + DAZZLER stretcher, bulk compressor. Before detailing these solutions, the building elements are presented. Finally, the different solutions are discussed.

8.3.1 Stretching and compression of broadband pulses

In this section, the different elements mentioned above are presented in more details, but not exhaustively.

Bulk material is used for its own dispersion. As explained previously in 5, the dispersion of the material modifies the spectral phase of the pulse, leading to an increase or a shortening of the pulse duration. Different materials and thicknesses might be combined for fine tuning of the spectral phase. The dispersion curve of each material presents a zero-crossing; the material dependent zero-dispersion wavelength (ZDW) varies between 1.275 µm for fused silica and 4.81 µm for ZnSe (*e.g.*: 1.6 µm for YAG, 1.545 µm for CaF_2, 1.315 µm for sapphire). For wavelengths below or above the ZDW, the dispersion is positive or negative, respectively.

Double-chirped mirrors (DCM) are Bragg mirrors with a double-periodic structure. These mirrors are usually designed in pair to cancel out fine oscillations in the spectral phase. Their spectral width is limited as well as the total attainable chirp: the broader the spectrum, the less achievable amount of chirp. Extending the spectral coverage over one octave is challenging and leads to reduced reflection values. A

DCM design up to two octaves has been demonstrated in [211], however with 95% reflection efficiency. Typically, DCMs are designed to introduce negative dispersion.

Prism, grating and grism are arranged geometrically to introduce negative or positive dispersion; grisms are a combination of gratings with a prism pair. Grating and prism pairs were presented in section 5: in these configurations, the higher order dispersion are geometrically determined. The sign of the higher orders alternate for odd and even orders. The combination of gratings and prisms forming a grism pair introduces flexibility in the design of the higher oder dispersion: designs with all negative dispersion orders or with different ratios between GDD, TOD and FOD are possible. These solutions are limited to less than one octave spectral width, because of the condition on the diffracted angle in gratings and prisms. They add orders of magnitude more dispersion than bulk materials or DCMs.

Spatial light modulators (SLM) introduce a spatial modulation on the intensity and/or on the phase of a laser pulse. Placed in the center of a zero dispersion pulse compressor, the SLM acts on the spatially chirped laser pulse, *i.e.* on each spectral component. The "zero dispersion pulse compressor" consists in two gratings and two lenses, arranged symmetrically to cancel the dispersion: compared to scheme 5.3, the distance between the image of the first grating and the second grating is set to 0. Due to the use of gratings, the maximum spectral width is limited to less than one octave. In one implementation, the SLM is constituted of a phase mask modulating the phase; another implementation relies on actuators, typically mirrors, to modulate the phase. The resolution is limited by the pixel or actuator size [212]. The throughput of this kind of SLM amounts to 30-50%, which is easily compensated by the next OPCPA stage. The energy is limited to a few µJ.

Dazzler or acousto-optic programmable dispersive filter (AOPDF) is a special type of acousto-optic modulator (AOM) able to modulate the phase and the amplitude of a laser pulse. The working principle of AOMs is to diffract the optical pulse by an acoustic pulse: the latter propagates from a transducer through the crystal, and is seen as a Bragg grating by the optical pulse. In the Dazzler, the spectral phase is modified by diffracting the spectral components at different locations in the crystal and the amplitude by the diffraction efficiency. This device is also limited in its spectral width and resolution, *e.g.* 1.6 nm for the IR Dazzler. The main limitation originates from the compensation of the Dazzler's own dispersion: the material (TeO_2) is less dispersive at 2 µm than in the NIR or in the visible; the Dazzler is able to compensate its own dispersion, still having capabilities to shape the pulses; in the NIR and visible spectral ranges, the higher order dipersion needs to be compensated externally, for example with a grism pair. The throughput of the Dazzler device is defined by the maximum diffraction efficiency, the RF power applied to each spectral components for amplitude shaping and the efficiency of the additional grism pair [213]. For example, a NIR Dazzler combined with a grism pair has an efficiency of ∼4% whereas a MIR one can diffract up to 40%.

8.3.2 Description of the different schemes

The above mentioned schemes for stretching and compressing the pulses will now be presented:

1. **Only bulk materials** used for dispersion compensation are well-adapted for fine-tuning the spectral phase, but presents two drawbacks: as the pulse propagates through the material, it accumulates nonlinear phase-shift and only a few materials have a ZDW high (low) enough to compensate the typically negative (positive) dispersion introduced by other materials in the MIR (NIR).

2. **Bulk stretcher, DCM compressor** In this scheme the stretching is realized by introducing positive dispersion via propagation of the pulses in a bulk material. The pulses are compressed with DCMs after amplification. The choice of materials with positive dispersion around 1.5 µm is limited to a few materials. A candidate is ZnSe, *e.g.* used for this purpose in [20], but the handling of this material is not trivial, in particular the polishing to optical quality. Fine-tuning of the dispersion is performed with wedges controlling the exact material thickness.

3. **DCM stretcher, bulk compressor** The stretcher is realized with DCMs, introducing negative dispersion, and the compressor with propagation through bulk material. Here also the fine-tuning of the dispersion is done with wedges controlling the exact material thickness.

4. **Prism or grating+ SLM stretcher, bulk compressor** In this method, the stretcher is implemented with an SLM based pulse shaper coupled to a prism pair for obtaining the proper dispersion. This introduces negative dispersion, which has to be compensated with a bulk compressor after amplification.

5. **Prism or grism + DAZZLER stretcher, bulk compressor** This metods replaces the SLM pulse shaper of method 4 with a Dazzler. The Dazzler, associated to a prism or grism pair, introduces negative dispersion, which has to be compensated with a bulk compressor adding positive dispersion.

8.3.3 Discussion

For amplification with BBO the dispersion added by the nonlinear crystal is positive for the NIR NOPA and the visible DOPA and negative for the MIR DOPA.

The solution based on bulk material for both stretching and compressing is ruled out due to the lack of materials with positive dispersion in the MIR.

The second and fourth solutions are comparable respectively with the third and fifth ones for the flexibility they offer. The stretcher of solutions 4 and 5 is based on free-programmable devices, which allows for an easy optimization of the dispersion for optimum pulse compression, whereas solutions 2 and 3 are limited by the available materials and their combinations.

The main difference between solutions 2 and 3 relies in the accumulation of nonlinearities during propagation through the materials: solution 2 minimizes the propagation of

the amplified pulses through material compared with solution 3. Using ZnSe for compensating dispersion after amplification is possible, but its nonlinear index of $1.19 \cdot 10^{-14}\mathrm{cm}^2/\mathrm{W}$ at 1.27 µm [214] is extremely high, *i.e.* the pulses accumulate a lot of nonlinear phase-shift. Solution 4 is limited to the bandwidth of the pulse shapers and would strongly narrow down the spectral bandwidth: for example, the bandwidth of the NIR NOPA would decrease from 680-1200 nm to 650-980 nm.

The solution using Dazzler is very flexible in the MIR, where the Dazzler can compensate its own dispersion and supports a spectral bandwidth between 1500 nm and 3000 nm, much broader than the spectral width amplified by the DOPA. On the contrary, the necessary additional compensation of the Dazzler's own dispersion in the NIR, *e.g.* by a grism pair, limits the overall bandwidth of the stretcher. In the NIR domain two designs of grism pairs were examined: the first one ranging from 650 nm to 950 nm is able to compensate the dispersion of the Dazzler up to the FOD, whereas a design supporting the whole bandwidth 650-1150 nm compensates only for the GVD and TOD of the 45 mm long crystal, but let 35000 fs^4 uncompensated. This high amount of FOD would not be compensable with materials or DCMs.

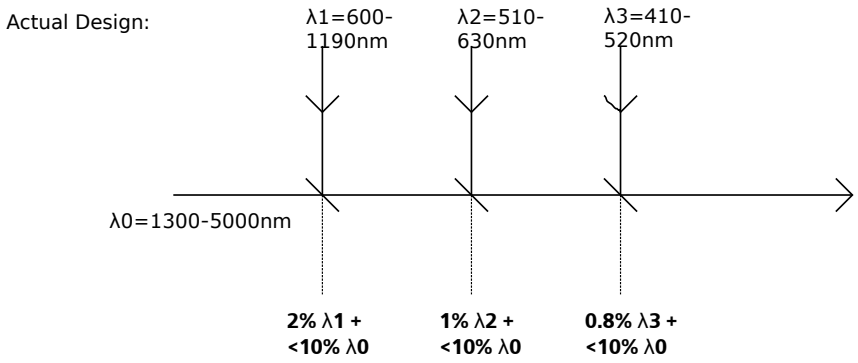

Figure 8.3: Layout for the recombination of all spectra.

In the dispersion management, the beam combiners have to be taken into account. In near future experiments, the amplified spectra will be recombined after the OPCPA stages powered by the regenerative amplifier. This corresponds to the stages demonstrated in the chapter 7. For that, some dichroic mirrors were designed by Layertec GmbH. The recombination will occur as described in figure 8.3: the mirrors transmit the long wavelengths and reflect the short ones, so that the latter are added to the main beam. The substrate of the beam combiners is CaF_2 for its transmission up to 5 µm. Great care was taken to flatten the phase shift introduced by these mirrors, as well in the group delay as in the group delay dispersion.

In the ytterbium based waveform synthesizer, a Dazzler will be used in the MIR to fine-tune the dispersion and to keep flexibility, whereas the NIR channel will be stretched and compressed with bulk materials and DCMs.

Figure 8.4 shows the linear combination of two pulses corresponding to the two channels discussed in chapter 7. The NIR one is centered at 850 nm and is 4 fs transform limited, and the MIR one is centered at 2150 nm and its transform limit is 15 fs. Both were assumed to be Gaussian in time. The obtained pulse duration after synthesis would be between

2.1 fs and 2.9 fs, depending on the energy ratio between the NIR and the MIR pulses. The energy of one pulse was assumed to be normalized to 1 and the energy of the second one varied with the ratios $\lambda_{MIR}/\lambda_{NIR}$, $\lambda_{NIR}/\lambda_{MIR}$, and 1. The electric fields present in the three cases different behaviors: the electric field is the strongest for a higher energy in the MIR than in the NIR with the ratio $\lambda_{MIR}/\lambda_{NIR}$. This situation corresponds simultaneously to the shortest pulse duration. The amount of energy spread in the pedestal is however higher than in the case with the inverse ratio $\lambda_{NIR}/\lambda_{MIR}$. Depending on the application, one configuration or the other might be more suitable.

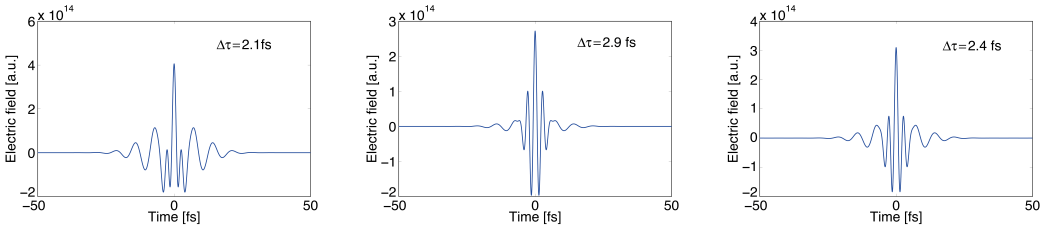

Figure 8.4: Synthesis of NIR and MIR channels: the amplified spectral bandwidth corresponds to 4 fs in the NIR and 15 fs. The energies between the NIR and MIR channels have the ratios: (a) $\lambda_{MIR}/\lambda_{NIR}$, (b) $\lambda_{NIR}/\lambda_{MIR}$, (c) 1 . The electric field is the strongest for a ratio of $\lambda_{MIR}/\lambda_{NIR}$.

The preliminary design of the compression of the MIR channel is shown in figure 8.6a. This shows the electric field of the pulse after each dispersive element. The dispersive elements represented in figure 8.5 comprise the YAG generating white-light, the material stretcher ZnSe, the amplifying BBO crystals, the Dazzler and the recompression with material and DCMs. The phase of the white-light is in the first step assumed to come from the material dispersion. In this scheme, the pulses are shortened during amplification in BBO and it was taken care that the chirp remains negative after each amplifier crystal. If not, the pulse would be compressed during amplification, which would first correspond to a nonmatched overlap of pump and signal pulses and second to ripples in the signal intensity due to non-compensated high-order dispersion leading to superfluorescence. The pulse duration is expected to be between 170 fs und 220 fs before each amplification stage. This design includes a CaF_2 window at the entrance of a vacuum chamber and the beam combiner in the chamber for combination with the other channels of the synthesizer. The final compression is here realized with DCMs to avoid high energies in material; the DCMs deisgned in [211] cover 2 octaves and compensate for 0.33 mm ZnSe. The remaining uncompressed phase shown in figure 8.6b demonstrates near perfect compression.

8.4 Summary

The timing of the pulses at the place of synthesis and the stability of the CEP are key to success in frequency synthesis. The timing compensation and CEP stabilization have been demonstrated in previous works. In this project, they will be implemented at a later stage for compensating the slow variations originating *e.g.* from thermal drifts. The noise sources will be investigated.

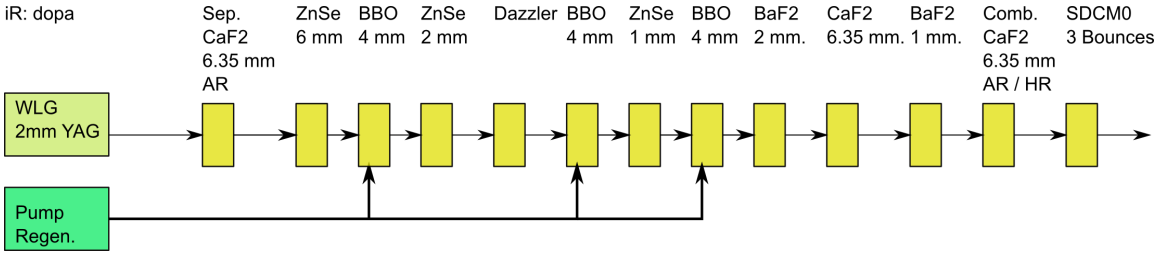

Figure 8.5: Layout for the overall amplification of the MIR channel amplified with the regenerative amplifier and its recompression.

After a discussion on the dispersion management of the synthesizer's channels, a preliminary sketch of the dispersion compensation for the MIR channel was shown, which will be adapted to the experiment after exact measurement of the phase of the amplified pulses. This way, the dispersion management will accomodate the insight gained during the building of the DOPA about the nonlinear phase of the white-light.

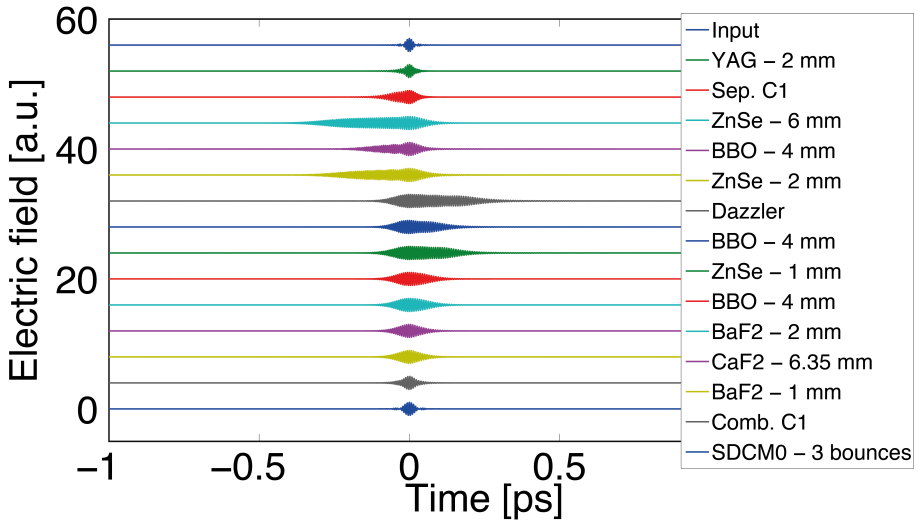

(a)

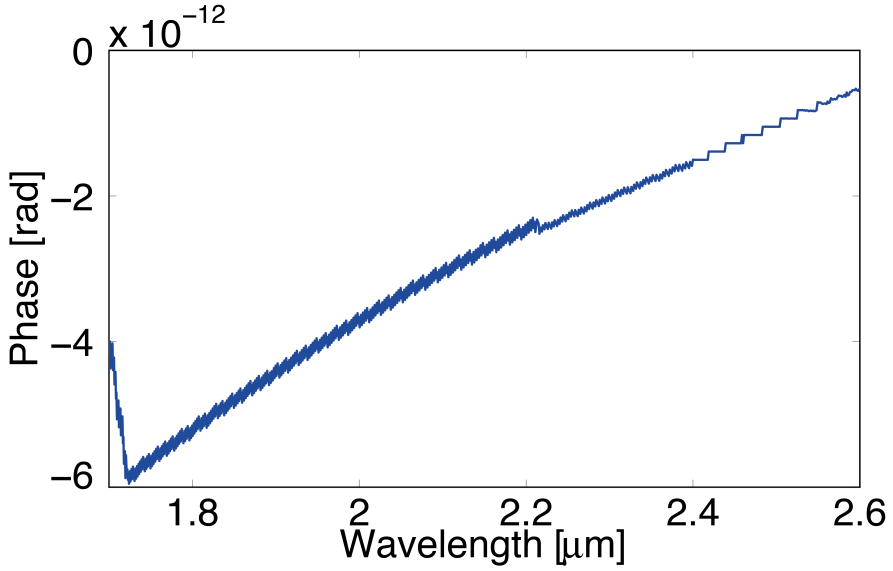

(b)

Figure 8.6: Recompression of the pulses of the MIR channel: (a) Electric field after each dispersive element and (b) remaining phase after compression.

9 Conclusion and outlook

Coherent frequency synthesizers, delivering single to sub-cycle pulses, are promising sources for soft X-ray isolated attosecond pulse generation. This work discussed the development of a high energy, high repetition rate, single-cycle source for such applications. The efficiency of high harmonic generation decreases with the wavelength of the driving pulses to the fifth power, whereas the cut-off photon energy increases with the square of this wavelength, neglecting phase-matching effects. Consequently, high energy, ultrashort pulses are required to fulfill simultaneously both conditions; they might be generated with parametric amplification of a broadband, low-energy seed. The source presented in this work aims at the mJ level, single-cycle pulses at 1 kHz repetition rate. The development of the high energy picosecond lasers for OPCPA pumping is impeded for high repetition rates because of the complex thermal management with high average powers. Ytterbium doped laser materials offer a scalability to high energies and powers, in contrast to Ti:sapphire lasers. The scalability of the spectral width of the broadband, low-energy pulses can be obtained with white-light generation and nonlinear frequency conversion.

In this work, the pump chain of the ytterbium based waveform synthesizer was implemented. It consisted of an oscillator, fiber amplifier, stretcher, regenerative amplifier, cryogenically cooled amplifier and compressor. The regenerative amplifier was based on a dual-crystal linear cavity. Two materials were mainly studied: Yb:CALGO and Yb:KYW. The amplification of 1029 nm centered pulses was limited in the former by the spectral gain shape inducing a strong gain narrowing. In the latter, 31 round trips amplified 0.6 nJ seed pulses to 6.5 mJ at 1 kHz repetition rate. The amplification was found to be in agreement with the simulations of the laser dynamics. The pulses, stretched with 0.8 $^{\mathrm{nm}}/_{\mathrm{ns}}$ with a chirped fiber Bragg grating pulse stretcher, were successfully compressed after the regenerative amplifier to 615 fs with 81% efficiency in a double-deck Treacy compressor. The output pulses of the regenerative amplifier were further amplified to 72 mJ in the cryogenically cooled Yb:YAG thin-disk multipass amplifier. Gain narrowing decreased the spectral bandwidth from 4.5 nm to 3.6 nm after the regenerative ampifier and 0.4 nm after the booster amplifier. The output of the booster amplifier is expected to be compressible to $\sim$3 ps.

The passively carrier envelope phase (CEP) stable front-end driven with part of the compressed output of the regenerative amplifier relied on one white-light generation stage, followed by 2 OPAs amplifying a fraction of the red broadened wing of the white-light for generating a CEP stable white-light in bulk. An experimental study determined the adapted and optimum parameters for generating white-light with sub-picosecond pulses. The spectrum generated in the second white-light generation stage extended from the visible to the mid-infrared and the CEP stability was demonstrated without active feedback over 11 h. The complete electric field of the signal was retrieved from a FROG

measurement and shows that the different stages of the front-end lead to smooth and compressible pulses.

The output of the CEP-stable front-end was split spectrally into the channels of the frequency synthesizer. In the MIR, a degenerate optical parametric amplifier amplified 2 µm centered, 20 fs transform-limit pulses to the µJ level. Finally, the dispersion management of the waveform synthesizer was discussed, with emphasis on the MIR channel.

Future work on the high energy pump chain is the recompression of the amplified pulses to a few picoseconds. After completion of the parametric amplification stages with the remaining energy of the regenerative amplifier, the channels of the synthesizer will be further parametrically amplified to the mJ level with these compressed pulses. After recompression, this source will be a powerful instrument for isolated attosecond generation and other scientific experiments.

10 Appendixes

The first appendix will cover the nonlinear broadening for the version of the Ytterbium waveform synthesizer based on Ti:Sapphire oscillator, as explained in 2: adiabatic frequency conversion will be presented with experimental resultsr. Further appendixes concern optional cavity designs for the regenerative amplifier, and an alternative stretcher design based on Offner stretcher. Finally, a list of abbreviations and a list of symbols complete the appendices.

Appendix A: Adiabatic SFG and DFG

The following text previously partially published in "Highly efficient broadband sum-frequency generation in the visible wavelength range" by Cankaya *et al.* [36].

Optical parametric amplifiers (OPAs) enable broadband amplification with relatively high efficiency. For these amplifier systems seed sources with nJ energy level are favorable to avoid excessive superfluorescence effects in the amplified pulse. Ti:sapphire oscillators are good candidates for seeding of OPAs because of the high, multi-nJ, output pulse energy, well-developed CEP stabilization techniques and ultra broadband spectral coverage in the near infrared region. This coverage is however limited to the near infrared regime, thus restricting the seed bandwidth of the OPAs.

Three-wave mixing processes inside a nonlinear crystal enable wavelength conversion to wavelength regions that are not covered by other broadband laser systems. The conversion bandwidth of the nonlinear processes depends on the phase mismatch parameter between pump, signal and idler pulses, where for ultrafast pulses, the signal bandwidth can reach more than 200 THz [215]. Such broad bandwiths are challenging to phase match. Thin nonlinear crystals can support the broadband three-wave mixing process but at the expense of efficiency. Several techniques were suggested in order to enhance the efficiency over a broad bandwidth such as quasi-phase matching with chirped grating design [216, 217], phase matching in bulk polycrystal [218], achromatic phase matching [219, 220, 221, 222], temperature gradient phase matching in a quasi-phase matched crystal [223] and use of several crystals [217]. While these methods improve efficiency or bandwidth of the conversion process all exhibit a trade-off between bandwidth and efficiency. By using the adiabatic frequency conversion method, based on a mechanism analogous to rapid adiabatic passage from atomic physics, one can overcome this limit [224].

From the analogy, it follows that in order to produce an adiabatic passage of energy from a seed pulse to the frequency converted pulse, the phase mismatch parameter should vary slowly during the conversion process, from a large negative phase mismatch value

to a large positive one (or vice versa). The phase mismatch Δk between the seed (ω_1), pump (ω_p) and SFG ($\omega_3 = \omega_1 + \omega_p$) beams must be swept from $\Delta k < 0$ to $\Delta k > 0$ along the propagation axis in a nonlinear crystal. In the presence of a sufficiently strong pump field, energy is efficiently converted from frequency ω_1 to ω_3. Thus, the adiabatic method relaxes the restriction of minimizing the phase mismatch between the interacting beams, and instead requires Δk to be varied slowly (*i.e.*, adiabatically) during the nonlinear interaction, allowing the system to adapt to the changes caused by the slow phase mismatch. Mathematically, adiabatic evolution means that the system remains in one of its eigenmodes for the entire dynamical evolution.

The amount of adiabaticity is determined by the adiabaticity inequality and can be estimated by the Landau-Zener adiabaticity criteria, detailed in Ref. [224, 225, 226, 227]. Using the adiabaticity criteria for all frequencies involved, a full transition from the signal (the lower state in two level atomic system) to the idler is possible, (the excited state in two level atomic system), thus efficient conversion for a broadband source is achieved. The conversion of each frequency component occurs at a different location along the nonlinear crystal, correlating with the location of $\Delta k(z) \approx 0$ for the interacting waves involved. When the phase matching is tuned over the entire signal spectrum, one can obtain full-photon conversion for very broadband spectra [219, 220, 221, 222].

Adiabatic sum-frequency generation (a-SFG) with over $92 \pm 0.5\%$ photon conversion efficiency was demonstrated using an aperiodically-adiabatively poled KTP crystal [11-14]. In this demonstration, a pulse spectrum covering the range between 660 nm and 990 nm produced by white-light generation is converted by a slowly varying quasi-phase matching grating in a 20-mm-long KTP crystal to the spectral range between 405 nm and 500 nm, corresponding to 140 THz bandwidth. To date of publication, this is the highest efficiency and widest photon up-conversion reported from a sum-frequency generation process. Previous research reported only 11% photon conversion efficiency for an ultrashort pulse with 44 THz bandwidth centered around 765 nm [13], and conversion efficiency of 74 % for a relatively narrow-band, tunable seed source between 1400 nm and 1700 nm [12]. The adiabatic conversion technique was applied not only for sum-frequency generation but also difference-frequency generation [15,16] and OPA's to enhance the efficiency [17,18], reporting nearly full photon conversion efficiency in the MIR [15,16].

The schematic of the experimental setup is shown in Figure 1. A Yb:KYW chirped pulse regenerative amplifier system (Amplitude S-Pulse HP2), delivering 1 mJ-pulses at 1 kHz with pulse duration of 450 fs, centered at 1030 nm wavelength, was used to generate both the signal and pump pulses for a-SFG. A small portion of the pump pulse ($\sim 1.5\%$) was used for pumping the white-light super continuum stage while only 2% of it was used to pump the a-SFG stage. The rest of the pump was kept for further experiments. The output of the amplifier was split by using thin film polarizers (TFPs) coupled with half-wave plates ($\lambda/2$s). The white-light supercontinuum generated in a 6-mm long YAG crystal was used as signal source to test the crystal for a-SFG. The pump beam was focused inside the YAG crystal by using a lens (L1) with 100-mm focal length. The spotsize was measured to be 25 µm. The pump intensity was finely adjusted by employing a variable attenuator before L1. From the white-light process, a continuum covering from 510 nm to the mid-infrared region was obtained. The output of the white-light was collimated by using an off-axis parabolic silver mirror.

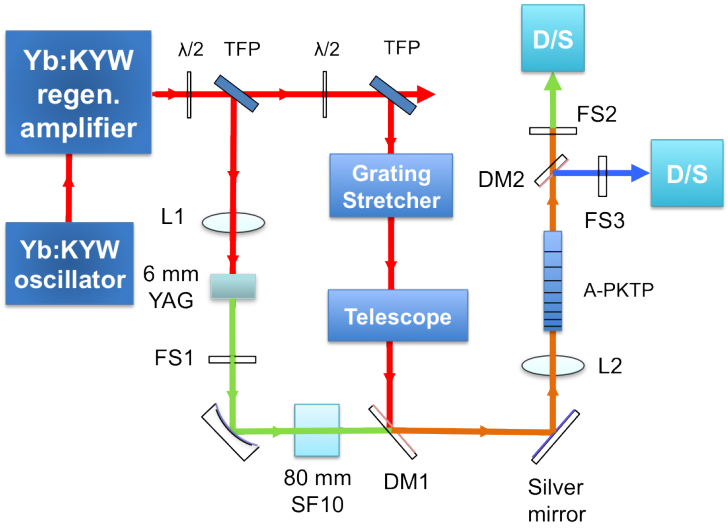

Figure 10.1: Layout of the adiabatic SFG experiment. The signal to be covered was generated via white-light continuum inside a YAG crystal.

An aperiodically-poled KTP crystal (a-PKTP) for a-SFG was designed by Haim Suchowsky supporting a seed spectral range between 660 nm and 990 nm. The poling period of the KTP crystal was varied between 2.1 µm and 5.6 µm, allowing phase matching for the signal wavelength range 660 nm to 990 nm. The corresponding period of the grating, with length of 20 mm is given by the function $K_{QPM} = -30z^3 - 120z^2 - 1900z - 11300[1/mm]$ in terms of distance along the propagation direction (z), centered at the middle of the crystal, where the design principles for the quasi-phasematched grating follow those given in Refs. [11,12]. In contrast to the previous works, the polynomial dependency of the function was directly linked to the bandwidth and the dispersion of the material, which allowed to preserve the adiabaticity condition for the broadband design. By filtering out the spectral range with a combination of short and long-pass filters (FS1), the functionality of the nonlinear crystal was verified in this specific wavelength range.

To minimize temporal walk-off between seed and pump pulses, both seed and pump pulses were stretched. The pump pulse was stretched to 10 ps using a grating pair, where the gold coated gratings with 1200 mm^{-1} grove density were oriented close to the blaze angle and separated by 12 cm from each other, while the seed pulse was stretched using an 80 mm long slab of SF10. The glass thickness was determined by optimizing the photon conversion efficiency in the a-SFG process. The pulse duration of the white-light continuum at the entrance of the crystal was estimated to be 9.6 ps by taking into account dispersion of YAG and SF10 plates.

The signal and pump pulses were combined by a dichroic mirror (DM1) which was highly-reflective (99.9%) at 1030 nm and 95% transmissive for the signal range. The average power of the signal was measured to be 6.5 µW before the crystal corresponding to 6.5 nJ per pulse. Both pump and signal pulses were then focused inside the aperiodically poled KTP crystal by using a lens (L2) with 500 mm focal length. A telescope was employed in the pump arm to match the spotsize of the pump with the signal at the focus inside the KTP crystal. The radii at $1/e^2$ of the pump beam with Gaussian beam

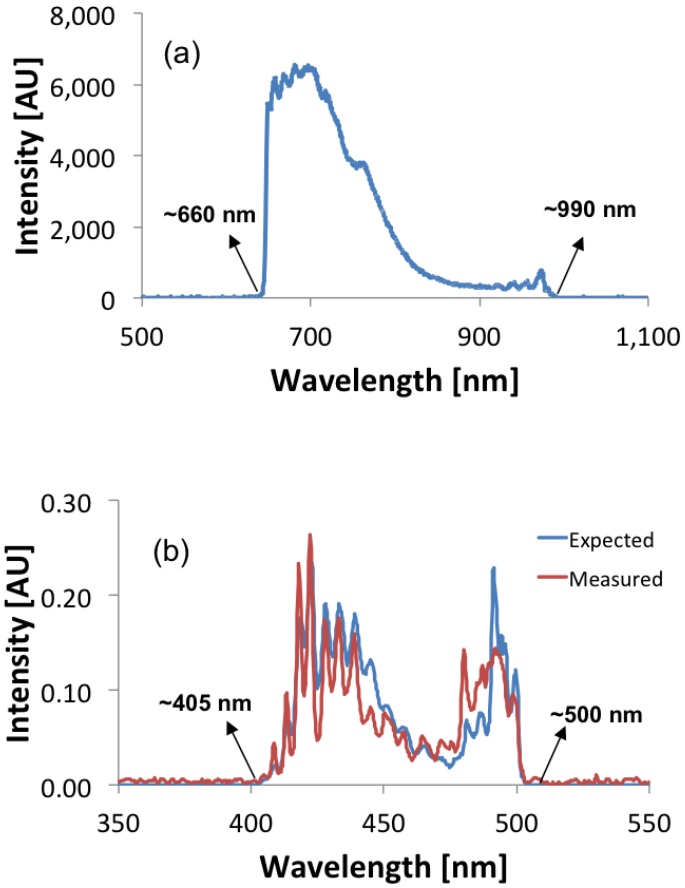

Figure 10.2: (a) Spectrum of white-light super-continuum after the short and longpass filters (FS1). (b) Measured and expected spectrum for a-SFG selected by short pass filters (FS3).

profile were measured to be 53 and 57 µm in x and y axes while the radius of the signal was measured to be 55 µm. An aperture was used in the signal line before focusing to clear up the spatial shape of the beam and reduce the effect of spatial chirp in the outer part of the beam originated from the generation of white-light continuum. During the experiments, the pump energy at the entrance of the crystal was increased up to 1.05 µJ. Assuming 15% Fresnel reflection loss from the surface of the crystal and an effective area of πw_0^2 (w_0 is the radius at $1/e^2$), this corresponds to an intensity of 0.94 $^{\mathrm{GW}}/_{\mathrm{cm}^2}$ inside the crystal to determine the conversion efficiency in the presence of the pump, the depletion of the signal was measured with both a photo-detector (EOT, ET-4000) and an intensity calibrated spectrometer (Ocean Optics, HR4000), (D/S). From the measured signals with and without the presence of the pump, the actual photon-number conversion efficiency was calculated. The SFG signal and the parasitic second-harmonic generation (SHG) signal at 515 nm due to the strong pump were separated by using a dichroic mirror (DM2), which was highly-reflective (> 99 %) for the SFG range and transmissive (> 90 %) at signal and pump wavelengths. During the efficiency measurement two band-pass filters (FS2) were employed to avoid the strong pump and the residual SHG signal present after DM2.

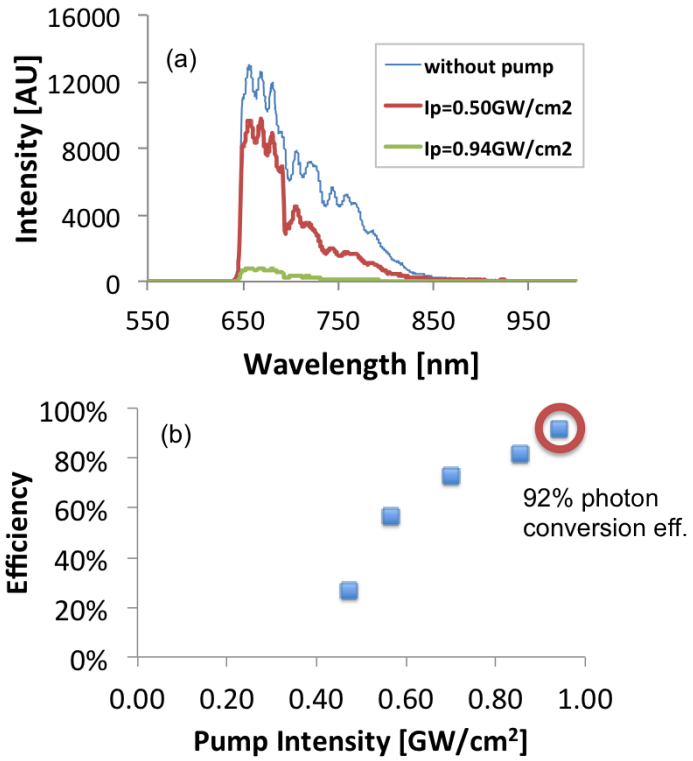

Figure 10.3: (a) Signal spectra in the absence and presence of the pump pulse with intensity of 0.50 $^{GW}/_{cm^2}$ and 0.94 $^{GW}/_{cm^2}$ (b) Photon conversion efficiency in a-SFG process as a function of pump intensity. The measurement accuracy was $\pm 0.5\%$.

The spectrum of the white light continuum before the crystal is shown Figure 2(a). In order to match the design signal wavelength range of the chirped KTP crystal the spectrum was filtered to cover the range between 660 nm and 990 nm. The ripples that are shown close to the lower and higher wavelength edges of the spectrum are due to the transmission of the filters (FS1). In Figure 2(b), the measured and expected spectra of the SFG signal are shown. The same spectrometer was used for the acquisition of the SFG spectra. During the measurement of the SFG spectrum, the parasitic SHG signal was suppressed by using two low pass filters (FS3). The expected SFG spectrum was calculated from the signal spectrum by taking into account the transmission through the short pass filters. The ripples in the SFG spectrum are due to the transmission spectrum of the filters (FS3) used during the measurement. As can be seen from Figure 2(b), there is an excellent agreement between the expected and measured SFG specta.

Figure 3(a) shows the spectra of the white-light supercontinuum after the filters (FS2) in the absence and presence of pump light with an intensity of 0.50 $^{GW}/_{cm^2}$. The modulations in the spectra were due to filters used to cut the pump and residual second harmonic resulting from the strong pumping. As can be seen, in the presence of the pump pulse, nearly uniform spectral depletion of the signal was observed. The discrepancy with the expected uniform spectral depletion was attributed to tolerances in the manufacturing of the aperiodically poled grating. Figure 3(b) shows the integrated photon conversion efficiency

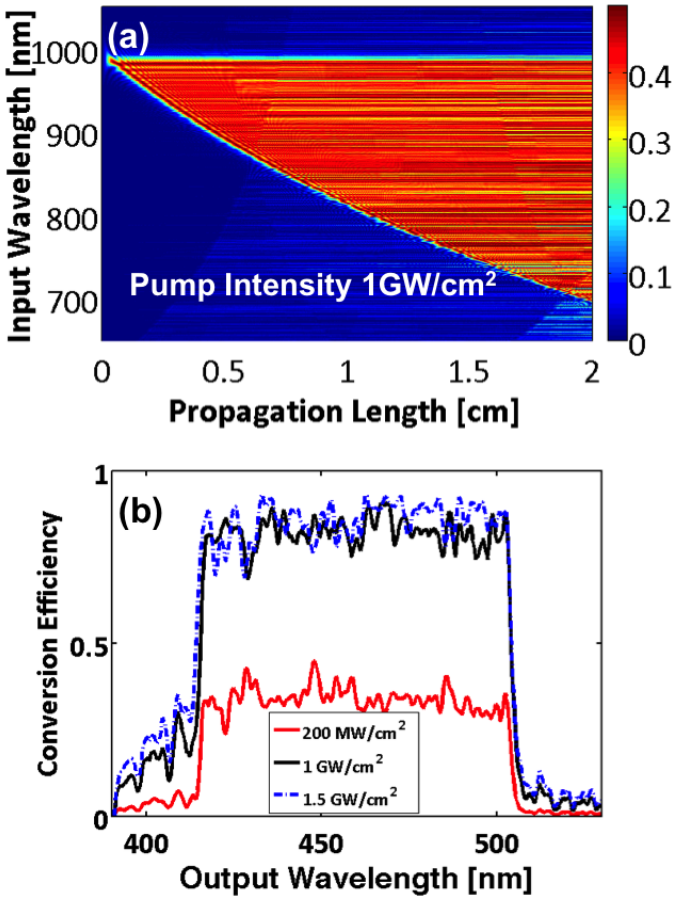

Figure 10.4: (a) Simulation for photon conversion efficiency along the crystal as a function of signal wavelength for pump intensity level 1 $^{GW}/_{cm^2}$ and (b) simulated conversion efficiency at the end of the crystal as a function of wavelength for various pumping levels.

over the spectrum as a function of pump intensity. This curve exhibits an asymptotic behaviour as a function of pump intensity, which is also consistent with the model described in [228]. When the pump intensity increased to 0.94 $^{GW}/_{cm^2}$, the SFG photon conversion efficiency increased up to $92 \pm 0.5\%$. Above that intensity value reproduceable damages on the surface of the crystal were observed.

Figure 4(a) shows numerical simulations of the photon conversion efficiency along the aperiodically-poled KTP as a function of signal wavelength for a pumping level of 1 $^{GW}/_{cm^2}$. The simulation, based on the finite difference method, was done for several pump intensities. As can be seen from the simulation, the conversion efficiency was constant along the crystal, which is also consistent with the experimentally measured signal depletion shown in Figure 3(a). In Figure 4(b), the conversion efficiency at the end of the crystal (L = 2 cm) is shown as a function of signal wavelength for three pumping levels: 200 $^{MW}/_{cm^2}$, 1 $^{GW}/_{cm^2}$ and 1.5 $^{GW}/_{cm^2}$. As can be seen, for a further increase in the pump intensity from 1 $^{GW}/_{cm^2}$ to 1.5 $^{GW}/_{cm^2}$, the conversion efficiency would increase only incrementally, following the prediction of the Landau-Zener adiabatic theory.

In conclusion, highly efficient sum frequency generation via Landau-Zener adiabatic transfer was experimentally demonstrated in an aperiodically poled KTP crystal for the spectral signal range of 660 nm to 990 nm. The photon conversion efficiency was measured to be $92 \pm 0.5\%$ for a very broad spectrum converted to 405 nm to 500 nm when the pump intensity was close to 1 $^{GW}/_{cm^2}$. This is the highest conversion efficiency demonstrated to date for SFG. Such broadband visible spectra can be used to seed a visible OPA for high harmonic generation or electron tip emission experiments.

Appendix B: Cavity designs

The simulations of different cavities for the regenerative amplifier are shown below.

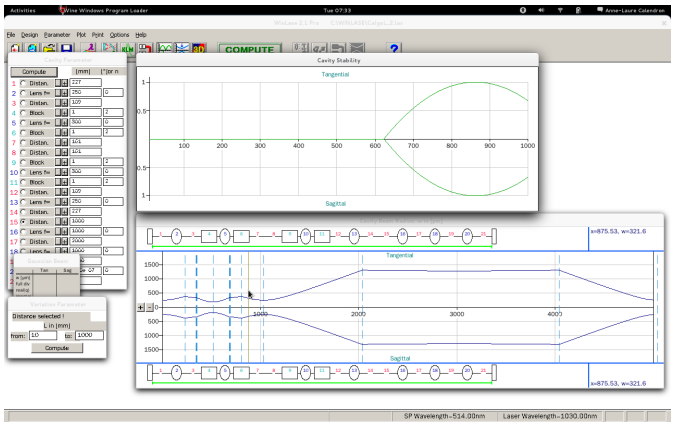

(a) Long cavity with 4-f telescope – f = 1000 mm

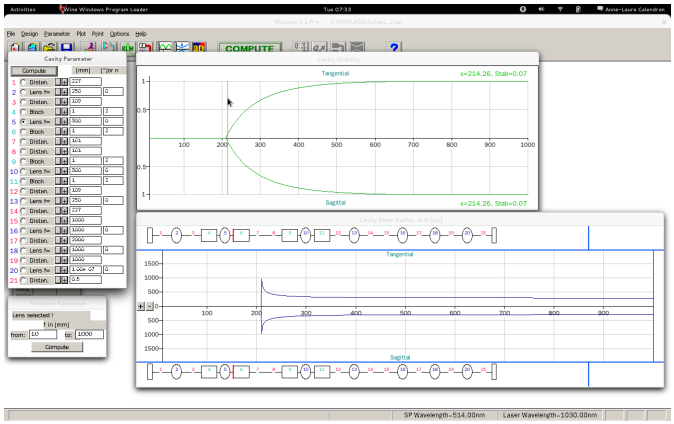

(b) Stability domain and spot variation in the crystal

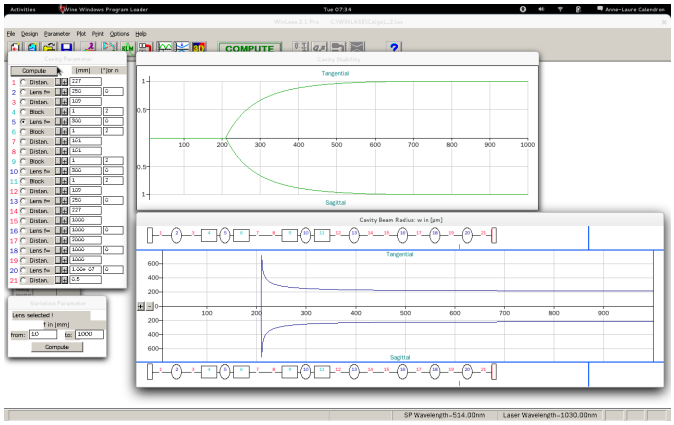

(c) Stability domain and spot variation on the end mirror

Figure 10.5: Long cavity with 4-f telescope based on 1000 mm focal lengths, with the sability domains and the waist evolution as a function of the thermal lens in one of the crystals

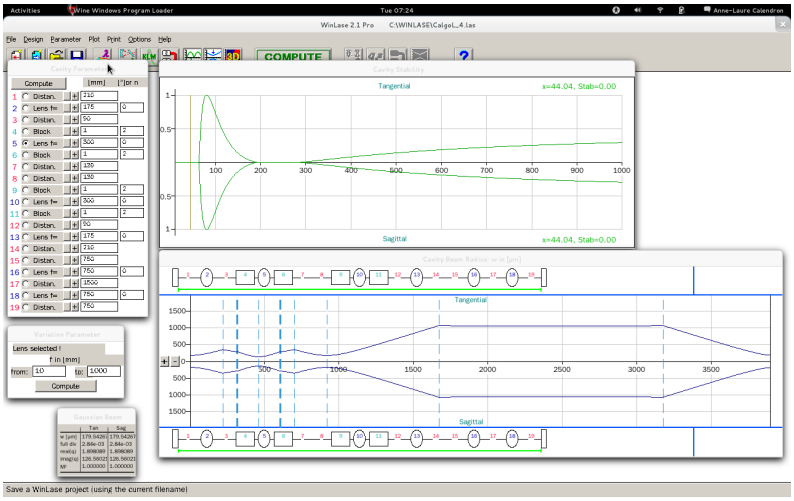

(a) Long cavity with 4-f telescope – f = 750 mm

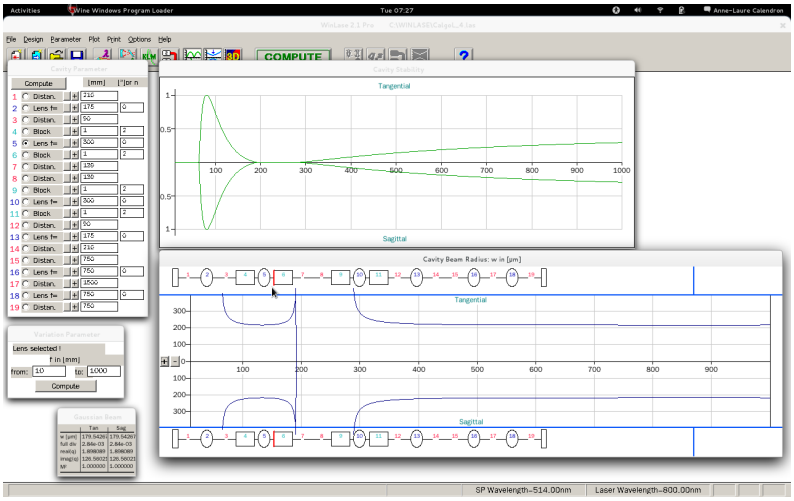

(b) Stability domain and spot variation in the crystal

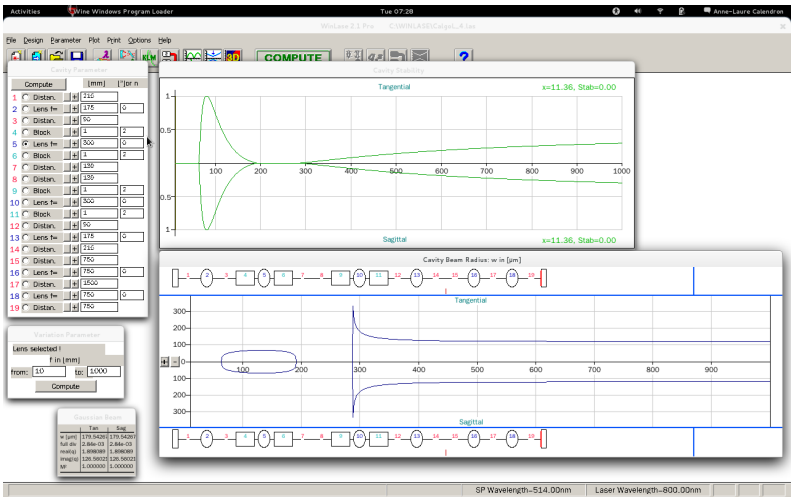

(c) Stability domain and spot variation on the end mirror

Figure 10.6: Long cavity number with 4-f telescope based on 1000 mm focal lengths, with the sability domains and the waist evolution as a function of the thermal lens in one of the crystals

Appendix C: Offner stretcher

The Offner stretcher (*cf.* figure 10.7) has the advantage of reducing the spatial aberrations introduced in the beam. Both convex and concave mirrors are centered in C. The image of the grating is slightly decentered. The grating is aligned close to Littrow angle, which makes the alignment easier and increases the stability of the whole system. The radius of curvature of the convex mirror is half the one of the concave mirror.

A geometric analysis of the Offner stretcher has been published in [147]. The distances are represented on figure 10.7. The formula of the slant distance b becomes:

$$b = \frac{G}{cos(\gamma - \theta_0 - \theta_6)} = (S_6 - S_1)\frac{cos(\gamma - \theta_0)}{cos(\gamma - \theta_0 - \theta_6)} \tag{10.1}$$

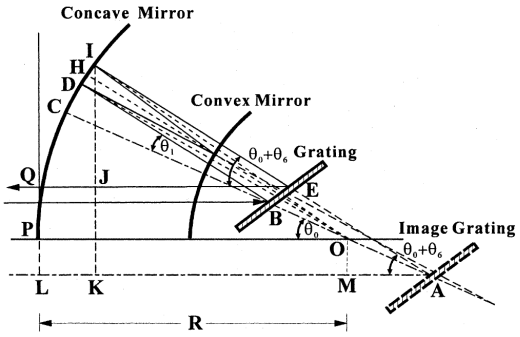

Figure 10.7: Layout of an Offner stretcher. [147]

Taking into account the minimal and maximal diffraction angle for the extreme wavelengths of the spectrum and the incoming beam radius of ∼1 mm, the beam radii of the spatially chirped beam are as follows: $w_0 = 18\ mm$, $w_1 = 8\ mm$, $w_2 = 34\ mm$, $w_3 = 26\ mm$. Both mirrors would be tilted by $-0.8°$ and $3.3°$ relative to the first diffracted beam. The mirror diameters, defined so that the spectrum is not clipped, are 440 mm and 73 mm. The grating aperture would be 340 mm under Littrow angle to contain the 4 beams with 3 times their radius to avoid clipping. The roof mirror width is 220 mm.

The calculated Offner stretcher only allows 2 ns for >7 nm spectrum (*cf.* sec. 5.2).

Appendix D: List of abbreviations

ASE	Amplified spontaneous emission
BBO	Beta baryum borate
BOC	Balance optical cross-correlator
CEP	Carrier envelope phase
CFBG	Chirped fiber Bragg grating
CPA	Chirped pulse amplification
CTD	Composite thin-disk
CVBG	Chirped volume Bragg grating
DCM	Double-chirped mirror
(a-)DFG	(adiabatic) Difference frequency generation
DOPA	Degenerate OPA
EUV	Extrem ultra-violet
FWHM	Full-width half-maximum
GD	Group delay
GDD	Group-delay dispersion
GVM	Group-velocity mismatch
LBO	Lithium tri-borate
MFD	Mode-field diameter
MIR	Mid-infrared
MPE	Multi-photon excitation
NIR	Near-infrared
NL	Nonlinear
OPA	Optical parametric amplifier
NOPA	Non-collinear OPA
OPCPA	Optical parametric chirped pulse amplifier
rms	Root-mean square
SC	Super-continuum
(a-)SFG	(adiabatic) Sum frequency generation
SHG	Second-harmonic generation
TOD	Third-order dispersion
UV	Ultra-violet
WL	Whilte-light
WLG	Whilte-light generation
Yb:CALGO	Ytterbium doped calcium gadolinium aluminium oxyde
YDFA	Ytterbium doped fiber amplifier
Yb:KYW	Ytterbium doped tungstate
Yb:YAG	Ytterbium doped yttrium aluminium garnet

Table 10.1: List of abbreviations

Appendix E: List of symbols

α	thermal expansion coefficient	$10^{-}6\ \mathrm{m}^{-1}\mathrm{K}^{-1}$
$\Delta\lambda$	spectral width	nm
κ	thermal conductivity	$\mathrm{m\ K}^{-1}$
λ	wavelength	nm
λ_P	pump wavelength (regenerative amplifier)	nm
λ_L	laser wavelength (regenerative amplifier)	nm
λ_F	fluorescence wavelength (regenerative amplifier)	nm
λ_p	pump wavelength	nm
λ_s	signal wavelength	nm
λ_i	idler wavelength	nm
ω	frequency	Hz
τ	pulse duration	s
B_{int}	nonlinear phase shift	–
E	energie	J
F	fluence	$^{J}/_{\mathrm{cm}^2}$
I	intensity	$^{W}/_{\mathrm{cm}^2}$
n_0	refractive index	–
n_2	nonlinear refractive index	$^{\mathrm{cm}^2}/_{W}$

Table 10.2: List of symbols with unit

List of Figures

List of Tables

Publication list

[1]A.-L. Calendron, H. Cankaya, G. Cirmi, and F. X. Kärtner, "White-light generation with sub-ps pulses," *Optics Express*, p. submitted, 2015.

[2]S. Carbajo, P. Alcorta, A.-L. Calendron, H. Cankaya, K. Ravi, X. Wu, F. Ahr, and F. X. Kärtner, "Towards GV/m terahertz transients," *Optica*, p. in preparation, 2015.

[3]L. E. Zapata, H. Lin, A.-L. Calendron, H. Cankaya, W. R. Huang, E. Granados, K.-H. Hong, and F. X. Kärtner, "Cryogenic Yb:YAG composite-thin-disk for high energy and average power amplifiers," *Optics Letters*, p. accepted for publication, 2015.

[4]A.-L. Calendron, H. Çankaya, and F. X. Kärtner, "High-energy kHz Yb:KYW dual-crystal regenerative amplifier," *Optics Express*, vol. 22, no. 20, pp. 24752–24762, 2014.

[5]H. Cankaya, A.-L. Calendron, H. Suchowski, and F. X. Kärtner, "Highly efficient broadband sum-frequency generation in the visible wavelength range," *Optics Letters*, vol. 39, no. 10, pp. 2912–2915, 2014.

[6]A.-L. Calendron, "Dual-crystal Yb:CALGO high power laser and regenerative amplifier," *Optics Express*, vol. 21, no. 22, pp. 26174–26181, 2013.

[7]A. L. Calendron, K. S. Wentsch, and M. J. Lederer, "High power cw and mode-locked oscillators based on Yb:KYW multi-crystal resonators," *Optics Express*, vol. 16, no. 23, pp. 18838–18843, 2008.

[8]A.-L. Calendron, H. Cankaya, L. E. Zapata, H. Lin, G. Cirmi, G. M. Rossi, O. D. Mücke, and F. X. Kärtner, "Dpg frühjahrstagung," in *DPG Frühjahrstagung*, p. K22 K4.2, Deutsche Physikalische Gesellschaft, 2015.

[9]M. Hemmer, F. Reichert, K. Zapata, M. Smrz, A.-L. Calendron, H. Cankaya, K.-H. Hong, F. X. Kärtner, and L. E. Zapata, "Picosecond 115 mJ energy, 200 Hz repetition rate cryogenic Yb:YAG bulk amplifier," in *2015 Conference on Lasers and Electro-Optics*, p. STu4O.3, Optical Society of America, 2015.

[10]P. Krötz, A. Rühl, K. Murari, H. Cankaya, A.-L. Calendron, F. X. Kärtner, I. Hartl, and R. J. D. Miller, "High energy and low noise Ho:YLF regenerative amplifiers: A noise and stability analysis," in *2015 Conference on Lasers and Electro-Optics*, p. SF1F.3, Optical Society of America, 2015.

[11]S. Carbajo, P. Alcorta, A.-L. Calendron, H. Cankaya, X. Wu, K. Ravi, F. Ahr, W. R. Huang, and F. X. Kärtner, "On extracting the maximum terahertz conversion efficiency from optical rectification in lithium niobate," in *2015 Conference on Lasers and Electro-Optics*, p. SM2H.3, Optical Society of America, 2015.

[12]H. Cankaya, A.-L. Calendron, G. Cirmi, and F. X. Kärtner, "Front-end of Yb-based high energy optical waveform synthesizer," in *2015 Conference on Lasers and Electro-Optics*, p. SW4O.7, Optical Society of America, 2015.

[13]A.-L. Calendron, H. Cankaya, G. Cirmi, G. M. Rossi, and F. X. Kärtner, "White-light generation pumped by sub-ps pulses," in *2015 Conference on Lasers and Electro-Optics*, p. FTu4D.3, Optical Society of America, 2015.

[14]F. Reichert, M. Hemmer, A.-L. Calendron, H. Cankaya, K. Zapata, M. Smrz, L. E. Zapata, and F. X. Kärtner, "100 mJ, 200 Hz, cryogenic Yb:YAG composite thin-disk laser amplifier," in *2015 European Conference on Lasers and Electro-Optics*, pp. CA–10.2, Optical Society of America, 2015.

[15]P. Krötz, A. Rühl, G. Chatterjee, K. Murari, H. Cankaya, A.-L. Calendron, F. X. Kärtner, I. Hartl, and R. J. D. Miller, "Highly stable and high pulse energy, double-z-cavity shaped Ho:YLF regenerative amplifier," in *2015 European Conference on Lasers and Electro-Optics*, pp. CA–4.2, Optical Society of America, 2015.

[16]A.-L. Calendron, H. Cankaya, G. Cirmi, and F. X. Kärtner, "Towards a dual-channel Yb-pumped broadband OPCPA synthesizer," in *2015 European Conference on Lasers and Electro-Optics*, pp. CF–9.1, Optical Society of America, 2015.

[17]A.-L. Calendron, L. E. Zapata, H. Cankaya, H. Lin, and F. X. Kärtner, "High energy, high repetition rate pump laser system for OPCPAs," in *6th EPS-QEOD Europhoton Conference*, pp. TuA–T1–O–05, European Physical Society, 2014.

[18]A. Choudhuri, H. Zia, A.-L. Calendron, H. Cankaya, F. X. Kärtner, I. Hartl, R. J. D. Miller, and A. Ruehl, "Full 3D simulation of white-light generation in bulk materials," in *6th EPS-QEOD Europhoton Conference*, pp. ThB–T1–O–07, European Physical Society, 2014.

[19]H. Cankaya, A.-L. Calendron, and F. X. Kärtner, "Passively CEP-stable front end for frequency synthesis," in *XIXth Conference on Ultrafast Phenomena*, p. 07.Mon.P1.58, OSA, 2014.

[20]A.-L. Calendron, H. Cankaya, and F. X. Kärtner, "1 kHz, multi-mJ Yb:KYW bulk regenerative amplifier," in *Research in Optical Sciences*, OSA Technical Digest of QIM conference, p. JW2A.16, Optical Society of America, 2014.

[21]A.-L. Calendron, H. Cankaya, and F. X. Kärtner, "1 kHz, multi-mJ Yb:KYW bulk regenerative amplifier," in *Research in Optical Sciences*, OSA Technical Digest of HILAS conference, p. JW2A.16, Optical Society of America, 2014.

[22]A.-L. Calendron, L. E. Zapata, H. Cankaya, H. Lin, and F. X. Kärtner, "Optimized temperature/bandwidth operation of cryogenic Yb:YAG composite thin-disk laser amplifier," in *Research in Optical Sciences*, OSA Technical Digest of QIM conference, p. JW2A.10, Optical Society of America, 2014.

[23]A.-L. Calendron, L. E. Zapata, H. Cankaya, H. Lin, and F. X. Kärtner, "Optimized temperature/bandwidth operation of cryogenic Yb:YAG composite thin-disk laser amplifier," in *Research in Optical Sciences*, OSA Technical Digest of HILAS conference, p. JW2A.10, Optical Society of America, 2014.

[24]A.-L. Calendron, M. Lederer, H. Cankaya, and F. X. Kärtner, "High power Yb:CALGO multi-crystal oscillator," in *2013 Conference on Lasers and Electro-Optics - International Quantum Electronics Conference*, p. CA_4_3, Optical Society of America, 2013.

[25]H. Cankaya, A.-L. Calendron, H. Suchowski, and F. X. Kärtner, "Adiabatic sum-frequency generation in the visible region," in *Advanced Solid-State Lasers Congress* (G. Huber and P. Moulton, eds.), OSA Technical Digest, p. ATu4A.9, Optical Society of America, 2013.

[26]L. E. Zapata, W. Huang, H. Cankaya, A.-L. Calendron, H. Lin, E. Granados, K.-H. Hong, and F. X. Kärtner, "High energy and power cryogenic composite-thin-disk Yb:YAG laser," in *2013 Conference on Lasers and Electro-Optics - International Quantum Electronics Conference*, p. CA_7_4, Optical Society of America, 2013.

[27]L. E. Zapata, H. Lin, H. Cankaya, A.-L. Calendron, W. Huang, K.-H. Hong, and F. X. Kärtner, "Cryogenic composite thin disk high energy pulsed, high average power, diffraction limited multi-pass amplifier," in *Advanced Solid-State Lasers Congress* (G. Huber and P. Moulton, eds.), OSA Technical Digest, p. AF3A.10, Optical Society of America, 2013.

[28]J. Lim, H.-W. Chen, A.-L. Calendron, G. Chang, and F. X. Kärtner, "Optimization of ultrafast Yb-doped fiber amplifiers to achieve high-quality compressed-pulses," in *XVIIIth Conference on Ultrafast Phenomena*, p. TUE.PII.2, OSA, 2012.

[29]A.-L. Calendron, K. S. Wentsch, J. Meier, and M. J. Lederer, "High power and high energy Yb:KYW regenerative amplifier using a chirped volume Bragg grating," in *2009 Conference on Lasers and Electro-Optics - International Quantum Electronics Conference*, vol. High Peak Intensity Lasers (CFD), p. CFD2, Optical Society of America, 2009.

Bibliography

[1] A. Einstein, "Friedrich Kottler's essay "Einstein's equivalence hypothesis and gravitation"," *Annalen Der Physik*, vol. 51, no. 22, pp. 639–642, 1916.

[2] A. L. Schawlow and C. H. Townes, "Infrared and optical masers," *Physical Review*, vol. 112, no. 6, pp. 1940–1949, 1958.

[3] T. H. Maiman, "Stimulated optical radiation in ruby," *Nature*, vol. 187, no. 4736, pp. 493–494, 1960.

[4] P. F. Moulton, "Spectroscopic and laser characteristics of Ti-Al_2O_3," *Journal of the Optical Society of America B-Optical Physics*, vol. 3, no. 1, pp. 125–133, 1986.

[5] F. Krausz and M. Ivanov, "Attosecond physics," *Reviews of Modern Physics*, vol. 81, no. 1, pp. 163–234, 2009.

[6] H. N. Chapman, "Microscopy a new phase for X-ray imaging," *Nature*, vol. 467, no. 7314, pp. 409–410, 2010.

[7] H. N. Chapman, P. Fromme, A. Barty, T. A. White, R. A. Kirian, A. Aquila, M. S. Hunter, J. Schulz, D. P. DePonte, U. Weierstall, R. B. Doak, F. R. N. C. Maia, A. V. Martin, I. Schlichting, L. Lomb, N. Coppola, R. L. Shoeman, S. W. Epp, R. Hartmann, D. Rolles, A. Rudenko, L. Foucar, N. Kimmel, G. Weidenspointner, P. Holl, M. N. Liang, M. Barthelmess, C. Caleman, S. Boutet, M. J. Bogan, J. Krzywinski, C. Bostedt, S. Bajt, L. Gumprecht, B. Rudek, B. Erk, C. Schmidt, A. Homke, C. Reich, D. Pietschner, L. Struder, G. Hauser, H. Gorke, J. Ullrich, S. Herrmann, G. Schaller, F. Schopper, H. Soltau, K. U. Kuhnel, M. Messerschmidt, J. D. Bozek, S. P. Hau-Riege, M. Frank, C. Y. Hampton, R. G. Sierra, D. Starodub, G. J. Williams, J. Hajdu, N. Timneanu, M. M. Seibert, J. Andreasson, A. Rocker, O. Jonsson, M. Svenda, S. Stern, K. Nass, R. Andritschke, C. D. Schroter, F. Krasniqi, M. Bott, K. E. Schmidt, X. Y. Wang, I. Grotjohann, J. M. Holton, T. R. M. Barends, R. Neutze, S. Marchesini, R. Fromme, S. Schorb, D. Rupp, M. Adolph, T. Gorkhover, I. Andersson, H. Hirsemann, G. Potdevin, H. Graafsma, B. Nilsson, and J. C. H. Spence, "Femtosecond X-ray protein nanocrystallography," *Nature*, vol. 470, no. 7332, pp. 73–U81, 2011.

[8] W. Wurth and D. Menzel, "Ultrafast electron dynamics at surfaces probed by resonant Auger spectroscopy," *Chemical Physics*, vol. 251, no. 1-3, pp. 141–149, 2000.

[9] A. Fohlisch, P. Feulner, F. Hennies, A. Fink, D. Menzel, D. Sanchez-Portal, P. M. Echenique, and W. Wurth, "Direct observation of electron dynamics in the attosecond domain," *Nature*, vol. 436, no. 7049, pp. 373–376, 2005.

[10] P. B. Corkum and F. Krausz, "Attosecond science," *Nature Physics*, vol. 3, no. 6, pp. 381–387, 2007.

[11] W. S. Graves, J. Bessuille, P. Brown, S. Carbajo, V. Dolgashev, K.-H. Hong, E. Ihloff, B. Khaykovich, H. Lin, K. Murari, E. A. Nanni, G. Resta, S. Tantawi, L. E. Zapata, F. X. Kärtner, and D. E. Moncton, "Compact X-ray source based on burst-mode inverse Compton scattering at 100 kHz," *Phys. Rev. ST Accel. Beams*, vol. 17, p. 120701, Dec 2014.

[12] S. Chen, N. D. Powers, I. Ghebregziabher, C. M. Maharjan, C. Liu, G. Golovin, S. Banerjee, J. Zhang, N. Cunningham, A. Moorti, S. Clarke, S. Pozzi, and D. P. Umstadter, "MeV-energy X rays from inverse Compton scattering with laser-wakefield accelerated electrons," *Phys. Rev. Lett.*, vol. 110, p. 155003, Apr 2013.

[13] C. Liu, G. Golovin, S. Chen, J. Zhang, B. Zhao, D. Haden, S. Banerjee, J. Silano, H. Karwowski, and D. Umstadter, "Generation of 9 MeV γ-rays by all-laser-driven Compton scattering with second-harmonic laser light," *Optics Letters*, vol. 39, no. 14, pp. 4132–4135, 2014.

[14] N. D. Powers, I. Ghebregziabher, G. Golovin, C. Liu, S. Chen, S. Banerjee, J. Zhang, and D. P. Umstadter, "Quasi-monoenergetic and tunable X-rays from a laser-driven Compton light source," *Nature Photonics*, vol. 8, no. 1, pp. 28–31, 2014.

[15] W. S. Graves, F. X. Kärtner, D. E. Moncton, and P. Piot, "Intense superradiant X rays from a compact source using a nanocathode array and emittance exchange," *Phys. Rev. Lett.*, vol. 108, p. 263904, Jun 2012.

[16] Z. Chang, *Fundamentals of attosecond optics*. CRC Press, 2011.

[17] G. Cirmi, C. J. Lai, E. Granados, S. W. Huang, A. Sell, K. H. Hong, J. Moses, P. Keathley, and F. X. Kärtner, "Cut-off scaling of high-harmonic generation driven by a femtosecond visible optical parametric amplifier," *Journal of Physics B-Atomic Molecular and Optical Physics*, vol. 45, no. 20, 2012.

[18] C. J. Lai, G. Cirmi, K. H. Hong, J. Moses, S. W. Huang, E. Granados, P. Keathley, S. Bhardwaj, and F. X. Kärtner, "Wavelength scaling of high harmonic generation close to the multiphoton ionization regime," *Physical Review Letters*, vol. 111, no. 7, 2013.

[19] G. Cirmi, G. Rossi, S. Fang, S.-H. Chia, O. D. M¸cke, C. Manzoni, P. Farinello, G. Cerullo, and F. X. Kärtner, "High-energy sub-optical-cycle parametric waveform synthesizer," in *19th International Conference on Ultrafast Phenomena*, OSA Technical Digest, p. 07.Mon.P1.55, Optical Society of America, 2014.

[20] G. M. Rossi, G. Cirmi, S. Fang, S.-H. Chia, O. D. Muecke, F. X. Kärtner, C. Manzoni, P. Farinello, and G. Cerullo, "Spectro-temporal characterization of all channels in a sub-optical-cycle parametric waveform synthesizer," in *CLEO: 2014*, OSA Technical Digest, p. SF1E.3, Optical Society of America, 2014.

[21] F. Bohle, M. Kretschmar, A. Jullien, M. Kovacs, M. Miranda, R. Romero, H. Crespo, U. Morgner, P. Simon, R. Lopez-Martens, and T. Nagy, "Compression of CEP-stable multi-mJ laser pulses down to 4 fs in long hollow fibers," *Laser Physics Letters*, vol. 11, no. 9, 2014.

[22] A. Wirth, M. T. Hassan, I. Grguras, J. Gagnon, A. Moulet, T. T. Luu, S. Pabst, R. Santra, Z. A. Alahmed, A. M. Azzeer, V. S. Yakovlev, V. Pervak, F. Krausz, and E. Goulielmakis, "Synthesized light transients," *Science*, vol. 334, no. 6053, pp. 195–200, 2011.

[23] G. Cerullo, A. Baltuska, O. D. Mucke, and C. Vozzi, "Few-optical-cycle light pulses with passive carrier-envelope phase stabilization," *Laser & Photonics Reviews*, vol. 5, no. 3, pp. 323–351, 2011.

[24] T. W. Hänsch, "Passion for precision," *Chemphyschem*, vol. 7, no. 6, pp. 1170–+, 2006.

[25] A. Harth, M. Schultze, T. Lang, T. Binhammer, S. Rausch, and U. Morgner, "Two-color pumped OPCPA system emitting spectra spanning 1.5 octaves from Vis. to NIR," *Optics Express*, vol. 20, no. 3, pp. 3076–3081, 2012.

[26] D. Grischkowsky and A. C. Balant, "Optical pulse-compression based on enhanced frequency chirping," *Applied Physics Letters*, vol. 41, no. 1, pp. 1–3, 1982.

[27] C. V. Shank, R. L. Fork, R. Yen, R. H. Stolen, and W. J. Tomlinson, "Compression of femtosecond optical pulses," *Applied Physics Letters*, vol. 40, no. 9, pp. 761–763, 1982.

[28] T. T. Luu, M. T. Hassan, A. Moulet, O. Razskazovskaya, N. Kaprowicz, V. Pervak, F. Krausz, and E. Goulielmakis, "Isolated optical attosecond pulses," in *CLEO: 2013*, OSA Technical Digest (online), p. QF1C.6, Optical Society of America.

[29] J. M. Mikhailova, A. Buck, A. Borot, K. Schmid, C. Sears, G. D. Tsakiris, F. Krausz, and L. Veisz, "Ultra-high-contrast few-cycle pulses for multipetawatt-class laser technology," *Optics Letters*, vol. 36, no. 16, pp. 3145–3147, 2011.

[30] D. Herrmann, L. Veisz, R. Tautz, F. Tavella, K. Schmid, V. Pervak, and F. Krausz, "Generation of sub-three-cycle, 16 TW light pulses by using noncollinear optical parametric chirped-pulse amplification," *Optics Letters*, vol. 34, no. 16, pp. 2459–2461, 2009.

[31] S. Fang, H. Ye, G. Cirmi, S.-H. Chia, S. Carbajo, O. D. Mücke, and F. X. Kärtner, "High-energy carrier-envelope phase-stable optical waveforms compressible to <1 fs using induced-phase modulation in argon-filled hollow-core fiber," in *Research in*

Optical Sciences, OSA Technical Digest, p. HW1C.2, Optical Society of America, 2014.

[32] S. W. Huang, G. Cirmi, J. Moses, K. H. Hong, S. Bhardwaj, J. R. Birge, L. J. Chen, E. Li, B. J. Eggleton, G. Cerullo, and F. X. Kärtner, "High-energy pulse synthesis with sub-cycle waveform control for strong-field physics," *Nature Photonics*, vol. 5, no. 8, pp. 475–479, 2011.

[33] K. Murari, H. Cankaya, P. Li, A. Ruehl, I. Hartl, and F. X. Kärtner, "1.2 mJ, 1 kHz, ps- pulses at 2.05 µm from a Ho:fibre / Ho:YLF laser," in *6th EPS-QEOD Europhoton Conference*, pp. ThD–T1–O–05, European Physical Society, 2014.

[34] H. Suchowski, V. Prabhudesai, D. Oron, A. Arie, and Y. Silberberg, "Robust adiabatic sum frequency conversion," *Optics Express*, vol. 17, p. 12731, 2009.

[35] J. Moses, H. Suchowski, and F. X. Kärtner, "Fully efficient adiabatic frequency conversion of broadband Ti:Sapphire oscillator pulses," *Optics Letters*, vol. 37, no. 9, pp. 1589–1591, 2012.

[36] H. Cankaya, A.-L. Calendron, H. Suchowski, and F. X. Kärtner, "Highly efficient broadband sum-frequency generation in the visible wavelength range," *Optics Letters*, vol. 39, no. 10, pp. 2912–2915, 2014.

[37] N. Bloembergen, "The influence of electron plasma formation on superbroadening in light filaments," *Optics Communications*, vol. 8, no. 4, pp. 285–288, 1973.

[38] J. Dudley and R. Taylor, *Supercontinuum generation in optical fibers*. Cambridge University Press, 1^{st} ed., 2010.

[39] G. Cirmi, C. Manzoni, D. Brida, S. De Silvestri, and G. Cerullo, "Carrier-envelope phase stable, few-optical-cycle pulses tunable from visible to near IR," *Journal of the Optical Society of America B-Optical Physics*, vol. 25, no. 7, pp. B62–B69, 2008.

[40] A. Baltuska, M. Uiberacker, E. Goulielmakis, R. Kienberger, V. S. Yakovlev, T. Udem, T. W. Hänsch, and F. Krausz, "Phase-controlled amplification of few-cycle laser pulses," *IEEE Journal of Selected Topics in Quantum Electronics*, vol. 9, no. 4, pp. 972–989, 2003.

[41] B. Borchers, S. Koke, A. Husakou, J. Herrmann, and G. Steinmeyer, "Carrier-envelope phase stabilization with sub-10 as residual timing jitter," *Optics Letters*, vol. 36, no. 21, pp. 4146–4148, 2011.

[42] K. Okamura and T. Kobayashi, "Octave-spanning carrier-envelope phase stabilized visible pulse with sub-3-fs pulse duration," *Optics Letters*, vol. 36, no. 2, pp. 226–228, 2011.

[43] M. Pergament, M. Kellert, K. Kruse, J. Wang, G. Palmer, L. Wissmann, U. Wegner, and M. J. Lederer, "Burst-mode femtosecond non-collinear parametric amplifier with arbitrary pulse selection," in *CLEO: 2014*, OSA Technical Digest, p. STh4E.4, Optical Society of America, 2014.

[44] M. D. Perry, D. Pennington, B. C. Stuart, G. Tietbohl, J. A. Britten, C. Brown, S. Herman, B. Golick, M. Kartz, J. Miller, H. T. Powell, M. Vergino, and V. Yanovsky, "Petawatt laser pulses," *Optics Letters*, vol. 24, pp. 160–162, 1999.

[45] H. Injeyan and G. D. Goodno, *High power laser handbook*. McGraw Hill, 1^{st} ed., 2011.

[46] K. Hong, J. Gopinath, D. Rand, A. M. Siddiqui, S. Huang, E. Li, B. J. Eggleton, J. D. Hybl, T. Fan, and F. X. Kärtner, "High-energy, kHz-repetition-rate, ps cryogenic Yb:YAG chirped-pulse amplifier," *Optics Letters*, vol. 35, p. 1752, 2010.

[47] P. Maine, D. Strickland, P. Bado, M. Pessot, and G. Mourou, "Generation of ultrahigh peak power pulses by chirped pulse amplification," *IEEE Journal of Quantum Electronics*, vol. 24, pp. 398–403, 1988.

[48] A. Dubietis, G. Jonušauskas, and A. Piskarskas, "Powerful femtosecond pulse generation by chirped and stretched pulse parametric amplification in BBO crystal," *Optics Communications*, vol. 88, no. 4–6, pp. 437–440, 1992.

[49] C. Horvath, A. Braun, H. Liu, T. Juhasz, and G. Mourou, "Compact directly diode-pumped femtosecond Nd:glass chirped-pulse-amplification laser system," *Optics Letters*, vol. 22, pp. 1790–1792, 1997.

[50] C. Jauregui, J. Limpert, and A. Tünnermann, "High-power fibre lasers," *Nature Photonics*, vol. 7, no. 11, pp. 861–867, 2013.

[51] J. Neuhaus, D. Bauer, J. Zhang, A. Killi, J. Kleinbauer, M. Kumkar, S. Weiler, M. Guina, D. H. Sutter, and T. Dekorsy, "Subpicosecond thin-disk laser oscillator with pulse energies of up to 25.9 microjoules by use of an active multipass geometry," *Optics Express*, vol. 16, no. 25, pp. 20530–20539, 2008.

[52] J. Neuhaus, J. Kleinbauer, A. Killi, S. Weiler, D. Sutter, and T. Dekorsy, "Passively mode-locked Yb:YAG thin-disk laser with pulse energies exceeding 13 µJ by use of an active multipass geometry," *Optics Letters*, vol. 33, no. 7, pp. 726–728, 2008.

[53] A. Giesen, H. Hugel, A. Voss, K. Wittig, U. Brauch, and H. Opower, "Scalable concept for diode-pumped high-power solid-state lasers," *Applied Physics B-Lasers and Optics*, vol. 58, no. 5, pp. 365–372, 1994.

[54] T. Metzger, A. Schwarz, C. Yuriko Teisset, D. Sutter, A. Killi, R. Kienberger, and K. F., "High-repetition-rate picosecond pump laser based on a Yb:YAG disk amplifier for optical parametric amplification," *Optics Letters*, vol. 34, p. 2123, 2009.

[55] J. Tümmler, R. Jung, H. Stiel, P. Nickles, and W. Sandner, "High repetition rate chirped-pulse-amplification thin disk laser system with Joule-level pulse energy," *Optics Letters*, vol. 34, p. 1378, 2009.

[56] S. Chenais, F. Druon, S. Forget, F. Balembois, and P. Georges, "On thermal effects in solid state lasers: The case of ytterbium-doped materials," *Progress in Quantum Electronics*, vol. 30, no. 4, pp. 89–153, 2006.

[57] L. F. Johnson, J. E. Geusic, and Vanuiter.Lg, "Coherent oscillations from Tm^{3+},Ho^{3+},Yb^{3+}, and Er^{3+} ions in yttrium aluminum garnet (threshold reduction by energy transfer E)," *Applied Physics Letters*, vol. 7, no. 5, pp. 127–129, 1965.

[58] W. F. Krupke, "Ytterbium solid-state lasers - the first decade," *IEEE Journal of Selected Topics in Quantum Electronics*, vol. 6, no. 6, pp. 1287–1296, 2000.

[59] D. Nickel, C. Stolzenburg, A. Giesen, and F. Butze, "Ultrafast thin-disk Yb : $KY(WO_4)_2$ regenerative amplifier with a 200-kHz repetition rate," *Optics Letters*, vol. 29, no. 23, pp. 2764–2766, 2004.

[60] A. Kessler, M. Hornung, S. Keppler, F. Schorcht, M. Hellwing, H. Liebetrau, J. Körner, A. Sävert, M. Siebold, M. Schnepp, J. Hein, and M. C. Kaluza, "16.6 J chirped femtosecond laser pulses from a diode-pumped Yb:CaF_2 amplifier," *Optics Letters*, vol. 39, no. 6, pp. 1333–1336, 2014.

[61] S. Rivier, X. Mateos, O. Silvestre, V. Petrov, U. Griebner, M. C. Pujol, M. Aguilo, F. Diaz, S. Vernay, and D. Rytz, "Thin-disk Yb:$KLu(WO_4)_2$ laser with single-pass pumping," *Optics Letters*, vol. 33, p. 735, 2008.

[62] D. Papadopoulos, A. Pellegrina, L. P. Ramirez, P. Georges, and F. Druon, "Broadband high energy diode pumped Yb:KYW multipass amplifier," *Optics Letters*, vol. 36, pp. 3816–3818, 2011.

[63] R. Peters, C. Kränkel, K. Petermann, and G. Huber, "Broadly tunable high power Yb:Lu_2O_3 thin disk laser with 80% slope efficiency," *Optics Letters*, vol. 15, p. 7075, 2007.

[64] S. Ricaud, A. Jaffres, P. Loiseau, B. Viana, B. Weichelt, M. Abdou-Ahmed, A. Voss, T. Graf, D. Rytz, M. Delaigue, E. Mottay, P. Georges, and F. Druon, "Yb:$CaGdAlO_4$ thin-disk laser," *Optics Letters*, vol. 36, pp. 4134–4136, 2011.

[65] A. L. Calendron, K. S. Wentsch, and M. J. Lederer, "High power cw and mode-locked oscillators based on Yb:KYW multi-crystal resonators," *Optics Express*, vol. 16, no. 23, pp. 18838–18843, 2008.

[66] J. Mende, G. Spindler, J. Speiser, and A. Giesen, "Concept of neutral gain modules for power scaling of thin-disk lasers," *Applied Physics B-Lasers and Optics*, vol. 97, no. 2, pp. 307–315, 2009.

[67] M. Delaigue, I. Manek-Hönninger, C. Hönninger, A. Courjaud, and E. Mottay, "1 mJ, multi-kHz, sub-500 fs diode-pumped ytterbium laser amplifier," in *Conference on Lasers and Electro-Optics/Quantum Electronics and Laser Science Conference and Photonic Applications Systems Technologies*, OSA Technical Digest Series, p. CMT2, Optical Society of America, 2007.

[68] J. Petit, P. Goldner, and B. Viana, "Laser emission with low quantum defect in Yb:$CaGdAlO_4$," *Optics Letters*, vol. 30, no. 11, pp. 1345–1347, 2005.

[69] J. Boudeile, F. Druon, M. Hanna, P. Georges, Y. Zaouter, E. Cormier, J. Petit, P. Goldner, and B. Viana, "Continuous-wave and femtosecond laser operation of Yb:$CaGdAlO_4$ under high-power diode pumping," *Optics Letters*, vol. 32, pp. 1962–1964, 2007.

[70] P. Loiko, F. Druon, P. Georges, B. Viana, and K. Yumashev, "Thermo-optic characterization of Yb:$CaGdAlO_4$ laser crystal," *Optical Materials Express*, vol. 4, no. 11, pp. 2241–2249, 2014.

[71] A. A. Lagatskii, N. V. Kuleshov, V. G. Shcherbitskii, V. F. Kleptsyn, V. P. Mikhailov, V. G. Ostroumov, and G. Huber, "Lasing characteristics of a diode-pumped Nd^{3+}: $CaGdAlO_4$ crystal," *Quantum Electronics*, vol. 27, no. 1, pp. 15–17, 1997.

[72] P. Loiko, K. V. Yumashev, N. V. Kuleshov, and A. A. Pavlyuk, "Thermo-optical properties of pure and Yb-doped monoclinic $KY(WO_4)_2$ crystals," *Applied Physics B*, vol. 106, pp. 663–668, 2011.

[73] P. Loiko, V. V. Filippov, K. V. Yumashev, N. V. Kuleshov, and A. A. Pavlyuk, "Thermo-optic coefficients study in $KGd(WO_4)_2$ and $KY(WO_4)_2$ by a modified deviation method," *Applied Optics*, vol. 51, no. 15, pp. 2951–2957, 2012.

[74] R. Peters, C. Kränkel, S. T. Fredrich-Thornton, K. Beil, K. Petermann, G. Huber, O. H. Heckl, C. R. E. Baer, C. J. Saraceno, T. Sudmeyer, and U. Keller, "Thermal analysis and efficient high power continuous-wave and mode-locked thin disk laser operation of Yb-doped sesquioxides," *Applied Physics B-Lasers and Optics*, vol. 102, no. 3, pp. 509–514, 2011.

[75] R. Peters, *Ytterbium-dotierte Sesquioxide als hocheffiziente Lasermaterialien*. PhD thesis, Universität Hamburg, 2009.

[76] M. Siebold, S. Bock, U. Schramm, B. Xu, J. L. Doualan, P. Camy, and R. Moncorgé, "Yb:CaF_2 - a new old laser crystal," *Applied Physics B*, vol. 97, no. 2, pp. 327–338, 2009.

[77] F. Jaffres, S. Ricaud, A. Suganuma, B. Viana, P. Loiseau, P. Georges, and F. Druon, "Thermal conductivity versus Yb^{3+} concentration in Yb:CALGO: a material for high power ultrafast laser," in *Proc. SPIE 8621, Optical Components and Materials X, 86211S* (SPIE, ed.), 2013.

[78] S. Chénais, F. Druon, S. Forget, F. Balembois, and P. Georges, "On thermal effects in solid-state lasers: The case of ytterbium-doped materials," *Progress in Quantum Electronics*, vol. 30, no. 4, pp. 89–153, 2006.

[79] T. Y. Fan, D. J. Ripin, R. L. Aggarwal, J. R. Ochoa, B. Chann, M. Tilleman, and J. Spitzberg, "Cryogenic Yb^{3+}-doped solid-state lasers," *IEEE Journal of selected topics in Quantum Electronics*, vol. 13, no. 3, pp. 448–459, 2007.

[80] R. Wynne, J. L. Daneu, and T. Y. Fan, "Thermal coefficients of the expansion and refractive index in YAG," *Applied Optics*, vol. 38, no. 15, pp. 3282–3284, 1999.

[81] F. Druon, S. Ricaud, D. N. Papadopoulos, A. Pellegrina, P. Camy, J. L. Doualan, R. Moncorge, A. Courjaud, E. Mottay, and P. Georges, "On Yb:CaF_2 and Yb:SrF_2: review of spectroscopic and thermal properties and their impact on femtosecond and high power laser performance [invited]," *Optical Materials Express*, vol. 1, no. 3, pp. 489–502, 2011.

[82] K. Beil, C. J. Saraceno, C. Schriber, F. Emaury, O. H. Heckl, C. R. E. Baer, M. Golling, T. Südmeyer, U. Keller, C. Kränkel, and G. Huber, "Yb-doped mixed sesquioxides for ultrashort pulse generation in the thin disk laser setup," *Applied Physics B*, vol. 113, pp. 13–18, 2013.

[83] B. Viana, J. Petit, R. Gaumé, P. Goldner, F. Druon, F. Balembois, and P. Georges, "Crystal chemistry approach in Yb doped laser materials," *Materials Science Forum*, vol. 494, p. 259, 2005.

[84] P.-H. Haumesser, R. Gaumé, B. Viana, and D. Vivien, "Determination of laser parameters of yttervium-doped oxide crystalline materials," *Journal of the Optical Society of America B*, vol. 19, no. 10, pp. 2365–2375, 2002.

[85] J. Dörring, A. Killi, U. Morgner, A. Lang, M. Lederer, and D. Kopf, "Period doubling and deterministic chaos in continuously pumped regenerative amplifiers," *Optics Express*, vol. 12, no. 8, pp. 1759–1768, 2004.

[86] D. E. McCumber, "Einstein relations connecting broadband emission and absorption spectra," *Physical Review*, vol. 136, no. 4A, pp. A954–A957, 1964.

[87] W. B. Fowler and D. L. Dexter, "Relation between absorption and emission probabilities in luminescent centers in ionic solids," *Physical Review*, vol. 128, no. 5, pp. 2154–2165, 1962.

[88] N. V. Kuleshov, A. A. Lagatsky, A. V. Podlipensky, V. P. Mikhailov, and G. Huber, "Pulsed laser operation of Yb-doped $KY(WO_4)_2$ and $KGd(WO_4)_2$," *Optics Letters*, vol. 22, no. 1, pp. 1317–1319, 1997.

[89] O. Svelto, *Principles of Lasers*. Springer, 4^{th} ed., 1998.

[90] M. Grishin, V. Gulbinas, and A. Michailovas, "Dynamics of high repetition rate regenerative amplifiers," *Optics Express*, vol. 15, p. 9434, 2011.

[91] M. Grishin, V. Gulbinas, and A. Michailovas, "Bifurcation suppression for stability improvement in Nd:YVO_4 regenerative amplifier," *Optics Express*, vol. 17, no. 18, pp. 15700–15708, 2009.

[92] A. Major, I. Nikolakakos, J. S. Aitchison, A. I. Ferguson, N. Langford, and P. W. E. Smith, "Characterization of the nonlinear refractive index of the laser crystal Yb:$KGd(WO_4)_2$," *Applied Physics B-Lasers and Optics*, vol. 77, no. 4, pp. 433–436, 2003.

[93] H. Liu, J. Nees, and G. Mourou, "Diode-pumped Kerr-lens mode-locked Yb:$KY(WO_4)_2$ laser," *Optics Letters*, vol. 26, no. 21, pp. 1723–1725, 2001.

[94] R. DeSalvo, A. A. Said, D. J. Hagan, E. W. Van Stryland, and M. Sheik-Bahae, "Infrared to ultraviolet measurements of two-photons absorption and n_2 in wide bandgap solids," *IEEE Journal of Quantum Electronics*, vol. 32, no. 8, pp. 1324–1333, 1996.

[95] M. Bache, H. Guo, B. Zhou, and X. Zeng, "The anisotropic Kerr nonlinear refractive index of the beta-barium borate (β-BaB_2O_4) nonlinear crystal," *Optical Materials Express*, vol. 3, no. 3, pp. 357–382, 2013.

[96] R. W. Boyd and G. L. Fischer, "Nonlinear optical materials," *Encyclopedia of Materials: Science and Technology*, p. 6237–6244, 2001.

[97] M. J. Weber, *Handbook of optical materials*. CRC Press, 1^{st} ed., 2002.

[98] D. M. Pennington, M. A. Henesian, and R. W. Hellwarth, "Nonlinear index of air at 1.053 µm," *Physical Review A*, vol. 39, no. 6, pp. 3003–3009, 1989.

[99] N. Grumman, "TGG (terbium gallium garnet)," *http://www.northropgrumman.com/BusinessVentures/SYNOPTICS/Products/ SpecialtyCrystals/Pages/TGG.aspx*, 2014.

[100] W. Koechner, *Solid-State Laser Engineering*. Springer, 6^{th} ed., 2006.

[101] S. Chénais, F. Balembois, F. Druon, G. Lucas-Leclin, and P. Georges, "Thermal lensing in diode-pumped ytterbium lasers - part I: theoretical analysis and wavefront measurements," *IEEE Journal of Quantum Electronics*, vol. 40, p. 1217, 2004.

[102] S. Chénais, F. Balembois, F. Druon, G. Lucas-Leclin, and P. Georges, "Thermal lensing in diode-pumped ytterbium lasers - part II: Evaluation of quantum efficiencies and thermo-optic coefficients," *IEEE Journal of Quantum Electronics*, vol. 40, p. 1235, 2004.

[103] V. Magni, "Multielement stable resonators containing a variable lens," *Journal of the Optical Society of America A*, vol. 4, pp. 1962–1969, 1987.

[104] R. L. Sutherland, *Handbook of Nonlinear Optics*. Marcel Dekker, Inc., 2^{nd} ed., 2003.

[105] A. Yariv, *Quantum Electronics*. John Wiley & Sons Inc, 1975.

[106] I. Khristov, I. Tomov, and S. Saltiel, "Self-heating effects in electro-optic leight modulators," *Optical and Quantum Electronics*, vol. 15, p. 289, 1983.

[107] G. Goodno, Z. Guo, R. Miller, I. Miller, J. Montgomery, S. Adhav, and R. Adhav, "Investigation of β-BaB_2O_4 as a Q-switch for high power applications," *Applied Physics Letters*, vol. 66, p. 1575, 1995.

[108] Rayleigh, "On the magnetic rotation of light and the second law of thermo dynamics," *Nature*, vol. 64, pp. 577–578, 1901.

[109] A.-L. Calendron, "Dual-crystal Yb:CALGO high power laser and regenerative amplifier," *Optics Express*, vol. 21, no. 22, pp. 26174–26181, 2013.

[110] A.-L. Calendron, H. Cankaya, and F. X. Kärtner, "High-energy kHz Yb:KYW dual-crystal regenerative amplifier," *Optics Express*, vol. 22, no. 20, pp. 24752–24762, 2014.

[111] ISO, "ISO 11146-2:2005 Lasers and laser-related equipment – Test methods for laser beam widths, divergence angles and beam propagation ratios – Part 2: General astigmatic beams," 2013.

[112] K. Naganuma, G. Lenz, and E. Ippen, "Variable bandwidth birefringent filter for stable femtosecond lasers," *IEEE Journal of Quantum Electronics*, vol. 28, no. 10, pp. 2142–2150, 1992.

[113] M. E. Fermann and I. Hartl, "Ultrafast fibre lasers," *Nature Photonics*, vol. 7, no. 11, pp. 868–874, 2013.

[114] G. Schmidt, T. Giesekus, C. Schnitzler, T. Mans, R. Wester, K. M. Du, P. Loosen, and R. Poprawe, "Modeling of partially end-pumped Nd:YAG slab laser," in *Conference on Lasers and Electro-Optics* (S. F. R. F. M. Brueck and F. Leonberger, eds.), OSA Technical Digest, p. CMJ5, Optical Society of America, 1994.

[115] T. Eidam, S. Hanf, E. Seise, T. Andersen, T. V.and Gabler, C. Wirth, T. Schreiber, J. Limpert, and A. Tünnermann, "Femtosecond fiber CPA system emitting 830 W average output power," *Optics Letters*, vol. 35, p. 94, 2010.

[116] F. Roser, T. Eidam, J. Rothhardt, O. Schmidt, D. N. Schimpf, J. Limpert, and A. Tünnermann, "Millijoule pulse energy high repetition rate femtosecond fiber chirped-pulse amplification system," *Optics Letters*, vol. 32, no. 24, pp. 3495–3497, 2007.

[117] J. Limpert, F. Roser, D. N. Schimpf, E. Seise, T. Eidam, S. Hadrich, J. Rothhardt, C. J. Misas, and A. Tünnermann, "High repetition rate gigawatt peak power fiber laser-systems: Challenges, design, and experiment," *IEEE Journal of Selected Topics in Quantum Electronics*, vol. 15, no. 1, pp. 159–169, 2009.

[118] P. Russbueldt, T. Mans, G. Rotarius, J. Weitenberg, H. D. Hoffmann, and R. Poprawe, "400 W Yb:YAG Innoslab fs-amplifier," *Optics Express*, vol. 17, no. 15, pp. 12230–12245, 2009.

[119] C. J. Saraceno, F. Emaury, C. Schriber, M. Hoffmann, M. Golling, T. Südmeyer, and U. Keller, "Ultrafast thin-disk laser with 80 µJ pulse energy and 242 W of average power," *Optics Letters*, vol. 39, no. 1, pp. 9–12, 2014.

[120] A. Giesen and J. Speiser, "Fifteen years of work on thin-disk lasers: Results and scaling laws," *IEEE Journal of Selected Topics in Quantum Electronics*, vol. 13, no. 3, pp. 598–609, 2007.

[121] Amphos GmbH, "Innoslab technology," *http://www.amphos.de/technology.*

[122] J. Dong and P. Deng, "Temperature dependent emission cross-section and fluorescence lifetime of Cr,Yb:YAG crystals," *Journal of Physics and Chemistry of Solids*, vol. 64, no. 7, pp. 1163–1171, 2003.

[123] D. C. Brown, J. M. Singley, K. Kowalewski, J. Guelzow, and V. Vitali, "High sustained average power cw and ultrafast Yb:YAG near-diffraction-limited cryogenic solid-state laser," *Optics Express*, vol. 18, no. 24, pp. 24770–24792, 2010.

[124] P. Mason, K. Ertel, S. Banerjee, P. J. Phillips, C. Hernandez-Gomez, and J. Collier, "An efficient high pulse energy and high average power cryogenic gas cooled multi-slab Yb:YAG amplifier," in *Conference on Lasers and Electro-Optics 2012*, OSA Technical Digest, p. CM3D.1, Optical Society of America, 2012.

[125] K.-H. Hong, C.-J. Lai, J. P. Siqueira, P. Krogen, J. Moses, C.-L. Chang, G. J. Stein, L. E. Zapata, and F. X. Kärtner, "Multi-mJ, kHz, 2.1 µm optical parametric chirped-pulse amplifier and high-flux soft X-ray high-harmonic generation," *Optics Letters*, vol. 39, no. 11, pp. 3145–3148, 2014.

[126] L. Zapata, F. X. Kärtner, E. Granado, and H. K.-H., "Methods, systems, and apparatus for high energy optical-pulse amplification at high average power," *Patent WO2014007900*, 03 2014. Filling num WO2013US34603 20130329.

[127] L. E. Zapata, W. Huang, H. Cankaya, A.-L. Calendron, H. Lin, E. Granados, K.-H. Hong, and F. X. Kärtner, "High energy and power cryogenic composite-thin-disk Yb:YAG laser," in *2013 Conference on Lasers and Electro-Optics - International Quantum Electronics Conference*, p. CA_7_4, Optical Society of America, 2013.

[128] L. E. Zapata, H. Lin, H. Cankaya, A.-L. Calendron, W. Huang, K.-H. Hong, and F. X. Kärtner, "Cryogenic composite thin disk high energy pulsed, high average power, diffraction limited multi-pass amplifier," in *Advanced Solid-State Lasers Congress* (G. Huber and P. Moulton, eds.), OSA Technical Digest, p. AF3A.10, Optical Society of America, 2013.

[129] Y. Takeuchi, J. Kawanaka, and M. Fujita, "Nonlinear refractive index of a YAG crystal at low temperature," in *CLEO Europe 2009*, 2009.

[130] G. P. Agrawal, *Fiber-Optic Communication Systems*. Wiley, 4^{th} ed., 2010.

[131] C. Rouyer, E. Mazataud, I. Allais, A. Pierre, S. Seznec, C. Sauteret, G. Mourou, and A. Migus, "Generation of 50-TW femtosecond pulses in a Ti:Sapphire / Nd:Glass chain," *Optics Letters*, vol. 18, no. 3, pp. 214–216, 1993.

[132] J.-C. Diels and W. Rudolph, *2 - Femtosecond Optics*, pp. 61–142. Ultrashort Laser Pulse Phenomena, Burlington: Academic Press, 2006.

[133] O. E. Martinez, "Grating and prism compressors in the case of finite beam size," *Journal of the Optical Society of America B*, vol. 3, no. 7, pp. 929–934, 1986.

[134] A. Offner, "Unit power imaging catoptric anastigmat," *Patent US3748015*, 7 1971. Filing num 19710621.

[135] J. H. Apfel, "Phase retardance of periodic multilayer mirrors," *Applied Optics*, vol. 21, no. 4, pp. 733–738, 1982.

[136] K. O. Hill, Y. Fujii, D. C. Johnson, and B. S. Kawasaki, "Photosensitivity in optical fiber waveguides - application to reflection filter fabrication," *Applied Physics Letters*, vol. 32, no. 10, pp. 647–649, 1978.

[137] G. Meltz, W. W. Morey, and W. H. Glenn, "Formation of Bragg gratings in optical fibers by a transverse holographic method," *Optics Letters*, vol. 14, no. 15, pp. 823–825, 1989.

[138] J. Martin and F. Ouellette, "Novel writing technique of long and highly reflective in-fiber gratings," *Electronics Letters*, vol. 30, no. 10, pp. 811–812, 1994.

[139] D. Richter, C. Voigtländer, R. G. Krämer, J. U. Thomas, A. Tünnermann, and S. Nolte, "Femtosecond laser pulse written volume Bragg gratings," in *Matec Web of Conferences*, vol. 08, p. 06014, EDP Sciences, 2013.

[140] L. Glebov, "Volume Bragg gratings in PTR glass–new optical elements for laser design," in *3rd Advanced Solid-State Photonics (ASSP) Topical Meeting* (ASSP, ed.), 2008.

[141] T. Komukai, T. Inui, and M. Nakazawa, "Origin of group delay ripple in chirped fiber Bragg gratings and its effective reduction method," *Electronics and Communications in Japan Part Ii-Electronics*, vol. 86, no. 8, pp. 76–84, 2003.

[142] O. M. Efimov, L. B. Glebov, L. N. Glebova, K. C. Richardson, and V. I. Smirnov, "High-efficiency Bragg gratings in photothermorefractive glass," *Applied Optics*, vol. 38, no. 4, pp. 619–627, 1999.

[143] Optigrate, "Specifications of CVBG," *http://optigrate.com/BragGrate_Pulse.html*.

[144] M. Sumetsky, P. I. Reyes, P. S. Westbrook, N. M. Litchinitser, B. J. Eggleton, Y. Li, R. Deshmukh, and C. Soccolich, "Group-delay ripple correction in chirped fiber Bragg gratings," *Optics Letters*, vol. 28, no. 10, pp. 777–779, 2003.

[145] G. Chériaux, *Ultrafast Laser Amplifier Systems*, book section 2, pp. 17–34. Strong Field Laser Physics, Springer New York, 2009.

[146] R. L. Fork, C. H. Brito Cruz, P. C. Becker, and C. V. Shank, "Compression of optical pulses to six femtoseconds by using cubic phase compensation," *Optics Letters*, vol. 12, no. 7, pp. 483–485, 1987.

[147] Z. G. Zhang, Y. R. Song, D. R. Sun, L. Chai, H. Sun, and C. Y. Wang, "Compact and material-dispersion-compatible Offner stretcher for chirped pulse amplifications," *Optics Communications*, vol. 206, no. 1-3, pp. 7–12, 2002.

[148] O. E. Martinez, J. P. Gordon, and R. L. Fork, "Negative group-velocity dispersion using refraction," *Journal of the Optical Society of America A*, vol. 1, no. 10, pp. 1003–1006, 1984.

[149] E. B. Treacy, "Optical pulse compression with diffraction gratings," *IEEE Journal of Quantum Electronics*, vol. 5, no. 9, pp. 454–462, 1969.

[150] A. C. Tien, S. Backus, H. Kapteyn, M. Murnane, and G. Mourou, "Short-pulse laser damage in transparent materials as a function of pulse duration," *Physical Review Letters*, vol. 82, no. 19, pp. 3883–3886, 1999.

[151] R. R. Alfano and S. L. Shapiro, "Emission in region 4000 to 7000 a via 4-photon coupling in glass," *Physical Review Letters*, vol. 24, no. 11, p. 584, 1970.

[152] F. Silva, D. R. Austin, A. Thai, M. Baudisch, M. Hemmer, D. Faccio, A. Couairon, and J. Biegert, "Multi-octave supercontinuum generation from mid-infrared filamentation in a bulk crystal," *Nature Communications*, vol. 3, 2012.

[153] L. Berge, S. Skupin, R. Nuter, J. Kasparian, and J. P. Wolf, "Ultrashort filaments of light in weakly ionized, optically transparent media," *Reports on Progress in Physics*, vol. 70, no. 10, pp. 1633–1713, 2007.

[154] S. L. Chin, *Femtosecond Laser Filamentation*. New York: Springer, 2010.

[155] A. Brodeur and S. L. Chin, "Ultrafast white-light continuum generation and self-focusing in transparent condensed media," *Journal of the Optical Society of America B*, vol. 16, no. 4, pp. 637–650, 1999.

[156] I. Buchvarov, A. Trifonov, and T. Fiebig, "Toward an understanding of white-light generation in cubic media - polarization properties across the entire spectral range," *Optics Letters*, vol. 32, no. 11, pp. 1539–1541, 2007.

[157] A. Brodeur and S. L. Chin, "Band-gap dependence of the ultrafast white-light continuum," *Physical Review Letters*, vol. 80, no. 20, pp. 4406–4409, 1998.

[158] E. O. Smetanina, V. O. Kompanets, S. V. Chekalin, and V. P. Kandidov, "Femtosecond laser pulse filamentation under anomalous dispersion in fused silica. Part 1. numerical investigation," *Quantum Electronics*, vol. 42, no. 10, pp. 913–919, 2012.

[159] C. Nagura, A. Suda, H. Kawano, M. Obara, and K. Midorikawa, "Generation and characterization of ultrafast white-light continuum in condensed media," *Applied Optics*, vol. 41, no. 18, pp. 3735–3742, 2002.

[160] E. O. Smetanina, V. O. Kompanets, S. V. Chekalin, and V. P. Kandidov, "Femtosecond laser pulse filamentation under anomalous dispersion in fused silica. Part 2. experiment and physical interpretation," *Quantum Electronics*, vol. 42, no. 10, pp. 920–924, 2012.

[161] J. B. Ashcom, R. R. Gattass, C. B. Schaffer, and E. Mazur, "Numerical aperture dependence of damage and supercontinuum generation from femtosecond laser pulses in bulk fused silica," *Journal of the Optical Society of America B*, vol. 23, no. 11, pp. 2317–2322, 2006.

[162] A. Pugzlys, P. Malevich, G. Andriukaitis, T. Floery, A. Fernandez, S. Alisauskas, A. Baltuska, L. Tan, C. F. Chua, and P. B. Phua, "High-repetition-rate multi-millijoule femtosecond 2.1 µm Ho:YAG laser," in *Advanced Solid-State Lasers*

Congress (G. Huber and P. Moulton, eds.), OSA Technical Digest, p. AF1A.4, Optical Society of America, 2013.

[163] S. Coean, A. H. L. Chau, R. Leonhardt, J. D. Harvey, J. C. Knight, W. J. Wadsworth, and P. S. J. Russell, "White-light supercontinuum generation with 60-ps pump pulses in a photonic crystal fiber," *Optics Letters*, vol. 26, no. 17, pp. 1356–1358, 2001.

[164] P. A. Champert, V. Coudec, P. Leproux, S. Février, V. Tombelaine, L. Labonté, P. Roy, C. Froehly, and P. Nérin, "White-light supercontinuum generation in normally dispersive optical fiber using original multi-wavelength pumping system," *Optics Express*, vol. 12, no. 19, pp. 4366–4371, 2004.

[165] I. H. Malitson, "Refraction and dispersion of synthetic sapphire," *Journal of the Optical Society of America*, vol. 52, no. 12, pp. 1377–1379, 1962.

[166] D. E. Zelmon, D. L. Small, and R. Page, "Refractive-index measurements of undoped yttrium aluminum garnet from 0.4 to 5.0 µm," *Applied Optics*, vol. 37, no. 21, pp. 4933–4935, 1998.

[167] Y. Takeuchi, J. Kawanaka, and M. Fujita, "Nonlinear refractive index of a YAG crystal at low temperature," *Conference on Lasers and Electro-Optics*, 2009.

[168] A. Major, F. Yoshino, I. Nikolakakos, J. S. Aitchison, and P. W. E. Smith, "Dispersion of the nonlinear refractive index in sapphire," *Optics Letters*, vol. 29, no. 6, pp. 602–604, 2004.

[169] M. D. Levenson, "Feasibility of measuring nonlinear index of refraction by third-order frequency mixing," *IEEE Journal of Quantum Electronics*, vol. Qe10, no. 2, pp. 110–115, 1974.

[170] V. P. Kandidov, O. G. Kosareva, I. S. Golubtsov, W. Liu, A. Becker, N. Akozbek, C. M. Bowden, and S. L. Chin, "Self-transformation of a powerful femtosecond laser pulse into a white-light laser pulse in bulk optical media (or supercontinuum generation)," *Applied Physics B-Lasers and Optics*, vol. 77, no. 2-3, pp. 149–165, 2003.

[171] M. Bellini and T. W. Hänsch, "Phase-locked white-light continuum pulses: toward a universal optical frequency-comb synthesizer," *Optics Letters*, vol. 25, no. 14, pp. 1049–1051, 2000.

[172] J. Darginavicius, D. Majus, V. Jukna, N. Garejev, G. Valiulis, A. Couairon, and A. Dubietis, "Ultrabroadband supercontinuum and third-harmonic generation in bulk solids with two optical-cycle carrier-envelope phase-stable pulses at 2 mu m," *Optics Express*, vol. 21, no. 21, pp. 25210–25220, 2013. 240HI Times Cited:4 Cited References Count:47.

[173] M. Bradler, P. Baum, and E. Riedle, "Femtosecond continuum generation in bulk laser host materials with sub-µJ pump pulses," *Applied Physics B-Lasers and Optics*, vol. 97, no. 3, pp. 561–574, 2009.

[174] H. Cankaya, A.-L. Calendron, and F. X. Kärtner, "Passively CEP-stable front end for frequency synthesis," in *XIXth Conference on Ultrafast Phenomena*, p. 07.Mon.P1.58, OSA, 2014.

[175] J.-C. Diels and W. Rudolph, *9 - Diagnostic Techniques*, pp. 457–489. Ultrashort Laser Pulse Phenomena, Burlington: Academic Press, 2006.

[176] R. Trebino, *Frequency-Resolved Optical Gating: The Measurement of Ultrashort Laser Pulses*. Springer, 2002.

[177] W. Putnam, R. Hobbs, Y. Yang, K. Berggren, and F. Kärtner, "Ultrafast optical-field controlled photoemission from plasmonic nanoparticle arrays," in *19th International Conference on Ultrafast Phenomena*, OSA Technical Digest, p. 08.Tue.B.3, Optical Society of America, 2014.

[178] G. Cerullo and S. De Silvestri, "Ultrafast optical parametric amplifiers," *Review of Scientific Instruments*, vol. 74, no. 1, pp. 1–18, 2003.

[179] P. A. Franken, G. Weinreich, C. W. Peters, and A. E. Hill, "Generation of optical harmonics," *Physical Review Letters*, vol. 7, no. 4, pp. 118–120, 1961.

[180] N. Bloembergen and P. S. Pershan, "Light waves at boundary of nonlinear media," *Physical Review*, vol. 128, no. 2, pp. 606–622, 1962.

[181] B. Boulanger, M. M. Fejer, R. Blachman, and P. F. Bordui, "Study of $KTiOPO_4$ gray-tracking at 1064, 532, and 355-nm," *Applied Physics Letters*, vol. 65, no. 19, pp. 2401–2403, 1994.

[182] C. T. Chen, "The optical properties and growth of a new type ultraviolet SHG crystal β-BaB_2O_4," *Scientia Sinica – Series B (Englisch Edition)*, vol. 7, p. 595, 1984.

[183] C. Chen, Y. Wu, A. Jiang, B. Wu, G. You, R. Li, and S. Lin, "New nonlinear-optical crystal: LiB_3O_5," *Journal of the Optical Society of America B*, vol. 6, no. 4, pp. 616–621, 1989.

[184] A. J. W. Brown, M. S. Bowers, K. W. Kangas, and C. H. Fisher, "High-energy, high-efficiency second-harmonic generation of 1064-nm radiation in KTP," *Optics Letters*, vol. 17, no. 2, pp. 109–111, 1992.

[185] Y. Akahane, M. Aoyama, K. Ogawa, K. Tsuji, S. Tokita, J. Kawanaka, H. Nishioka, and K. Yamakawa, "High-energy, diode-pumped, picosecond Yb:YAG chirped-pulse regenerative amplifier for pumping optical parametric chirped-pulse amplification," *Optics Letters*, vol. 32, no. 13, pp. 1899–1901, 2007.

[186] D. Herrmann, C. Homann, R. Tautz, M. Scharrer, P. S. Russell, F. Krausz, L. Veisz, and E. Riedle, "Approaching the full octave: Noncollinear optical parametric chirped pulse amplification with two-color pumping," *Optics Express*, vol. 18, no. 18, pp. 18752–18762, 2010.

[187] O. Gobert, G. Mennerat, R. Maksimenka, N. Fedorov, M. Perdrix, D. Guillaumet, C. Ramond, J. Habib, C. Prigent, D. Vernhet, T. Oksenhendler, and M. Comte, "Efficient broadband 400 nm noncollinear second-harmonic generation of chirped femtosecond laser pulses in BBO and LBO," *Applied Optics*, vol. 53, no. 12, pp. 2646–2655, 2014.

[188] K.-H. Hong, S.-W. Huang, J. Moses, X. Fu, C.-J. Lai, G. Cirmi, A. Sell, E. Granados, P. Keathley, and F. X. Kärtner, "High-energy, phase-stable, ultrabroadband kHz OPCPA at 2.1 µm pumped by a picosecond cryogenic Yb:YAG laser," *Optics Express*, vol. 19, no. 16, pp. 15538–15548, 2011.

[189] J. Matyschok, T. Lang, T. Binhammer, O. Prochnow, S. Rausch, M. Schultze, A. Harth, P. Rudawski, C. L. Arnold, A. L'Huillier, and U. Morgner, "Temporal and spatial effects inside a compact and CEP stabilized, few-cycle OPCPA system at high repetition rates," *Optics Express*, vol. 21, no. 24, pp. 29656–29665, 2013.

[190] P. Tzankov, J. Zheng, M. Mero, D. Polli, C. Manzoni, and G. Cerullo, "300 µJ noncollinear optical parametric amplifier in the visible at 1 kHz repetition rate," *Optics Letters*, vol. 31, no. 24, pp. 3629–3631, 2006.

[191] M. Pergament, M. Kellert, K. Kruse, J. Wang, G. Palmer, L. Wissmann, U. Wegner, and M. J. Lederer, "High power burst-mode optical parametric amplifier with arbitrary pulse selection," *Optics Express*, vol. 22, no. 18, pp. 22202–22210, 2014.

[192] T. Stanislauskas, R. Budriunas, R. Antipenkov, A. Zaukevicius, J. Adamonis, A. Michailovas, L. Giniunas, R. Danielius, A. Piskarskas, and A. Varanavicius, "Table top TW-class OPCPA system driven by tandem femtosecond Yb:KGW and picosecond Nd:YAG lasers," *Optics Express*, vol. 22, no. 2, pp. 1865–1870, 2014.

[193] F. Tavella, A. Marcinkevicius, and F. Krausz, "90 mJ parametric chirped pulse amplification of 10 fs pulses," *Optics Express*, vol. 14, no. 26, pp. 12822–12827, 2006.

[194] Q. Zhang, G. Feng, J. Han, B. Li, Q. Zhu, and X. Xie, "High repetition rate laser pulse induced damage in KTP crystal: Gray-tracking and catastrophic damage," *Optik - International Journal for Light and Electron Optics*, vol. 122, no. 15, pp. 1313–1318, 2011.

[195] Schott, "Bubbles and inclusions in optical glass," *Technical Information Advanced Optics*, vol. TIE-28, p. 1, 2014.

[196] L. Kovács, Z. Szaller, K. Lengyel, and G. Corradi, "Hydroxyl ions in stoichiometric $LiNbO_3$ crystals doped with optical damage resistant ions," *Optical Materials*, vol. 37, no. 0, pp. 55–58, 2014.

[197] R. Riedel, J. Rothhardt, K. Beil, B. Gronloh, A. Klenke, H. Höppner, M. Schulz, U. Teubner, C. Kränkel, J. Limpert, A. Tünnermann, M. J. Prandolini, and F. Tavella, "Thermal properties of borate crystals for high power optical parametric chirped-pulse amplification," *Optics Express*, vol. 22, no. 15, pp. 17607–17619, 2014.

[198] A. V. Smith, W. J. Alford, T. D. Raymond, and M. S. Bowers, "Comparison of a numerical-model with measured performance of a seeded, nanosecond KTP optical parametric oscillator," *Journal of the Optical Society of America B-Optical Physics*, vol. 12, no. 11, pp. 2253–2267, 1995.

[199] A. V. Smith and M. S. Bowers, "Phase distortions in sum-frequency and difference-frequency mixing in crystals," *Journal of the Optical Society of America B-Optical Physics*, vol. 12, no. 1, pp. 49–57, 1995.

[200] A. V. Smith, R. J. Gehr, and M. S. Bowers, "Numerical models of broad-bandwidth nanosecond optical parametric oscillators," *Journal of the Optical Society of America B-Optical Physics*, vol. 16, no. 4, pp. 609–619, 1999.

[201] H. P. Li, C. H. Kam, Y. L. Lam, and W. Ji, "Femtosecond Z-scan measurements of nonlinear refraction in nonlinear optical crystals," *Optical Materials*, vol. 15, no. 4, pp. 237–242, 2001.

[202] J. Moses, C. Manzoni, S. W. Huang, G. Cerullo, and F. X. Kärtner, "Temporal optimization of ultrabroadband high-energy OPCPA," *Optics Express*, vol. 17, no. 7, pp. 5540–5555, 2009.

[203] D. X. Zhang, Y. F. Kong, and J. Y. Zhang, "Optical parametric properties of 532-nm-pumped beta-barium-borate near the infrared absorption edge," *Optics Communications*, vol. 184, no. 5-6, pp. 485–491, 2000.

[204] T. Lang, A. Harth, J. Matyschok, T. Binhammer, M. Schultze, and U. Morgner, "Impact of temporal, spatial and cascaded effects on the pulse formation in ultrabroadband parametric amplifiers," *Optics Express*, vol. 21, no. 1, pp. 949–959, 2013.

[205] J. Kim, J. A. Cox, J. Chen, and F. X. Kärtner, "Drift-free femtosecond timing synchronization of remote optical and microwave sources," *Nature Photonics*, vol. 2, no. 12, pp. 733–736, 2008.

[206] M. Ferianis, A. O. Borga, A. Bucconi, M. Predonzani, F. Rossi, and L. Pavlovic, "All-optical femtosecond timing system for the Fermi@Elettra FEL," in *FEL2011*, FEL Proceedings, p. FROAI2, FEL'11/EPS-AG, 2011.

[207] C. Lechner, A. Azima, M. Drescher, L. L. Lazzarino, T. Maltezopoulos, V. Miltchev, T. Plath, J. Rönsch-Schulenburg, J. Roßbach, M. Wieland, S. Ackermann, J. Bödewadt, H. Dachraoui, N. Ekanayake, B. Faatz, M. Felber, K. Honkavaara, T. Laarmann, J. M. Mueller, H. Schlarb, S. Schreiber, S. Schulz, G. Angelova Hamberg, K. E. Hacker, S. Khan, R. Molo, P. M. Salen, and P. van der Meulen, "Measurements of the timing stability at the FLASH1 seeding experiment," in *Proceedings of FEL2014, Basel, Switzerland*, FEL Technology and Hardware: Electron Diagnostics, Timing, Synchronization and Controls, p. THP076, FEL2014, 2014.

[208] C. Manzoni, D. Polli, and G. Cerullo, "Two-color pump-probe system broadly tunable over the visible and the near infrared with sub-30 fs temporal resolution," *Review of Scientific Instruments*, vol. 77, no. 2, 2006.

[209] C. Manzoni, O. D. Mücke, G. Cirmi, S. Fang, J. Moses, S.-W. Huang, K.-H. Hong, G. Cerullo, and F. X. Kärtner, "Cohrerent puls synthesis: towards sub-cycle optical waveforms." preprint, available at `www.wileyonlinelibrary.com`, 2014.

[210] S.-H. Chia, L.-J. Chen, Q. Zhang, O. D. Mücke, G. Chang, and F. X. Kärtner, "Broadband continuum generation in mode-locked lasers with phase-matched output couplers," *Optics Letters*, vol. 39, no. 6, pp. 1445–1448, 2014.

[211] S.-H. Chia, G. Cirmi, S. Fang, G. M. Rossi, O. D. Mücke, and F. X. Kärtner, "Two-octave-spanning dispersion-controlled precision optics for sub-optical-cycle waveform synthesizers," *Optica*, vol. 1, no. 5, pp. 315–322, 2014.

[212] A. M. Weiner, "Ultrafast optical pulse shaping: A tutorial review," *Optics Communications*, vol. 284, no. 15, pp. 3669–3692, 2011.

[213] V. K. Chauhan, J. Cohen, P. M. Vaughan, P. Bowlan, and R. Trebino, "Distortion-free single-prism/grating ultrashort laser pulse compressor," *Ieee Journal of Quantum Electronics*, vol. 46, no. 12, pp. 1726–1731, 2010. 681XT Times Cited:1 Cited References Count:20.

[214] T. D. Krauss and F. W. Wise, "Femtosecond measurement of nonlinear absorption and refraction in CdS, ZnSe, and ZnS," *Applied Physics Letters*, vol. 65, no. 14, pp. 1739–1741, 1994.

[215] R. Ell, U. Morgner, F. X. Kärtner, J. G. Fujimoto, E. P. Ippen, V. Scheuer, G. Angelow, T. Tschudi, M. J. Lederer, A. Boiko, and B. Luther-Davies, "Generation of 5-fs pulses and octave-spanning spectra directly from a Ti:Sapphire laser," *Optics Letters*, vol. 26, no. 6, pp. 373–375, 2001.

[216] M. A. Arbore, A. Galvanauskas, D. Harter, M. H. Chou, and M. M. Fejer, "Engineerable compression of ultrashort pulses by use of second-harmonic generation in chirped-period-poled lithium niobate," *Optics Letters*, vol. 22, no. 17, pp. 1341–1343, 1997.

[217] M. Baudrier-Raybaut, R. Haidar, P. Kupecek, P. Lemasson, and E. Rosencher, "Random quasi-phase-matching in bulk polycrystalline isotropic nonlinear materials," *Nature*, vol. 432, no. 7015, pp. 374–376, 2004.

[218] K. Mizuuchi, K. Yamamoto, M. Kato, and H. Sato, "Broadening of the phase-matching bandwidth in quasi-phase-matched 2^{nd}-harmonic generation," *IEEE Journal of Quantum Electronics*, vol. 30, no. 7, pp. 1596–1604, 1994.

[219] O. E. Martinez, "Achromatic phase matching for 2^{nd} harmonic-generation of femtosecond pulses," *IEEE Journal of Quantum Electronics*, vol. 25, no. 12, pp. 2464–2468, 1989.

[220] G. Szabo and Z. Bor, "Broad-band frequency doubler for femtosecond pulses," *Applied Physics B-Photophysics and Laser Chemistry*, vol. 50, no. 1, pp. 51–54, 1990.

[221] T. R. Zhang, H. R. Choo, and M. C. Downer, "Phase and group-velocity matching for 2^{nd} harmonic-generation of femtosecond pulses," *Applied Optics*, vol. 29, no. 27, pp. 3927–3933, 1990.

[222] J. J. Huang, L. Y. Zhang, W. C. Zhang, S. R. Yan, S. Z. Pu, and W. X. Ren, "Theory of second harmonic generation of ultrashort pulses for collinear achromatic phase matching," *Journal of the Optical Society of America B-Optical Physics*, vol. 30, no. 2, pp. 431–438, 2013.

[223] Y. L. Lee, Y. C. Noh, C. Jung, T. J. Yu, D. K. Ko, and J. Lee, "Broadening of the second-harmonic phase-matching bandwidth in a temperature-gradient-controlled periodically poled Ti : $LiNbO_3$ channel waveguide," *Optics Express*, vol. 11, no. 22, pp. 2813–2819, 2003.

[224] H. Suchowski, D. Oron, A. Arie, and Y. Silberberg, "Geometrical representation of sum frequency generation and adiabatic frequency conversion," *Physical Review A*, vol. 78, no. 6, 2008.

[225] H. Suchowski, V. Prabhudesai, D. Oron, A. Arie, and Y. Silberberg, "Robust adiabatic sum frequency conversion," *Optics Express*, vol. 17, pp. 12731–12740, 2009.

[226] H. Suchowski, B. D. Bruner, A. Ganany-Padowicz, I. Juwiler, A. Arie, and Y. Silberberg, "Adiabatic frequency conversion of ultrafast pulses," *Applied Physics B*, vol. 105, no. 4, pp. 697–702, 2011.

[227] H. Suchowski, G. Porat, and A. Arie, "Adiabatic processes in frequency conversion," *Laser & Photonics Reviews*, pp. 1–35, 2013.

[228] C. R. Phillips, C. Langrock, D. Chang, Y. W. Lin, L. Gallmann, and M. M. Fejer, "Apodization of chirped quasi-phasematching devices," *Journal of the Optical Society of America B-Optical Physics*, vol. 30, no. 6, pp. 1551–1568, 2013.